

Modeling the interaction between a few-cycle relativistic laser pulse and a plasma mirror : from electron acceleration to harmonic generation

Maxence Thévenet

▶ **To cite this version:**

Maxence Thévenet. Modeling the interaction between a few-cycle relativistic laser pulse and a plasma mirror : from electron acceleration to harmonic generation. Plasma Physics [physics.plasm-ph]. Université Paris Saclay (COmUE), 2016. English. ⟨NNT : 2016SACLX112⟩. ⟨tel-01485500⟩

HAL Id: tel-01485500

https://pastel.hal.science/tel-01485500v1

Submitted on 8 Mar 2017

HAL is a multi-disciplinary open access archive for the deposit and dissemination of scientific research documents, whether they are published or not. The documents may come from teaching and research institutions in France or abroad, or from public or private research centers.

L'archive ouverte pluridisciplinaire **HAL**, est destinée au dépôt et à la diffusion de documents scientifiques de niveau recherche, publiés ou non, émanant des établissements d'enseignement et de recherche français ou étrangers, des laboratoires publics ou privés.



HAL Authorization

NNT : 2016 SACLX023

THÈSE DE DOCTORAT DE L'UNIVERSITÉ PARIS-SACLAY
PRÉPARÉE À L'ÉCOLE POLYTECHNIQUE

École Doctorale n°288 – Ondes et Matière
Spécialité : Physique des plasmas

par

Maxence THÉVENET

Modeling the interaction between relativistic laser pulses and plasma mirrors: from electron acceleration to harmonic generation

Thèse présentée et soutenue à Palaiseau le 05/12/2016 :

Pr. Caterina RICONDA	UPMC, Paris	Présidente du jury
Dr. Patrick AUDEBERT	LULI, Palaiseau	Examinateur
Dr. Laurent GREMILLET	CEA, Arpajon	Examinateur
Dr. Emmanuel d'HUMIÈRES	CELIA, Bordeaux	Rapporteur
Pr. Luís O. SILVA	IST, Lisbonne	Rapporteur
Dr. Jérôme FAURE	LOA, Palaiseau	Directeur de thèse

Laboratoire d'Optique Appliquée – UMR 7639

Remerciements

J'ai effectué cette thèse dans le groupe APPLI du Laboratoire d'Optique Appliquée d'octobre 2013 à décembre 2016. Je tiens à remercier toutes les personnes qui m'ont permis de mener ce travail à son terme dans les meilleures conditions.

Mes premiers remerciements vont à mon directeur de thèse Jérôme Faure, responsable du groupe APPLI, qui a su réunir les conditions nécessaires pour que je réalise ce doctorat : un sujet pertinent, un excellent encadrement scientifique et un réel accompagnement humain. Jérôme m'a laissé beaucoup d'autonomie, tout en suivant mon travail et en prodiguant des conseils lorsque j'en avais besoin. Par ailleurs, sa connaissance organique de la physique et sa rigueur m'ont largement inspiré. Enfin, ses critiques, extrêmement constructives et toujours accompagnées d'encouragements, m'ont permis de réellement progresser pendant ces trois années passées dans son groupe.

La physique étant une science de la nature, ce travail théorique et numérique doit beaucoup aux collaborations avec des physiciens expérimentateurs. Je remercie ainsi les membres du groupe UHI au CEA-Iramis, en particulier le chef de groupe Fabien Quéré pour son dynamisme et son enthousiasme communicatif. Merci également à Adrien Leblanc, dont les résultats de très grande qualité sur le laser UHI100 ont toujours été partagés avec efficacité et bonne humeur. Je remercie d'autre part les membres du groupe PCO au LOA, qui développent et exploitent le remarquable laser de la Salle Noire. Grâce notamment au responsable du groupe Rodrigo Lopez-Martens et à Maïmouna Bocoum, j'ai pu participer à l'interprétation de résultats sans avoir à aligner le moindre faisceau.

L'atmosphère du LOA combine qualité scientifique et convivialité, ce qui en fait un excellent cadre de recherche. Je tiens donc à remercier Antoine Rousse, le directeur du laboratoire, qui entretient ce climat. Merci également à l'équipe administrative pour leur efficacité et leur bonne humeur. Je souhaiterais également remercier les rapporteurs Luís O. Silva et Emmanuel d'Humières ainsi que Caterina Riconda, Patrick Audebert et Laurent Gremillet, les examinateurs de cette thèse, pour le temps qu'ils ont consacré à mon travail et pour leurs questions et remarques pertinentes le jour de la soutenance.

Je dois également beaucoup aux membres du groupe APPLI, notamment Aline, Benoît, Geoffrey et Diego. J'ai pu avancer avec confiance dans ce travail grâce à leur amitié et leur sympathie, mais aussi leur qualité de grimpeur ou de joueur de volleyball. Henri m'a étroitement accompagné pendant ma première année de doctorat, et a su m'orienter aux moments opportuns. Je lui dois par ailleurs, ainsi qu'à Agustin, beaucoup de mes connaissances numériques. Je les remercie tous chaleureusement, ainsi que Florian, Jean-Baptiste, Dominykas, Frederik, Magali et tous les autres.

Une thèse est une expérience parfois éprouvante, et je dois beaucoup à mon entourage qui m'a accompagné tout au long de ce projet. Je remercie sincèrement mes amis pour m'avoir parfois supporté dans les moments délicats. Je remercie mes parents et mes frères, Aymeric et Vivien, pour leur soutien inconditionnel et pour la préparation du buffet de soutenance. Je dois enfin beaucoup à Irène, grâce à qui j'ai abordé la rédaction de ce manuscrit et la soutenance avec une relative sérénité. Je la remercie profondément.

Contents

1 Basics of laser-overdense plasma interaction **5**
- 1.1 Laser-generated overdense plasmas . . . 6
  - 1.1.1 Laser-plasma interaction . . . 6
  - 1.1.2 Plasma mirror creation . . . 13
- 1.2 Bourdier boosted frame . . . 18
  - 1.2.1 Lorentz transform . . . 18
  - 1.2.2 Physics in the boosted frame . . . 20
- 1.3 Electron heating mechanisms . . . 22
  - 1.3.1 Resonant absorption . . . 22
  - 1.3.2 Vacuum heating . . . 24
  - 1.3.3 $J \times B$ heating . . . 27
  - 1.3.4 Review of experimental results . . . 29
- 1.4 High harmonic generation on plasma mirrors . . . 33
  - 1.4.1 Train of ultrashort pulses and high harmonic generation . . . 33
  - 1.4.2 Coherent Wake Emission . . . 34
  - 1.4.3 Relativistic Oscillating Mirror . . . 40

2 Numerical tools **51**
- 2.1 Particle-in-cell simulations for laser-plasma interaction . . . 52
  - 2.1.1 The Vlasov-Maxwell system . . . 52
  - 2.1.2 Vlasov numerical method . . . 53
  - 2.1.3 Particle-in-cell method . . . 54
  - 2.1.4 Steps of a PIC code . . . 56
  - 2.1.5 PIC: limits, noise and errors . . . 59
  - 2.1.6 Study on numerical parameters . . . 60
  - 2.1.7 Typical 2D PIC simulation . . . 63
- 2.2 Electron in a laser pulse in vacuum . . . 65
  - 2.2.1 Electron in a monochromatic plane wave . . . 65
  - 2.2.2 Gaussian pulse and paraxial approximation . . . 69
  - 2.2.3 Non-paraxial corrections in the tightly-focused regime . . . 70
  - 2.2.4 Ponderomotive force . . . 71
  - 2.2.5 Finite-duration correction . . . 72

3 Backward electron acceleration from plasma mirrors **75**
- 3.1 Theoretical studies on electron ejection . . . 76
  - 3.1.1 Electron ejection in PIC simulations . . . 76
  - 3.1.2 Density gradient scale length . . . 77
  - 3.1.3 Electron ejection angle . . . 78
  - 3.1.4 Gyromagnetic effect . . . 79

3.1.5 Electron ejection in 1D PIC simulations . . . 82
3.2 Electron ejection with a step-like density profile . . . 84
3.2.1 Phenomenology of electron ejection . . . 84
3.2.2 Push-pull mechanism . . . 86
3.2.3 Relativistic Electronic Spring by Gonoskov . . . 89
3.2.4 Model for electron ejection with a step-like profile . . . 93
3.2.5 Discussion . . . 96
3.3 Electron ejection with an exponential density gradient . . . 97
3.3.1 Surface dynamics . . . 98
3.3.2 Scan $a_0 - L$ with 1D PIC simulations . . . 102
3.3.3 Toy model for the electron ejection . . . 105
3.3.4 Comparison with 2D PIC simulations . . . 109

4 Vacuum Laser Acceleration 113
4.1 Basics of vacuum laser acceleration . . . 115
4.1.1 Particle acceleration . . . 115
4.1.2 Lawson-Woodward theorem . . . 117
4.2 Electron in a laser pulse: typical behaviors . . . 120
4.2.1 Introduction . . . 120
4.2.2 *Ponderomotive* behaviour . . . 121
4.2.3 *VLA* behaviour . . . 123
4.2.4 *VLA/ponderomotive* ratio . . . 128
4.3 Vacuum laser acceleration using a plasma mirror injector . . . 131
4.3.1 Experimental attempts for vacuum laser acceleration . . . 131
4.3.2 Principle . . . 133
4.3.3 Experiment by Adrien Leblanc (UHI100 at CEA) . . . 134
4.3.4 Model . . . 136
4.3.5 Interpretation of the experimental results . . . 139

5 Electron acceleration and high harmonic generation 141
5.1 Anticorrelation CWE/electrons in the low-intensity regime $a_0 < 1$ . . . 143
5.1.1 Experimental results from the *Salle Noire* laser (LOA) by Maïmouna Bocoum . . . 143
5.1.2 Dynamics of ejected electrons . . . 148
5.2 Correlation ROM/electrons in the high-intensity regime $a_0 > 1$ . . . 149
5.2.1 Expected correlation . . . 150
5.2.2 Experimental results from the UHI100 laser (CEA) by Adrien Leblanc . . . 150
5.2.3 Confirmation from PIC simulations . . . 152

A Parameters for numerical simulations I

B Extended Brunel model V

C Summary in French VII

D Publications IX

Introduction

Context

Understanding the dynamics of matter is a major topic in contemporary science, and observing chemical reactions or resolving the motion of atoms in a crystal are extremely challenging because many processes occur on extremely rapid timescales. In a water molecule, the OH bond stretch vibrations have a 10 fs period (1 fs $= 10^{-15}$ s), and one would require a time resolution of a few femtoseconds to observe directly these oscillations.

The study of ultrafast dynamics is achieved via pump-probe experiments, where an ultrashort pump creates an excitation in the sample. The system evolves from this out-of-equilibrium state down to an equilibrium state. This evolution is recorded using another pulse, the probe, that measures the state of the sample some delay τ after the excitation by the pump. By repeating this experiment and scanning the pump-probe delay τ, one can determine the evolution of the material towards the equilibrium state. The time resolution is largely determined by the duration of the probe, and should be in the femtosecond scale to resolve a large number of mechanisms like phonons [Ziman, 1960] or bond breaking.

When the sample is a crystal, the probe forms a diffraction pattern that depends on the crystal state, which provides extremely rich information on the crystal dynamics. In this case, the wavelength of the probe must be smaller than the typical distance between two atoms in a crystal $\sim$ 1Å, so that a photon probe must be in the X-ray range. Such X-ray pulses with a < 100 fs duration are available on the Linac Coherent Light Source at Stanford [Emma *et al.*, 2010], but they require extremely large and expensive facilities. This justifies the current efforts to build cheaper sources, accessible to a broader community.

Bunches of electrons provide a good alternative to X-ray pulses for several reasons: (i) their De Broglie wavelength can be easily made smaller than 1Å; (ii) the cross section of electrons for elastic scattering is five orders of magnitude higher than the one of X-ray photons, so that one requires a bunch with less particles; (iii) their cross section for inelastic scattering is smaller, so they deposit less energy. The risk of damaging the crystal is lowered; (iv) short electron bunches with $\sim$ 100 keV energy and < 100 fs temporal resolution are currently available with electron guns, which are table-top facilities.

Yet, electron guns have intrinsic limitations, and their time resolution cannot be improved indefinitely. A reasonable alternative can be found in laser-plasma interaction. The advent of chirped-pulse amplification [Strickland & Mourou, 1985] opened the possibility to generate high-intensity ($I \sim 10^{18}\,\mathrm{W \cdot cm^{-2}}$) laser pulses with femtosecond duration. When focused on any target, the material is rapidly ionized and turned into a plasma, which can sustain huge electric and magnetic fields. The most popular technique for plasma-based electron acceleration is the laser wakefield accel-

eration method [Esarey *et al.*, 2009; Faure *et al.*, 2004; Geddes *et al.*, 2004; Mangles *et al.*, 2004; Tajima & Dawson, 1979]. In this scheme, a laser pulse propagates through a low-density plasma and creates a cavity in its wake where electric fields as high as $100\,\mathrm{GV}\cdot\mathrm{m}^{-1}$ accelerate electrons up to relativistic energies within a few centimeters. These extremely compact and efficient accelerators are commonly used for accelerating electrons to very high energies ($100\,\mathrm{MeV}-1\,\mathrm{GeV}$). Based on this technique, the APPLI and PCO groups at LOA are developing an original system: the *Salle Noire* laser that provides short electron bunches with a modest energy ($1-10\,\mathrm{MeV}$), more adapted to ultrafast electron diffraction. The possibility to reach a temporal resolution of a few femtoseconds is being investigated. Besides, it is the first system working at a kilohertz rate, which is crucial to have good statistics in pump-probe experiments. Finally, note that the laser pulse and the electron bunch are perfectly synchronized, which makes them ideal candidates for the pump and the probe respectively.

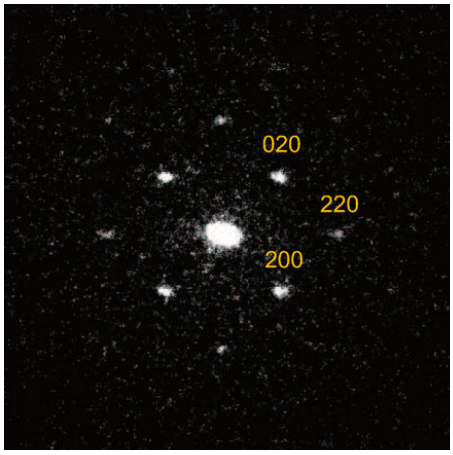


Figure 1: Electron diffraction pattern in Tokita's experiment.

While laser wakefield acceleration relies on the propagation of a laser pulse into an underdense (transparent) plasma, electron acceleration can also occur during the reflection of a laser pulse upon an overdense (opaque) plasma. The very promising results obtained in reference [Tokita *et al.*, 2010] lead us to investigate this field. In their experiment, an ultrashort laser pulse with oblique incidence and p polarization reflects off a very thin film, which surface is immediately ionized and turned into an overdense plasma. A bunch of electrons is accelerated at the surface and propagates through the target, in the frontward direction. This bunch is reshaped using permanent magnets and sent onto a gold crystal, resulting in a very clear diffraction pattern in a single-shot regime, shown in figure 1. Besides, they measure the bunch duration, which is $\sim 500\,\mathrm{fs}$. Yet, this promising scheme suffers from an intrinsic limitation: the electrons have to cross the target, where multiple collisions with atoms result in the bunch elongation, so a better time resolution is unlikely. In order to bypass this limit, we propose to investigate electron ejection in the backward direction, namely in the half-space containing the incident and reflected pulses.

This work is focused on the plasma mirror regime: an ultrashort ($< 100\,\mathrm{fs}$) ultraintense ($I \sim 10^{18}\,\mathrm{W}\cdot\mathrm{cm}^{-2}$) laser pulse is focused onto an overdense plasma. At the target surface, the plasma density does not drop abruptly from the bulk density $n \sim 10^{23}\,\mathrm{cm}^{-3}$ to zero outside the plasma, but rather decreases continuously in a density gradient, on a distance L typically smaller than the laser wavelength λ. The motivation for studying this regime came from the idea of generating attosecond light pulses. While promising results had been obtained in transparent plasmas [Cavalieri *et al.*, 2007; Corkum, 1993; Drescher *et al.*, 2002; Uiberacker *et al.*, 2007], one can expect to generate attosecond pulses with higher intensity using opaque plasmas. When a laser pulse reflects off a plasma mirror, non-linear effects result in the generation of a train of attosecond pulses in the reflected field via two distinct mechanisms: coherent wake emission [Quéré *et al.*, 2006] and the relativistic oscillating mirror effect [Burnett *et al.*, 1977]. Combined with a smart method called *attosecond lighthouse* [Wheeler *et al.*, 2012], this process lead to the observation of isolated attosecond bunches, giving hope that this technique could

lead to shorter and shorter pulses with higher and higher intensity.

Both mechanisms for the generation of attosecond bunches show high harmonics of the laser frequency. While high harmonic generation in the plasma mirror regime is well-understood, the backward electron ejection mechanism remains unclear, in spite of a large amount of experimental results. Besides, the possibility to use this system as a source of electron bunches has not been investigated at all. The opportunity to use a plasma mirror as a unique source to generate simultaneously attosecond light pulses and relativistic electron bunches was too intriguing to leave this question unanswered.

Objectives

I worked on the reflection of a laser pulse onto a plasma mirror in the relativistic regime, and followed three lines of research. The first one is to understand the physics of backward electron ejection, namely to identify the mechanism and highlight the role of the main parameters: the laser intensity and, though it is often omitted, the density gradient scale length L. After electrons are ejected from the plasma, they can be accelerated in vacuum by the electromagnetic fields in the reflected pulse. The possibility to reach this unexplored regime, called vacuum laser acceleration [Haaland, 1995], is the subject of my second topic. The third one is the link between the electron ejection mechanism and the two well-identified mechanisms for high harmonic generation.

The experimental results presented in this manuscript were obtained on two cutting-edge laser systems: the *Salle Noire* system at LOA operated by the PCO and APPLI teams, and delivering pulses with 30 fs duration and 3 mJ energy at a kilohertz rate. The second system is the UHI100 laser facility at CEA, operated by the LIDyL team at CEA-Iramis, that delivers pulses with 30 fs duration and 1 J energy in a single-shot regime. I worked in close collaboration with these experimental teams, and my role was to provide theory and interpretation of their results, so that both works could enrich one another.

I extensively used numerical tools, in particular the particle-in-cell algorithm, so that my thesis enters the general field of computational physics that consists in solving equations with numerical methods when no analytical solution is (or can be) found. This branch of science emerged in Los Alamos in the 1940's and became popular through essential contributions ranging from the field of molecular dynamics [Alder & Wainwright, 1959] to the discovery of the butterfly effect [Lorenz, 1963]. Its contribution to modern science was clearly stated in three Nobel Prizes in chemistry (1985, 1998 and 2013) as well as one in physics (1993). More practically, it provides an extremely powerful tool that considerably extends our understanding of the physics at play in experiments.

Outline

The first chapter introduces basic considerations to study the reflection of a laser pulse upon an overdense plasma. The high harmonic generation processes leading to attosecond pulses are explained in details. The main mechanisms leading to electron ejection from plasma mirrors are presented, and a review of experimental results highlights the need for a better understanding of the backward ejection process.

Chapter 2 introduces the numerical tools I used all along this work: the particle-in-cell method and its implementation in the open-source code EPOCH. A benchmark

of numerical simulations relevant to my purpose is presented.

In the third chapter, the backward electron ejection process is identified, and the role of the laser intensity and the gradient scale length are stated. It is shown that there is an optimal gradient length, for which the ejection of electrons is maximum.

The fourth chapter is dedicated to vacuum laser acceleration. First, general considerations regarding the dynamics of an electron in a laser pulse are given. Second, we show how electrons ejected from the plasma mirror can be injected in the reflected laser pulse, solving the long-standing issue of electron injection for vacuum laser acceleration.

The fifth and last chapter strongly relies on experimental results. We confirm theoretical predictions from chapter 3, in particular we observe the optimal density gradient with the two laser systems operating in very distinct regimes, which consolidates our theory. Then, we investigate the correlation between high harmonic generation and electron ejection.

Toy models and studies in simplified conditions are presented all along this work. I hope that this approach, where complex physical problems are reduced to their skeleton, can provide a valuable understanding to the reader.

Chapter 1

Basics of laser-overdense plasma interaction

Contents

1.1 Laser-generated overdense plasmas 6
1.1.1 Laser-plasma interaction 6
1.1.2 Plasma mirror creation 13
1.2 Bourdier boosted frame 18
1.2.1 Lorentz transform 18
1.2.2 Physics in the boosted frame 20
1.3 Electron heating mechanisms 22
1.3.1 Resonant absorption 22
1.3.2 Vacuum heating 24
1.3.3 $J \times B$ heating 27
1.3.4 Review of experimental results 29
1.4 High harmonic generation on plasma mirrors 33
1.4.1 Train of ultrashort pulses and high harmonic generation . . . 33
1.4.2 Coherent Wake Emission 34
1.4.3 Relativistic Oscillating Mirror 40

Introduction

When an intense laser pulse is focused onto a solid target, say a piece of glass, the material is instantly ionized and forms a plasma with a density gradient on its front side. The first section 1.1 is dedicated to the founding principles of this interaction: how the plasma is ionized, how the gradient is formed and why the laser pulse does not propagate through, but instead reflects off the plasma. An indispensable theoretical tool, the Bourdier boosted frame, is presented in section 1.2.

Experiments performed in this regime showed electrons ejected from the target surface. Section 1.3 gives a review of experimental results as well as the basic mechanisms that can lead to electron acceleration during this interaction, depending on the configuration (angle of incidence, laser intensity, scale length of the density gradient). This section serves several purposes: first, it shows the great variety of experimental results. Second, it brings the essential tools frequenty invoked to explain these results. Third, it shows how the mechanism for electrons accelerated in the backward direction remains unclear.

The reflection off an overdense plasma differs from what happens on a perfect mirror: the reflected field is distorted because of non-linear mechanisms at the plasma surface. The last section 1.4 presents the two non-linear mechanisms that can occur, namely the coherent wake emission and the relativistic oscillating mirror effect, and describes how they lead to high harmonic generation in the reflected pulse.

More generally, this chapter aims at giving the basic tools to understand the reflection of a laser pulse upon a plasma mirror as well as a global intuition of the mechanisms involved in this interaction.

1.1 Laser-generated overdense plasmas

1.1.1 Laser-plasma interaction

Electromagnetic wave in a non-relativistic plasma: fluid model

We present here the equations governing the propagation of an electromagnetic wave in a plasma. The electric and magnetic fields are $\boldsymbol{E}$ and $\boldsymbol{B}$ respectively. The plasma is characterized by the charge density $\rho = en_i - en_e$ and the current density vector $\boldsymbol{J} = en_i\boldsymbol{v_i} - en_e\boldsymbol{v_e}$, with e the elementary charge and n and $\boldsymbol{v}$ the charge density and velocity respectively. Index i is used for ion quantities, and e for electron quantities. Let us derive the Helmholtz equation in a homogeneous plasma, assuming that:

- the plasma is cold, unmagnetized and non-relativistic;
- collisions are negligible;
- ions are immobile.

Using these assumptions, we can use a fluid model where the equations for the local electron density n_e and local electron speed $\boldsymbol{v_e}$ are given by the continuity and the fluid equations:

$$\frac{\partial n_e}{\partial t} + \nabla \cdot (n_e \boldsymbol{v_e}) = 0 \tag{1.1}$$

$$m_e n_e \left(\frac{\partial \boldsymbol{v_e}}{\partial t} + (\boldsymbol{v_e} \cdot \nabla)\boldsymbol{v_e} \right) = -\nabla P - en_e\boldsymbol{E} - en_e\boldsymbol{v_e} \times \boldsymbol{B} \tag{1.2}$$

where m_e is the electron mass and P is the local pressure, which is zero in the non-collisional regime. This system is completed by Maxwell's equations

$$\nabla \cdot \boldsymbol{E} = \frac{\rho}{\epsilon_0} \qquad \text{Gauss's law} \tag{1.3}$$

$$\nabla \cdot \boldsymbol{B} = 0 \qquad \text{Gauss's law for magnetism} \tag{1.4}$$

$$\nabla \times \boldsymbol{E} = -\frac{\partial \boldsymbol{B}}{\partial t} \qquad \text{Faraday's law} \tag{1.5}$$

$$\nabla \times \boldsymbol{B} = \mu_0 \left(\boldsymbol{J} + \epsilon_0 \frac{\partial \boldsymbol{E}}{\partial t} \right) \qquad \text{Ampère's law} \tag{1.6}$$

Assuming a small plasma perturbation, we hereafter derive the Helmholtz equation for a transverse electromagnetic wave with angular frequency ω, such that $\boldsymbol{E} = \bar{\boldsymbol{E}} e^{i\omega t}$. After linearization, equation 1.2 gives the Ohm's law

$$\boldsymbol{J} = -i \frac{\omega_p^2}{\omega} \epsilon_0 \boldsymbol{E} \tag{1.7}$$

where ω_p is the electron plasma frequency, given by

$$\omega_p = \sqrt{\frac{n_e e^2}{m_e \epsilon_0}}. \tag{1.8}$$

The electron plasma frequency only depends on physical constants and on the electron density, and varies as $\propto \sqrt{n_e}$.

Combining Faraday's and Ampère's laws and injecting Ohm's law (equations 1.5, 1.6 and 1.7 respectively), we get the Helmholtz equation for a transverse electromagnetic wave in a plasma

$$\left[\Delta + \frac{\omega^2}{c^2} \left(1 - \frac{\omega_p^2}{\omega^2} \right) \right] \bar{\boldsymbol{E}} = \boldsymbol{0}. \tag{1.9}$$

It is straightforward to define the relative permittivity of the plasma

$$\epsilon_r = 1 - \frac{\omega_p^2}{\omega^2}. \tag{1.10}$$

Finally, for an electromagnetic mode (ω,$\boldsymbol{k}$) such that $\bar{\boldsymbol{E}} = \boldsymbol{E_0} e^{-i\boldsymbol{k}\cdot\boldsymbol{r}}$, the dispersion relation reads

$$\boxed{k^2 c^2 = \omega^2 - \omega_p^2}\,. \tag{1.11}$$

For a given electromagnetic angular frequency ω, say the laser angular frequency, this equation shows two distinct plasma regimes:

underdense plasma ($\omega_p < \omega$): The dielectric constant verifies $\epsilon_r > 0$. The plasma is a transparent medium with a refractive index smaller than one

$$N(\omega) = \sqrt{\epsilon_r} = \sqrt{1 - \frac{\omega_p^2}{\omega^2}}. \tag{1.12}$$

overdense plasma ($\omega_p > \omega$): The dielectric constant verifies $\epsilon_r < 0$. The plasma behaves as a reflective medium, with a skin depth

$$\delta = \frac{1}{\sqrt{-\epsilon_r}}\frac{c}{\omega} = \frac{c}{\sqrt{\omega_p^2 - \omega^2}}. \tag{1.13}$$

Given the angular frequency ω, the plasma is reflective if $n_e > n_c$ where the critical density n_c is given by

$$n_c = \frac{m_e \epsilon_0 \omega^2}{e^2}, \tag{1.14}$$

which clarifies the terms underdense and overdense. For 800 nm Ti:Sapphire lasers, $n_c = 1.74 \times 10^{21}\,\mathrm{cm}^{-3}$.

Laser parameters

For a laser pulse with wavelength λ, angular frequency ω_0 and wave vector $\boldsymbol{k} = k\boldsymbol{e_z} = \omega_0/c$, linearly polarized along x, the electric field near the focus ($z = 0$) in the paraxial approximation (see [Siegman, 1986]) reads

$$\boldsymbol{E}(t,x,y,z) = E_0 \frac{w_0}{w(z)} e^{-\frac{r^2}{w^2(z)}} e^{-\frac{t^2}{\tau^2}} \sin\left[kz - \omega_0 t + k\frac{r^2}{2R(z)} + \mathrm{atan}\left(\frac{z}{z_R}\right)\right]\boldsymbol{e}_x \tag{1.15}$$

with E_0 the peak electric field amplitude, w_0 the beam waist and τ the pulse duration. The radial coordinate, Rayleigh length, beam width and radius of curvature are respectively $r = \sqrt{x^2+y^2}$, $z_R = kw_0^2/2$, $w(z) = w_0\sqrt{1+z^2/z_R^2}$ and $R(z) = z(1+z_R^2/z^2)$. For the sake of simplicity, we neglected the deformation of the temporal envelope along propagation. More details can be found in chapter 2.

Relativistic regime: The interaction regime is said to be relativistic when an electron driven by the laser fields reaches a relativistic velocity. We define the normalized laser amplitude as

$$a_0 = \frac{eE_0}{m_e \omega_0 c}. \tag{1.16}$$

This dimensionless parameter differentiates the **non-relativistic regime** $a_0 \ll 1$ and the **relativistic regime** $a_0 \gtrsim 1$. Note the dependence on the electron mass-to-charge ratio and on the laser amplitude and angular frequency.

The normalized amplitude can be expressed in terms of the laser intensity as:

$$a_0 = \sqrt{\frac{I}{I_0}} \text{ with } I_0\lambda^2 = 1.37 \times 10^{18}\,\mathrm{W\cdot cm^{-2}\cdot \mu m^2}. \tag{1.17}$$

For a $\lambda = 800\,\mathrm{nm}$ Ti:sapphire laser, $a_0 = 1$ reads $E_0 = 4.02 \times 10^{12}\,\mathrm{V\cdot m^{-1}}$ and $I = 2.14 \times 10^{18}\,\mathrm{W\cdot cm^{-2}}$. The terms *low intensity*, *non-relativistic* and *sub-relativistic* refer to the $a_0 \ll 1$ regime.

Ponderomotive potential: The dynamics of an electron propagating in a laser pulse can be fairly complex. In this paragraph, we derive the average ponderomotive force and the associated potential in the non-relativistic regime, neglecting the magnetic

theory/simulations	experiments
w_0 half-width $1/e$ (amplitude)	spot size $= \sqrt{2\log 2} w_0 \simeq 0.78 w_0$ FWHM (intensity)
τ half-width $1/e$ (amplitude)	pulse duration $= \sqrt{2\log 2}\tau \simeq 0.78\tau$ FWHM (intensity)
1 laser period ($\lambda = 800\,\mathrm{nm}$)	2.67 fs
field amplitude: $a_0 = \sqrt{I/I_0}$ with $I_0\lambda^2 = 1.37 \times 10^{18}\,\mathrm{W\cdot cm^{-2}\cdot}\,\mu\mathrm{m}^2$	
$I_0 = 2.14 \times 10^{18}\,\mathrm{W\cdot cm^{-2}}$ for $\lambda = 800\,\mathrm{nm}$	
pulse energy: $\mathcal{E} = \frac{\pi^{3/2}}{2\sqrt{2}} 10^4 I_0 \tau w_0^2 a_0^2$	

Table 1.1: Conversion table between practical quantities for theory and experiments.

force. Another approach can be found in reference [Kibble, 1966]. The equation of motion reads

$$\dot{\boldsymbol{v}} = -\frac{e}{m_e}\boldsymbol{E}(\boldsymbol{r})\sin(\omega_0 t) \tag{1.18}$$

$$\dot{\boldsymbol{r}} = \boldsymbol{v} \tag{1.19}$$

During one laser period, we assume the electron oscillates around position $\boldsymbol{r}_0$ with small displacement $\delta\boldsymbol{r}$ such that the pulse envelope does not vary much during one oscillation:

$$\dot{\boldsymbol{v}} = -\frac{e}{m_e}\left[\boldsymbol{E}(\boldsymbol{r_0}) + \delta\boldsymbol{r}\nabla\cdot\boldsymbol{E}(\boldsymbol{r_0})\right]\sin(\omega_0 t) \tag{1.20}$$

with $|\delta\boldsymbol{r}\nabla\cdot\boldsymbol{E}(\boldsymbol{r_0})| \ll |\boldsymbol{E}(\boldsymbol{r_0})|$. The dominating term in equation 1.20 gives the linear velocity and displacement

$$\boldsymbol{v}_l = \frac{e}{m_e\omega_0}\boldsymbol{E}(\boldsymbol{r}_0)\cos(\omega_0 t) \tag{1.21}$$

$$\delta\boldsymbol{r}_l = \frac{e}{m_e\omega_0^2}\boldsymbol{E}(\boldsymbol{r}_0)\sin(\omega_0 t) \tag{1.22}$$

and the first-order non-linear term $m_e\dot{\boldsymbol{v}}_{nl} = -e\delta\boldsymbol{r}_l\nabla\cdot\boldsymbol{E}(\boldsymbol{r_0})\sin(\omega_0 t)$ gives the ponderomotive force when averaged over one laser period

$$\boldsymbol{F}_p = <m_e\dot{\boldsymbol{v}}_{nl}>_t = -\frac{e^2}{4m_e\omega_0^2}\nabla\boldsymbol{E}^2(\boldsymbol{r_0}) \tag{1.23}$$

Finally, $\boldsymbol{F}_p = -\nabla\phi_p$, where ϕ_p is the ponderomotive potential:

$$\phi_p = \frac{e^2\boldsymbol{E}^2}{4m_e\omega_0^2} = m_e c^2\frac{a_0^2}{4}. \tag{1.24}$$

This expression is valid in the non-relativistic regime only, where $a_0 \ll 1$. Note that the ponderomotive potential grows as a_0^2.

While equations are easily readable in the form of 1.15, experimentalists do not deal directly with w_0, τ or E_0. Table 1.1 helps with basic conversion with parameters more practical for experimentalists in the case of Gaussian time and space envelopes.

laser system	**UHI100**	***Salle Noire***
wavelength	800 nm	800 nm
duration	30 fs	25 fs
peak power	100 TW	0.2 TW
repetition rate	1 Hz	1 kHz
spot size	5.5 μm	1.7 μm
peak intensity	$2 \cdot 10^{19}$ W $\cdot$ cm^{-2}	10^{18} W $\cdot$ cm^{-2}
peak a_0	3.1	0.7

Table 1.2: Description of the UHI100 laser at CEA and *Salle Noire* laser at LOA, with which experiments described in this manuscript were performed.

Scope of the present work

The theoretical work described in this thesis is based on experiments performed with two laser systems: the UHI100 laser at CEA and the *Salle Noire* laser at Laboratoire d'Optique Appliquée (LOA). Both systems use the chirped-pulse amplification technique and deliver ultrashort (few periods FWHM) and ultraintense (relativistic intensity) pulses. Their respective features are summarized in table 1.2, along with usual focusing conditions.

Let us assume the half space $x > 0$ is filled with a uniform, cold and unmagnetized plasma with electron density n_e and plasma frequency ω_p. An incident electromagnetic wave with wave vector $\boldsymbol{k_i} = (k_{ix}, k_{iy}, 0)$ such that $k_{ix} > 0$, and angular frequency $\omega_i < \omega_p$ so that the plasma is overdense, is reflected by the plasma edge with 100% reflectivity. In the linear regime, *i.e.* low-intensity regime, the reflected wave has the same angular frequency as the incident one ($\omega_r = \omega_i$) and the wave vector is $\boldsymbol{k_r} = (-k_{rx}, k_{ry}, 0)$.

In this section, we describe non-linear effects that occur when two of the previous hypotheses are broken: (i) the incident wave intensity is high, and (ii) the plasma is not homogeneous, with a density gradient from 0 to the bulk density n_{bulk} around $x = 0$. Typical non-linear effects are

- plasma heating, resulting in a $< 100\%$ reflectivity;
- particle acceleration;
- harmonic generation in the reflected wave, and hence $\omega_r \neq \omega_i$;
- Excitation of plasma waves $\rightarrow$ collective effects.

We study the interaction of an ultrashort ultraintense laser pulse with an overdense plasma with a density gradient on its front side. In common experiments, the density gradient is created by sending a prepulse before the main pulse on an optically flat solid target (usually fused silica SiO_2) to ionize the target and create the plasma. The plasma expands in vacuum, creating a density gradient; the gradient length is determined by the delay between the prepulse and the main pulse. Note that an uncontrolled density gradient can also appear after ionization by the nanosecond pedestal of the laser pulse due to amplified spontaneous emission if the laser contrast is poor.

Figure 1.1 shows the general setup investigated in this thesis, namely the reflection of an obliquely-incident p-polarized ultraintense laser pulse on a plasma mirror. The

plasma is highly overdense ($n_{bulk} \sim 200 n_c$) and the density gradient is usually smaller than the wavelength of the incident wave. Details on the plasma formation and its properties (maximum density, gradient length) are given in section 1.1.2. In this work, the terms *density gradient* and *preplasma* will be synonymous.

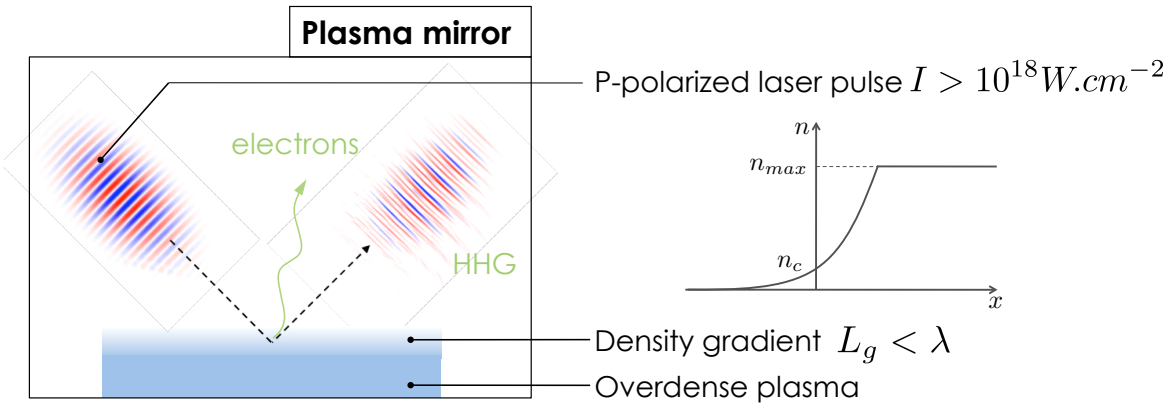


Figure 1.1: Schematic of a plasma mirror. The laser pulse is obliquely-incident, p-polarized, ultraintense ($a_0 \sim 1$) and ultrashort ($\tau \sim 25\,\mathrm{fs}$). The plasma is highly overdense ($n_{bulk} \sim 200 n_c$) and has an exponential density gradient on its front side, with a scale length smaller than the wavelength of the incident wave. As will be described below, this interaction leads to high harmonic generation (HHG) and electron acceleration.

In this thesis, we investigate the ultrashort ($\tau \simeq$ few laser periods), tightly focused ($w_0 \simeq$ few wavelengths), relativistic ($a_0 \gtrsim 1$) regime.

Plasma parameters

The plasma state is the seat of phenomena with extremely disparate space and time scales (binary collisions between particles, collective magnetohydrodynamics effects in stars). Depending on the conditions, different assumptions can be made, that lead to different descriptions of the plasma state, as shown on diagram 1.2. Here, we show characteristic plasma parameters that help understand which physics is at play in a dense plasma, as well as which description of the plasma is relevant. Typically, we should determine whether electron-ion collisions should be considered, and if the plasma is dominated by short or long distance interactions.

Numerical values are given for the reflection of a laser pulse with intensity $a_0 \sim 1$ on a plasma with electron temperature $T_e = 100\,\mathrm{eV}$ and density $n_e = 5 \times 10^{23}\,\mathrm{cm}^{-3}$ to give orders of magnitude of the main parameters in the preplasma.

Average distance between two electrons: This distance is related to the electron density n_e via

$$d_e = n_e^{-1/3}. \tag{1.25}$$

In the regime we study, $d_e \simeq 100\,\mathrm{pm} \simeq \lambda/10000$.

Landau length: When an electron travels with very high velocity in a plasma, it is hardly deviated by collisions with other particles. This remark can be extended to the whole electron population: if the mean (thermal) kinetic energy $k_B T_e$ is much higher than the electron-electron Coulomb potential $e^2/4\pi\epsilon_0 r$, the effect of each collision is

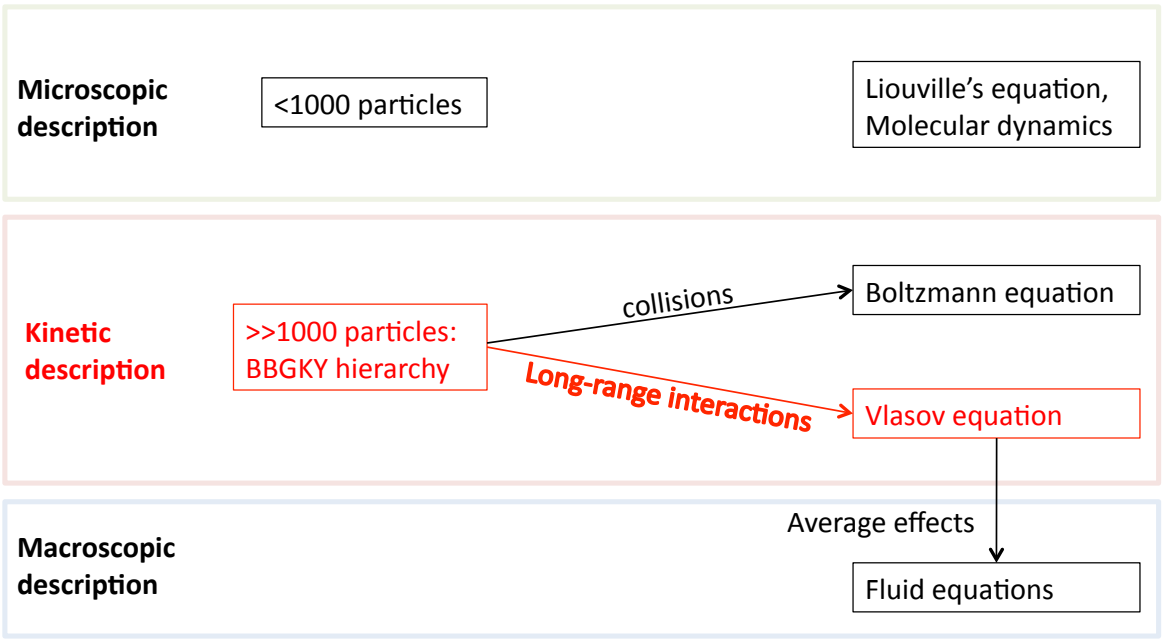


Figure 1.2: Appropriate description depending on the plasma parameters. BBGKY stands for Bogoliubov-Born-Green-Kirkwood-Yvon.

negligible (though multiple collisions might play a role in large systems). The Landau length is defined as the length for which both quantities match:

$$\lambda_{La} = \frac{e^2}{4\pi\epsilon_0 k_B T_e}. \tag{1.26}$$

If the mean distance between two electrons is much smaller than this distance ($d_e \ll \lambda_{La}$), the mean Coulomb potential is much higher than the mean kinetic energy of the electrons. In this case, the plasma dynamics is dominated by particle-particle interaction, *i.e.* collisions. On the opposite, if $d_e \gg \lambda_{La}$, the electrons travel without seeing their closest neighbors, and collisions are negligible. In the preplasma case, $\lambda_{La} \simeq 10\,\mathrm{pm} \simeq \lambda/100000$, so that $d_e/\lambda_{La} \simeq 10$. This ratio is far higher during the reflection process, which typically takes place at lower densities and with suprathermal electrons. As a consequence, collisions are negligible during the reflection process.

Debye length: When a single charge is added to a neutral plasma, the induced potential is screened by the neighboring charges that surround it. This is a collective effect, which involves many electrons instead of binary interactions. Assuming the electron population behaves like a fluid, the screened potential reads $\phi_{De} = e^2 e^{r/\lambda_{De}}/4\pi\epsilon_0 r$, where λ_{De} is the characteristic screening (or shielding) length, called the Debye lenth, and defined as

$$\lambda_{De} = \sqrt{\frac{\epsilon_0 k_B T_e}{n_e e^2}}. \tag{1.27}$$

The Debye length is the first length that characterizes collective phenomena because it involves the shielding of an electron by a collection of other electrons. Yet the fluid hypothesis holds true only if there is a large number of electrons in a Debye sphere, *i.e.* $n_e \lambda_{De}^3 \gg 1$. It is the case in the regime we study where $\lambda_{De} \simeq 10\,\mathrm{nm} \simeq \lambda/100$, so that $n_e \lambda_{De}^3 \sim 10^5$. In this condition, the plasma dynamics is governed by long-range average interactions, which is best described by the Vlasov equation.

regime	a_0	n_e	T_e	duration τ	ν_{ei}	$\tau\nu_{ei}$	collisions
prepulse	0.01	$50n_c$	10 eV	30 fs	$20\,\text{fs}^{-1}$	600	**yes**
expansion	-	$50n_c$	10 eV	10 ps	$20\,\text{fs}^{-1}$	10^5	**yes**
main pulse	1	$1-10n_c$	100 keV	30 fs	$1\,\text{ns}^{-1}$	10^{-5}	**no**

Table 1.3: Collisions during the ionization, expansion and main pulse reflection processes. The main pulse is reflected around the critical density $n = n_c$. The electron temperature is estimated via the ponderomotive potential.

Electron-ion collision frequency: Though the Landau length gives hints about whether the plasma is dominated by collisions or kinetic effects, it does not take into account the duration and scale length of the processes we are interested in. The electron-ion collision frequency gives a more precise tool to determine if collisions should or should not be taken into account. As can be found in [Dendy, 1995; Kruer, 1988], it reads

$$\nu_{ei} = \frac{4(2\pi)^{1/2}}{3}\frac{n_e Z^* e^4}{m_e^2 v_{te}^3}\ln\Lambda \tag{1.28}$$

$$= 2.91\times10^{-6}Z^*\frac{n_e[\,\text{cm}^{-3}]}{T_e[eV]^{3/2}}\ln\Lambda \tag{1.29}$$

with Z^* the charge state, v_{te} the electron thermal velocity and $\ln\Lambda$ the Coulomb logarithm were Λ is the ratio between the largest and the smallest cross sections $\Lambda = b_{max}/b_{min}$, for example the Debye length and the distance of closest approach respectively. The Coulomb logarithm is $\ln\Lambda \sim 5-15$. As expected, collisions are more likely when the density is higher. Furthermore, the higher the temperature, the lower the effective cross section, and the lower the total collision frequency.

In the following section 1.1.2, three different regimes will be considered: (i) the plasma ionization with a low-intensity prepulse, (ii) the plasma expansion in vacuum and (iii) the reflection of the main pulse on the plasma mirror. Table 1.3 summarizes the role of collisions in these three regimes. The double inequality is satisfied for the reflection of the main laser pulse $\lambda_{La} \ll d_e \ll \lambda_{De}$ and the collisionless kinetic description is appropriate, see [Delcroix & Bers, 1994]. The heating by the prepulse and the plasma expansion must be treated with different tools including collisions. This is done in the following section.

1.1.2 Plasma mirror creation

As described in the previous section, the plasma mirror regime consists of an overdense plasma with a density gradient on its front side, on which a laser pulse is reflected. The role of the density gradient characteristic length is of paramount importance in the physics involved and will be described in chapter 3. While creating an overdense plasma proves rather simple in experiments (it consists in focusing an intense enough laser pulse onto any solid material), controlling the preplasma characteristic length is much more challenging.

In the experiments, the preplasma is created by picking off a tiny fraction of the laser pulse and focusing it onto the target before the main pulse in order to ionize its atoms/molecules and create the plasma. Then, the plasma expands in vacuum, forming the density gradient with an exponential shape. The gradient characteristic length is controlled by setting the delay between the prepulse and the main pulse.

The prepulse intensity must be high enough to ionize the target. Its waist is generally much larger than that of the main pulse for the gradient length to be the same over the whole focal spot. It typically has a sub-relativistic intensity and the same duration as the main pulse (few tens of femtoseconds).

The following sections describe each of the steps that lead to the controlled gradient length: ionization, heating and expansion. Finally, at the end of this section, table 1.5 shows the plasma density, temperature and expansion speed for the two laser systems we used.

Ionization by the prepulse

The energy of laser photons is $\epsilon = \hbar\omega \simeq 1.5\,\mathrm{eV}$, far below the ionization energy of electrons in the outermost occupied shell of common atoms. Possible ionization mechanisms induced by the laser field in this regime are (i) multiphoton ionization if the atom binding potential is not significantly disturbed by electric field or (ii) tunnel ionization and (iii) barrier-suppression ionization if the atom binding potential is strongly distorted by the laser electric field. These mechanisms are illustrated in figure 1.3.

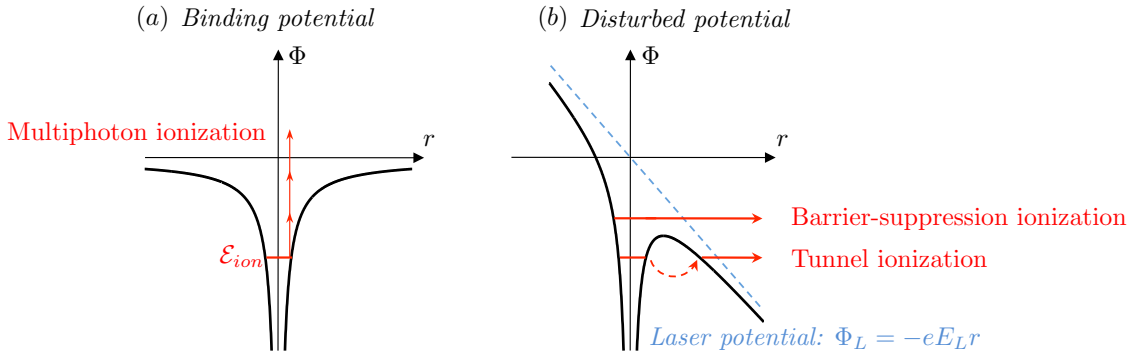


Figure 1.3: (a) The external electric field is weak, the atom binding potential is not distorted and the prevailing mechanism is multiphoton ionization. (b) The strong external field disturbs the binding potential, and ionization occurs via tunnel ionization or barrier-suppression ionization.

The prepulse intensity is strong enough for barrier-suppression ionization to be the dominant mechanism. The simplified 1D model described below can be found in reference [Gibbon, 2004]. Let $E_L > 0$ be the amplitude of the x-polarized laser electric field. The total electric potential for the electron reads

$$\Phi(x) = -\frac{Z^* e^2}{4\pi\epsilon_0 x} - eE_L x \tag{1.30}$$

where Z^* is the ionization degree (also called charge state) to take into account the effect of the mean ion binding potential. As shown in figure 1.3, barrier-suppression ionization (BSI) occurs when $\max_{[x>0]}(\Phi) \leq \mathcal{E}_i$ where $\mathcal{E}_i$ is the ionization energy for the test-electron. Hence, the threshold for the field amplitude is given by $E_{BSI} = \pi\epsilon_0 \mathcal{E}_i^2 / Z^* e^3$, and the intensity threshold is

$$I_{BSI[\,\mathrm{W\cdot cm^{-2}}]} = 4 \times 10^9 \frac{\mathcal{E}_{i[eV]}^4}{Z^{*2}}. \tag{1.31}$$

ionization state	ionization energy $\mathcal{E}_{i[eV]}$	intensity threshold $I_{BSI[\mathrm{W\cdot cm^{-2}}]}$
Si^{+}	8.15	1.76×10^{13}
Si^{2+}	16.3	7.06×10^{13}
Si^{3+}	33.5	5.60×10^{14}
Si^{4+}	45.1	1.03×10^{15}
Si^{5+}	167	1.24×10^{17}
Si^{6+}	205	1.96×10^{17}
Si^{7+}	247	3.04×10^{17}
Si^{8+}	304	5.34×10^{17}
Si^{9+}	351	7.50×10^{17}
Si^{10+}	401	1.03×10^{18}
Si^{11+}	476	1.70×10^{18}
Si^{12+}	523	2.08×10^{18}
Si^{13+}	2440	8.35×10^{20}
O^{+}	13.6	1.37×10^{14}
O^{2+}	35.1	1.52×10^{15}
O^{3+}	54.9	4.04×10^{15}
O^{4+}	77.4	8.97×10^{15}
O^{5+}	114	2.70×10^{16}
O^{6+}	138	4.03×10^{16}
O^{7+}	739	2.43×10^{19}

Table 1.4: Intensity threshold for barrier-suppression ionization for electrons in silicon and oxygen.

As an example related to experiments, we consider a pure SiO_2 target. The ionization energies for single atoms of silicon and oxygen are presented in table 1.4, along with the corresponding intensity threshold.

The plasma density is the molecular density multiplied by the number of electrons ionized in each atom of the molecule. For example, the $3.5 \times 10^{14}\,\mathrm{W \cdot cm^{-2}}$ prepulse from the *Salle Noire* system ionizes two electrons of the silicon atom and one electron of each oxygen atom, which gives a total of 4 electrons per SiO_2 molecule. The molecular density n_{mol} in fused silica is $n_{mol} = 2.2 \times 10^{22}\,\mathrm{cm^{-3}}$, which gives the maximum plasma density $n_{bulk} = 8.8 \times 10^{22}$, or $n_{bulk} = 50 n_c$.

Finally, we can calculate the energy lost by the prepulse to ionize the target. We assume that the volume of plasma reads $V = \delta_s w_0^2$ where δ_s is the plasma skin depth and w_0 is the prepulse waist. The total energy required to create the plasma reads

$$\mathcal{E}_{ionization} = \sum_{atom} \sum_{level} \epsilon_{a,i} n_{mol} \delta_s w_0^2 \tag{1.32}$$

where the first sum is performed on the atoms of each molecule and the second one on the ionization levels of each atom. $\epsilon_{a,i}$ is the ionization energy for atom a and level i. This expression gives $\mathcal{E}_{ionization} = 250\,\mathrm{nJ}$, namely 2.5% of the $10\,\mu\mathrm{J}$ prepulse energy.

Collisional heating by the prepulse

The prepulse ionizes the target and heats electrons while ions remain immobile. This process results in a two-fluid plasma: electrons with temperature T_e and ions with

temperature $T_i = 0$. We hereafter derive a rough estimate of the electron temperature T_e.

An order of magnitude for the electron temperature can be obtained directly from the absorption coefficient measured in experiments. As can be found in [Borot, 2012; Chen *et al.*, 2008; Gibbon, 1996; Vincenti *et al.*, 2014] and in the experiments on the UHI100 laser, the absorption for an ultrashort ($\tau \ll 1\,\mathrm{ps}$) laser pulse with intensity $I \sim 10^{12-15}\,\mathrm{W\cdot cm^{-2}}$ on a largely overdense ($n \gg n_c$) plasma with a step-like profile is of the order of $5 - 30\%$. We take $\eta_a = 1/10$ for the absorbed fraction.

Under these conditions, a simple description for the collisional plasma heating by an ultrashort laser pulse is presented in reference [Gibbon, 2004]. The energy transport equation reads

$$\frac{\partial \epsilon}{\partial t} + \nabla \cdot (\boldsymbol{h} + \boldsymbol{f}_a) = 0 \tag{1.33}$$

where ϵ is the energy density, $\boldsymbol{h}$ is the heat flow and $\boldsymbol{f}_a$ is the absorbed laser flux. We assume that the heat flow is negligible during the pulse reflection because the pulse is ultrashort. Hence, the plasma is heated as a whole. Besides, we assume that the characteristic length for the plasma heating is the plasma skin depth $\delta_s = c/\omega_p$. Noting that $\delta_s \ll w_0$ where w_0 is the laser beam waist, the problem is reduced to a 1D geometry along the target normal direction x. Hence, the absorbed laser flux reads $\boldsymbol{f}_a = f_a \boldsymbol{e_x}$ and we approximate the spatial derivative as $\nabla \cdot \boldsymbol{f}_a = -f_a/\delta_s$. Writing the absorbed laser flux as a fraction of the incident laser flux $f_a = \eta_a f_L$ and the energy density $\epsilon = 3/2 n_e k_B T_e$, the heating rate reads

$$\frac{d}{dt} k_B T_e = 4 \frac{f_a[\,\mathrm{W\cdot cm^{-2}}]}{n_e[\mathrm{cm^{-3}}]\delta_s[\mathrm{cm}]}\,\mathrm{keV\cdot\,fs^{-1}}. \tag{1.34}$$

The final electron temperature is given by this heating rate times the pulse duration. We apply this to the *Salle Noire* laser system, approximating the 25 fs Gaussian time envelope by a 20 fs square envelope, with maximum intensity $3.5 \times 10^{14}\,\mathrm{W\cdot cm^{-2}}$. The value for the plasma density was calculated in the previous paragraph $n_e = 50 n_c$, and the related skin depth is $\delta_s \simeq \lambda/44$, giving a temperature $T_e = 16\,\mathrm{eV}$.

Expansion

After the prepulse reflection, the two-fluid plasma evolves freely. As shown in [Kruer, 1988], a fraction of the thermal electron energy is transferred to ions via collisions, and the plasma expands in vacuum on a picosecond timescale. Neglecting the magnetic force, the fluid equation of motion for the electron population reads

$$m_e n_e \left(\frac{\partial \boldsymbol{v_e}}{\partial t} + (\boldsymbol{v_e} \cdot \nabla)\boldsymbol{v_e} \right) = -\nabla P_e - e n_e \boldsymbol{E} \tag{1.35}$$

with P_e the electron thermal pressure. We assume that this process is quasistatic and neglect electron inertia. Hence, the LHS term in equation 1.35 is zero, which gives the electric field as a function of the electron pressure $e n_e \boldsymbol{E} = -\nabla P_e$. The process is 1D along x, so that the nabla operator simplifies to $\nabla \sim \partial_x$.

Adding the following assumptions:

- Equation of state for the electrons $P_e = n_e k_B T_e$;
- Ion pressure negligible relative to the electron pressure;

- The plasma is neutral on the mesoscopic scale $n_e = Z^* n_i$ with Z^* the ion charge state.

Using these assumptions, the ion continuity equation and force equation along x read

$$\partial_t n_i + \partial_x (n_i v_i) = 0 \tag{1.36}$$

$$\partial_t v_i + v_i \partial_x v_i = \frac{Ze}{m_i} E_x = -c_s^2 \frac{\partial_x n_i}{n_i} \tag{1.37}$$

where c_s is the ion sound velocity given by

$$c_s = \sqrt{\frac{Z k_B T_e}{m_i}}. \tag{1.38}$$

Kruer proposes a self-similar solution via the new parameter $\xi = x/t$ with $n_i(x,t) = N(\xi)$ and $v_i(x,t) = V(\xi)$, so that for these new functions $\partial_x \equiv (t^{-1})\times$ and $\partial_t \equiv (-\xi/t)\times$. The system 1.36 and 1.37 reads

$$(V - \xi)N' + NV' = 0 \tag{1.39}$$

$$(V - \xi)V' + c_s^2 \frac{N'}{N} = 0 \tag{1.40}$$

from which one can show

$$V = \xi + c_s \tag{1.41}$$

$$\frac{N'}{N} = -\frac{1}{c_s} \tag{1.42}$$

where the second equation shows an exponential solution. Finally, this self-similar solution reads

$$v_i = c_s + \frac{x}{t} \tag{1.43}$$

$$n_i = n_0 \exp(-\frac{x}{c_s t}), \tag{1.44}$$

which describes an exponential density gradient with a time-dependent characteristic length

$$L = c_s t. \tag{1.45}$$

The gradient expands at the ion sound velocity, which can be calculated using the temperature from the previous paragraphs. Numerical values for each step of the gradient creation can be found in table 1.5 for the *Salle Noire* and the UHI100 laser systems. The expansion velocity shows good agreement with experimental measurements.

Finally, the gradient length can be tuned by controlling the delay between the prepulse and the main pulse. Note that the maximum density values presented above stand between the plasma ionization by the prepulse and the end of the expansion phase. When the front edge of the main pulse reaches the plasma, it ionizes additional electrons from each ion without moving the ions themselves. This results in a density gradient with the gradient length L calculated above, and a maximum plasma density depending on the main pulse intensity. These values are typically $n = 250 n_c$ and $n = 300 n_c$ for the *Salle Noire* and the UHI100 lasers respectively.

In the following sections, we study the interaction of the main pulse with the plasma, taking the laser intensity, the angle of incidence and the gradient scale length as free parameters. The following section introduces an indispensable tool for this study: the boosted frame.

units	I $\mathrm{W \cdot cm^{-2}}$	Z^{Si} -	Z^{O} -	n n_c	δ_s λ	T_e eV	c_s^{Si} nm/ps	c_s^{O} nm/ps	c_s^{exp} nm/ps
Salle Noire	3.5×10^{14}	2	1	50	1/44	16	10	10	10.8
UHI100	10^{16}	4	4	150	1/80	300	65	90	70

Table 1.5: Numerical values for preplasma formation. The expansion speed is given for each element, and can be compared with experimental measurements.

1.2 Bourdier boosted frame

The reflection of an obliquely-incident p-polarized laser pulse on a plane target is a 3D phenomenon. If the laser pulse is approximated by a plane wave, the problem does not depend on the z direction anymore, perpendicular to the plane of incidence $x-y$, and the problem is reduced to a two-dimensional study. This is illustrated in figure 1.4 a), where the notations are defined. In reference [Bourdier, 1983], the author proposed a Lorentz transformation which reduces this problem to a 1D problem along the target normal x.

This reduction has two major advantages: first, numerical simulations of a 1D phenomenon requires much less computer resources (more details on particle-in-cell simulations can be found in chapter 2). Second, the physics can be equivalently studied in both frames of reference, and the Bourdier boosted frame can simplify the study of some observables. This section introduces the basics of this transformation as well as its relevance to study the reflection of a laser pulse.

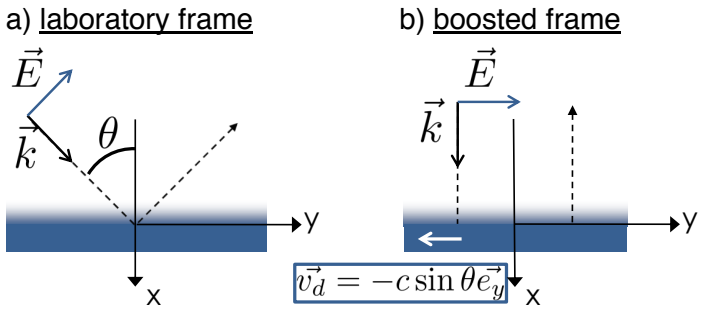


Figure 1.4: a) Diagram for the reflection of an electromagnetic wave on a plasma mirror. The incident wave is p-polarized and the angle of incidence is θ. b) Same setup in the boosted frame introduced by Bourdier. After a Lorentz transform, the incident wave is normally incident on the plasma mirror which drifts with speed $v_d = -c \sin\theta$ in the y direction.

1.2.1 Lorentz transform

Let $\mathcal{R}$ be the laboratory frame and $\mathcal{R}'$ the boosted frame, moving with normalized speed $\boldsymbol{\beta} = \beta \boldsymbol{e_y}$. The associated Lorentz factor is $\gamma = 1/\sqrt{1-\beta^2}$. Let us derive the appropriate drift velocity that turns the oblique incidence into normal incidence, as well as the transformation for the electromagnetic fields and canonical momentum.

Electromagnetic field transformation

The four-vector of the incident wave $(\omega_0/c,\boldsymbol{k}) = \omega_0/c(1,\cos\theta,\sin\theta,0)$ is transformed as

$$\begin{pmatrix}\omega_0'/c\\ k_x'\\ k_y'\\ k_z'\end{pmatrix} = \begin{pmatrix}\gamma & 0 & -\gamma\beta & 0\\ 0 & 1 & 0 & 0\\ -\gamma\beta & 0 & \gamma & 0\\ 0 & 0 & 0 & 1\end{pmatrix}\begin{pmatrix}\omega_0/c\\ \omega_0/c\cos\theta\\ \omega_0/c\sin\theta\\ 0\end{pmatrix} = \frac{\omega_0}{c}\begin{pmatrix}\gamma(1-\beta\sin\theta)\\ \cos\theta\\ \gamma(\sin\theta-\beta)\\ 0\end{pmatrix}. \tag{1.46}$$

Choosing $\beta = \sin\theta$ (hence $\gamma = 1/\cos\theta$) gives $k_y' = 0$, which results in the incident wave to be normally-incident on the plane target in the boosted frame with angular frequency $\omega_0' = \cos\theta\omega_0$. The result is shown in figure 1.4 b), and the problem becomes one-dimensional in the x direction.

To get a better understanding on the boosted frame, let us look at the fields transformation directly.

$$\boldsymbol{k} = \tfrac{\omega_0}{c}\begin{pmatrix}\cos\theta\\ \sin\theta\\ 0\end{pmatrix} \quad \boldsymbol{E} = E_0\sin\phi\begin{pmatrix}-\sin\theta\\ \cos\theta\\ 0\end{pmatrix} \quad \boldsymbol{B} = B_0\sin\phi\begin{pmatrix}0\\ 0\\ 1\end{pmatrix} \tag{1.47}$$

with $k = \omega_0/c$ and the phase $\phi = \omega_0 t - k\cos\theta x - k\sin\theta y$. The space-time transformation reads

$$t' = \gamma(t - \beta\frac{y}{c}) \tag{1.48}$$
$$x' = x \tag{1.49}$$
$$y' = \gamma(y - c\beta t) \tag{1.50}$$
$$z' = z \tag{1.51}$$

with $\beta = \sin\theta$ and $\gamma = 1/\cos\theta$. The phase ϕ is readily transformed as

$$\phi' = \omega_0\cos\theta t' - \frac{\omega_0\cos\theta}{c}x'. \tag{1.52}$$

The fields transformation reads

$$\boldsymbol{E}_{/\!/}' = \boldsymbol{E}_{/\!/} \tag{1.53}$$
$$\boldsymbol{B}_{/\!/}' = \boldsymbol{B}_{/\!/} \tag{1.54}$$
$$\boldsymbol{E}_{\perp}' = \gamma(\boldsymbol{E}_{\perp} + c\boldsymbol{\beta}\times\boldsymbol{B}_{\perp}) \tag{1.55}$$
$$\boldsymbol{B}_{\perp}' = \gamma(\boldsymbol{B}_{\perp} - \frac{1}{c}\boldsymbol{\beta}\times\boldsymbol{E}_{\perp}) \tag{1.56}$$

where the subscript $/\!/$ stands for the component parallel to the boost speed and $\perp$ stands for the orthogonal ones. The incident laser electric and magnetic fields are transformed as

$$E_x' = 0 \tag{1.57}$$
$$E_y' = E_0\cos\theta\sin\phi' \tag{1.58}$$
$$E_z' = 0 \tag{1.59}$$
$$B_x' = 0 \tag{1.60}$$
$$B_y' = 0 \tag{1.61}$$
$$B_z' = B_0\cos\theta\sin\phi' \tag{1.62}$$

These expressions, along with 1.52, are those of a plane wave propagating along the x direction (normally incident onto the plasma), with angular frequency $\omega_0' = \omega_0 \cos\theta$ and amplitude $E_0' = E_0 \cos\theta$. Note that the normalized amplitude is unchanged after the transformation: $a_0' = a_0$.

The plasma density is a number of particles $\delta^3 N$ per unit volume. A given density in the laboratory frame n is transformed in the boosted frame as $n' = \delta^3 N/(\delta x' \times \delta y' \times \delta z') = \delta^3 N/(\delta x \times \cos\theta \delta y \times \delta z)$. Finally, the plasma density is transformed as

$$n' = n/\cos\theta. \tag{1.63}$$

Canonical momentum transformation

The energy-momentum 4-vector is transformed via the boost matrix, which reads

$$\begin{pmatrix} \mathcal{E}' \\ p_x'c \\ p_y'c \\ p_z'c \end{pmatrix} = \begin{pmatrix} \gamma & 0 & -\gamma\beta & 0 \\ 0 & 1 & 0 & 0 \\ -\gamma\beta & 0 & \gamma & 0 \\ 0 & 0 & 0 & 1 \end{pmatrix} \begin{pmatrix} \mathcal{E} \\ p_x c \\ p_y c \\ p_z c \end{pmatrix} = \begin{pmatrix} \gamma\mathcal{E} - \beta\gamma p_y x \\ p_x c \\ -\beta\gamma\mathcal{E} + \gamma p_y c \\ p_z c \end{pmatrix}. \tag{1.64}$$

with $\mathcal{E} = \sqrt{1 + (p/m_e c)^2} m_e c^2$ the particle energy. The only component of the momentum modified in this transformation is the one parallel to the boost speed p_y. One can easily check that an electron at rest in the laboratory frame travels with momentum $p_y' = -\tan\theta m_e c$ in the boosted frame. As a consequence, the plasma is not initially at rest in the boosted frame: it drifts with speed $\beta_y = -c\sin\theta$ instead.

Finally, the transformation of the main quantities upon this Lorentz transform are summarized below:

$$a_0' = a_0 \qquad \omega_0' = \omega_0 \cos\theta \qquad n' = n/\cos\theta \tag{1.65}$$

$$dx' = dx \qquad dy' = dy\cos\theta \qquad dz' = dz \tag{1.66}$$

$$E_0' = E_0\cos\theta \qquad B_0' = B_0\cos\theta \qquad \lambda' = \lambda/\cos\theta \tag{1.67}$$

1.2.2 Physics in the boosted frame

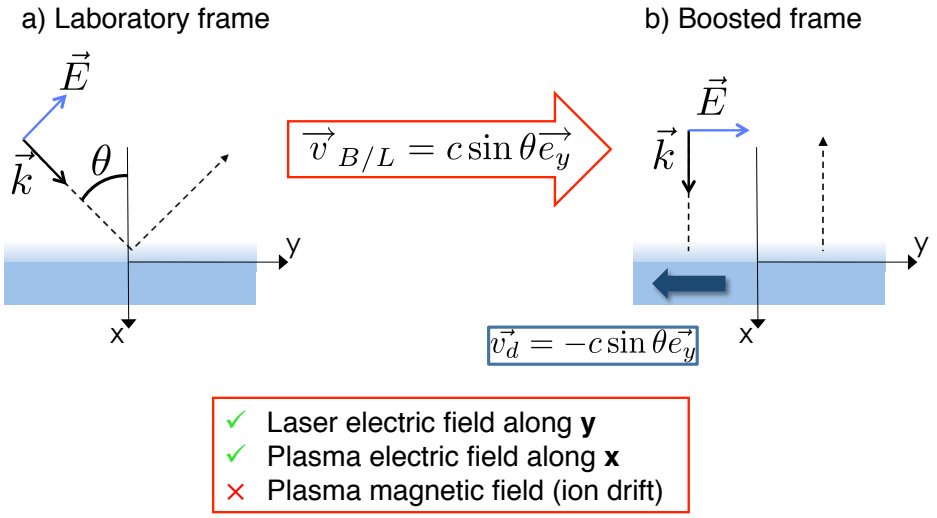


Figure 1.5: Advantages and drawbacks of the Lorentz transformation introduced by Bourdier.

Assuming the incident wave is a plane wave, the system is invariant along the y direction in the boosted frame, and the problem moves from a 2D problem (x, y) in the laboratory frame to a 1D problem (x) in the boosted frame. One can perform the physical analysis in this frame, and the major changes are listed below:

- As shown in figure 1.5, the laser electric field is along y in this frame.
- Since the plasma density $\rho(x, t)$ is independent of y, Gauss's law shows that plasma charge-separation fields are along x only. As a consequence, the electromagnetic and electrostatic contributions are separated along y and x respectively.
- As a counterpart, a charge separation $\rho(x, t) \neq 0$ results in a plasma current density $\boldsymbol{J} /\!\!/ \boldsymbol{e_y}$ via Ampère's law due to the ion and electron drift in the boosted frame, which generates a plasma magnetic field.

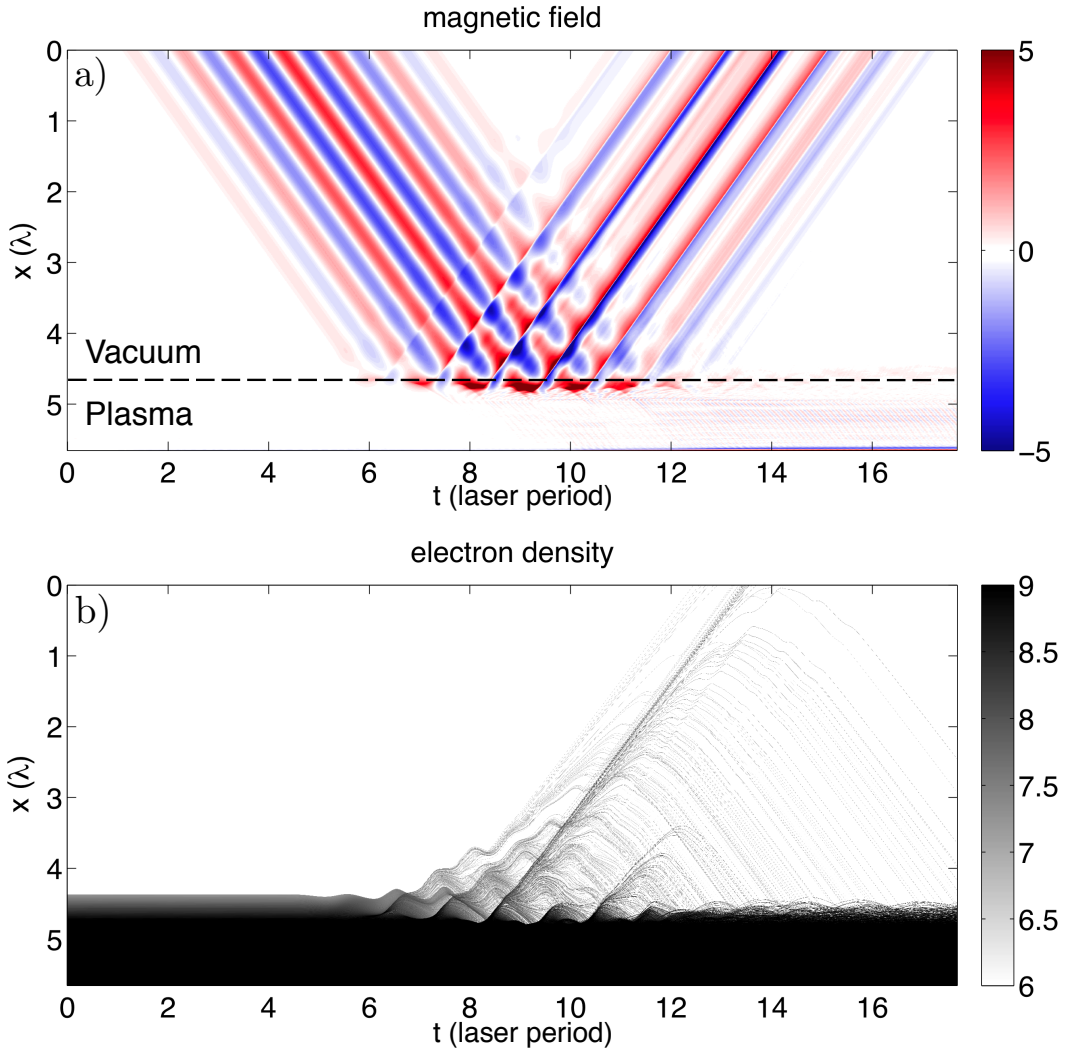


Figure 1.6: a) Magnetic field along time and space from a 1D PIC simulation performed in the boosted frame with physical conditions (given in the laboratory frame) $a_0 = 3$, $\tau = 25\,\mathrm{fs}$, $L = \lambda/8$, $n_{bulk} = 100 n_c$. The area $x > 4.7\lambda$ is filled by the overdense plasma. b) Same representation for the log-scale electron density. A bunch of electrons can be seen propagating in vacuum towards the $x < 0$ direction, *i.e.* along the reflected pulse.

In this thesis, 1D PIC simulations and the physical description are performed in the boosted frame. As a first illustration, figure 1.6 shows the magnetic field and electron

density along time and space from a 1D PIC simulation in the boosted frame. On panel a), one can see the 5 fs laser pulse propagating along the $+x$ direction for $t < 6T_L$ where T_L is the laser period. It is reflected at $x \simeq 4.7\lambda$ when it reaches the plasma, and the reflected pulse propagates in the $-x$ direction. The bottom panel shows the electron density. The plasma ripples during the laser pulse reflection. A bunch of electrons then propagates in the $-x$ direction, along the reflected pulse, while some electrons also move back to the plasma.

1.3 Electron heating mechanisms

When the laser pulse is reflected on the plasma surface, electrons can be ejected and propagate in vacuum. Taking a look at the literature on experimental results, I noticed how striking the variety of experimental parameters is, in terms of incidence angle, laser intensity or gradient scale length. This diversity leads to ejection of electron bunches with extremely heterogeneous energies and directions. However, only three mechanisms are usually invoked to explain these experimental results.

This section aims at (i) introducing three fundamental mechanisms: resonant absorption, vacuum heating and $J \times B$ heating; (ii) give intuition on the role of the main parameters to help understand which mechanism is dominant in which conditions; (iii) highlight how electron ejection in the backward direction, *i.e.* in the half-space $x < 0$ containing the incident and the reflected pulses, remains unclear.

Subsections 1.3.1-1.3.3 present a detailed description of the three above-mentioned mechanisms. An overdense plasma lies in the half-space $x > 0$, and an electromagnetic plane wave propagates in vacuum with angular frequency and wave vector (ω_0,$\boldsymbol{k} = (k_x, k_y, 0)$) with $k_x > 0$. The plasma is collisionless, ions are immobile and the thermal pressure will be neglected compared to the laser pressure.

The last subsection 1.3.4 presents a large review of experiments performed in the last twenty years. An analysis of these results shows how the role of the density gradient is often underestimated, which makes it difficult to understand properly the mechanisms responsible for electron acceleration.

1.3.1 Resonant absorption

A p-polarized electromagnetic wave with angular frequency ω_0 impinges in oblique incidence on an overdense plasma with a linear density gradient $n(x)$ on its front side, as shown in figure 1.7. We assume the incident wave has a non-relativistic intensity ($a_0 < 1$) and use the notation $\boldsymbol{E} = \bar{\boldsymbol{E}} e^{i\omega_0 t}$.

Mechanism

The Helmholtz equation (eq. 1.9) reads

$$\left[\frac{\partial^2}{\partial x^2} + \frac{\partial^2}{\partial y^2} + \frac{1}{c^2}(\omega^2 - \omega_p^2)\right] \bar{\boldsymbol{E}} = \boldsymbol{0}. \tag{1.68}$$

The system is translationally invariant along the y coordinate. As a consequence of Noether's theorem, the y component of the wave vector $k_y = k \sin\theta$ is conserved upon the wave reflection: $\bar{\boldsymbol{E}}(x, y) = \tilde{\boldsymbol{E}}(x) e^{-i\omega_0 \sin\theta y/c}$. This allows us to write equation 1.68 as

$$\tilde{\boldsymbol{E}}''(x) - \frac{\omega_0^2 \cos^2\theta - \omega_p^2}{c^2} \tilde{\boldsymbol{E}}(x) = 0, \tag{1.69}$$

so that the wave reflection occurs for $\omega_p = \omega_0 \cos\theta$ or, in terms of plasma density,

$$n = n_c \cos^2\theta. \tag{1.70}$$

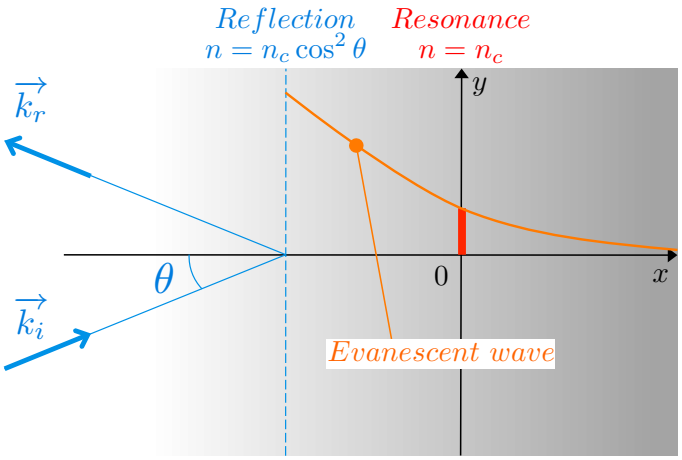


Figure 1.7: Diagram for resonance absorption. The p-polarized incident wave reflects under oblique incidence on an overdense plasma (grey area) with a density gradient on its front side. The density at the reflection point is $n_c \cos^2\theta$, where θ is the angle of incidence. An evanescent wave (orange) with angular frequency ω sets up behind the reflection point, and its normal component along x resonantly excites plasma waves at $x = 0$, where the evanescent wave angular frequency and the electron plasma frequency match. This resonance is shown in red.

As shown in section 1.1.1, an evanescent wave with angular frequency ω_0 penetrates into the plasma within a skin depth δ_s.

Gauss's law reads $\nabla \cdot (\epsilon_r \bar{\boldsymbol{E}}) = 0$. For a linear density gradient with characteristic length L, $n = n_c(1 + x/L)$ and $\epsilon_r(x) = -x/L$ for $x > -L$. Thus:

$$\nabla \cdot (\epsilon_r \bar{\boldsymbol{E}}) = -\frac{1}{L}\left(x\frac{\partial \bar{E}_x}{\partial x} + \bar{E}_x\right) = 0 \tag{1.71}$$

so that

$$\frac{\partial E_x}{\partial x} = -\frac{\bar{E}_x}{x} \tag{1.72}$$

which clearly shows a resonant response for $x = 0$, *i.e.* $n = n_c$ or $\omega_p = \omega_0$.

A scaling law for the absorbed fraction of a non-relativistic laser can be found in references [Forslund *et al.*, 1975; Kruer, 1988]. It only depends on the parameter $\alpha = \left(\frac{\omega_0 L}{c}\right)^{1/3} \sin\theta$, and is optimal for $\alpha \simeq 0.8$. $\theta = 45°$ gives an optimal length $L_{opt} = \lambda/4$.

Physically, the incident wave is reflected at $x = -L\sin\theta$ where $\omega_p = \omega_0 \cos\theta$, and an evanescent wave reaches $x = 0$ and resonantly excites plasma waves since $\omega_p(x = 0) = \omega_0$. The energy transfer is due to the normal component of the electric field. A laser beam can significantly heat the plasma via this mechanism, transfering up to 70% of the laser pulse energy to the plasma.

The normalized amplitude of the plasma waves in the low-intensity $a_0 \ll 1$ regime can be found in references [Denisov, 1957; Estabrook *et al.*, 1975; Ginzburg, 1964], and an upper bound is given by

$$a_{pw} \sim \frac{1}{(4\pi)^2}\frac{\lambda}{L}a_0 \tag{1.73}$$

for a long density gradient.

Wavebreaking: The phase velocity of plasma waves is directed towards the lower densities. In the low-intensity regime $a_0 \ll 1$, the plasma wave is carried by electrons with the displacement δ of an harmonic oscillator $\delta(x_0, t) \propto \sin(\omega_p t)$ with x_0 the electron initial position and ω_p the local plasma frequency. When the intensity increases, this displacement becomes anharmonic. Wavebreaking occurs when electrons with different initial positions are superimposed (see reference [Bergmann & Mulser, 1993]), which reads

$$\frac{\partial \delta}{\partial x_0} = -1. \tag{1.74}$$

This phenomenon is well-known for waves on the water's surface, when smooth waves turn into rollers when they reach the shore. In this case, condition 1.74 is satified when the steepest part of the leading edge of the wave becomes vertical.

When wavebreaking occurs in the density gradient, electrons are trapped in the wave and accelerated to suprathermal energies towards the lower density region. At high intensity, this mechanism saturates when a high number of trapped electrons load the plasma wave, which strongly decreases the wave amplitude with respect to equation 1.73. Besides, for long laser pulses ($\tau_L > 1\,\mathrm{ps}$), the ponderomotive force exerted by the electron plasma wave on the ions bores a hole in the density gradient and prevents the electrons from being further accelerated, as shown in reference [Forslund *et al.*, 1975].

Electron jets: Trapped electrons are accelerated in the plasma wave and can leave the plasma. In reference [Forslund *et al.*, 1977], the authors show that the hot electrons have a Maxwellian distribution and the temperature scales as $T_{hot} \propto (I\lambda^2)^{1/3}$. The energy of ejected electrons scales weakly with the laser intensity because of the loading effect. These hot electrons travel in vacuum towards $-x$, and a fraction is recalled back to the plasma due to charge-separation fields. This leads to wide electron jets centered around the target-normal direction, both in the backward ($x < 0$) and in the forward ($x > 0$) directions.

1.3.2 Vacuum heating

A p-polarized wave with non-relativistic intensity ($a_0 \ll 1$) impinges on an overdense plasma with a step-like density profile $n(x > 0) = n_0 \gg n_c$ under oblique incidence. Electrons from the surface circulate in vacuum during one laser period before returning to the plasma with non-zero velocity. These electrons are called Brunel electrons. The incident wave is screened in the plasma bulk $x > 0$, so Brunel electrons can travel freely in the $x > 0$ half-space, where they deposit energy via collisions. This non-resonant mechanism was initially studied to account for extra absorption of laser light in overdense plasmas in reference [Brunel, 1987].

Brunel electrons: The incident wave is a monochromatic plane wave (ω_0,$\boldsymbol{k_i}$), with amplitude E_0 and angle of incidence θ. Brunel developed a simple model to describe the electron dynamics, relying on the following hypotheses:

- The mechanism takes place in the low-intensity regime: relativistic effects are neglected, as well as the magnetic force. The incident electric field reads

$$\boldsymbol{E_i}(\boldsymbol{r},t) = E_0 \sin(\omega t - \boldsymbol{k_i}\cdot\boldsymbol{r})[\sin\theta \boldsymbol{e_x} + \cos\theta \boldsymbol{e_y}] \tag{1.75}$$
$$= E_{ix}(\boldsymbol{r},t)\boldsymbol{e}_x + E_{iy}(\boldsymbol{r},t)\boldsymbol{e}_y \tag{1.76}$$

  where $\boldsymbol{r} = (x, y)$.

- The plasma has a step-like density profile, which is equivalent to an infinitely steep density gradient.

- The plasma is assumed to behave as a perfect mirror. Hence, the interface conditions read

$$E_x(0^-, y, t) = 2E_{ix}(0, y, t) \tag{1.77}$$
$$E_y(0^-, y, t) = 0. \tag{1.78}$$

  From equation 1.78, we can see that there is no motion along y: the problem is purely 1D along x and the dependence in y will be skipped in what follows. The charge density is a linear charge density with $n(x) = n_0\Theta(x)$ where Θ is the Heaviside step function defined by $\Theta(x < 0) = 0$ and $\Theta(x \geq 0) = 1$. Besides, the perfect mirror hypothesis implies that all fields are zero in the plasma: $\boldsymbol{E}(x > 0, t) = \boldsymbol{0}$.

- Electrons start at $t = 0$ and travel in the $x < 0$ half-space during a laser period. We assume their maximum excursion d in vacuum verifies $d \ll \lambda$, which is reasonable in the low-intensity regime. Hence, the electric field at an electron's position does not differ significantly from its value at the plasma border:

$$E_x(x, t) = E_x(0^-, t)\ \forall x < 0. \tag{1.79}$$

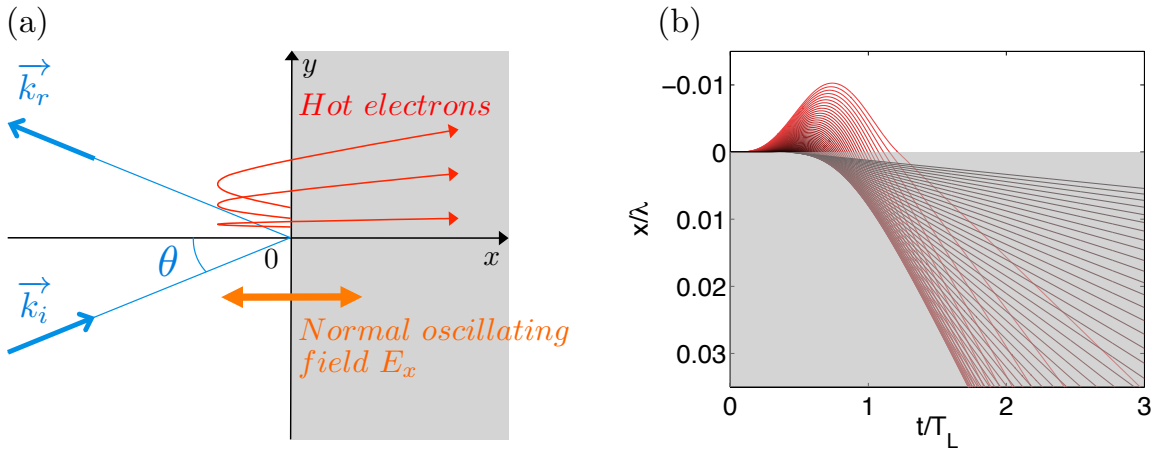


Figure 1.8: (a) Diagram for vacuum heating. An obliquely incident wave impinges on an overdense plasma. The electric field normal to the target (orange) drives electrons (red trajectories) from the surface towards vacuum and accelerates them back to the plasma, where they deposit energy. (b) Surface electron trajectories. Black lines stand for electrons released in vacuum later that red ones. The grey area stands for the plasma.

When electrons move from the plasma to vacuum, the plasma becomes non-neutral and creates an electrostatic field E_p along x. This field is given by Gauss's law for electron j:

$$E_p(x_j) = \int_{-\infty}^{x_j} \frac{n(x)}{\epsilon_0} dx. \tag{1.80}$$

The electrostatic field on electron j located at x_j depends on the total charge at $x < x_j$. We assume the electrons do not cross during their motion, so that the total charge on the left of electron j is unchanged: $\forall t > 0$, $E_p(x_j, t) = E_{pj}$ with $E_{pj} \leq 0$. Electron j is immobile until its starting time t_j when the total field at its position is zero:

$$E_x(t_j) = 2E_0 \sin\theta \sin\omega_0 t_j + E_{pj} = 0. \tag{1.81}$$

Given the parameter t_j, this equation gives the plasma's restoring electrostatic field

$$E_{pj} = -2E_0 \sin\theta \sin\omega_0 t_j. \tag{1.82}$$

Finally, the equation of motion for electron j reads

$$\ddot{x}_j = -\frac{2eE_0}{m_e}(\sin\omega_0 t - \sin\omega_0 t_j) \tag{1.83}$$

for $x < 0$ and $\ddot{x}_j = 0$ for $x > 0$, giving

$$kx_j(t) = 2\frac{eE_0}{m_e\omega_0 c}\left[\sin\omega_0 t - \sin\omega_0 t_j - (\omega_0 t - \omega_0 t_j)\cos\omega_0 t_j + \frac{\sin\omega_0 t_j}{2}(\omega_0 t - \omega_0 t_j)^2\right]. \tag{1.84}$$

Figure 1.8 b) shows the corresponding trajectories. An estimate of the absorption coefficient can be found in [Brunel, 1987]. **Vacuum heating is the dominant absorption mechanism upon the reflection of a low-intensity laser pulse on an overdense plasma without, or with a very short, density gradient on its front side**.

This mechanism can lead to distinct populations of hot electrons, which we can split in two parts:

Frontward electron jets: If the target is thin enough, Brunel electrons can travel through the plasma and be detected behind. This jet of electrons is consistent with Brunel's model.

Backward electron jets: Brunel model relies on strong hypotheses:

- monochromatic plane incident wave, reduced to a 1D problem;
- no plasma effect except the recall force;
- small electron excursion in vacuum → uniform fields;
- magnetic force neglected;
- non-relativistic dynamics.

In more realistic conditions, a fraction of the electrons travelling in vacuum never return to the plasma and are ejected in the backward ($x < 0$) direction. We extended Brunel's model and added relativistic and magnetic effects, as well as non-uniform fields that depend on the electron position (equations are given in appendix B). Electron trajectories calculated via this model are shown in figure 1.9. The electron dynamics is more complex than in Brunel's model (see figure 1.8 on page 25). A jet of electrons propagates towards vacuum (along $-x$). The model equations can be found in the appendix.

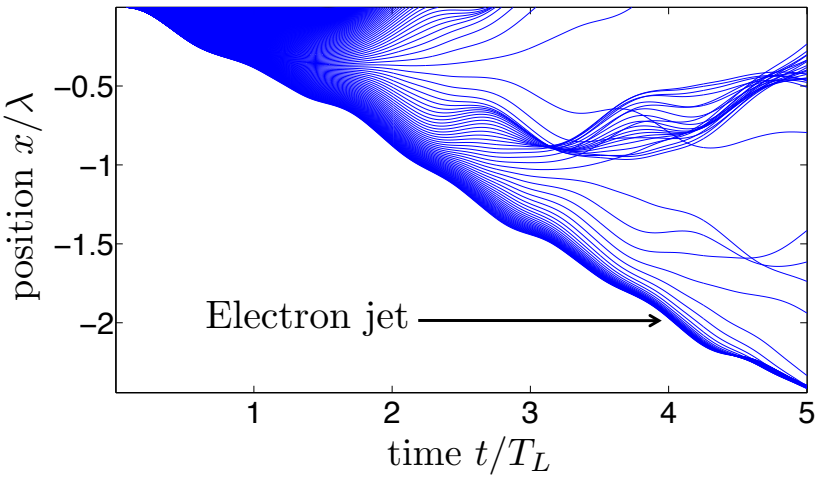


Figure 1.9: Electron trajectories calculated from the extended Brunel model including magnetic and relativistic effects. Note that some electron trajectories cross each other around $t/T_L = 3$, which breaks one of the hypotheses of the model. A jet of electrons propagates towards vacuum.

In the literature, authors refer to Brunel electrons to interpret experimental results on backward electron ejection. However, the dynamics of backward ejected electrons strongly differs from Brunel electrons, especially because they never return to the plasma. Besides, the extended model presented above shows severe restrictions: the non-crossing hypothesis is broken within only three laser periods, and the role of the plasma fields is completely neglected. Hence, the term *Brunel electron* is an abuse of language suggesting that backward electron ejection remains a grey area. This trend is emphasized in the review of experimental results presented in section 1.3.4.

1.3.3 $J \times B$ heating

A plane wave polarized along $\boldsymbol{e_y}$, with angular frequency ω_0 and relativistic intensity ($a_0 \gtrsim 1$) impinges on an overdense plasma under normal incidence. We assume the density gradient is sharp ($L \ll \lambda$). Electrons oscillate along the plasma surface $/\!/\boldsymbol{e_y}$, driven by the electric field $\boldsymbol{E} /\!/ \boldsymbol{e_y}$. The magnetic force drives them towards the plasma bulk, where they deposit energy via collisions.

The model presented here can be found in reference [Kruer & Estabrook, 1985]. We assume that the y component of the electric field close to the plasma surface (in the skin depth $\delta_s \ll \lambda$) reads $E_y = E_0(x)\cos(\omega_0 t)$, and we derive the magnetic field using

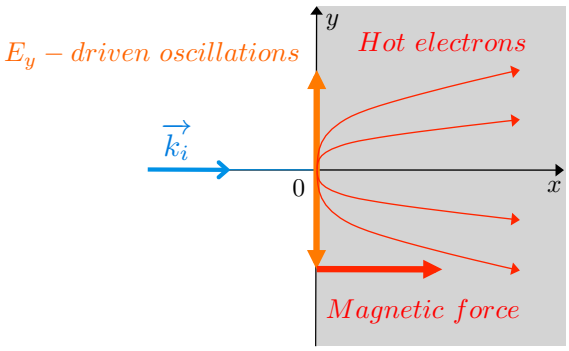


Figure 1.10: Diagram for $\boldsymbol{J} \times \boldsymbol{B}$ heating. A relativistically-intense electromagnetic wave hits an overdense plasma under normal incidence. The incident electric field drives electrons to relativistic speeds along the polarization direction, and the wave magnetic force pushes them towards the plasma bulk where they deposit energy and heat the plasma.

Faraday's law 1.5, which gives the final electric and magnetic fields

$$\boldsymbol{E} = E_0(x)\cos(\omega_0 t)\boldsymbol{e_y} \tag{1.85}$$

$$\boldsymbol{B} = -\frac{1}{\omega_0}\frac{dE_0}{dx}\sin(\omega_0 t)\boldsymbol{e_z}. \tag{1.86}$$

For the sake of simplicity, we consider the non-relativistic equations, and assume $v_x \ll c$. Neglecting the higher-order convective term in the time derivative, Euler's equation 1.2 at the first order reads

$$\frac{\partial v_x}{\partial t} = -e v_y B_z \tag{1.87}$$

$$\frac{\partial v_y}{\partial t} = -e E_y. \tag{1.88}$$

Equation 1.88 gives $v_y = -\frac{eE_0(x)}{m_e\omega_0}$, and then equation 1.87 gives the magnetic force along x:

$$F_{mag} = -\frac{e^2}{4m\omega_0^2}\frac{dE_0^2(x)}{dx}[1-\cos(2\omega_0 t)]. \tag{1.89}$$

Since $\frac{dE_0^2}{dx} < 0$ in the skin depth, $F_{mag} > 0$ and drives electrons inside the plasma at an angular frequency $2\omega_0$. A more appropriate expression of this force is

$$F_{mag} = -\frac{m_e}{4}\frac{dv_y^2(x)}{dx}[1-\cos(2\omega_0 t)]. \tag{1.90}$$

This is a magnetic second-order effect, as shown by the square dependence on the light amplitude as well as the double frequency $2\omega_0$. Hence, it is perceptible only for $a_0 \gtrsim 1$. Ruhl ([Ruhl, 1996]) presented a model describing the transition from $J \times B$ heating to vacuum heating when increasing the angle of incidence, and highlighted the transition from a first-order to a second-order phenomenon.

Electron jets: Electrons acquire energy by oscillating along the target surface and propagate towards the normal direction because of the magnetic force. Their energy is easily derived via the canonical momentum conservation (see [Wilks, 1993]) and reads $E = (\sqrt{1+a_0^2}-1)m_e c^2$, where we assumed $p_x^2 \ll p_y^2$. Hot electrons generated via this

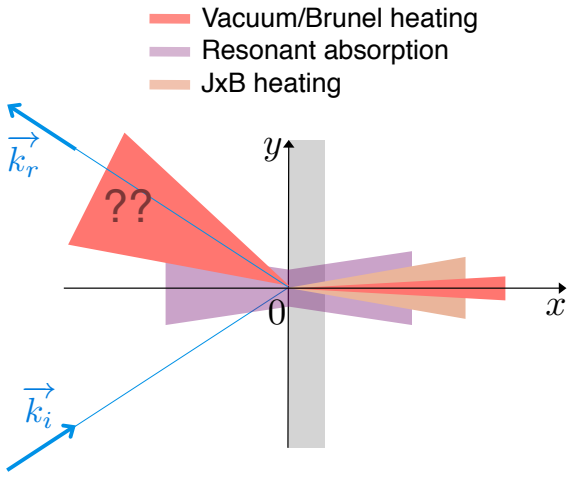


Figure 1.11: Angular distribution of ejected electrons due to the main heating mechanisms. The length of the jets are an indication of typical electron energies.

mecanism escape the plasma forming a very broad angle around the target normal in the frontward direction ($x > 0$).

An overview of the three mechanisms described here is shown in figure 1.11. Electron jets due to resonant absorption, $J \times B$ heating and Brunel electrons are expected to be observed along the target normal direction. The mechanism for backward electrons away from the target normal direction is not well understood yet, though frequenty associated with Brunel electrons.

1.3.4 Review of experimental results

Introduction

In this section, we present a large review of experiments performed during the last twenty years. These experiments all investigate electron ejection during the reflection of a short and intense linearly-polarized (p-polarized in the case of oblique incidence) laser pulse, off an overdense plasma. The experimental conditions show a great diversity (orders of magnitude in laser intensity, normal/oblique incidence, thin/thick target, long/short gradient) and result in extremely diverse electron bunches in terms of charge, energy and ejection angle. The goals of this study are (i) to pinpoint the lack of understanding of the backward electron ejection and (ii) to show that the role of the density gradient length is often underestimated.

Backward electron ejection in experiments

Figure 1.12 shows experimental results from references [Mordovanakis *et al.*, 2009] (a and b) and [Li *et al.*, 2006b] (c, d and e). Figure 1.12 a) shows electrons ejected around the specular direction, with relativistic energy. By changing the angle of incidence, Li *et al.* switched the emission angle from nearly normal for $\theta = 45°$ (c) to grazing direction for $\theta = 70°$ (d), by simply tilting the target. Besides, the corresponding electron spectra plotted in figures 1.12 b) and e) show that electrons have an energy centered around the relativistic value $\mathcal{E} = 0.8\,\mathrm{MeV}$ in Mordovanakis' experiment, while the bottom spectrum has a typical thermal shape, with a Maxwellian distribution corresponding to a temperature of 300 keV.

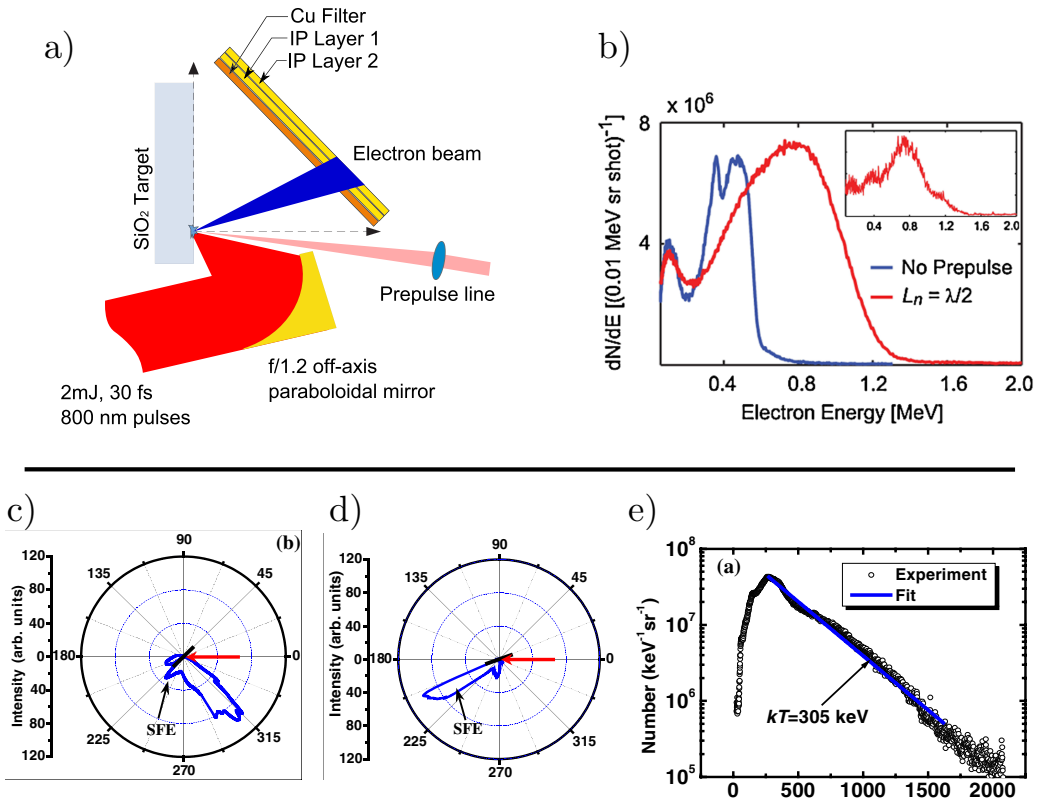


Figure 1.12: [Panels a) and b) are from reference [Mordovanakis *et al.*, 2009]] a) Schematic of the experiment, showing the electron jet direction. The laser parameters are $I = 1.4 \times 10^{18}\,\mathrm{W \cdot cm^{-2}}$, $\theta = 45°$, $w_0 = 1.5\,\mu\mathrm{m}$, $\tau = 30\,\mathrm{fs}$. b) Electron spectrum in the specular direction. [Panels c), d) and e) are from reference [Li *et al.*, 2006b]] c) Electron angular distribution. The parameters are $I = 1.4 \times 10^{18}\,\mathrm{W \cdot cm^{-2}}$, $\theta = 45°$, $w_0 = 10\,\mu\mathrm{m}$, $\tau = 30\,\mathrm{fs}$. The gradient scale length is not known because of the poor laser contrast. d) Same setup, with $\theta = 70°$. The electron jet switched from normal direction to grazing direction. e) Electron spectrum along target for $\theta = 70°$.

These results clearly show backward electron jets, away from the target normal direction, which cannot be explained by the three above-mentioned mechanisms. The authors develop phenomenological models to explain their results. Yet the apparent similarity between these examples suggests that there is a unique mechanism underlying the process of electron ejection.

Table 1.6 shows an extensive review of experimental results obtained during the last twenty years. This table allows a more systematic study. Electrons accelerated via resonance absorption (RA) show similar distributions: they are ejected along the target normal direction in the frontward or backward direction, with an energy of a few 100 keV. Few articles report directly on $J \times B$ heating, but references [Malka & Miquel, 1996] and [Santala *et al.*, 2000] show similar results, with electrons of a few MeV energy ejected along the target normal in the frontward direction.

Other published experiments, where electron acceleration was claimed to be due to vacuum heating or other mechanisms may result in extremely different ejection angles (backward and frontward normal, specular direction, between normal and specular direction and even along the target surface). Whether all these distributions result from a similar mechanism is not clear, and such a mechanism is not proposed.

Density gradient length in experiments

References [Cai *et al.*, 2003] and [Li *et al.*, 2006a] show electron ejection for similar parameters. However, their final results differ significantly. This observation holds for several experiments shown in table 1.6. **Experimental results for backward electron ejection are extremely diverse because the density gradient length, which is a key parameter, is either poorly controlled or not measured, if not totally omitted in the analysis.**

The reason is that the gradient is extremely difficult to measure and can appear because of unwanted prepulses or a nanosecond pedestal before the main pulse, if the laser contrast is not high enough. To play with this parameter, several groups have developed a specific diagnostic, as presented in [Bocoum *et al.*, 2015; Geindre *et al.*, 1994; Kahaly *et al.*, 2013], to tackle the issue of laser contrast and control the prepulse–main pulse delay.

reference	$I\lambda^2[\mathrm{W}\cdot\mathrm{cm}^{-2}\cdot\mu\mathrm{m}^2]$	θ	w_0	τ_L	Δ	L	$(T)-\mathcal{E}_{fast}$	θ_{out}	mech.
[Malka & Miquel, 1996]	1.2×10^{19}	45°	$>10\,\mu$m	400 fs	$30\,\mu$m	$>10\lambda$	1 MeV	90°	VH?
[Malka & Miquel, 1996]	1.2×10^{19}	0°	$>10\,\mu$m	400 fs	$30\,\mu$m	$>10\lambda$	1 MeV	180°	JB
[Bastiani *et al.*, 1997]	3×10^{16}	45°	$20\,\mu$m	120 fs	∞	$<\lambda$	(180 keV)	45°	VH?
[Beg *et al.*, 1997]	1.4×10^{18}	30°	$12\,\mu$m	1 ps	∞	$>\lambda$	$(100-400\,\mathrm{keV})$	0°	RA
[Wharton *et al.*, 1998]	3×10^{19}	25°	$15\,\mu$m	400 fs	$50\,\mu$m	$\gg\lambda$	$(100-500\,\mathrm{keV})$	180°	RA
[Santala *et al.*, 2000]	1×10^{19}	45°	$>10\,\mu$m	1 ps	1/8 mm	λ	10 MeV	180°	VH?
[Santala *et al.*, 2000]	1×10^{19}	0°	$>10\,\mu$m	1 ps	1.8 mm	10λ	10 MeV	180°	JB
[Chen *et al.*, 2001]	1.4×10^{16}	45°	$15\,\mu$m	150 fs	∞	$<\lambda$	(250 keV)	$0-55°$	VH?
[Chen *et al.*, 2001]	1.4×10^{16}	45°	$15\,\mu$m	150 fs	∞	$<\lambda$	$(>50\,\mathrm{keV})$	180°	VH?
[Cai *et al.*, 2003]	2×10^{17}	45°	$25\,\mu$m	60 fs	$100\,\mu$m	λ	(200 keV)	0°	VH?
[Cai *et al.*, 2003]	2×10^{17}	45°	$25\,\mu$m	60 fs	$100\,\mu$m	λ	1 MeV	45°	VH?
[Cai *et al.*, 2003]	2×10^{17}	45°	$25\,\mu$m	60 fs	$100\,\mu$m	λ	(200 keV)	0°	RA
[Cai *et al.*, 2004]	2×10^{17}	45°	$25\,\mu$m	60 fs	$100\,\mu$m	λ	(150 keV)	0°	RA
[Cai *et al.*, 2004]	2×10^{17}	45°	$25\,\mu$m	60 fs	$100\,\mu$m	λ	500 keV	45°	VH?
[Tommasini *et al.*, 2004]	5×10^{16}	0°	$2\,\mu$m	150 fs	thin	$\ll\lambda$	(35 keV)	180°	-
[Li *et al.*, 2006a]	7×10^{17}	45°	$8\,\mu$m	70 fs	$30\,\mu$m	3λ	1 MeV	90°	VH?
[Li *et al.*, 2006a]	7×10^{17}	45°	$8\,\mu$m	70 fs	∞	3λ	(440 keV)	180°	RA
[Li *et al.*, 2006b]	1.4×10^{18}	70°	$10\,\mu$m	30 fs	$30\,\mu$m	$<\lambda$	500 keV	90°	VH?
[Brandl *et al.*, 2009]	1.4×10^{16}	45°	$3.5\,\mu$m	10 fs	∞	λ	150 keV	$15-35°$	VH?
[Mordovanakis *et al.*, 2009]	1.4×10^{18}	45°	$1.5\,\mu$m	30 fs	∞	$<\lambda$	MeV	45°	VH?
[Tian *et al.*, 2012]	6×10^{17}	$30-80°$	$8\,\mu$m	65 fs	∞	$0.1-0.5\lambda$	150 keV	$0-\theta$	VH?

Table 1.6: Review of experimental results. The angle of ejection θ_{out} is defined in the clockwise polarization plane $x-y$ with origin in the target normal direction $(-x)$. 180° is the forward direction along the target normal, 0° is the backward direction along the target normal, and the specular direction is typically around 45°. τ_L is the pulse duration, Δ is the target thickness. L is the gradient length, either given by the authors or roughly estimated from their experimental conditions. The $(T)-\mathcal{E}_{fast}$ column shows the ejected electron temperature if the distribution is Maxwellian (in this case, the value is in brackets) or the fast electron energy. The last column shows the ejection mechanism claimed by the authors with JB=$J\times B$ heating, RA=Resonant Absorption and VH=Vacuum Heating. More information can be found in the references. This study is focused on ejected electrons via vacuum heating and is not claimed to be exhaustive on other mechanisms, for which a large amount of literature can be found. Experiments that showed several electron jets are listed as several lines.

Outcome of the review

In spite of these numerous experimental results, the ejection process remains unclear. Reference [Ruhl *et al.*, 1999] shows a model based on the conservation of the transverse canonical momentum, and is probably the most advanced predictive tool for the direction of backward ejected electrons. Nevertheless, it works for a step-like density profile and does not aim at describing the ejection mechanism and the plasma dynamics. Besides, this model fails to describe results from experiments with a controlled gradient. For example, in the experiment presented in reference [Mordovanakis *et al.*, 2009], electrons were detected around $\theta_{out} = 40°$ whereas Ruhl's model predicted $\theta_{out} = 23°$.

In this thesis, we have used experimental results obtained in very clean experiments with well-controlled density gradients in order to establish the phenomenology of backward electron ejection. This has been the basis of the models we have developed, and that are presented in the next chapters. Besides, we show that the dynamics in vacuum in the electromagnetic fields can change dramatically the distribution of ejected electrons.

Backward electrons originate from the surface, which is known to be the source of intense high harmonic generation. There is a vast literature on this subject and the processes are relatively well-understood. Thus, one of the goals of this thesis is to determine if there is a link between harmonic generation and electron ejection. The following section presents the mechanisms for harmonic generation on plasma mirrors.

1.4 High harmonic generation on plasma mirrors

We hereafter discuss the high harmonics generated when an intense laser pulse ($a_0 \sim 1$) reflects under oblique incidence off an overdense plasma ($250n_c$) with a sub-wavelength density gradient scale length ($L < \lambda$), and describe two possible mechanisms in sections 1.4.2 and 1.4.3. In both cases, a non-linear process takes place during each optical cycle that generates a single attosecond bunch with a broad spectrum. This periodic mechanism leads to a train of attosecond bunches in the time domain, equivalent to a harmonic spectrum showing multiples of the fundamental frequency ω_0. This equivalence is stated in section 1.4.1.

1.4.1 Train of ultrashort pulses and high harmonic generation

A train of attosecond pulses in the time domain S and its Fourier transform $\tilde{S}$ are shown in figure 1.13 a) and e) respectively, for harmonics generated by a laser with angular frequency ω_0 and $T_L = 2\pi/\omega_0$. The spectrum consists of peaks for multiples of ω_0, called harmonics. The pulse train in the temporal domain is given by

$$S = A * [H \times E] \tag{1.91}$$

where $*$ stands for the convolution operator, A is the short pulse signal, H is the temporal Dirac comb and E is the large global train envelope. They are shown in figures 1.13 b), c) and d) respectively.

Figures 1.13 f), g) and h) show the Fourier transforms of functions A, H and E, noted with tilde symbols. The final spectrum is given by

$$\tilde{S} = \tilde{A} \times [\tilde{H} * \tilde{E}]. \tag{1.92}$$

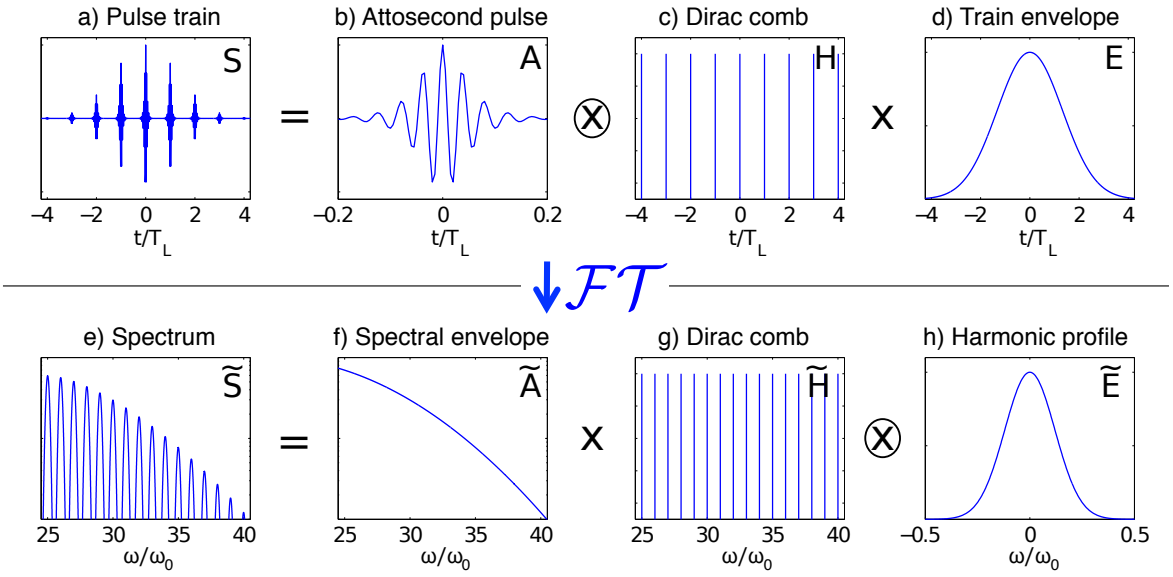


Figure 1.13: First line: train of attosecond pulses in the time domain (a) as a combination of a single attosecond pulse (b), a Dirac comb (c) to stand for the T_L periodicity of the mechanism and the train envelope (d) representing the finite duration of the main femtosecond pulse. Second line: same as the first one in the Fourier domain.

A signal with duration Δt in the time domain results in a spectrum with width $\Delta\omega \propto 1/\Delta t$ in the Fourier domain. The wider the global train envelope E, the thinner the harmonics $\tilde{E}$. Equivalently, the shorter the attosecond pulse A, the wider the spectral envelope $\tilde{A}$.

1.4.2 Coherent Wake Emission

Mechanism

For a sub-relativistic laser intensity $a_0 < 1$ and a very sharp density gradient $L \sim \lambda/40$, the dominant mechanism is Coherent Wake Emission (CWE, see [Malvache, 2011; Quéré *et al.*, 2006; Thaury & Quéré, 2010; Thaury *et al.*, 2007]). The basic mechanism is shown in figure 1.14, and relies on Brunel electrons (see 1.3.2 on page 24). The plasma density has an exponential shape with electron density $n_e(x) = n_c \exp(x/L)$ were n_c is the plasma critical density in the laboratory frame of reference and θ is the incident angle. The CWE mechanism occurs at each laser period, and can be split up in three steps:

- Brunel electrons are pulled towards vacuum for $0 < t < T_L/2$ and sent back to the plasma for $T_L/2 < t < T_L$. They cross each other in the density gradient, forming a local density peak of electrons propagating along $+x$. Electron trajectories are shown as grey lines in figure 1.14. The black dashed line stands for the density peak trajectory. Note that this peak exists because electron trajectories cross in the plasma. This crossing requires electrons to have different speeds when they return to the plasma, with the slowest first and the fastest last.

- When the density peak goes through position x, it excites plasma waves at the local plasma frequency $\omega_p(x) = \omega_0\sqrt{n(x)/n_c}$. The deeper inside the density gradient, the faster the plasma oscillations. The quantity $(n_e - n_i)/n_c$ is shown in figure 1.14 as the blue-red colourmap. The frequency of plasma oscillations increases

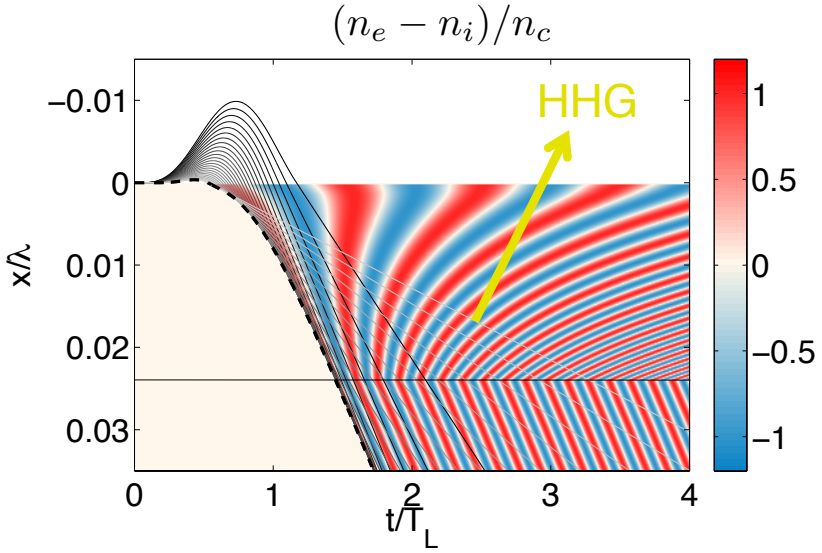


Figure 1.14: Illustration of the CWE mechanism during one laser period. Brunel electrons (grey solid lines) travel in vacuum and return to the plasma, where they form a density peak (black dashed line) propagating towards $x > 0$. The colourmap shows the plasma density. The density peak excites plasma oscillations at the local plasma frequency. These oscillations radiate an attosecond bunch in the reflected field. HHG stands for High Harmonic Generation.

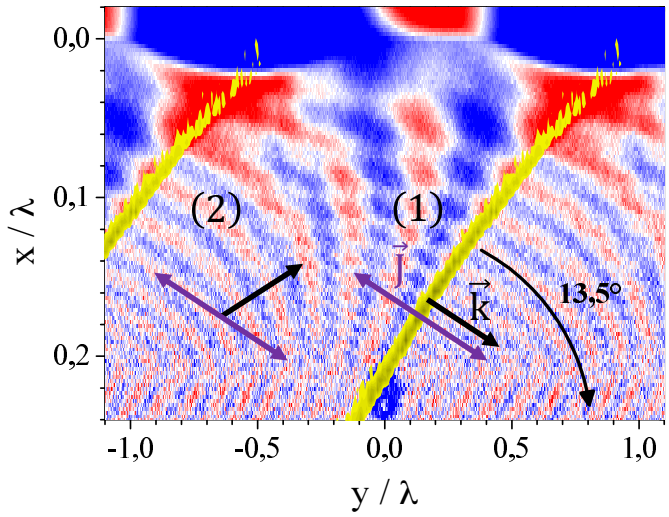
with x up to $x = 0.024\lambda$, which corresponds to the end of the density gradient (black solid line). The region $x > 0.024\lambda$ is occupied by the plasma bulk, where the local plasma frequency does not depend on x. Plasma oscillations around position x_0 involve electron oscillating with $x(t) = x_0 + \delta x \cos\left[\omega_p(x_0)(t - t_0(x_0))\right]$, where $t_0(x_0)$ is the time at which the density peak reaches x_0. This is valid as long as the electron sees the same plasma frequency along its oscillations, which reads $\delta x \ll L$.

- These plasma oscillations coherently radiate an attosecond bunch in the reflected field, with frequencies up to the maximum plasma frequency. Usually $\max(\omega_p) \leq 20\omega_0$. This emission occurs via *linear mode conversion*, and relies on the presence of the density gradient, as described in the following box. This periodic mechanism results in a train of attosecond bunches in the reflected field, hence a spectrum with harmonics of the laser frequency in the Fourier domain.

Figure 1.15 shows the electron density map from particle-in-cell (PIC) simulation `these_cwe2` with $a_0 = 0.3$ and $L = \lambda/60$, as well as CWE attosecond bunches propagating in the $-x$ direction. These bunches are generated deeper than the critical point $x_c = 0$ where $n_e(x_c) = n_c$. More details on PIC simulations can be found in chapter 2.

Finally, the repetition of this process over the full laser pulse duration leads to a train of attosecond pulses in the specular direction. The highest frequency generated is the maximum plasma frequency in the plasma bulk, so there is a cutoff at the maximum plasma frequency ω_p^{max} in the harmonic spectrum. A typical harmonics spectrum for CWE emission is shown in figure 1.16. The plasma maximum density was $250n_c$, which gives a maximum plasma frequency of $\omega_p^{max} = 15\omega_0$. The cutoff is clearly visible.

Electrostatic to electromagnetic wave conversion in CWE



An electrostatic plane wave in a homogeneous plasma is longitudinal: the wave vector and the electric field are parallel $\boldsymbol{k} /\!/ \boldsymbol{E}$. In this case, the electron motion also occurs in the same direction: $\boldsymbol{J} /\!/ \boldsymbol{k}$.

An electromagnetic plane wave in a homogeneous plasma is transverse: the wave vector and the electric field are orthogonal $\boldsymbol{k} \perp \boldsymbol{E}$. Using $\nabla \equiv -i\boldsymbol{k}\times$ and $\boldsymbol{k} \cdot \boldsymbol{E} = 0$, Helmholtz equation reads

$$\left(k^2 - \frac{1}{c^2}\frac{\partial^2}{\partial t^2}\right)\boldsymbol{E} = \mu_0 \frac{\partial \boldsymbol{J}}{\partial t}. \tag{1.93}$$

This equation shows that the source term on the RHS can generate an electromagnetic wave only if $\boldsymbol{J}$ has a component normal to $\boldsymbol{k}$ (parallel to $\boldsymbol{E}$). As a consequence, electrostatic waves in a homogeneous plasma cannot be converted into electromagnetic waves.

In a heterogeneous plasma, namely in the sharp density gradient, plasma oscillations can be converted into electromagnetic waves. The image in the box [from reference [Thaury, 2008]] shows a snapshot of the component of the electric field normal to the plasma E_x from a 2D simulation of CWE in the laboratory frame. Brunel electrons are shown in yellow. Each electron travels along $+x$, and the front is inclined by 13.5° with respect to the y axis because of the oblique incidence.

The front of Brunel electrons triggers plasma oscillations in the direction perpendicular to this front (1), so that the electron motion $\boldsymbol{J}$ (purple arrow) and the wave vector $\boldsymbol{k}$ (black arrow) are parallel. Zone (2) shows vectors $\boldsymbol{J}$ and $\boldsymbol{k}$ at the same depth x, where approximately half a laser period has passed after the trigger. The direction of electron oscillations $\boldsymbol{J}$ remains the same whereas the wave fronts have curved because the plasma frequency is space-dependent. The consequence is straightforward: $\boldsymbol{J} \times \boldsymbol{k} \neq 0$: $\boldsymbol{J}$ has a component normal to $\boldsymbol{k}$, and electrostatic waves can be transformed into electromagnetic waves. More information can be found in reference [Thaury *et al.*, 2007].

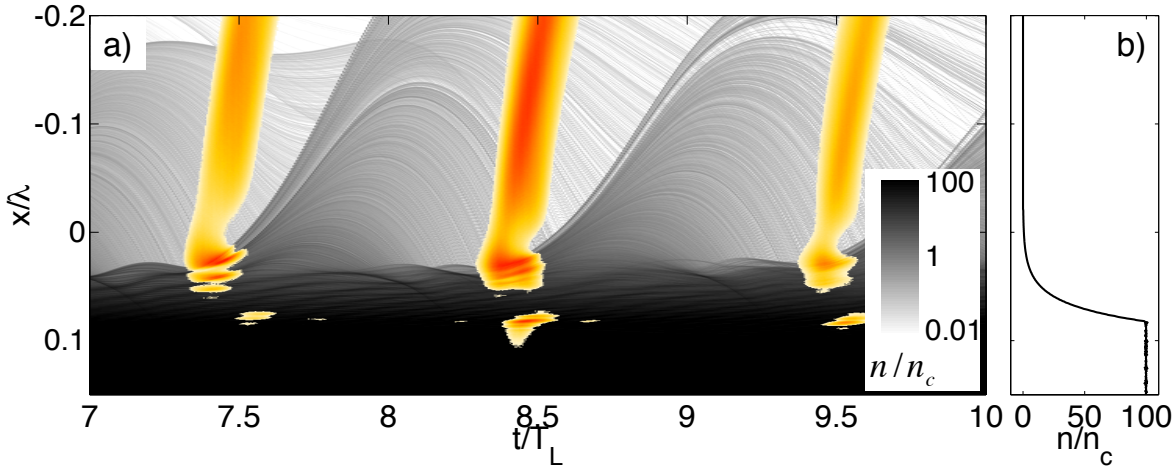


Figure 1.15: Attosecond bunches from the CWE mechanism from 1D PIC simulation `these_cwe2` with $a_0 = 0.3$, $L = \lambda/60$, $n_{bulk} = 100n_c$ and $\tau_L = 4T_L$ FWHM with a $\sin^2$ envelope. a) The grey scale shows the electron density, and the yellow-red scale shows the envelope of the attosecond reflected pulses. A Fourier filter was applied to keep harmonics order above 8, propagating in the $-x$ direction. The critical density $n = n_c$ is located at $x = 0\lambda$. One CWE attosecond bunch is generated during each laser period deep inside the plasma where the electron density is high, due to plasma oscillations in the overdense region. b) Initial plasma density.

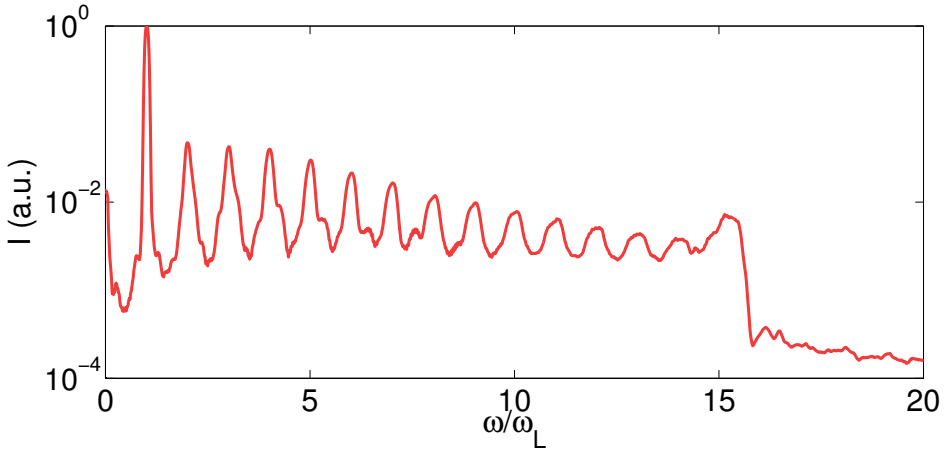


Figure 1.16: Reflected field spectrum from a 1D PIC simulation performed with the code EPOCH for $a_0 = 0.4$, $n_{bulk} = 250n_c$ and $L = \lambda/40$. ω_0 is the incident laser frequency. The cutoff at the maximum plasma frequency $\omega_p^{max} = \sqrt{250}\omega_0 \simeq 15.8\omega_0$ is clearly visible.

CWE in 1D PIC simulations

The result of 1D PIC simulation `these_cwe` for CWE is shown in figure 1.17. The simulation parameters are, in the laboratory frame, $\theta = 45°$, $\lambda = 0.8\,\mu$m, $a_0 = 0.1$, $L = \lambda/50$ and $n_{bulk} = 250 n_c$. The electron initial temperature is zero, and the pulse has a square temporal envelope. The ions are immobile. The numerical conditions were $\Delta x = \lambda/5000$ and we used 500 particles per cell (see chapter 2).

Figure 1.17 a) shows electron trajectories (grey lines) as well as the driving field B_z. They are driven toward vacuum for $0.7 < t/T_L < 1.2$ and are accelerated back to the plasma starting from $t/T_L = 1.2$. Their trajectories cross in the density gradient, where they excite plasma waves. This is shown in figure 1.17 b), where the plasma electric field E_x is shown is the same (x, t) representation. The image is strongly saturated, so that one can clearly see plasma oscillations even in the plasma bulk, which occupies the region $x > 0.11\lambda$ in this simulation. Note that the oscillations start when the electron trajectories cross in the plasma.

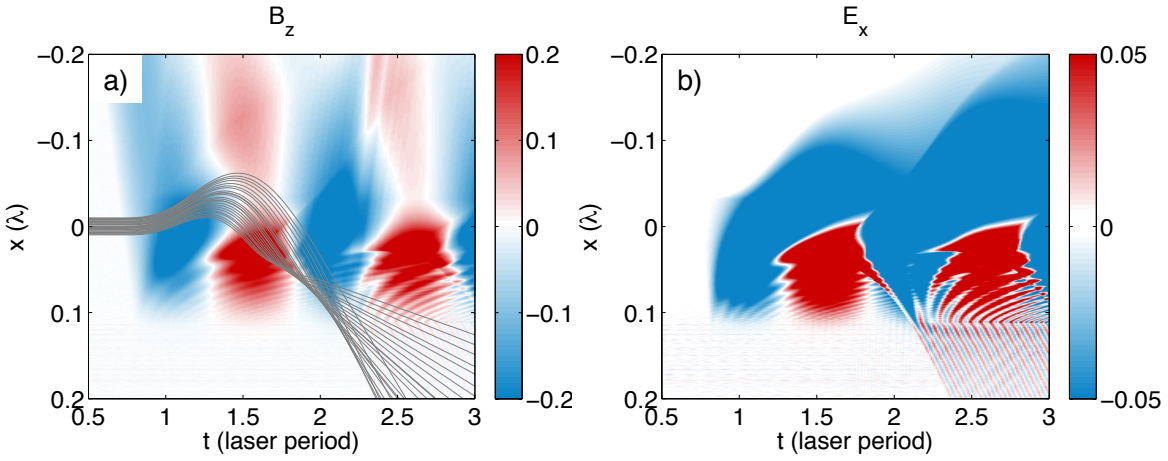


Figure 1.17: a) Time-space map of the magnetic field B_z at the plasma surface from 1D PIC simulation `these_cwe` in the boosted frame. The critical density $n = n_c$ is located at $x = 0\lambda$. Trajectories of Brunel electrons are shown as grey lines. b) Electric field E_x at the plasma surface. The map is saturated to highlight plasma oscillations.

Optimal conditions

This paragraph presents the global trends for the CWE harmonic efficiency. It aims at introducing the role of the main parameters a_0 and L, rather than presenting an extensive study of the mechanism. A thorough qualitative and quantitative analysis for coherent wake emission can be found in references [Thaury & Quéré, 2010] and [Malvache, 2011].

Figure 1.18 shows the electron density peak propagating in the plasma from simulation `these_cwe`. Snapshots of the quantity $n_e - n_i$ are shown along x for successive times. The time interval is the same between consecutive snapshots. The following observations may be drawn from:

- The density peak width and height are not constant along its propagation in the plasma. In this particular case, its amplitude becomes lower and its width becomes larger.

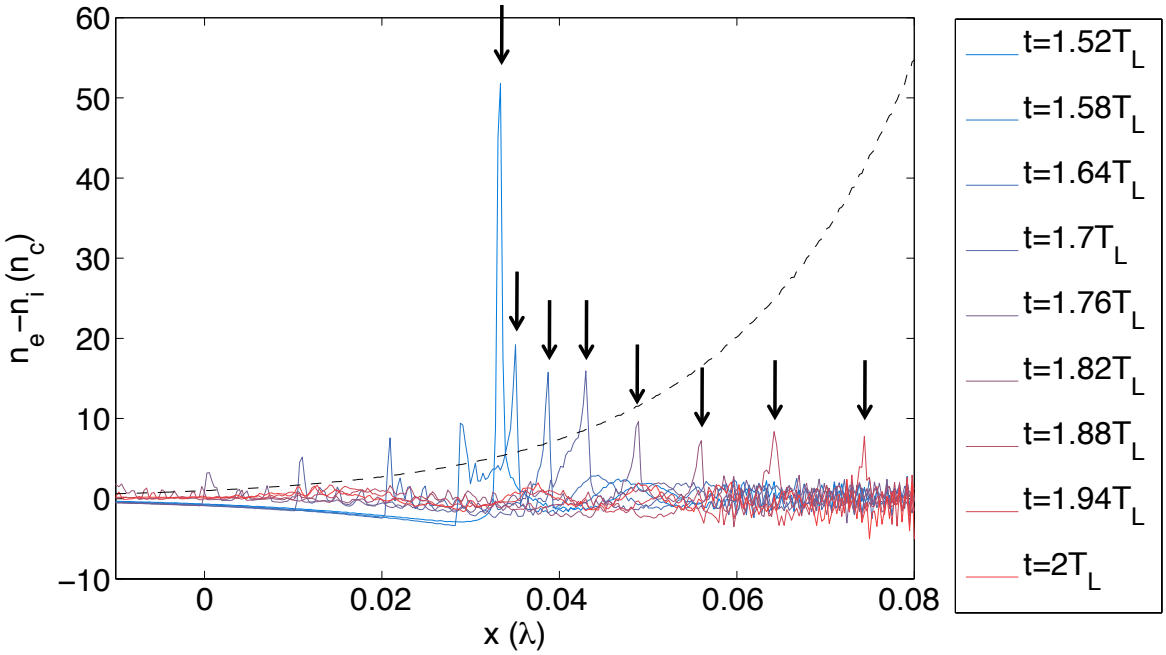


Figure 1.18: Quantity $(n_e - n_i)/n_c$ along x for different times, separated by $\Delta t = 0.06T_L$ intervals. The peak propagates towards $+x$ with mean velocity $v \simeq 0.1c$, and its speed, height and width change along its propagation. The dashed line stands for the ion density.

- The distance between two consecutive positions of the peak increases: the peak speed increases. Note that the peak is due to trajectory crossing. As a result, its velocity can increase along its propagation even though it involves electrons with constant speed.

Dependence on a_0: When a_0 is too small, electrons travelling in vacuum return to the plasma with an extremely large velocity distribution. They cross before the critical surface x_c defined by $n(x_c) = n_c$. There is no sharp density peak for $x > x_c$ and no high-frequency plasma waves are excited. Thaury and Quéré show that CWE could be generated provided $a_0 > 3.4L/\lambda$. On the opposite, when a_0 is too large, the plasma dynamics can be strongly distorted. The amplitude of plasma oscillation is so large that $\delta x \sim L$, and the mechanism breaks. **Coherent Wake Emission typically occurs for $0.01 < a_0 < 1$.**

Dependence on L: Linear mode conversion occurs in an inhomogeneous plasma only, so no harmonics are generated when $L = 0$. When the peak propagates towards $x > 0$ in the density gradient, it gets broader and broader. On the opposite, the plasma wavelength $\lambda_p(x)$ decreases with x. For too long a gradient, the density peak width $\delta_{peak}(x)$ becomes larger than the local plasma wavelength $\delta_{peak}(x) > \lambda_p(x)$ and no longer triggers plasma waves. Besides, electrons originate from different initial positions, which makes the peak broader and smaller. Hence, the harmonic efficiency decreases for long gradients. **CWE is efficient when $L \sim \lambda/100$ approximately.**

Shape of the harmonic spectrum: Harmonic spectra from CWE are characterized by a cutoff at the maximum plasma frequency $\omega_p^{max} = \omega_0\sqrt{n_{bulk}/n_c}$. Figure 1.19 shows CWE spectra from PIC simulations were $a_0 = 0.2$, $n_{bulk} = 110n_c$ and $L = \lambda/15$ and $\lambda/100$ respectively. Both cases show a cutoff at $\sqrt{110}\omega_0 \simeq 10\omega_0$. In figure 1.19 a),

the harmonic power decreases with the harmonic order whereas in figure 1.19 b), the harmonic power peaks for $\omega = 4\omega_0$. Thaury and Quéré showed that the shape of the harmonic spectrum depends on the peak dynamics: if the electron peak height $N(x)$ reaches a maximum for $x = x_{max}$, the highest power is generated for $\omega = \omega_p(x_{max})$. For example, in figure 1.18, the peak height decreases along its propagation, so the resulting spectrum should be similar to that shown in 1.19 a).

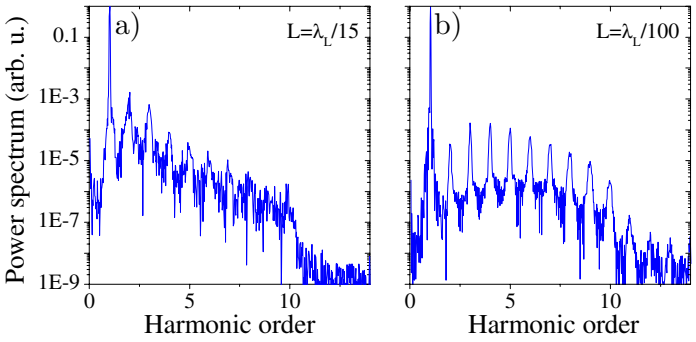


Figure 1.19: [Image from [Thaury & Quéré, 2010]] a) CWE spectrum from a 1D PIC simulation with $\theta = 45°$, $a_0 = 0.2$, $n_{bulk} = 110n_c$ and $L = \lambda/15$. b) shows the same for $L = \lambda/100$.

1.4.3 Relativistic Oscillating Mirror

For relativistic intensities $a_0 > 1$, the dominant mechanism for high harmonic generation is the Relativistic Oscillating Mirror [Burnett *et al.*, 1977; Dromey *et al.*, 2006; Thaury *et al.*, 2007]. The laser intensity is high enough for the oscillations of electrons at the plasma surface to be nonlinear. This is shown in figure 1.20. Once per laser period, electrons from the plasma surface acquire a relativistic speed directed toward vacuum $\beta_x \simeq -1$ where $\beta_x = v_x/c$ is the normalized velocity, and radiate an attosecond bunch. This mechanism leads to a train of attosecond bunches in the reflected field, hence harmonics of the laser frequency in the spectral domain. Note that, contrary to coherent wake emission, these harmonics are generated indifferently at $x < x_c = 0\lambda$ or $x > x_c$ because they do not rely on plasma waves.

A representative spectrum for ROM emission is shown in figure 1.21. The plasma maximum density is $250n_c$, which gives a maximum plasma frequency of $15\omega_0$, and no cutoff can be observed. Contrary to coherent wake emission, this mechanism does not rely on a density gradient, and the simplest study involves a homogeneous overdense plasma with a density slightly higher than the critical density, typically $n_0 \sim 5n_c$. However, studying the mechanism in presence of a density gradient is nevertheless important because (i) experimentally, it is much easier to make a very dense plasma bulk with a density gradient on its front side rather than a plasma with density $\sim 5n_c$ and sharp plasma-vacuum transition, (ii) a gradient exists in most experiments because of uncontrolled laser prepulses, and (iii) it can lead to an enhancement of the ROM harmonic generation.

Three references provide milestones of the theory of high harmonic generation via the ROM mechanism: [Lichters *et al.*, 1996], [Baeva *et al.*, 2006] and [Gonoskov *et al.*, 2011]. The two first models are given in this section to provide insight into the mechanism. The third one is developed in chapter 3 within the scope of electron ejection.

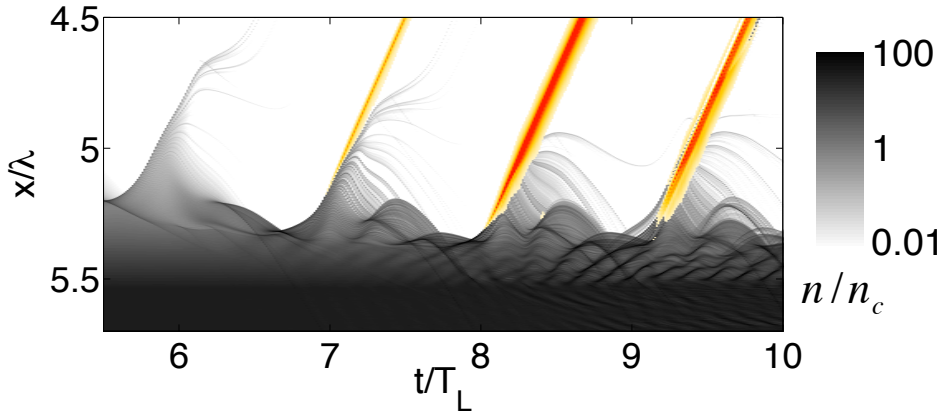


Figure 1.20: Attosecond bunches from ROM mechanism from 1D PIC simulation `these_rom2` with $a_0 = 5$, $L = \lambda/8$, $n_{bulk} = 50n_c$ and $\tau_L = 4T_L$ FWHM with a $\sin^2$ envelope. The grey scale stands for electron density, and the yellow-red scale stands for the envelope of the attosecond reflected field. A Fourier-filter was applied to keep harmonics order above 9. The critical density $n = n_c$ is located at $x = 0\lambda$. One ROM attosecond bunch is generated during each laser period when electrons are accelerated to a relativistic speed towards $-x$.

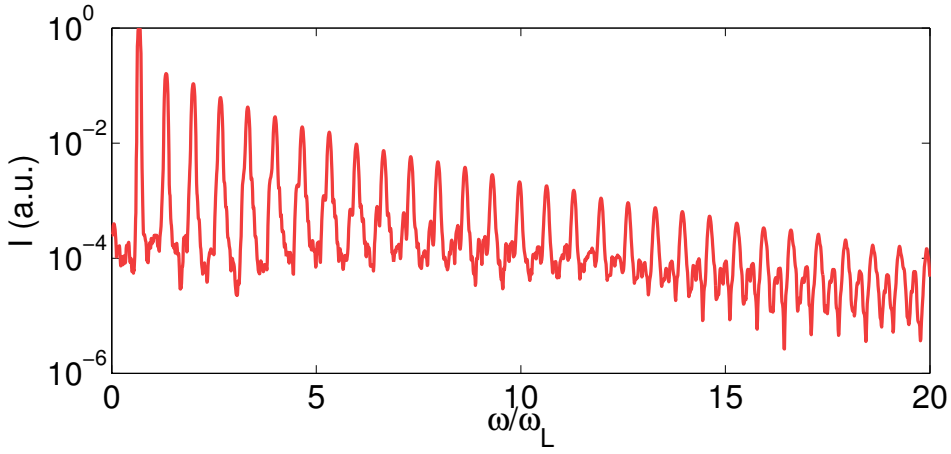


Figure 1.21: Reflected field spectrum from a PIC simulation for $a_0 = 10$, $n_{bulk} = 250n_c$ and $L = \lambda/8$. ω_0 is the incident laser frequency.

Doppler harmonics

The first models for ROM harmonics relied on the Doppler effect (see reference [Bulanov *et al.*, 1994]), which is why ROM harmonics are equivalently called Doppler harmonics. We assume that the plasma has a step-like density profile, and that ions are immobile. The electron surface forms a moving mirror, that reflects the incident field. The shape of the reflected field is modified by the Doppler effect, which changes the frequency of the reflected wave with respect to the incident wave.

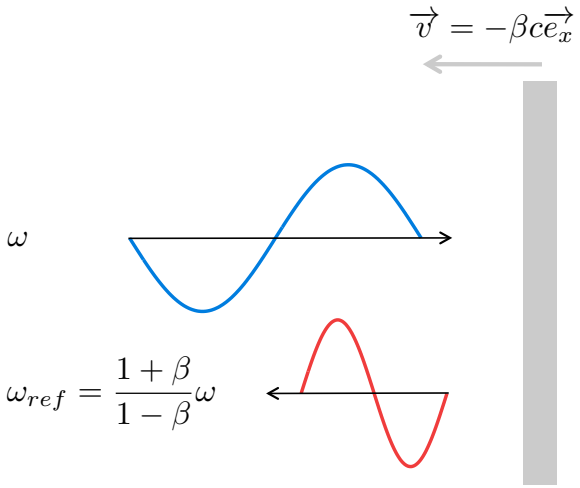


Figure 1.22: Doppler effect. The incident wave (blue) impinges under normal incidence onto a mirror moving with constant speed along $-x$. The frequency of the reflected wave is strongly shifted.

Consider an electromagnetic wave with angular frequency ω incident on a mirror moving with constant speed $\boldsymbol{v} = -v\boldsymbol{e_x} = -\beta c\boldsymbol{e_x}$. This is illustrated in figure 1.22. The incident and reflected waves read *a priori*

$$\psi(x,t) = \psi_0 \cos\left[\omega(t - x/c)\right] \tag{1.94}$$
$$\psi_{ref}(x,t) = \psi_0 \cos[\omega_{ref}(t + x/c)]. \tag{1.95}$$

The boundary condition on the perfect mirror reads

$$\psi(x = -vt, t) = \pm\psi_{ref}(x = -vt, t) \tag{1.96}$$

with $+$ if ψ is the magnetic field and $-$ if ψ is the electric field. This has no consequence on the Doppler effect, so we take $+$ in the following discussion. The incident field on the moving mirror is given by $\psi_{mirror}(t) = \psi(x = -vt, t) = \psi_0 \cos\omega' t$ with $\omega' = \omega(1+\beta)$. The moving mirror acts as a light source, with position $x = -vt$ and local frequency ω'.

In order to calculate the frequency of the reflected wave, we introduce the concept of retarded time that will be used in the next section. Consider the signal ψ_{ref}, propagating with speed c in the $-x$ direction, is emitted at position χ. The signal received by an observer located at position x and time t was emitted earlier, at time t_{ret}:

$$\psi_{ref}(x,t) = \psi_{ref}(\chi, t_{ret}) \tag{1.97}$$
$$\text{with } t_{ret} = t + \frac{x-\chi}{c}. \tag{1.98}$$

We define $t^{(1)}$ and $t^{(2)}$ as

$$\omega_{ref}(t^{(1)} + x/c) = 0 \tag{1.99}$$
$$\omega_{ref}(t^{(2)} + x/c) = 2\pi \tag{1.100}$$

so that the period of the reflected wave received by an observer located at x reads $T_{ref} = t^{(2)} - t^{(1)}$. These signals were emitted by the moving mirror at times $t^{(1)}_{ret}$ and $t^{(2)}_{ret}$ respectively, given by

$$t^{(1)}_{ret} = t^{(1)} + \frac{x - x_m(t^{(1)}_{ret})}{c} \tag{1.101}$$
$$t^{(2)}_{ret} = t^{(2)} + \frac{x - x_m(t^{(2)}_{ret})}{c} \tag{1.102}$$

where $x_m(t) = -\beta t$ stands for the mirror position. Note that $t^{(2)}_{ret} - t^{(1)}_{ret} = T'$ where $T' = 2\pi/\omega'$ is the period of the wave emitted on the moving mirror. We get

$$t^{(2)}_{ret} - t^{(1)}_{ret} = t^{(2)} - t^{(1)} - \frac{x_m(t^{(2)}_{ret}) - x_m(t^{(1)}_{ret})}{c} \tag{1.103}$$
$$= t^{(2)} - t^{(1)} + \beta(t^{(2)}_{ret} - t^{(1)}_{ret}) \tag{1.104}$$
$$\text{and } T_{ref} = (1-\beta)T' \tag{1.105}$$
$$\text{or } \omega_{ref} = \frac{\omega'}{1-\beta}. \tag{1.106}$$

Finally, the frequency shift after reflection reads (see references [Einstein, 1905a,b])

$$\frac{\omega_{ref}}{\omega} = \frac{1+\beta}{1-\beta}. \tag{1.107}$$

Assuming the mirror travels with highly relativistic speed $\beta \simeq 1$, the frequency shift reads

$$\frac{\omega_{ref}}{\omega} \simeq 4\gamma^2 \tag{1.108}$$

with $\gamma = (1-\beta^2)^{-1/2}$.

This expression gives the cutoff for ROM harmonics (see reference [Bulanov *et al.*, 1994]). We consider that the electron surface oscillates as a whole, with a maximum Lorentz factor γ_{max}, and generates harmonics in the reflected field via the Doppler effect. The maximum harmonic order, *i.e.* the cutoff in the reflected field spectrum, reads

$$\frac{\omega_{ref}}{\omega} = 4\gamma^2_{max}. \tag{1.109}$$

However, this results gives the cutoff in the reflected spectrum as a function of the parameter γ_{max}, which is all but reachable in experiments or theory.

Liénard-Wiechert potentials

Though the Doppler effect is a convenient model to understand ROM emission, the underlying physics relies on the radiation of electromagnetic waves by moving electrons, described by the Liénard-Wiechert potentials. Consider an observer located at $\boldsymbol{r} = \boldsymbol{0}$.

The electric field radiated by an electron with position $\boldsymbol{r}$ and normalized speed $\boldsymbol{\beta}$ at the observer's position reads (see reference [Jackson, 1999]):

$$\boldsymbol{E} = \frac{-e}{4\pi\epsilon_0}\left\{-\frac{\boldsymbol{u}+\boldsymbol{\beta}}{\gamma^2(1+\boldsymbol{u}\cdot\boldsymbol{\beta})^3 r^2} + \frac{\boldsymbol{u}\times\left[(\boldsymbol{u}+\boldsymbol{\beta})\times\dot{\boldsymbol{\beta}}\right]}{c(1+\boldsymbol{u}\cdot\boldsymbol{\beta})^3 r}\right\}_{t_{ret}} \tag{1.110}$$

where $\boldsymbol{u}$ is the unit vector defined by $\boldsymbol{u} = \boldsymbol{r}/r$ and t_{ret} is the retarded time. The first term is the static term, and does not depend on particle acceleration. It decreases as $1/r^2$ and will be neglected in this discussion, as in reference [Thaury, 2008]. Let us consider the second term, which is proportional to the charge acceleration $\dot{\boldsymbol{\beta}}$.

To apply this formula to the ROM emission on plasma mirrors, we describe this system in the boosted frame (see section 1.2). The target normal is x, and the incident pulse propagates along x and is polarized along y. The electrons at the plasma surface move along x and y only, and we consider the reflected field, *i.e.* the emission along $-x$:

$$\boldsymbol{u} = \begin{pmatrix}1\\0\\0\end{pmatrix} \quad \boldsymbol{\beta} = \begin{pmatrix}\beta_x\\\beta_y\\0\end{pmatrix}, \tag{1.111}$$

giving

$$\boldsymbol{E} = \left\{\frac{e}{4\pi\epsilon_0 c r}\left[\frac{\dot{\beta}_y}{(1+\beta_x)^2} - \frac{\beta_y\dot{\beta}_x}{(1+\beta_x)^3}\right]\right\}_{t_{ret}} \boldsymbol{e}_y. \tag{1.112}$$

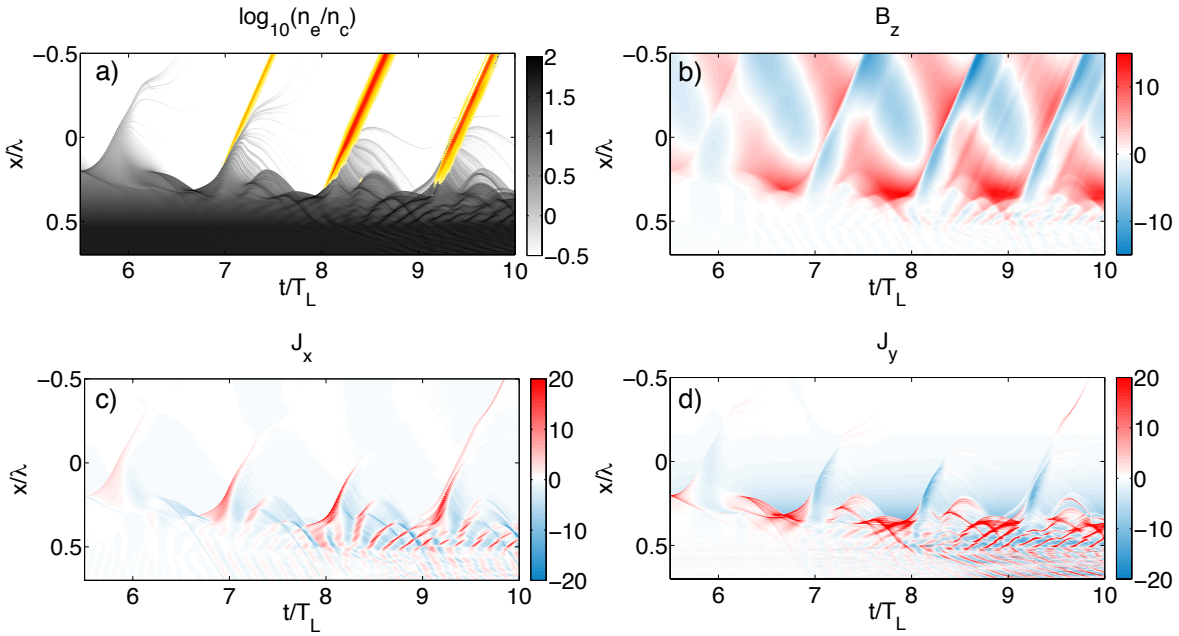


Figure 1.23: Surface dynamics in simulation `these_rom1`. a) Log-scale electron density. One electron jet travels towards vacuum once per laser period. Colours stand for attosecond bunches. A Fourier filter was applied to the magnetic field to keep only high frequencies. b) Magnetic field. c) Transverse current J_x. d) Longitudinal current J_y.

In the ROM mechanism, an attosecond bunch is generated when a large amount of electrons are accelerated towards vacuum. This is shown in figure 1.23 a), where the electron density from the 1D PIC simulation `these_rom1` is represented along with attosecond bunches in the reflected field. In this image, the first attosecond bunch is

generated around $t/T_L = 7$. The total magnetic field is shown in panel b): attosecond bunches correspond to a discontinuity in the reflected field.

Such a bunch is generated when $\boldsymbol{E}$ diverges, *i.e.* $\beta_x \to -1$ in equation 1.112. At this time, electrons travel with relativistic speed towards vacuum. This is depicted in figure 1.23 c), where the density current normal to the target J_x is represented. It peaks when attosecond bunches are generated.

Also, $\beta_x \to -1$ implies $\beta_y = 0$: the transverse density current is zero during the attosecond bunch generation. This can be seen in figure 1.23 d), where the transverse density current switches from positive to negative upon the attosecond bunch generation. **We define the ROM emission time t_e as $\beta_y(t_e) = 0$.**

Finally, the second term in equation 1.112 vanishes at the emission time t_e, and the electric field radiated by an electron in the layer reduces to

$$\boldsymbol{E} \simeq \left\{ \frac{e}{4\pi\epsilon_0 cr} \frac{\dot{\beta}_y}{(1+\beta_x)^2} \right\}_{t_{ret}} \boldsymbol{e_y} \tag{1.113}$$

showing that high frequencies are emitted when $\beta_x \to -1$, hence $\beta_y = 0$, and $\dot{\beta}_y$ is maximum. Therefore, high harmonic generation is clearly related to electron acceleration at the plasma surface.

The ROM model by Lichters

In reference [Lichters *et al.*, 1996], the authors derive an elegant model that gives the temporal shape of the reflected field. We hereafter describe the basics of this model. We assume that the $x > 0$ area is filled with a plasma with uniform density $n_0 \gg n_c$. The angle of incidence is θ and we choose to work in the boosted frame. The ions are immobile, and the electrons move as a bulk, as shown in figure 1.24.

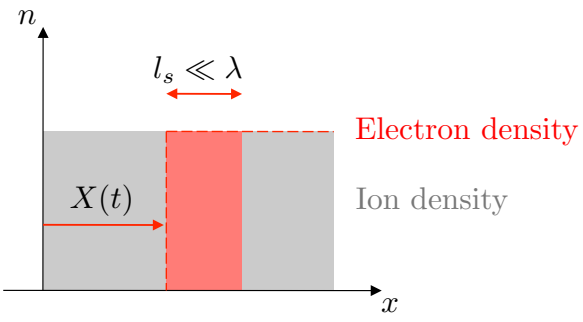


Figure 1.24: Electron and ion density in the boosted frame, in Lichters' model. The ion density forms a background with $\boldsymbol{J} = -en_0 c \sin\theta \boldsymbol{e_y}$. The electron density is $n_e = n_0 \Theta(x - X(t))$ where Θ is the Heaviside function, with $\Theta(x > 0) = 1$ and $\Theta(x \leq 0) = 0$. Only electrons within $[X(t), X(t) + l_s]$ are affected by the laser. Electrons located at $x > X(t) + l_s$ are unperturbed, and create a density current $\boldsymbol{J} = +en_0 c \sin\theta \boldsymbol{e_y}$, so that the total current in this area is zero.

As in reference [Thaury & Quéré, 2010], we can first calculate the radiated field as a function of the transverse current $\boldsymbol{J}_\perp$ defined by $\nabla \cdot \boldsymbol{J}_\perp = 0$. $\boldsymbol{J}_\perp$ is responsible for the electromagnetic component of the electric field, and verifies $\boldsymbol{J}_\perp \in (y, z)$ in our 1D case. The wave equation in the Coulomb gauge $\nabla \cdot \boldsymbol{A} = 0$ reads

$$\partial_x^2 \boldsymbol{A} - \frac{1}{c^2} \partial_t^2 \boldsymbol{A} = -\mu_0 \boldsymbol{J}_\perp \tag{1.114}$$

$$\text{or } L\boldsymbol{A} = -\mu_0 \boldsymbol{J}_\perp \tag{1.115}$$

where $L = \partial_x^2 - \frac{1}{c^2}\partial_t^2$ is a linear operator. A Green's function for this operator, defined by $LG[(x,t),(\chi,\tau)] = \delta(x-\chi, t-\tau)$ is

$$G[(x,t),(\chi,\tau)] = \Theta\left[t - \tau - \frac{|x-\chi|}{c}\right] \tag{1.116}$$

where Θ is the Heaviside function. Note that the Green's function depends on $(x-\chi)$ and $(t-\tau)$ instead of the four variables independently because L has constant coefficients.

Finally,

$$\boldsymbol{A}(x,t) = -\mu_0 c \int_{\chi=-\infty}^{+\infty}\int_{\tau=-\infty}^{+\infty} G[(x,t),(\chi,\tau)]\boldsymbol{J}_\perp(\chi,\tau)d\tau d\chi \tag{1.117}$$

$$= -\mu_0 c \int_{\chi=-\infty}^{+\infty}\int_{\tau=-\infty}^{+\infty} \Theta\left[t - \tau - \frac{|x-\chi|}{c}\right]\boldsymbol{J}_\perp(\chi,\tau)d\tau d\chi. \tag{1.118}$$

The support of the integrand is shown in figure 1.25. We restrict ourselves to the $\chi > x$ area to account for light propagating in the $-x$ direction (the reflected light) and perform the integral along the red lines.

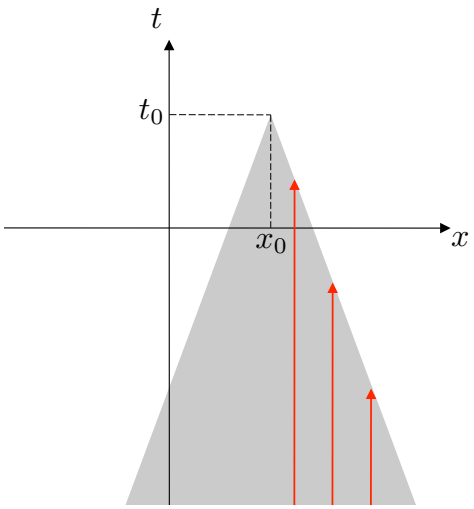


Figure 1.25: Integration area in equation 1.118 (grey area). The integration is performed along t for a given x, as illustrated by the red arrows. Only the $x > 0$ region is considered, where electromagnetic waves propagate along $-x$.

Hence, equation 1.118 for the reflected light reads

$$\boldsymbol{A}^r(x,t) = -\mu_0 c \int_{\chi=x}^{+\infty}\int_{\tau=-\infty}^{t-(\chi-x)/c} \boldsymbol{J}_\perp(\chi,\tau)d\tau d\chi. \tag{1.119}$$

Using equation $\boldsymbol{E}^r = -\partial_t \boldsymbol{A}^r$, the reflected electric field is finally given by

$$\boldsymbol{E}^r(x,t) = +\mu_0 c \int_x^{+\infty} \boldsymbol{J}_\perp\left(\chi, t - \frac{\chi - x}{c}\right) d\chi. \tag{1.120}$$

This formal derivation involves the retarded time $t_{ret} = t - (\chi - x)/c$. This result has a physical meaning: the total field at (x,t) is the field radiated at (χ, t_{ret}), summed over all $\chi > x$. Let us now apply this general formula to our specific case.

The transverse current reads

$$\boldsymbol{J}_\perp = -en_e\boldsymbol{v}_{e\perp} + en_i\boldsymbol{v}_{i\perp} \tag{1.121}$$

where n_e is the electron density and $\boldsymbol{v}_{e\perp}$ is the electron transverse speed (orthogonal to x). Subscripts i stand for ion quantities. In the boosted frame, the ions drift with speed $\boldsymbol{v}_{i\perp} = -c\sin\theta\boldsymbol{e_y}$, and the ion density equals the initial density at all time: $n_i = n_0$.

Let us derive the electron contribution, starting from the conservation of canonical momentum

$$\boldsymbol{p}_{e\perp} - e\boldsymbol{A}_\perp = \boldsymbol{p}_{e\perp 0} - e\boldsymbol{A}_0 \tag{1.122}$$

$$= -m_e c\frac{\sin\theta}{\sqrt{1-\sin^2\theta}}\boldsymbol{e_y} \tag{1.123}$$

$$= -m_e c\tan\theta\boldsymbol{e_y}. \tag{1.124}$$

This gives

$$\boldsymbol{J}_\perp(x,t) = -ec\left\{\frac{n_e(x,t)}{\gamma(x,t)}[\boldsymbol{a}_\perp(x,t) - \tan\theta\boldsymbol{e_y}] + n_0(x,t)\sin\theta\boldsymbol{e_y}\right\} \tag{1.125}$$

where $\boldsymbol{a}_\perp = e\boldsymbol{A}_\perp/m_e c$ and γ is the electron Lorentz factor. The (x,t) dependence will be skipped when possible, in order to avoid heavy notations.

We can rewrite the Lorentz factor γ as

$$\gamma = \sqrt{1 + \left(\frac{p_{e\perp}}{m_e c}\right)^2 + \gamma\beta_{e/\!/}^2} \tag{1.126}$$

$$\text{giving } \gamma = \sqrt{\frac{1 + (\boldsymbol{a}_\perp - \tan\theta\boldsymbol{e_y})^2}{1-\beta_{e/\!/}^2}}. \tag{1.127}$$

Finally, we assume that the electron surface is located at position $X(t)$ as shown in figure 1.24, and that the transverse current differs from the drift current $-c\sin\theta\boldsymbol{e_y}$ only in the skin layer l_s. Besides, we assume that the plasma is highly overdense, so that

$$\frac{l_s}{\lambda} = \sqrt{\frac{n_c}{n_e}} \ll 1. \tag{1.128}$$

In this case, equation 1.120 gives the field radiated by the electron distribution

$$\boldsymbol{E}_e^r(x,t) = \mu_0 c l_s \boldsymbol{J}_{e\perp}\left(X(t_{ret}), t_{ret}\right) \tag{1.129}$$

$$\text{with } t_{ret} = t - \frac{X(t_{ret}) - x}{c}. \tag{1.130}$$

And the ion radiation reads, assuming $\forall t\ X(t) \ll \lambda$,

$$\boldsymbol{E}_i^r(x,t) = \mu_0 c[X(t_{ret}) + l_s](-en_i c\tan\theta\boldsymbol{e_y}). \tag{1.131}$$

The reflected field reads

$$\boldsymbol{E}^r(x,t) = -\frac{e}{\epsilon_0}\left[\frac{l_s n_e\sqrt{1-\dot{X}^2(t_{ret})/c^2}}{\sqrt{1+(\boldsymbol{a}_\perp - \tan\theta\boldsymbol{e_y})^2}}(\boldsymbol{a}_\perp - \tan\theta\boldsymbol{e_y}) + [X(t_{ret}) + l_s]n_i\sin\theta\boldsymbol{e_y}\right] \tag{1.132}$$

where $\boldsymbol{a}_\perp \equiv \boldsymbol{a}_\perp(X(t_{ret}), t_{ret})$.

At this point, $\boldsymbol{a}_\perp$ and $X(t)$ are still unknown. We assume that $\boldsymbol{a}_\perp$ is due to the incident field only (so that the reflected field is neglected):

$$\boldsymbol{a}_\perp = a_0(x,t)\sin(\omega_0 t - kx)\boldsymbol{e_y} \tag{1.133}$$

where $a_0(x,t)$ stands for the temporal envelope. Let us assume that $X(t)$ is a harmonic motion due to the incident field. This reads

$$X(t) = X_1 \cos(\omega_0 t + \phi_1) \tag{1.134}$$

$$= \frac{c}{\omega_0} \frac{2a_0(x,t)\sin\theta}{\sqrt{1 + [2a_0(x,t)\sin\theta]^2}} \cos(\omega_0 t + \phi_1) \tag{1.135}$$

with $\phi_1 = 0$ for an electron in a plane wave.

This is the strongest approximation of the model: the dynamics of the electron surface is imposed *a priori*, though one can clearly see in figure 1.20 that the dynamics is far from harmonic, and rather complex. Lichters *et al.* allow a non-harmonic surface dynamics via oscillations at frequencies $2\omega_0$, $3\omega_0$ etc. Still, the amplitude and phase of these higher harmonics X_2, ϕ_2 and X_3, ϕ_3 must be chosen.

Finally, one has to find t_{ret} in equation 1.132 to determine the reflected field. Yet t_{ret} is defined by the recursive equation 1.130, and cannot be calculated analytically. $X(t_{ret})$ is the fixed point of the contraction mapping $f : \chi \mapsto X(t - (\chi - x)/c)$, it can be calculated for a given t as the limit of the sequence:

$$X_0 = X(t) \tag{1.136}$$

$$X_{n+1} = X(t - \frac{X_n - x}{c}). \tag{1.137}$$

As a confirmation, this model was applied to a pulse with duration 8 fs and $a_0 = 5$. As is done in Lichters' article, we assume the reflection takes place at the critical density, hence $n_0 = n_c$. Yet the skin depth is still $l_s \ll \lambda$. We took $l_s = \lambda/200$. The loop for t_{ret} converges after $\simeq 1000$ iterations.

Figure 1.26 a) shows the full incident field. Functions $X(t)$ and $X(t_{ret})$ are plotted in figure 1.26 b). The second one clearly differs from a pure sine wave, the only cause being the retarded time. The dynamics becomes anharmonic because of the relativistic time-dependent Doppler effect. The reflected field is shown in figure 1.26 c). A filter was applied to only keep harmonics above 10, shown as the black line. Finally, the reflected field spectrum is shown in figure 1.26 d). The harmonic efficiency decreases as $n^{-10/3}$ where n is the harmonic order.

This models embraces the electron dynamics, the relativistic Doppler effect and provides the temporal shape of the reflected field. However, it relies on strong hypotheses (the electron dynamics is imposed), and does not give scaling laws for the harmonic efficiency decrease and cutoff.

The BGP model

The next important milestone for modeling harmonic generation via the ROM mechanism is presented in reference [Baeva *et al.*, 2006], where the authors extend the idea of the oscillating mirror. They assume that a perfectly reflecting mirror is located at $X(t)$, where the sum of the incident and reflected fields is zero. As for Lichters'

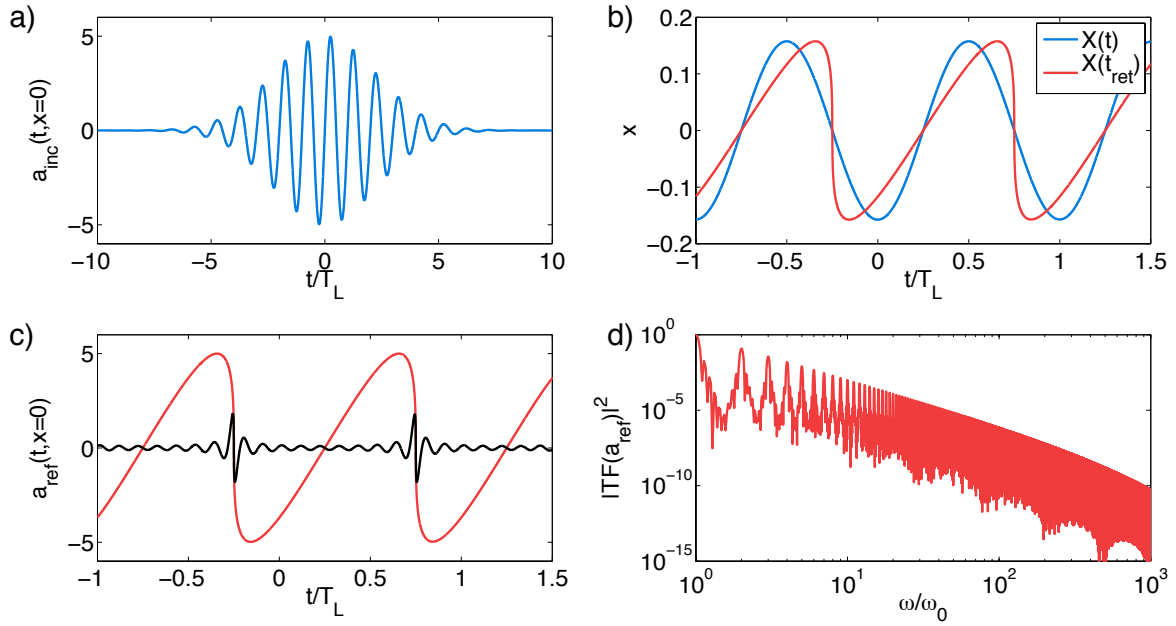


Figure 1.26: Example of Lichters' model. a) incident field ($a_0 = 5$, $\theta = 45°$, $\tau_L = 8\,\mathrm{fs}$ with a Gaussian time-envelope). b) Surface position $X(t)$ and $X(t_{ret})$, where the deformation from a pure sine wave is a signature for Doppler effect and high harmonic generation. c) Full reflected field (red). A filter was applied to keep only harmonic orders > 10 (black line). d) Spectrum of the reflected field.

model, high harmonics are generated in the reflected field because the mirror moves with relativistic velocity. Yet they do not link $X(t)$ with any physical quantity.

They show that the harmonic generation efficiency decreases as $n^{-8/3}$ where n is the harmonic order. Furthermore, they demonstrate that the maximum harmonic order (the cutoff) varies as γ_{max}^3, where γ_{max} is the maximum Lorentz factor of the oscillating mirror. This result seems to contradict the cutoff derived form the Doppler effect in equation 1.109, which varies as $4\gamma_{max}^2$. The reason for this discrepancy is that the mirror does not move with constant speed v, but rather emits high harmonics during a very short time $\delta t \propto 1/\gamma_{max}$. The cutoff varies as $\delta t/4\gamma_{max}^2 \propto 1/\gamma_{max}^3$.

Figure 1.27 a) shows the reflected field as a function of time for the simulation named `these_rom1`. The $n^{-8/3}$ scaling was added to the spectrum as a comparison. In this case, this prediction from the BGP model is well verified. Yet their model suffers two essential weaknesses: first, as it relies on the Doppler effect, the peak amplitude of the reflected field cannot exceed the amplitude of the incident field. In figure 1.27 a), the peak amplitude of the reflected field is much higher than the peak amplitude of the incident field $a_0 = 5$. The second limit to their model is that $X(t)$ does not correspond to any physical quantity. Indeed, for a given time t, one cannot always find a point where the total field cancels. As a consequence, γ_{max} is not easy to determine. Besides, the $n^{-8/3}$ law is not absolutely universal, as shown in reference [Boyd & Ondarza-Rovira, 2008].

Conclusion: This chapter introduced the main theoretical tools for the reflection of a laser pulse upon an overdense plasma. First, this interaction can lead to electron ejection via three distinct mechanisms: resonance absorption, vacuum heating and $J \times B$ heating. Second, harmonics can be generated in the reflected field via two processes: coherent wake emission and the relativistic oscillating mirror effect. Both

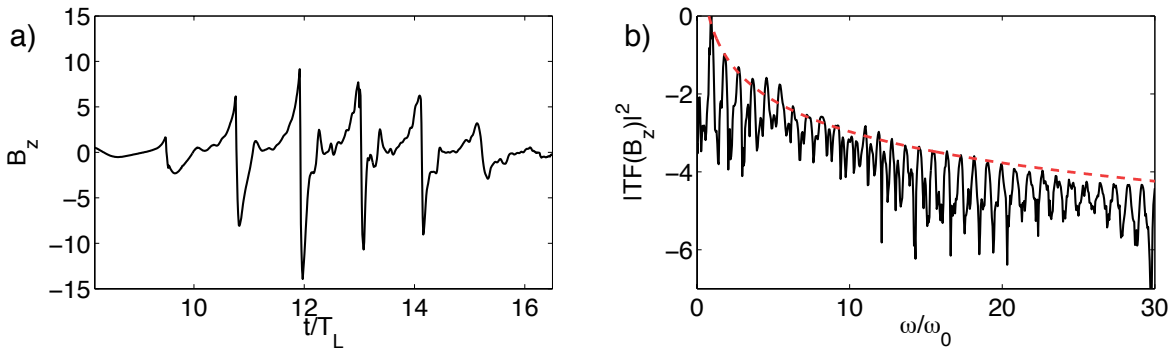


Figure 1.27: a) Reflected field from PIC simulation `these_rom1`. $\theta = 45°$, $a_0 = 5$, $n_{bulk} = 50n_c$, $L = \lambda/8$. The ions are immobile. The numerical parameters are $\Delta x = \lambda/1000$ with 500 particles per cell. b) shows the spectrum of the reflected field. The harmonic decrease predicted by the BGP model is shown as a red dashed line.

harmonic generation and electron emission are observable in experiments, and a better understanding of the surface dynamics provides significant help to analyse experimental results.

Yet a review of many experimental results shows that the mechanism for backward electron ejection remains unclear, and is not compatible with any of the three effects mentioned above. In particular, the role of the density gradient is often omitted since it is badly controlled in experiments. The mechanism for backward electron ejection is studied in chapter 3, and the gradient length is shown to play a major role. chapter 2 introduces the indispensable numerical tools that were intensively used within the scope of this work.

Chapter 2

Numerical tools

Contents

2.1 Particle-in-cell simulations for laser-plasma interaction . . 52

2.1.1 The Vlasov-Maxwell system 52

2.1.2 Vlasov numerical method 53

2.1.3 Particle-in-cell method 54

2.1.4 Steps of a PIC code 56

2.1.5 PIC: limits, noise and errors 59

2.1.6 Study on numerical parameters 60

2.1.7 Typical 2D PIC simulation 63

2.2 Electron in a laser pulse in vacuum 65

2.2.1 Electron in a monochromatic plane wave 65

2.2.2 Gaussian pulse and paraxial approximation 69

2.2.3 Non-paraxial corrections in the tightly-focused regime 70

2.2.4 Ponderomotive force 71

2.2.5 Finite-duration correction 72

2.1 Particle-in-cell simulations for laser-plasma interaction

Only a limited number of plasma phenomena can be described via an analytical approach. Even restricting ourselves to the case of kinetic plasmas, the first difficulty lies in the equation of dynamics itself, the Vlasov equation, which belongs to the general class of partial differential equations. The mathematical difficulty inherent to these equations is the main motivation for developing numerical tools.

Besides, in a large variety of regimes ranging from stellar plasmas to laboratory plasmas, relativistic phenomena must be taken into account, when the particle speed approaches the speed of light. The relativistic plasma regime leads to strongly nonlinear dynamics, which adds further difficulty on top of that instrinsic to the Vlasov equation.

These issues led to the development of a new field, computational plasma physics, in which basic plasma equations are solved numerically to study the temporal evolution of a plasma with given initial conditions. The power of this tool is that it allows an unlimited range of new observables, which can absolutely not be reached in experiments. Yet, just like any model, these numerical tools rely on hypotheses, they have a limited domain of validity, and they can lead to misinterpretations. One of the most widespread numerical method for plasma physics is the particle-in-cell method, which solves the Vlasov-Maxwell system governing plasma dynamics.

We hereafter present the set of equations governing kinetic plasmas, and detail the particle-in-cell method that we used extensively in this work. Finally, we show a set of typical numerical simulations performed in the scope of this thesis.

2.1.1 The Vlasov-Maxwell system

The Vlasov equation describes the plasma dynamics in the collisionless regime, where the plasma dynamics is due to average collective fields. Let f_s be the distribution function of species s, with particle mass m_s and charge q_s. The number of particles δN in the 6-dimensional volume $\delta\boldsymbol{r}\delta\boldsymbol{p}$ at time t is given by $\delta N = N_t f_s(t, \boldsymbol{r}, \boldsymbol{p})\delta\boldsymbol{r}\delta\boldsymbol{p}$ where N_t is the total number of particles. The distribution function is a general tool thanks to which one can derive the usual quantities: charge density ρ and current density $\boldsymbol{J}$ as the 0^{th} and 1^{st} moments of the distribution function

$$\rho_s = q_s \int_{-\infty}^{\infty} f_s d\boldsymbol{p} \tag{2.1}$$

$$\boldsymbol{J}_s = q_s \int_{-\infty}^{\infty} f_s \frac{\boldsymbol{p}}{\sqrt{1+\boldsymbol{p}^2}} d\boldsymbol{p}. \tag{2.2}$$

The total charge and current density are the sum on the ensemble of species S in the plasma

$$\rho = \sum_{s\in S} \rho_s \tag{2.3}$$

$$\boldsymbol{J} = \sum_{s\in S} \boldsymbol{J}_s. \tag{2.4}$$

Typically, the simplest case for a neutral plasma is S={electrons,ions}.

The Vlasov equation reads

$$\frac{\partial f_s}{\partial t} + \frac{d\boldsymbol{r}}{dt}\cdot\frac{\partial f_s}{\partial \boldsymbol{r}} + \frac{d\boldsymbol{p}}{dt}\cdot\frac{\partial f_s}{\partial \boldsymbol{p}} = 0. \tag{2.5}$$

The first term is the time evolution of the function. The second term is the advection term, and the third term stands for the application of forces:

$$\frac{d\boldsymbol{p}}{dt} = q_s(\boldsymbol{E} + \boldsymbol{v} \times \boldsymbol{B}) \tag{2.6}$$

with $\boldsymbol{p} = m_s\gamma\boldsymbol{v}$ and $\gamma = (1 - v^2/c^2)^{-1/2}$.

A plasma involves displacements of charges that modify the electric and magnetic fields, so $\boldsymbol{E}$ and $\boldsymbol{B}$ have to be included in the plasma dynamics. This is done by adding Maxwell's equation to the Vlasov equation:

$$\nabla \cdot \boldsymbol{E} = \frac{\rho}{\epsilon_0} \qquad \nabla \times \boldsymbol{E} = -\frac{\partial \boldsymbol{B}}{\partial t} \tag{2.7}$$

$$\nabla \cdot \boldsymbol{B} = 0 \qquad \nabla \times \boldsymbol{B} = \mu_0 \left(\boldsymbol{J} + \epsilon_0 \frac{\partial \boldsymbol{E}}{\partial t} \right). \tag{2.8}$$

This non-linear system of partial differential equations can seldom be solved analytically, and one often has to resort to numerical resolution. We hereafter introduce two equivalent ways of expressing the Vlasov equation, the Eulerian and the Lagrangian approaches, each of which results in a numerical method for solving the Vlasov-Maxwell system. Finally, both methods are exposed, and much more detail is given on the one based on the Lagrangian approach for particles, called the particle-in-cell method, that we used extensively in this work.

Eulerian approach: The observer is fixed at position $\boldsymbol{r}$ and considers the flow of the plasma fluid. $f_s(\boldsymbol{r}, \boldsymbol{p}, t)d\boldsymbol{r}d\boldsymbol{p}$ is the number of particles of species s in a volume element $d\boldsymbol{r}d\boldsymbol{p}$ around position $\boldsymbol{r}$ and momentum $\boldsymbol{p}$. This formulation is relevant when dealing with average plasma quantities, and reduces to the plasma Euler equations involving the plasma density ρ and current density $\boldsymbol{J}$ when only moments with order smaller than two or three are considered.

Lagrangian approach: This approach consists in following the motion of each single particle along its trajectory. Then, $f_s(t, \boldsymbol{r_1}, ..., \boldsymbol{r_N}, \boldsymbol{p_1}, ..., \boldsymbol{p_N})d\boldsymbol{r_1}...d\boldsymbol{r_N}d\boldsymbol{p_1}...d\boldsymbol{p_N}$ is the probability for each particle i to be in a volume element $d\boldsymbol{r_i}d\boldsymbol{p_i}$ around position $\boldsymbol{r_i}$ and momentum $\boldsymbol{p_i}$. This formulation is well-adapted to solve the equation of motion for single particles.

Maxwell's equations use the Eulerian approach. The Vlasov-Maxwell system can be solved numerically using the two approaches described above for the plasma dynamics: the Eulerian approach leads to the so-called Vlasov numerical method and is explained in section 2.1.2, and the Lagrangian approach leads to the particle-in-cell numerical method that we used in this work, and which is detailed starting from section 2.1.3.

2.1.2 Vlasov numerical method

Vlasov codes rely on a discretization of the $(\boldsymbol{r}, \boldsymbol{p})$ phase space. For a 2D simulation in phase space x, p_x, f is discretized on a grid $(\{x_i,\ 0 \leq i < n_x\},\{p_{xk},\ 0 \leq k < n_p\})$ and along time using a time-step Δt, such that $f^n_{i,k} = f(x_i, p_{xk}, n\Delta t)$. The resolution uses the Finite-Difference Time Domain (FDTD) [Yee *et al.*, 1966] method to calculate quantities at time iteration n using their values at iteration $n-1$. Figure 2.1 illustrates very schematically the iteration performed at every time-step for a Vlasov code to calculate $f^{n+1}_{i,k}$ knowing $f^n_{i,k}$. This diagram provides a simplified picture of the core loop

of the algorithm. The implementation relies on leapfrog methods, and involves more elaborate resolution schemes for solving the Vlasov equation like the time-splitting scheme developed in reference [Cheng & Knorr, 1976] as well as the positive and flux conservation method developed in [Filbet *et al.*, 2001]. More details can be found in [Grassi *et al.*, 2016].

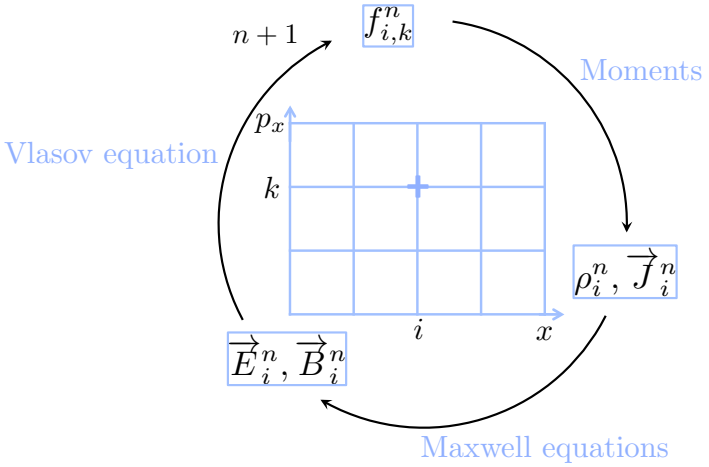


Figure 2.1: Diagram for a 2D (x, p_x) Vlasov simulation. Consider that the distribution function $f^n_{i,k}$ at iteration n is known on the whole grid. (i) ρ^n_i and $\boldsymbol{J}^n_i$ are calculated as moments of the distribution, summing on the p_x grid direction. (ii) $\boldsymbol{E}^n_i$ and $\boldsymbol{B}^n_i$ are determined solving Maxwell's equations. (iii) The Vlasov equation is solved using these fields to get $f^{n+1}_{i,k}$.

Pros: Since they involve no particles, there is no problem of lack of statistics and there is no particle fluctuation. Consequently, simulation results show relatively little noise.

Cons: They require up to 6D $(\boldsymbol{r}, \boldsymbol{p})$ grids for full 3D simulations, and their computational cost can be notably high. In specific conditions, this issue can be solved via the Vlasov-Fokker-Plank method [Thomas *et al.*, 2012] to reduce the problem to a 3D grid.

2.1.3 Particle-in-cell method

The particle-in-cell (PIC) approach relies on the Eulerian approach for Maxwell's equations and the Lagrangian approach for the Vlasov equation. Space is discretized to solve Maxwell's equations. The distribution function is a sum of N elementary functions, called macroparticles. Each macroparticle p is characterized by its charge, mass and shape, and has position $\boldsymbol{r}_p$ and momentum $\boldsymbol{p}_p$. In the ideal case, each macroparticle would stand for a single physical particle, say an electron, with charge $-e$, mass m_e and a Dirac shape $\delta(\boldsymbol{r} - \boldsymbol{r}_p)$. In the particle-in-cell method, each particle usually stands for a large number of physical particles of the same species, and shows a non-Dirac shape function. For example, macroelectron p has charge q_p and mass m_p, verifying the ratio $q_p/m_p = e/m_e$. This is described in a following paragraph.

A PIC simulation consists of (i) a **grid** on which the fields are calculated solving the discretized Maxwell's equations and (ii) **particles** moving freely in space and contributing to the local charge and current density. The equation of motion is solved

to move every particle, and their contribution to ρ and $\boldsymbol{J}$ is calculated on the neighboring grid nodes. As a consequence, interpolations between particle variables $\{\boldsymbol{r}_p, \boldsymbol{p}_p\}$ and grid variables $(\boldsymbol{E},\boldsymbol{B},\rho,\boldsymbol{J})$ are required. The core loop for the PIC method is depicted in figure 2.2. Fundamental properties of macroparticles are detailed in the next paragraph.

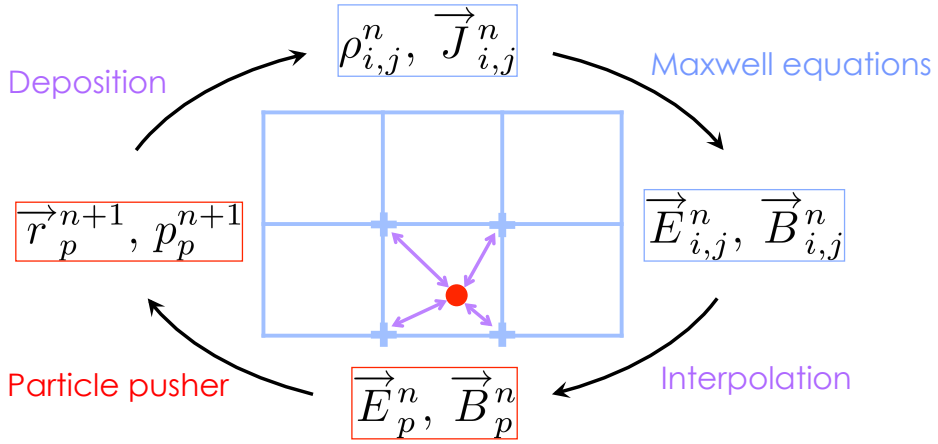


Figure 2.2: Diagram for a 2D (x, y) PIC simulation. Starting from the charge density and density current on every grid point at iteration n, each loop iteration proceeds in four steps: (i) Maxwell's equations are solved to calculate the electric and magnetic fields at every grid point. (ii) The fields are interpolated at the position of each particle. (iii) The equation of motion is solved for each particle with the fields calculated in the previous step to determine the position and speed at iteration $n+1$. (iv) Each particle contributes to the charge density and current density through its charge and charge×speed respectively. Its contribution is deposited on the neighboring grid points. The blue and red colors stand for grid and particle processing respectively. Transition steps are shown in purple.

Macroparticles: Assuming that the volume of a particle is zero (*i.e.* neglecting quantum effects), the distribution function for a finite number of particles N reads

$$f(t, \boldsymbol{r}, \boldsymbol{p}) = \frac{1}{N} \sum_{p=1}^{N} \delta(\boldsymbol{r} - \boldsymbol{r}_p)\delta(\boldsymbol{p} - \boldsymbol{p}_p). \tag{2.9}$$

A simulation with a real number of physical particles is far above the computational power available today, so each macroparticle should stand for a high number of physical particles. This is performed by giving each particle p a weight s_p, that stands for the number of physical particles it represents. Besides, the contribution of each particle to $\boldsymbol{J}$ is calculated on the neighboring grid points during the deposition phase. The simplest method consists in depositing the particle current to the nearest grid point (NGP method). Yet, when a particle travels through the grid, its contribution suddenly shifts from one grid point to its neighbor, which results in a large field noise. This effect is smoothed by giving each particle a finite size in space via a weight function W_p through which the particle contribution is assigned to several neighbors. Hence, the discretized distribution function for N macroparticles reads

$$f_d(\boldsymbol{r}, \boldsymbol{p}, t) = \frac{1}{N} \sum_{p=1}^{N} s_p W_p(\boldsymbol{r} - \boldsymbol{r}_p)\delta(\boldsymbol{p} - \boldsymbol{p}_p). \tag{2.10}$$

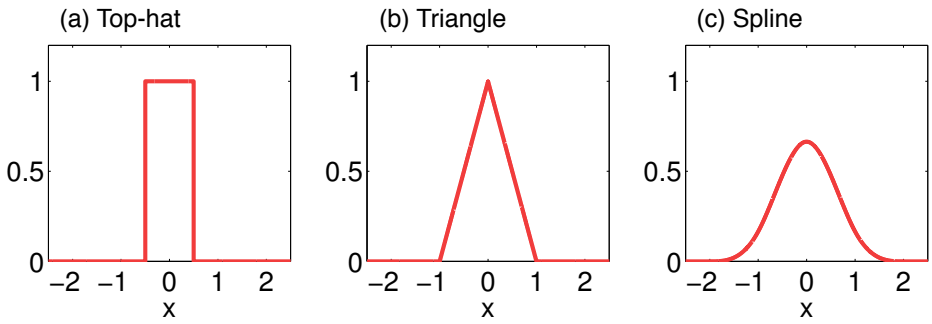


Figure 2.3: Particles weight functions in direction x, in units of grid cells. a) is the top-hat function. b) is the convolution of the top-hat function with itself once. c) is the fourth-order spline, the convolution of the top-hat function with itself three times. They are normalized so that the integral is 1. The higher the order, the wider the support of the function.

Common weighting functions are depicted in figure 2.3. They are spline functions, and can be calculated via n convolutions of the top-hat function with itself.

The simulations presented in this work were performed with the open-source PIC code EPOCH, developed in the University of Warwick. In section 2.1.4, we give more details on the four steps of the PIC loop, as well as the method used in EPOCH for each of them, which is always the most widespread method. More details can be found in [Arber *et al.*, 2015]. The full equations are given for 2D simulation. We use the following notations:

$$Q^n_{i,j} = Q(i\Delta x, j\Delta y, n\Delta t) \tag{2.11}$$

for any quantity Q.

2.1.4 Steps of a PIC code

Maxwell solver

Gauss's law and Gauss's law for magnetism are not explicitly time-dependent. As a consequence, they will be verified all along the simulation, provided they are verified at initialization and provided their conservation is ensured in numerical methods. The time evolution of the system is therefore determined by Ampère's and Faraday's laws. Starting from $\boldsymbol{J}$ on the grid nodes, these two equations are solved with an explicit solver using the finite-difference time domain (FDTD) method presented in [Yee *et al.*, 1966].

Space discretization: The electric and magnetic fields are discretized on a staggered grid, so the fields at the grid point (i, j) are defined at half space-steps around this point $(i \pm 1/2, j \pm 1/2)$. This scheme increases the order of convergence to 2 without increasing the computational cost significantly, provided the fields are defined at the appropriate position. It is designed so that all the spatial derivatives are centered. The

scalar equations are

$$\partial_t B_x = \partial_z E_y - \partial_y E_z \tag{2.12}$$
$$\partial_t B_y = \partial_x E_z - \partial_z E_x \tag{2.13}$$
$$\partial_t B_z = \partial_y E_x - \partial_x E_y \tag{2.14}$$
$$\partial_t E_x = c^2 \partial_y B_z - c^2 \partial_z B_y - 1/\epsilon_0 J_x \tag{2.15}$$
$$\partial_t E_y = c^2 \partial_z B_x - c^2 \partial_x B_z - 1/\epsilon_0 J_y \tag{2.16}$$
$$\partial_t E_z = c^2 \partial_x B_y - c^2 \partial_y B_x - 1/\epsilon_0 J_z. \tag{2.17}$$

As an illustration, equation 2.12 is centered in space if E_y is defined with a $\Delta z/2$ offset along z with respect to B_x. The Yee staggered grid allows this condition to be verified for all components of $\boldsymbol{E}$ and $\boldsymbol{B}$. The 2D grid is shown in figure 2.4, along with position of fields relevant for our purpose.

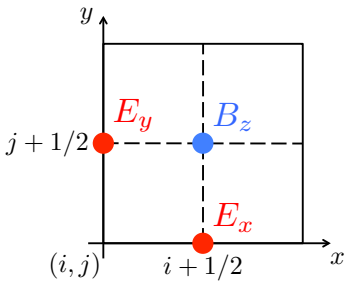


Figure 2.4: Yee staggered grid for cell (i, j) and location of the relevant electric and magnetic fields.

Time discretization: Since the time derivatives of the magnetic field B only involve the electric field E, the system of equations is perfectly fitted for a leapfrog scheme, for which the time derivatives are centered, with B defined at iteration n and E defined at $n + 1/2$. Yet the coupling with the macroparticles via the source term $\boldsymbol{J}$ has to be dealt with, and both fields are calculated for all half-time-steps. Hence, equation 2.15 is solved as follows, removing E_z, B_x, B_y from these equations, for simplicity and because they are zero in our 2D case:

$$\frac{E^{n+1/2}_{x;i+1/2,j} - E^{n}_{x;i+1/2,j}}{\Delta t/2} = \frac{B^{n}_{z;i+1/2,j+1/2} - B^{n}_{z;i+1/2,j-1/2}}{\Delta y} - \frac{1}{\epsilon_0} J^{n}_{x;i+1/2,j} \tag{2.18}$$

The other components of the electric field are calculated similarly, giving $\boldsymbol{E}^{n+1/2}$. This value is used to calculate $\boldsymbol{B}^{n+1/2}$. At this stage, the particle pusher is invoked (see 2.1.4) to get J_{n+1}, and the second half-time-step is performed in the same way with the new value J_{n+1}.

Interpolation

The fields defined at the grid points must be interpolated at each particle position to solve the equation of motion. This is performed using the same particle weight function (see figure 2.3) as for the current deposition. Hence, the electric field E_x on particle p is

$$E^{n}_{x;p} = \sum_{(i,j)} E^{n}_{x;i,j} W_p(x^n_p - i\Delta x, y^n_p - j\Delta y) \tag{2.19}$$

where we ignored half-indices due to the Yee grid for the sake of simplicity. All components of $\boldsymbol{E}$ and $\boldsymbol{B}$ are processed this way.

Particle pusher

Knowing the fields at particle positions, the equations of motion can be solved to update the particles' position and speed. A leapfrog method can be applied again to move from $(\boldsymbol{r}_p^{n-1/2}, \boldsymbol{v}_p^n)$ to $(\boldsymbol{r}_p^{n+1/2}, \boldsymbol{v}_p^{n+1})$ with the field values at $n+1/2$. This is performed using the quick and accurate Boris pusher, taking place in three steps:

1. Half-step acceleration by the electric field $\rightarrow \widetilde{\boldsymbol{p}}$;
2. Full rotation due to the magnetic field $\rightarrow \overline{\boldsymbol{p}}$;
3. Second half-step acceleration by the electric field $\rightarrow \boldsymbol{p}_p^{n+1}$.

We also use $\widetilde{\boldsymbol{v}} = \widetilde{\boldsymbol{p}}/\sqrt{1+\widetilde{p}^2}$ and $\overline{\boldsymbol{v}} = \overline{\boldsymbol{p}}/\sqrt{1+\overline{p}^2}$.

Step 1 is

$$\widetilde{\boldsymbol{p}} = \boldsymbol{p}_p^n + q_p \frac{\Delta t}{2} \boldsymbol{E}^{n+1/2} \tag{2.20}$$

Step 2 is a rotation involving the following substeps:

$$\boldsymbol{h} = \frac{q_p}{m_p} \frac{\Delta t}{2} \boldsymbol{B}^{n+1/2} \tag{2.21}$$

$$\boldsymbol{s} = \frac{2}{1+h^2} \boldsymbol{h} \tag{2.22}$$

$$\overline{\boldsymbol{v}} = \widetilde{\boldsymbol{v}} + (\widetilde{\boldsymbol{v}} + (\widetilde{\boldsymbol{v}} \times \boldsymbol{h})) \times \boldsymbol{s} \tag{2.23}$$

Step 3 reads

$$\boldsymbol{p}_p^{n+1} = \overline{\boldsymbol{p}} + q_p \frac{\Delta t}{2} \boldsymbol{E}^{n+1/2}. \tag{2.24}$$

Current deposition

After the particle pusher is applied, resulting in the new position $x_p^{n+3/2}$ and speed $\boldsymbol{v_p^{n+1}}$ for particles, each particle contribution to $\boldsymbol{J}$ at the neighboring grid points (ρ does not appear in the time-dependent Maxwell's equations) has to be processed.

As already mentioned in the paragraph regarding the Maxwell solver, only the time-dependent Maxwell-Ampère and Maxwell-Faraday laws are solved at every time-step, while the Maxwell-Gauss and Maxwell-Thomson equations are only used during the simulation initialization. Since the Maxwell-Thomson equation does not involve any source term, it will be verified all along the simulation using the FDTD scheme.

The Maxwell-Gauss equation is also verified along the simulation provided the charge conservation equation $\partial_t \rho + \nabla \cdot \boldsymbol{J} = 0$ is verified (This is shown by deriving Maxwell-Gauss equation with respect to t and injecting the charge conservation equation). Verifying the charge conservation equation is of paramount importance, and is easier than verifying the Maxwell-Gauss equation because it only involves ρ and $\boldsymbol{J}$. This is taken care of in the current deposition step, where $\boldsymbol{J}$ is updated.

In reference [Villasenor & Buneman, 1992], the authors develop a method for current deposition assuming a top-hat shape function for particles. When a particle travels in cell (i, j), its current contribution is based on the particle charge that crossed the (i, j) cell borders. This is shown in figure 2.5, where the contribution of the particle to the

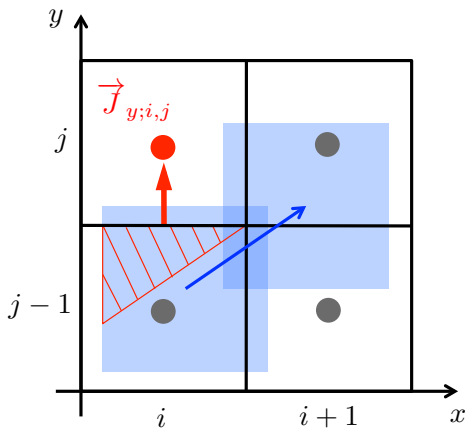


Figure 2.5: Villasenor and Buneman current deposition. Blue squares stand for the particle at iterations n and $n+1$, the blue arrow shows the displacement vector. The dots show the grid points, and the black line stand for their borders. We did not take effects of the staggered grid in consideration for the sake of simplicity. The particle contribution to current on cell (i,j) is $\boldsymbol{j}_p = s_p \sigma \boldsymbol{v}_p$ with s_p and $\boldsymbol{v}_p$ the particle weight and speed respectively, and σ is the area crossed by the particle in one time-step, represented with red hatchings.

bottom border of cell (i,j) is $\boldsymbol{j}_p = s_p \sigma \boldsymbol{v}_p$ with s_p and $\boldsymbol{v}_p$ the particle weight and speed respectively, and σ is the area crossed by the particle in one time-step through the bottom border of cell (i,j), represented with red hatchings.

In figure 2.5, the particle travels through four cell borders. This scheme is extended by the authors to the case when the particle travels through seven and ten borders, and is demonstrated to be charge-conserving.

Finally, this method was extended in reference [Esirkepov, 2001] to any particle shape function. In this reference, the author demonstrates that, assuming the particles travels linearly from $\boldsymbol{r}_p^n$ to $\boldsymbol{r}_p^{n+1}$, there is only one way to deposit current on neighbor grid nodes that allows charge conservation, and give its general form as a function of the particle shape W_p. Esirkepov's method is the one implemented in most modern PIC codes, including EPOCH.

2.1.5 PIC: limits, noise and errors

The full grid in a basic PIC simulation can contain hundreds of million nodes, with as many particles in the simulation box. A simulation in these conditions requires hundreds of Gigabytes memory and takes tens of thousand hours to run. As a consequence, the whole simulation cannot be performed on a single processor. PIC simulations run on several processors, and are consequently part of the high-performance computing (HPC) field. The parallelization is performed as follows: the full grid of the simulation box is divided in sub-domains. A single computer core is assigned to a single sub-domain, and performs the PIC loop on the sub-domain (including solving Maxwell's equations on the sub-domain and pushing particles that are in the sub-domain). At the end of every time-step, each computer core exchanges information with its nearest neighbors to deal with particles flowing from one sub-domain to another, as well as Maxwell's equation on the sub-domain borders. Communications between computer cores are performed via the Message Passing Interface (MPI) protocol. This allows to perform simulations that require much more memory than what is available on a single core, and run much faster.

For PIC simulations to reproduce physical dynamics, numerical instabilities should

be avoided, numerical noise should be kept as small as possible and the relevant dynamics should be resolved. Here are the main relevant numerical conditions that should be satisfied in our PIC simulation:

CFL condition: The Courant-Friedrichs-Lewy condition, or simply Courant condition, relates the time-step and space-step for the explicit finite-difference Yee method with $\Delta t < \Delta x/c$ in 1D and

$$(c\Delta t)^2 \left(\frac{1}{\Delta x^2} + \frac{1}{\Delta y^2} \right) < 1 \tag{2.25}$$

in the 2D case. In practice, we set the space-step Δx, and the time-step Δt is set as:

$$\Delta t = 0.95 \frac{\Delta x}{c} \text{ in 1D} \tag{2.26}$$

$$\Delta t = 0.95 \frac{1}{c} \frac{\Delta x \Delta y}{\sqrt{\Delta x^2 + \Delta y^2}} \text{ in 2D.} \tag{2.27}$$

Highest harmonic resolved: The n^{th} harmonic is resolved in the simulation provided the Shannon condition is verified, giving $\Delta x < \lambda/2n$.

Plasma wavelength: The plasma dynamics require the smallest plasma wavelength to be resolved in the simulations. This reads $\Delta x < \lambda_p^{min}/2$ with $\lambda_p^{min} = 2\pi c/\omega_p^{max}$ the plasma wavelength at the maximum density. This condition is more easily given as a function of the maximum plasma density n^{max} with $\Delta x < \lambda/\sqrt{n^{max}/n_c}$ with n_c the critical density.

Debye length: As stated in [Langdon & Birdsall, 1970] and [Birdsall & Langdon, 2004], a numerical instability can grow because of space discretization if the Debye length is not resolved. This effect leads to numerical heating, which may drastically change the physics involved, and should be kept below 1%. In practical units more adapted to numerical simulations, the Debye length is given by

$$\lambda_{De} = 7 \times 10^{-3} \sqrt{\frac{T_e[\,\mathrm{keV}]}{n_e[n_c]}} \lambda. \tag{2.28}$$

As an illustration, for our physical conditions ($T_e[\mathrm{keV}] = 0.01$ and $n_{e,max}[n_c] = 250$), $\lambda_{De} = \lambda/23000$. Fortunately, this condition can be made more flexible using a higher-order shape function. For the 4^{th}-order spline shown in figure 2.3c), $\Delta x \sim 10\lambda_{De}$ is a satisfying condition for a limited numerical heating (for a given simulation time). Besides, the Debye length can be increased using a higher plasma temperature in the simulations. Doing so, one must verify that the plasma dynamics is not substantially changed.

In our simulations, the last condition is by far the most stringent. More details are given in the following sections 2.1.6 and 2.1.7.

2.1.6 Study on numerical parameters

We performed a scan of 2D PIC simulations using the code EPOCH to show the role of the space step and the plasma electron temperature. It was done as follows:

	a_0	τ	w_0	n_{bulk}	L	T_e	T_i
v2	3	25 fs	3.6 μm	$100n_c$	$\lambda/16 - \lambda$	0 eV	0 eV
v3	3	25 fs	3.6 μm	$100n_c$	$\lambda/16 - \lambda$	100 eV	10 eV
v4	3	25 fs	3.6 μm	$100n_c$	$\lambda/16 - \lambda$	100 eV	10 eV
	ppc	box size	Δx	particle shape	n_{min}	width	cells
v2	10	$35\lambda \times 70\lambda$	$\lambda/200$	b-spine 3	$n_c/5$	4λ	7000×14000
v3	10	$35\lambda \times 70\lambda$	$\lambda/200$	b-spine 3	$n_c/5$	4λ	7000×14000
v4	10	$35\lambda \times 70\lambda$	$\lambda/300$	b-spine 3	$n_c/5$	4λ	11000×21000

Table 2.1: Scan conditions. the number of particles per cell is given in the *ppc* column, and column "width" shows the width of the plasma bulk. The plasma is initialized where $n > n^{min}$, and the plasma density is artificially dropped to zero for $n < n^{min}$.

For a given set of numerical parameters, we studied the influence of the gradient length on electron ejection and harmonic generation. This study was repeated changing the numerical conditions, to determine the influence of numerical parameters on (i) the harmonic generation efficiency and (ii) the ejected electric charge. Besides, we also checked if the numerical parameters influenced the dependence of these two physical variables on the density gradient length.

Three sets (`versions`) of simulations were performed, which conditions are listed in table 2.1. Three simulations were performed for each version, named `injectorv2_L1s16`, `injectorv2_L1s8`, `injectorv2_L1s1` for `v2`, with gradient scale length respectively $\lambda/16$, $\lambda/8$ and λ. The same set was performed for `v3` and `v4`. The angle of incidence is $\theta = 45°$ in all simulations. Basically, the difference between `injectorv2` and `injectorv3` is the plasma temperature, and the difference between `injectorv3` and `injectorv4` is the space step Δx.

The bottom of the simulation box ($x \gtrsim 31\lambda$) is filled with an overdense plasma with density $n_{bulk} = 100n_c$, and the area before is filled with the exponential density gradient. The simulation box is adjusted so that the critical density $n = n_c$ is always located at $x = 25\lambda$. A longer gradient length results in a longer box. In order to avoid filling the whole box with an extremely underdense plasma, we artificially drop the plasma density to zero where the density is below a threshold $n < n^{min} = 0.2n_c$.

For $T_e = 100\,\text{eV}$, the Debye length reads $\lambda_{De} = \lambda/4500$, and the two space-steps we used read, in units of Debye lengths, $\Delta x = 23\lambda_{De}$ and $\Delta x = 15\lambda_{De}$. The simulations were run on the *Curie* supercomputer, hosted in the CCRT (Centre de Calcul Recherche et Technologie) center, at CEA Bruyères-le-Châtel. The computational cost is depicted on table 2.2. It depends on the space step Δx as well as the density gradient L: a longer density gradient results in a larger area verifying $n > n_{min}$, hence a higher number of macroparticles at initialization.

The result of the scan is presented in figure 2.6. The harmonics in the reflected field are due to the relativistic oscillating mirror mechanism. Figure 2.6 a) brings the following comments: first, the harmonic spectra significantly depend on the electron temperature and space step in this range. Increasing the temperature reduces the harmonic efficiency. A smaller Δx highly increases the harmonic signal. Besides, a large bump in the three spectra is observed around $\omega = 20\omega_0$. These results are illustrated in figure 2.6 b), which shows the efficiency of the fifth harmonic.

Figure 2.6 c) shows that the fifteenth harmonic efficiency weakly depends on the gradient length, because the noise level at this frequency is high. Finally, the harmonic

simulation	L	N_{cells}	$N_{particles}$	walltime	cost
`injectorv2_L1s8`	$\lambda/8$	10^8	1.3×10^8	1h20	1400h
`injectorv2_L1s1`	λ	1.1×10^8	2.7×10^8	4h15	4000h
`injectorv3_L1s8`	$\lambda/8$	10^8	1.3×10^8	1h20	1400h
`injectorv3_L1s1`	λ	1.1×10^8	2.7×10^8	4h15	4000h
`injectorv4_L1s8`	$\lambda/8$	2.3×10^8	2.9×10^8	6h	6100h
`injectorv4_L1s1`	λ	2.6×10^8	6×10^8	17h40	18000h

Table 2.2: Computational cost of numerical simulations. Simulations were performed on 1024 processing units on the Curie machine at CCRT. The ions are immobile. Walltime stands for the actual time that the run took: a 10-hours-walltime run performed on 8 processing units costs 80 hours.

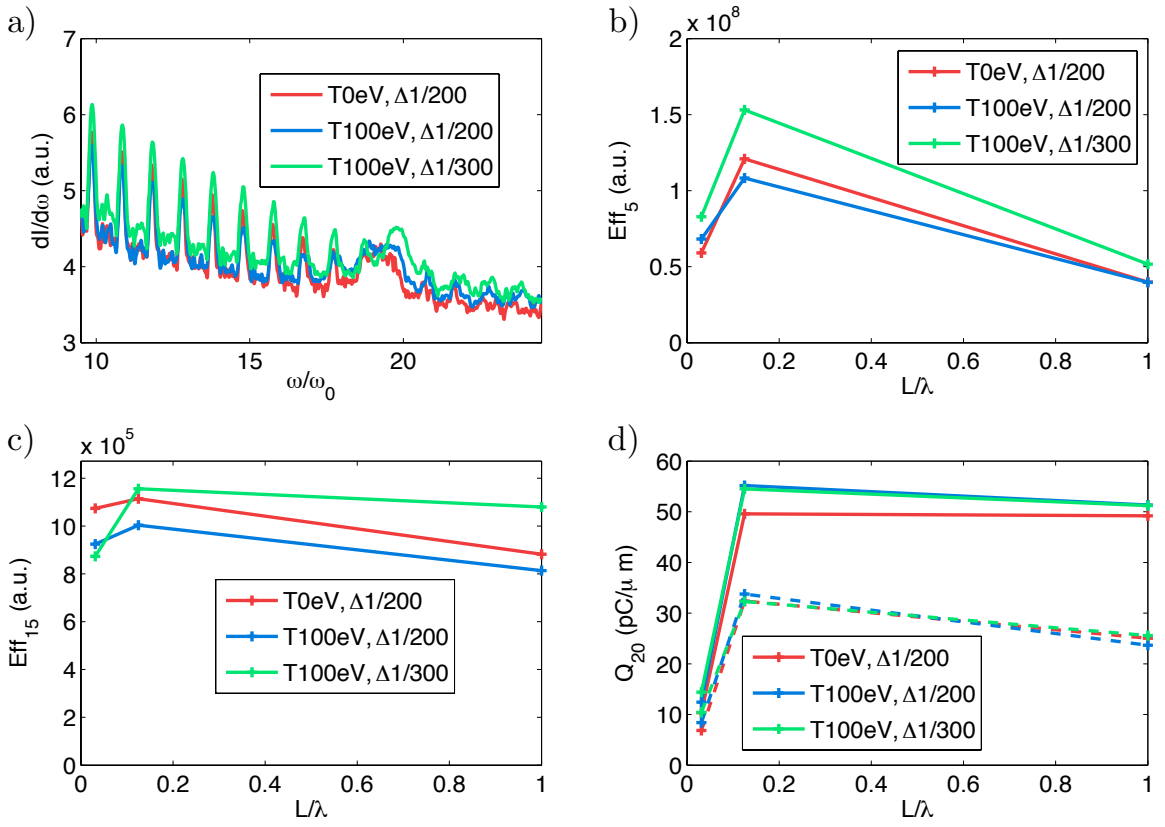


Figure 2.6: Scan result. Red: `injectorv2`, blue: `injectorv3`, green: `injectorv4`. a) Harmonic spectra in the reflected field for $L = \lambda/8$. The squared norm of the magnetic field Fourier transform $|\mathcal{F}(B)|^2$ is plotted along ω/ω_0 where ω_0 is the laser angular frequency. b) Fifth harmonic efficiency. It is the integral of the harmonic spectrum between $\omega = 4.5\omega_0$ and $\omega = 5.5\omega_0$. c) Fifteenth harmonic efficiency. d) Absolute value of the total electric charge (solid line) and the charge of electron verifying an angular condition (dashed line). Electrons were considered ejected when they crossed a line parallel to the plasma surface, 20λ away from the reflection point, or when they crossed a line perpendicular to the plasma surface, 20λ away from the reflection point, to record electrons ejected along the target surface.

λ	a_0	w_0	τ_L	n_{bulk}	L
800 nm	3	3.6λ	25 fs	$100n_c$	$\lambda/4$
θ	T_e	T_i	Δx	ppc	
45°	100 eV	10 eV	$\lambda/300$	10	

Table 2.3: Physical and numerical parameters for the 2D PIC simulation `injectorv4_L1s4`

signal strongly depends on Δx in the range we study. Yet the three scans show the same trends for harmonic generation as a function of the density gradient scale length L. On the opposite, the ejected charge shown in figure 2.6 d) is extremely stable. In particular, the total ejected charge follows exactly the same line for $\Delta x = \lambda/200$ and $\Delta x = \lambda/300$.

This study shows that harmonic generation is much more sensitive to the electron initial temperature and space step than the electron ejection signal. The trends for harmonic generation are similar for the three scans, but the efficiency shows significant variations. On the opposite, the electron signal is mostly independent on the plasma temperature and the space step in the range we studied. We conclude that $\Delta x = \lambda/300$ is a satisfying space step to study electron ejection in 2D PIC simulations with $T_e = 100\,\text{eV}$.

2.1.7 Typical 2D PIC simulation

A typical numerical simulation (`injectorv4_L1s4`) is shown in figure 2.7. The obliquely-incident laser pulse enters the simuation domain via the x^- border and reflects off the plasma target located close to the x^+ border. We are interested in electrons ejected in the $-x$ direction, as well as high harmonic generation in the reflected field. This scheme will be used in most numerical simulations in this thesis.

Electron ejection: Electrons are considered to be ejected if they travel *far enough* from the plasma border in the $-x$ direction. Ideally, they should be detected at a distance much greater than the Rayleigh length, after which the laser fields have strongly decreased.

Harmonics generation: Harmonics generated in the reflected field are detected using a field streak, a line onto which the electric and magnetic fields are recorded as a function of time, represented as a grey dashed line in figure 2.7. Harmonics are very sensitive to numerical noise and should ideally be performed with $\Delta x \sim \lambda_{De}$, and > 100 particles per cell (ppc), but do not require a large box.

Satisfying numerical conditions for both electron ejection and harmonics generation proves extremely computer intensive. Simulation `injectorv4_L1s4` was processed with mitigated conditions (box size $\sim z_R$, $\Delta x = 15\lambda_{De}$ and 10ppc). A comparison with `injectorv3_L1s4`, where all the conditions are identical except the space-step $\Delta x = \lambda/200$ gave identical results for the ejected charge and different results for high harmonic generation. The trends are the same in all cases. Numerical and physical parameters shown on table 2.3.

This set of parameters give $\lambda_{De} = \lambda/900$, so the simulation space-step verifies $\Delta x \simeq 3\lambda_{De}$, $\Delta x = \lambda_p^{min}/30$ and the highest harmonic resolved is the 150^{th}. These

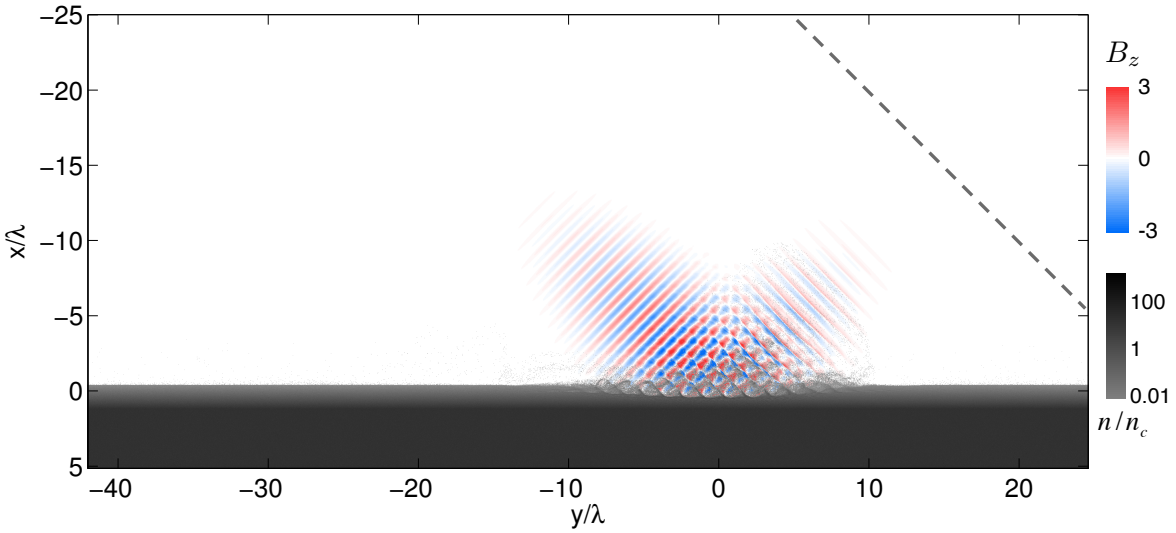


Figure 2.7: Snapshot of the magnetic field (blue-red colourmap) and electron density (greyscale) in a 2D PIC simulation with numerical and physical conditions given in table 2.3. The electric and magnetic fields are recorded along the streak line, represented as a grey dashed line.

simulation parameters will be used in order to obtain physical results in chapter 3 to study the influence of the gradient length on the electron ejection process.

2.2 Electron in a laser pulse in vacuum

The previous section was dedicated to numerical simulation of plasma dynamics. In the next chapters, we will see that, upon the reflection of a laser pulse on a plasma mirror, the dynamics of electrons ejected from the plasma can be strongly affected by the laser fields far away from the plasma. This chapter focuses on the dynamics of an electron in an electromagnetic wave in different conditions. First, the equations of motion for an electron in a monochromatic plane wave with relativistic intensity are derived. Then, we give the expressions for the magnetic and electric field in a tightly-focused Gaussian pulse, beyond the paraxial approximation. Finally, we present the relativistic ponderomotive force that acts on an electron propagating in an electromagnetic wave with time- or space-dependent envelope.

2.2.1 Electron in a monochromatic plane wave

We consider the motion of an electron in a linearly polarized monochromatic plane wave, and derive the conservation of canonical momentum as well as the electron orbits in the relativistic regime $a_0 \sim 1$.

Canonical momentum conservation

An electromagnetic wave propagates along z and is polarized along x, $\boldsymbol{k} = 2\pi/\lambda \boldsymbol{e_z}$. The electric and magnetic fields, and the vector potential read

$$\boldsymbol{E} = E_0 \sin(\omega_0 t - kz)\boldsymbol{e_x} \tag{2.29}$$
$$\boldsymbol{B} = B_0 \sin(\omega_0 t - kz)\boldsymbol{e_y} \tag{2.30}$$
$$\boldsymbol{A} = A_0 \cos(\omega_0 t - kz)\boldsymbol{e_x} \tag{2.31}$$

with $B_0 = E_0/c$ and $A_0 = E_0/\omega_0$, where we use the Coulomb gauge $\nabla \cdot \boldsymbol{A} = 0$.

The system is invariant along the x and y directions. As a consequence of Noether's theorem, the transverse components of the canonical momentum for an electron in a plane wave are conserved along its trajectory, reading

$$P_x = p_x - eA_x = P_{x0} \tag{2.32}$$
$$P_y = P_{y0}. \tag{2.33}$$

The electron hamiltonian reads

$$\mathcal{H} = \sqrt{1 + \left(\frac{p}{m_e c}\right)^2} \tag{2.34}$$
$$= \sqrt{1 + \frac{[P_{x0} + eA_0 \cos(\omega_0 t - kz)]^2 + P_{y0}^2 + p_z^2}{m_e^2 c^2}}. \tag{2.35}$$

As an illustration, we can also derive the canonical momentum conservation in a straightforward way. The equation of motion for an electron in electromagnetic fields reads

$$\frac{d\boldsymbol{p}}{dt} = -e\boldsymbol{E} - e\boldsymbol{v}\times\boldsymbol{B} \tag{2.36}$$
$$= -e\left(-\nabla\phi - \frac{\partial \boldsymbol{A}}{\partial t}\right) + q\boldsymbol{v}\times(\nabla\times\boldsymbol{A}) \tag{2.37}$$
$$= -e\left(-\nabla\phi - \frac{\partial \boldsymbol{A}}{\partial t}\right) + q\left[\nabla(\boldsymbol{v}.\boldsymbol{A}) - (\boldsymbol{v}.\nabla)\boldsymbol{A}\right]. \tag{2.38}$$

Rearranging these terms, the time derivative of the canonical momentum can be calculated as

$$\frac{d(\boldsymbol{p}-e\boldsymbol{A})}{dt} = \frac{d\boldsymbol{p}}{dt} - e\frac{\partial \boldsymbol{A}}{\partial t} - e(\boldsymbol{v}.\nabla)\boldsymbol{A} \tag{2.39}$$
$$= e\nabla\phi - e\nabla(\boldsymbol{v}.\boldsymbol{A}) \tag{2.40}$$
$$= -e\nabla(-\phi + \boldsymbol{v}.\boldsymbol{A}). \tag{2.41}$$

Finally, assuming that A and ϕ only depend on z, the x and y coordinates of this equation read

$$\frac{d(p_x - eA_x)}{dt} = -e\frac{\partial}{\partial x}(-\phi + \boldsymbol{v}.\boldsymbol{A}) = 0 \tag{2.42}$$
$$\frac{d(p_y - eA_y)}{dt} = -e\frac{\partial}{\partial y}(-\phi + \boldsymbol{v}.\boldsymbol{A}) = 0 \tag{2.43}$$

so the quantities $p_x - eA_x$ and $p_y - eA_y$ are conserved along the electron motion.

Relativistic orbits in a plane wave $a_0 \gtrsim 1$

Here, we follow the presentation found in [Hartemann *et al.*, 1995] and derive the relativistic orbits for an electron propagating in a monochromatic plane wave in vacuum. The full set of equations reads

$$\frac{d\boldsymbol{p}}{dt} = -e\boldsymbol{E} - e\boldsymbol{v}\times\boldsymbol{B} \tag{2.44}$$
$$\frac{d\gamma}{dt} = -\frac{e}{m_e c^2}\boldsymbol{v}\cdot\boldsymbol{E} \tag{2.45}$$
$$\boldsymbol{E} = E_0 \sin\phi \boldsymbol{e_x} \tag{2.46}$$
$$\boldsymbol{B} = E_0/c \sin\phi \boldsymbol{e_y} \tag{2.47}$$
$$\text{with } \phi = \omega_0 t - kz(t) \tag{2.48}$$

where z is the electron position at time t. We use the standard notations $\boldsymbol{\beta} = \boldsymbol{v}/c; \gamma = (1-\beta^2)^{-1/2}; \boldsymbol{p} = \gamma m_e c\boldsymbol{\beta}$. The initial conditions read $\boldsymbol{\beta}(t=0) = \beta_{z0}\boldsymbol{e_z}$ and $\gamma_0 = (1-\beta_{z0}^2)^{-1/2}$ and $z = 0$ at $t = 0$. The scalar equations of motion read

$$d_t(\gamma\beta_x) = \frac{-eE_0}{m_e c}(1-\beta_z)\sin\phi \tag{2.49}$$
$$d_t(\gamma\beta_y) = 0 \tag{2.50}$$
$$d_t(\gamma\beta_z) = \frac{-eE_0}{m_e c}\beta_x \sin\phi \tag{2.51}$$
$$d_t\gamma = \frac{-eE_0}{m_e c}\beta_x \sin\phi, \tag{2.52}$$

so $\beta_y = 0$ since we assumed $\beta_y(t = 0) = 0$, and equations 2.49 and 2.52 give one constant of motion:

$$\gamma(1 - \beta_z) = \gamma_0(1 - \beta_{z0}). \tag{2.53}$$

We start from the definition of γ to get one useful equation:

$$\frac{1}{\gamma^2} = 1 - \beta_x^2 - \beta_z^2 \tag{2.54}$$

$$= 1 - \beta_x^2 - \left[1 - \frac{\gamma_0}{\gamma}(1 - \beta_{z0})\right]^2 \tag{2.55}$$

$$\text{reordering: } \gamma = \frac{1}{2\gamma_0(1 - \beta_{z0})}\left[1 + \gamma_0^2(1 - \beta_{z0})^2 + \gamma^2\beta_x^2\right] \tag{2.56}$$

$$\gamma = \gamma_0\left[1 + \gamma^2\beta_x^2\frac{1 + \beta_{z0}}{2}\right] \tag{2.57}$$

where we used

$$\gamma_0(1 - \beta_{z0}) = \frac{1}{\gamma_0(1 + \beta_{z0})}. \tag{2.58}$$

This formula comes directly from the definition of the Lorentz factor. Now, let us use ϕ as the new parameter, and use $d_t\phi = \omega_0(1 - \beta_z)$ from the definition. Equation 2.49 can be integrated with respect to ϕ, and reads, allowing a non-zero initial phase ϕ_0

$$\gamma\beta_x = a_0(\cos\phi - \cos\phi_0), \tag{2.59}$$

so we can calculate γ from equation 2.57, then β_x from equation 2.59 and β_z from equation 2.53:

$$\gamma(\phi) = \gamma_0\left[1 + a_0^2(\cos\phi - \cos\phi_0)^2\frac{1 + \beta_{z0}}{2}\right] \tag{2.60}$$

$$\beta_x(\phi) = \frac{1}{\gamma_0}\frac{2a_0(\cos\phi - \cos\phi_0)}{2 + a_0^2(1 + \beta_{z0})(\cos\phi - \cos\phi_0)^2} \tag{2.61}$$

$$\beta_z(\phi) = 1 - \frac{2(1 - \beta_{z0})}{2 + a_0^2(1 + \beta_{z0})(\cos\phi - \cos\phi_0)^2} \tag{2.62}$$

Finally, we note that $dx/d\phi = (dx/dt)(dt/d\phi)$, and straightforward integrations give the electron position as a function of ϕ,

$$kx(\phi) = \frac{a_0}{\gamma_0(1 - \beta_{z0})}\left[\sin\phi - \sin\phi_0 - \cos\phi_0(\phi - \phi_0)\right] \tag{2.63}$$

$$\begin{aligned} kz(\phi) = \frac{1}{2(1 - \beta_{z0})}\Bigg\{ & \left[2\beta_{z0} + a_0^2(1 + \beta_{z0})(\cos^2\phi_0 + \frac{1}{2})\right](\phi - \phi_0) \\ & - 2a_0^2(1 + \beta_{z0})\cos\phi_0(\sin\phi - \sin\phi_0) \\ & + \frac{a_0^2}{4}(1 + \beta_{z0})(\sin 2\phi - \sin 2\phi_0)\Bigg\}. \end{aligned} \tag{2.64}$$

Electron trajectories are shown in figure 2.8 for different values of a_0 with $\phi_0 = \pi/2$ and $\beta_{z0} = 0$, for $\phi \in [\phi_0, \phi_0 + 2\pi]$. Note that $\phi_0 = \pi/2$ corresponds to $E_x(\phi_0) = E_0$: the field is maximum. In the non-relativistic case ($a_0 = 0.01$), the electron motion is mostly

along x, namely in the polarization direction, while it is mostly in the propagation direction (along z) in the ultrarelativistic case. Note that the $x-z$ trajectories look like homothetic transformations of each other. This is not valid for $\beta_{z0} \neq 0$.

Let us consider the $a_0 = 100$ case. The electron travels a distance far longer than the wavelength during a 2π phase shift (a single laser period). Besides, $\beta_z \ll 1$ in the non-relativistic regime ($a_0 = 0.01$) whereas $\beta_z \simeq 1$ in the relativistic case ($a_0 = 100$). The electron travels around the speed of light along z because of the $\boldsymbol{v} \times \boldsymbol{B}$ force, which is the only force with a z component.

The transverse excursion of the electron in the x direction reaches tens of λ in the relativistic case. In a more realistic case, the electron travels in a finite-width pulse and may exit the pulse in these conditions.

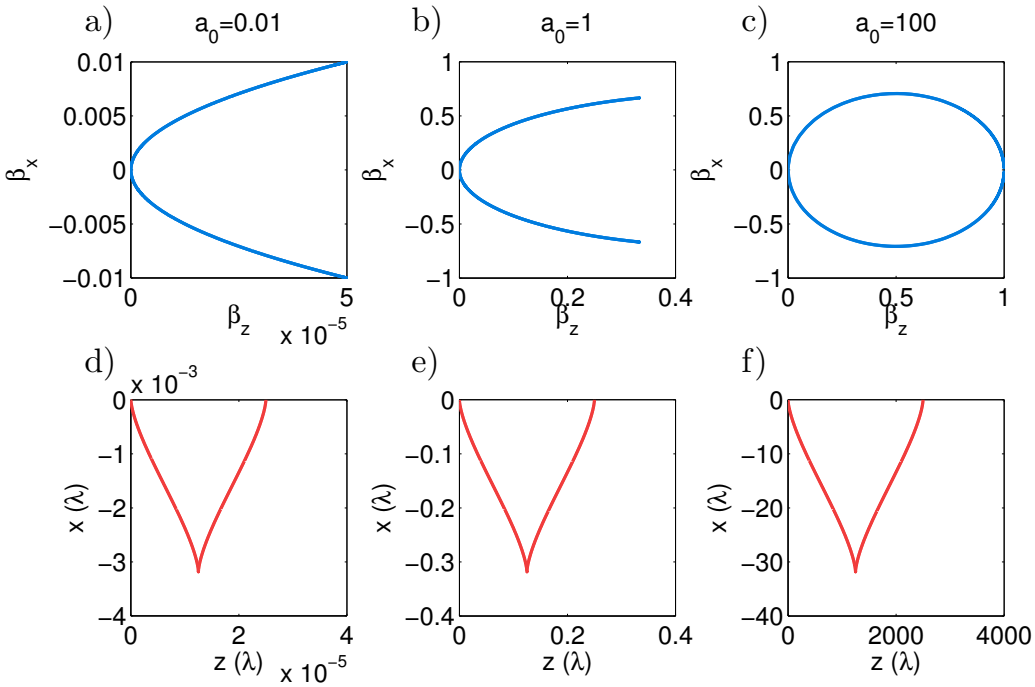


Figure 2.8: a) Trajectory of an electron in the $\beta_x - \beta_y$ phase space from equations 2.61 and 2.62. The conditions are $a_0 = 0.01$, $\phi_0 = \pi/2$ and $\beta_{z0} = 0$. d) shows the $x - z$ phase space for the same electron. b) & e) and c) & f) show the same plots as a) & d) for $a_0 = 1$ and $a_0 = 100$ respectively.

Finally, these equations give the maximum γ factor for an electron oscillating in a plane wave as

$$\gamma_{max} = \gamma_0 \left[1 + 2(1 + \beta_{z0})a_0^2\right]. \tag{2.65}$$

This is the maximum value an electron can gain when propagating into an electromagnetic wave.

In equation 2.63, one can see that if $\cos\phi_0 \neq 0$, the electron position averaged upon one period drifts as

$$< x >_{\phi\in[0,2\pi]} = \frac{-a_0 \cos\phi_0}{\gamma_0(1-\beta_{z0})}\phi. \tag{2.66}$$

Choosing $\phi_0 = \pi/2$, the electron oscillates around position $x = 0$, with maximum

quiver velocity and amplitude in the polarization direction

$$\beta_{quiv} = \sqrt{\frac{1-\beta_{z0}}{2}}\gamma_0 \tag{2.67}$$

$$kx_{quiv} = a_0\gamma_0(1+\beta_{z0}). \tag{2.68}$$

2.2.2 Gaussian pulse and paraxial approximation

To study the electron dynamics in a realistic laser pulse, the plane wave approximation is no longer satisfactory and one should describe the more realistic fields in a laser beam. The pulse properties are established in the laser cavity, see reference [Siegman, 1986]. Putting aside considerations about the pulse finite duration, the study usually relies on two approximations: (i) the scalar approximation states that the electric and magnetic fields can be described by a single scalar quantity U; for example, in the plane wave described above, $\boldsymbol{E} = U\boldsymbol{e_x}$ and $\boldsymbol{B} = U/c\boldsymbol{e_y}$. (ii) the paraxial approximation when the laser cavity is much longer than any transverse dimension. Assuming the long direction is z and $U = \psi(x,y,z)e^{ikz}$, this approximation reads $|\partial^2\psi/\partial z^2| \ll k|\partial\psi/\partial z|$. Equivalently, the angle between the $\boldsymbol{k}$ vector and the z axis is small in the cavity.

The spatial profile of the laser beam can be decomposed in cylindrical modes. The lowest-order, and consequently the most stable and more common one, is the Gaussian mode, which reads

$$U(x,y,z) = \frac{e^{ikz}}{1+iz/z_R}\exp\left[-\frac{r^2/w_0^2}{1+iz/z_R}\right] \tag{2.69}$$

$$= \frac{w_0}{w(z)}\exp\left[-\frac{r^2}{w^2(z)}\right]\exp\left[ikz + ik\frac{r^2}{2R(z)} - i\,\mathrm{atan}\left(\frac{z}{z_R}\right)\right] \tag{2.70}$$

with the radial coordinate $r^2 = x^2 + z^2$, the Rayleigh length $z_R = kw_0^2/2$, the beam width $w(z) = w_0\sqrt{1+z^2/z_R^2}$ and the radius of curvature $R(z) = z + z_R^2/z$. w_0 is the beam waist, *i.e.* the beam size at focus $z = 0$. Figure 2.9 shows the intensity profile of a Gaussian mode.

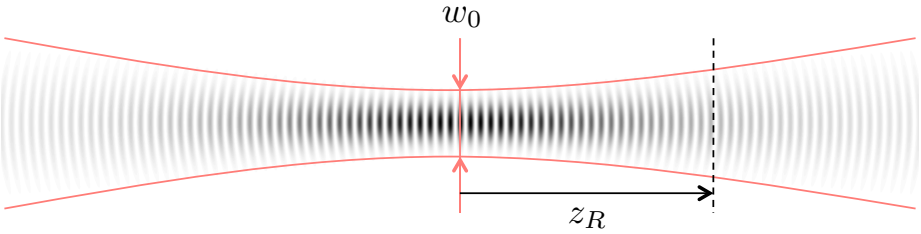


Figure 2.9: squared amplitude of the electric field for a monochromatic Gaussian mode with beam waist $kw_0 = 10$.

The maximum angle α of the $\boldsymbol{k}$ vector in the beam reached for $r = w(z)$, and is given by

$$\tan\alpha = \frac{w(z)}{R(z)} \to \frac{2}{kw_0} \text{ when } z \to \infty. \tag{2.71}$$

The paraxial approximation holds as long as $\alpha \ll \pi$, *i.e.* $kw_0 \gg 1$.

2.2.3 Non-paraxial corrections in the tightly-focused regime

One can easily show that the previous equation verifies Maxwell's equations only in the paraxial limit, for instance the Maxwell-Gauss equation in vacuum is not verified $\partial U/\partial x \neq 0$ (with $U = E_x$). When the laser beam is tightly focused $w_0 \gtrsim \lambda$, this error becomes manifest, and corrections to the paraxial expressions must be added.

An approach developed in references [Cicchitelli *et al.*, 1990] and [Quesnel & Mora, 1998] consists in expanding Maxwell's equations near the paraxial solution given in 2.70 as a power series of the small parameter $\epsilon = 1/kw_0$. Refer to Brice Quesnel's PhD thesis [Quesnel, 1998] or references mentioned above for a full proof as well as a more detailed analysis. Calculation of higher orders in ϵ are performed using the angular spectrum method from references [Agrawal & Pattanayak, 1979; Carter, 1970]:

1. Start from $U(x, y, 0)$, the scalar field in the plane $z = 0$, and its Fourier-transform in the $x - y$ plane $\tilde{U}_0(p, q)$. They are linked via
$$U(x, y, 0) = \int\int \tilde{U}_0(p, q) e^{i(px+qy)} dpdq;$$
2. Propagate the Helmholtz equation along z in the $p - q$ Fourier space;
3. $U(x, y, z)$ is given by
$$U(x, y, z) = \int\int \tilde{U}_0(p, q) e^{i(px+qy+mz)} dpdq$$
with $m = \sqrt{1 - p^2 - q^2}$ if $p^2 + q^2 \leq 1$ or $m = i\sqrt{p^2 + q^2 - 1}$ if $p^2 + q^2 > 1$.

This method was applied to a Gaussian laser pulse to calculate the corrected expressions as a power series in ϵ. For our purpose, we restrict ourselves to the first-order terms ϵ^1, since they are sufficient to describe the ponderomotive force (see below). The 0^{th}-order E_x and B_y fields are unchanged while 1^{st}-order longitudinal components E_z and B_z are added. One can verify that these expressions satisfy Maxwell's equations to first order.

$$E_x = E_0 \frac{w_0}{w(z)} \exp\left[-\frac{r^2}{w^2(z)}\right] \sin\phi_0 \tag{2.72}$$
$$E_y = 0 \tag{2.73}$$
$$E_z = 2E_0\epsilon \frac{w_0 x}{w^2(z)} \exp\left[-\frac{r^2}{w^2(z)}\right] \cos\phi_1 \tag{2.74}$$
$$B_x = 0 \tag{2.75}$$
$$B_y = E_x/c \tag{2.76}$$
$$B_z = 2\frac{E_0}{c}\epsilon \frac{w_0 x}{w^2(z)} \exp\left[-\frac{r^2}{w^2(z)}\right] \cos\phi_1 \tag{2.77}$$

with

$$\phi_0 = \omega_0 t - kz - k\frac{r^2}{2R(z)} + \operatorname{atan}\left(\frac{z}{z_R}\right) \tag{2.78}$$
$$\phi_1 = \omega_0 t - kz - k\frac{r^2}{2R(z)} + 2\operatorname{atan}\left(\frac{z}{z_R}\right). \tag{2.79}$$

Test-particle code: As explained below, these corrections are essential, at least to the first order, to properly describe the dynamics of an electron in a Gaussian pulse and have been implemented in the `test-particle code`. This code, parallelized with `OpenMP`, solves the equations of motion for electrons in the analytical fields described above, using the Boris particle pusher presented in 2.1.4. The original `C++` code was written by Olle Lundh. The role of the main parameters of this interaction, the laser parameters (w_0, duration τ_L, peak amplitude a_0) and the initial conditions for electrons (momentum, position and phase in the pulse), will be studied in chapter 4.

2.2.4 Ponderomotive force

An electron oscillating in an electromagnetic wave undergoes an average force depending on the wave envelope only, and directed towards the low-intensity regions: the ponderomotive force. While the non-relativistic expression is well-known, its generalization to the relativistic case was performed in reference [Quesnel & Mora, 1998]. Besides, the authors prove that corrections in ϵ to an order ≥ 1 are necessary to describe properly ponderomotive effects.

This description relies on a timescale separation, where every quantity q is written as $q = \overline{q} + \widetilde{q}$ with $\overline{q}$ varying slowly and $\widetilde{q}$ varying rapidly. An analogy can be made with a boat moored in a harbour in an ocean. If q is the height of the center of mass of the boat, then $\overline{q}$ shows slow oscillations (one or two per day) because of the tide while $\widetilde{q}$ shows fast oscillations due to the waves, and the final height is the sum of these two contributions. Similarly, a particle with charge q in an electromagnetic wave undergoes slow oscillations due to pulse envelope changes on the particle position and fast oscillations due to the $\sin(\omega_0 t - kz)$ term.

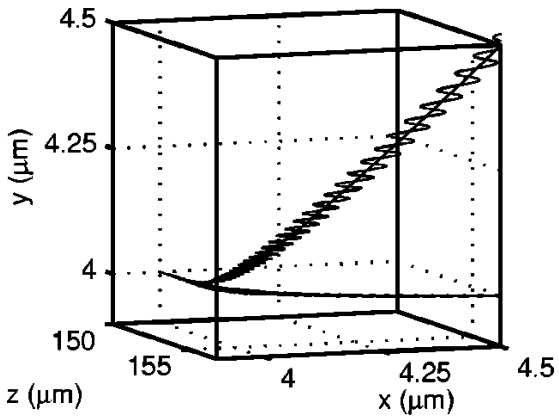


Figure 2.10: [This image was taken from [Quesnel & Mora, 1998]]$a_0 = 0.3$, $\tau = 200\,\mathrm{fs}$, $w_0 = 10\,\mu\mathrm{m}$, $p_{z0} = 0.1 m_e c$, $z_0 = 150\,\mu\mathrm{m}$. Upper lines show the electron trajectory using the first-order development and the theoretical expression for the ponderomotive force respectively. The line in the lower part shows the electron trajectory in the zeroth-order fields. It is confined in the polarization plane.

The ponderomotive force takes place on the slow timescale, which means it affects $\overline{\boldsymbol{p}}$ and not $\widetilde{\boldsymbol{p}}$, and reads

$$\frac{d\overline{\boldsymbol{p}}}{dt} = -\frac{1}{2m_e\overline{\gamma}}\nabla\overline{|q\widetilde{\boldsymbol{A}}_\perp|^2} \tag{2.80}$$

$$\text{with } \overline{\gamma}^2 = 1 + \frac{1}{m_e^2c^2}\left[|\overline{\boldsymbol{p}}_\perp|^2 + \overline{p}_z^2 + \overline{|q\widetilde{\boldsymbol{A}}_\perp|^2}\right]. \tag{2.81}$$

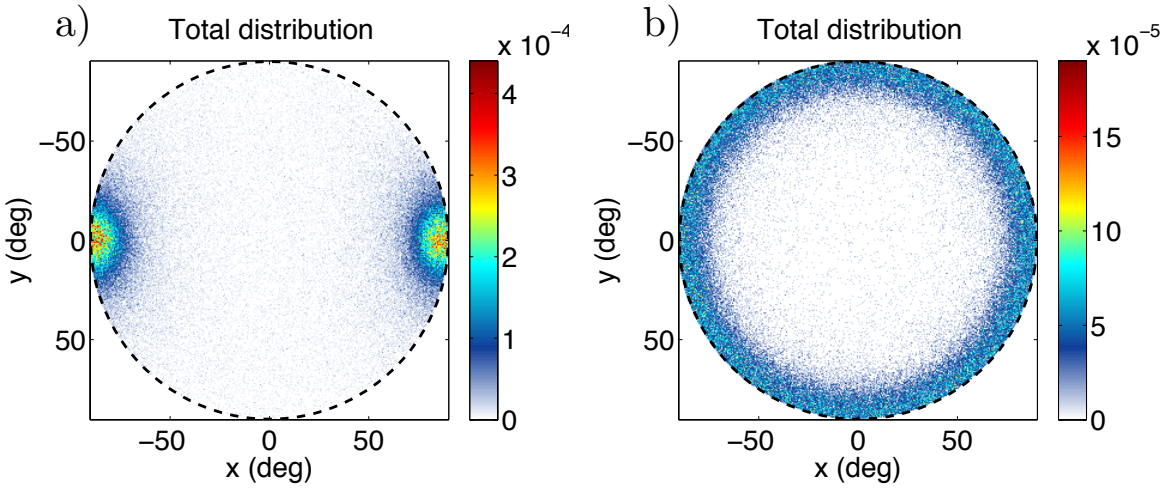


Figure 2.11: Final distribution for electrons interacting with a Gaussian pulse, without first-order correction (a) and with first-order correction (b). The laser pulse propagates in the z direction, is polarized along the x direction, $a_0 = 0.5$, $w_0 = 15\,\mu$m, $\tau = 100\,$fs, $\lambda = 800\,$nm. It is focused at $z = 0$ and $t = 0$, and starts at $t \ll \tau$. 10^5 electrons are initialized with a Gaussian distribution in space with standard deviation $\sigma = w_0/2$ centered around the origin, and a uniform Maxwellian temperature $T_e = 300\,$eV. The dashed black line shows $\theta = 90°$.

This force does not depend on the laser polarization and acts on particles provided they oscillate in many laser periods. It is the main reason for which additional terms in ϵ^1 are added in the `test-particle code`. As an example, the trajectory of an electron in a long laser pulse is shown in figure 2.10. It is calculated with the fields with first-order corrections. It shows fast oscillations in the x direction and a slow drift in the y direction. The second line in the upper part shows the dynamics of the same electron driven by the ponderomotive force only. It reproduces perfectly the electron motion on the slow time scale. For comparison, the electron dynamics in 0^{th} order fields is also shown in this figure. The electron remains in the same $z - x$ plane.

The importance of these fields is shown in figure 2.11, where the final distribution of electrons interacting with a Gaussian laser pulse was calculated using a solver without (a) and with (b) first-order corrections. The pulse envelope is axisymmetric, and so must the final electron distribution be. One can see that this is absolutely not verified when first-order corrections are not taken into account.

2.2.5 Finite-duration correction

In the development above, the pulse finite duration was not mentioned for the sake of simplicity. When adding a time envelope to the laser pulse, the paraxial electric field is modified as

$$E_x = E_0\frac{w_0}{w(z)}\exp\left[-\frac{r^2}{w^2(z)}\right]\sin\phi_0 f(t - z/c) \tag{2.82}$$

where f accounts for the finite pulse duration and reads, for a Gaussian temporal profile, $f_g(\tau) = \exp(-\tau^2/\tau_L^2)$ where τ_L is the pulse duration. This expression relies on the slowly-varying envelope approximation (similar to the WKB approximation in mathematics), which states that the envelope does not change significantly during one laser period. For the Gaussian example f_g, it is valid when $\tau_L \gg T_L$ where T_L is the laser period.

When this condition is not verified, the expression given above does not verify Maxwell's equations and should be corrected, just like the paraxial approximation. The same method can be applied, based on the development in power series of the small parameter $\nu = 1/\omega_0\tau_L$. Yet, in our conditions, $\tau_L/t_L \sim 10$, and the corrections are extremely small. Besides, temporal corrections were shown to have much less effect than spatial corrections in reference [Varin *et al.*, 2005]. As a consequence, they were not included in the `test-particle code`.

Chapter 3

Backward electron acceleration from plasma mirrors

Contents

3.1 Theoretical studies on electron ejection 76
3.1.1 Electron ejection in PIC simulations 76
3.1.2 Density gradient scale length 77
3.1.3 Electron ejection angle 78
3.1.4 Gyromagnetic effect 79
3.1.5 Electron ejection in 1D PIC simulations 82
3.2 Electron ejection with a step-like density profile 84
3.2.1 Phenomenology of electron ejection 84
3.2.2 Push-pull mechanism 86
3.2.3 Relativistic Electronic Spring by Gonoskov 89
3.2.4 Model for electron ejection with a step-like profile 93
3.2.5 Discussion 96
3.3 Electron ejection with an exponential density gradient . . 97
3.3.1 Surface dynamics 98
3.3.2 Scan $a_0 - L$ with 1D PIC simulations 102
3.3.3 Toy model for the electron ejection 105
3.3.4 Comparison with 2D PIC simulations 109

Introduction

The reflection of an ultrashort ultraintense laser pulse upon an overdense plasma leads to the acceleration of electrons. The main parameters of this interaction are the laser pulse intensity I, its duration τ_L, the polarization angle, the incidence angle θ and the shape of the plasma profile. A wide range of experimental conditions has been explored (see synthetic review in chapter 1 page 32), and in most cases the backward electron ejection mechanisms remain unknown.

In this chapter, we focus on the plasma mirror regime, where the p-polarized laser has a relativistic intensity $I\lambda^2 > 10^{18}\,\mathrm{W}\cdot\mathrm{cm}^{-2}\,\mu\mathrm{m}^2$, $\tau_L \sim 25\,\mathrm{fs}$, and impinges under oblique incidence (with $\theta \simeq 45°$) on an overdense plasma with a sharp density gradient on its front side. This set of parameters is typical of current laser facilities, and an application is shown in chapter 4.

Using 1D and 2D PIC simulations (see chapter 2), we describe and model the backward electron ejection mechanism at the plasma surface. We show that it is a periodic push-pull mechanism, which takes place at every laser period.

The state of the art of the field is presented in section 3.1, where the main theoretical results are shown. Section 3.2 describes the electron ejection mechanism in a simplified configuration with a top-hat laser pulse envelope and step-like plasma density profile. Section 3.3 extends this study to the case of an exponential plasma density gradient, which is much more relevant to experiments. A model of the ejection process is proposed.

3.1 Theoretical studies on electron ejection

3.1.1 Electron ejection in PIC simulations

The ejection of electrons during the reflection of an obliquely incident ultrashort ultraintense laser pulse on an overdense plasma was first observed in PIC simulations in reference [Naumova *et al.*, 2004a]. The laser pulse parameters are $\lambda = 800\,\mathrm{nm}$, $\tau = 15\,\mathrm{fs}$, $a_0 = 10$. It is focused down to a spot size $w_0 = 1\,\mu\mathrm{m}$ with angle of incidence $\theta = 70°$ with p-polarization on a step-like overdense plasma with density $n_0 = 25n_c$.

Snapshots of this interaction are shown in figure 3.1. Extremely short bunches (attosecond duration, much shorter than the laser period $T_L = 2.66\,\mathrm{fs}$) of relativistic electrons ($25 - 30\,\mathrm{MeV}$) are ejected from the plasma during the pulse reflection and propagate in vacuum. One electron bunch per laser period is generated. The authors show that up to $\sim 15\%$ of the electromagnetic energy within one laser period is transferred to the attosecond electron bunch, which is a very high efficiency compared to other plasma-based electron accelerators (maximum a few percents for laser wakefield accelerators, see reference [Esarey *et al.*, 2009]).

This article brought new results which motivated this field of research: (i) the reflection of an ultraintense laser pulse can generate attosecond bunches of fast electrons; (ii) one attosecond bunch is generated at each laser period; (iii) this process is highly efficient for an obliquely-incident p-polarized laser pulse because of the component of the electric field normal to the target.

Yet the authors only present observations from PIC simulations with a qualitative explanation, and some important questions remained unaddressed. First, very little

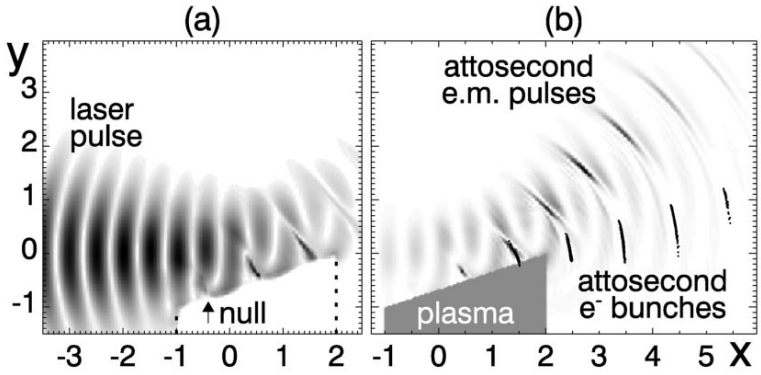


Figure 3.1: [Image from reference [Naumova *et al.*, 2004a]] Reflection of a laser pulse ($a_0 = 10$, $\tau = 15\,\mathrm{fs}$) on an overdense plasma ($n_0 = 25n_c$) and generation of attosecond electron bunches. a) Electromagnetic energy density at $t = -3T_L$. b) Electromagnetic energy density at $t = +3T_L$. Black dots indicate $25 - 30\,\mathrm{MeV}$ electrons.

of the study is dedicated to the plasma surface dynamics, for example the strength of plasma fields is not shown. The authors provide a qualitative explanation for the role of the incident and reflected fields, but do not show whether plasma fields play a role or not. Second, the study focuses on a plasma with uniform density $n_0 = 25n_c$, which is extremely difficult to produce using a laser pulse as intense as $a_0 = 10$. Experiments usually involve strongly ($> 200n_c$) overdense plasmas, for which plasma effects can be radically different. Besides, many experiments involve a density gradient that can play a major role, which is not described in this study. Finally, this article motivated the research field and gave a picture of electron ejection, but further investigation is required.

3.1.2 Density gradient scale length

Another milestone was provided by [Geindre *et al.*, 2010], where the authors demonstrate that, during the reflection of an ultrashort ultraintense laser pulse on a highly-overdense plasma with a density gradient on its front side, the gradient scale length could play a role on the electron ejection process.

Using 1D PIC simulations in the Bourdier boosted frame (see section 1.2), the authors study the reflection of a laser beam with $\lambda = 1\,\mu\mathrm{m}$, $\tau = 12\,\mathrm{fs}$, $a_0 = 5$ on an overdense plasma with bulk density $n_0 = 80n_c$ and an exponential density gradient on its front side. The density gradient scale length is typically $L = 0 - 0.2\lambda$.

The space-time electron density for $L = \lambda/13$, $L = 0$ and $L = \lambda/7$ is shown in figure 3.2. In the $L = \lambda/7$ case, one ultrashort bunch of electrons propagates in vacuum along $-x$ per laser period. This observation corroborates the results obtained by [Naumova *et al.*, 2004a]. The $L = 0$ case (figure 3.2b) shows no ejected electrons, which illustrates the importance of the density gradient length.

The result of their study is summarized in table 3.1. Using an optimal gradient length $L = \lambda/7$ can result in a tenfold increase in electron energy with respect to the $L = 0$ case. The authors assume that adding a density gradient inhibits the gyromagnetic effect (see section 3.1.4).

The authors demonstrate that the backward acceleration of attosecond electron bunches could result in a significant increase in laser absorption. When increasing the gradient length, the regime transitions from almost no absorption ($L = 0$), through

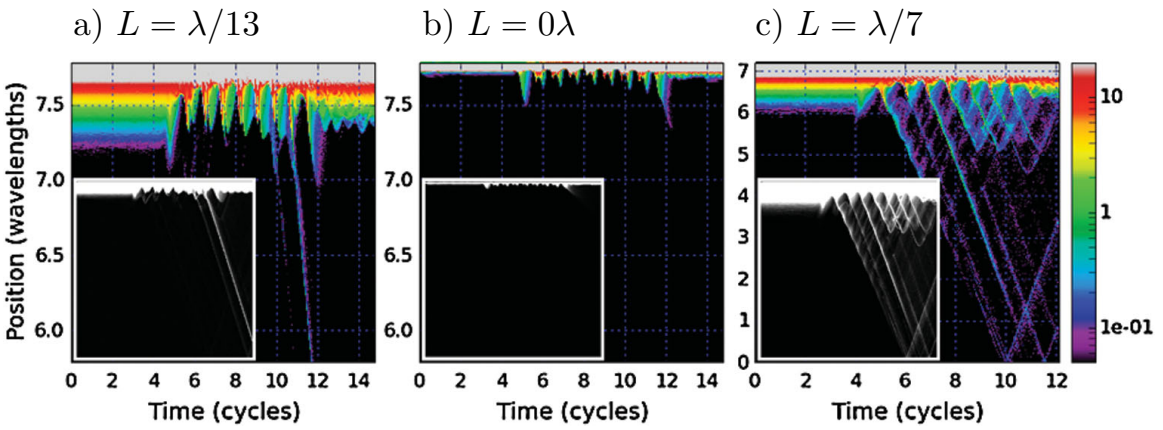


Figure 3.2: [Image from reference [Geindre *et al.*, 2010]] a) electron density in units of n_c along time and space for an initial gradient scale length $L = \lambda/13$. b) and c) show the same representation for $L = 0\lambda$ and $L = \lambda/7$.

case	mechanism	absorption %	E_{max}
$L = \lambda/13$	Brunel	22%	3.5 MeV
$L = 0\lambda$	-	3%	2.2 MeV
$L = \lambda/7$	fast electrons	32%	20 MeV

Table 3.1: Dominant absorption mechanism, ratio of the incident energy absorbed by the plasma and maximum electron energy in the three cases shown in figure 3.2.

Brunel-type absorption ($L = \lambda/13$) to a regime where most of the absorbed laser energy is transferred to backward electron bunches ($L = \lambda/7$).

Finally, the ejected electrons are accelerated *in vacuum* by the laser fields after they leave the plasma. This is illustrated in figure 3.3, where (x, p_x) phase diagrams are plotted at different times. The electron momentum p_x reaches strongly relativistic values during the propagation in vacuum.

Their study brings two conclusions: (i) the gradient length plays a role on the electron ejection efficiency, and (ii) ejected electrons can gain energy in vacuum.

However, no clear description of the mechanism is provided, and the role of the gradient is not investigated in detail. Also, the electron maximum energy decreases for very long gradients, showing that the role of the gradient length is not straightforward. Finally, the acceleration of electrons in vacuum is described by 1D simulations (*i.e.* for a plane wave). It allows the authors to describe the basic principles, but a more realistic description should be performed if we wish to compare theoretical predictions with experimental results.

3.1.3 Electron ejection angle

In reference [Ruhl *et al.*, 1999], the authors investigate the reflection of a laser pulse on a step-like overdense plasma with $n = n_0 > n_c$ for $x > 0$ where x is the target-normal direction. They assume the region $x < 0$ is filled with an underdense plasma called the *plasma corona*, with density $n(x < 0) = n_c/10$ on a distance of several wavelengths.

Starting from the Vlasov equation, the authors derive the final angle of backward ejected electrons. Their study relies on the following hypotheses:

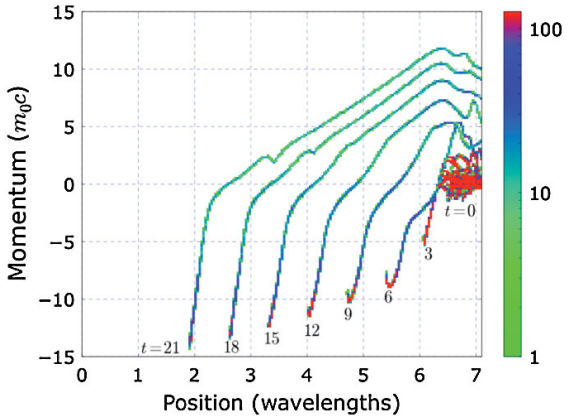


Figure 3.3: [Image from reference [Geindre *et al.*, 2010]] (x, p_x) electron phase space from a 1D PIC simulation with a single-cycle laser pulse (duration 4 fs, $a_0 = 5$). The gradient length is $L = \lambda/7$. Each line stands for a (x, p_x) phase space at a different time with three-laser-cycles intervals.

code	frame	θ	a_0	w_0	n_{bulk}	θ'
PIC	lab	30°	1.2	8 μm	$4n_c$	17°
Vlasov	boosted	45°	0.27	5 μm	$8n_c$	14°

Table 3.2: Simulation parameters in [Ruhl *et al.*, 1999]. In both cases, the wavelength is $\lambda = 1\,\mu$m and the pulse duration is 100 fs. The PIC simulation was run with 100 particles per cell. θ' is the angle of the outgoing electron stream.

- the ions are immobile;
- The initial electron distribution is Maxwellian;
- The incident wave is approximated by a plane wave, so the transverse canonical momentum is conserved;
- The average p_x of the outgoing electrons is proportional to the laser amplitude $< p_x >= \gamma_b m_e c\sqrt{\alpha I\lambda^2}$ with $\gamma_b = 1/\cos\theta$ the γ-factor of the Lorentz transform.

Under these assumptions, the ejected electron stream direction θ' in the laboratory frame is given by

$$\tan\theta' = \frac{\sqrt{1+\alpha I\lambda^2}-1}{\sqrt{\alpha I\lambda^2}}\tan\theta \tag{3.1}$$

where α is a calibration parameter. This parameter is derived from two 2D simulations, one using a PIC code and the other using a Vlasov code in the boosted frame, which parameters are summarized in table 3.2. Both simulations give $\alpha^{-1} \simeq 8\times10^{17}\,\mathrm{W\cdot cm^{-2}}\,\mu\mathrm{m}^2$. This expression is in good agreement with experimental results(see references [Cai *et al.*, 2003; Li *et al.*, 2006b]), provided the plane wave approximation is acceptable.

3.1.4 Gyromagnetic effect

High harmonic generation during the reflection of a laser pulse on a plasma mirror is a non-linear phenomenon. As a consequence, it was believed that the higher the

intensity, the more efficient the harmonic generation. This idea was tempered in reference [Geindre *et al.*, 2006], where the authors show that the dynamics of surface electrons could be inhibited by the strong magnetic field of extremely intense light, leading to a decrease in the harmonic generation efficiency. This mechanism, called gyromagnetic effect, involves important considerations on the electron dynamics, and is detailed below.

Consider the reflection of a p-polarized obliquely incident laser pulse on an overdense plasma with a step-like density profile filling the $x > 0$ half-space. The laser pulse is approximated by a plane wave with wave vector $\boldsymbol{k} = \cos\theta \boldsymbol{e_x} + \sin\theta \boldsymbol{e_y}$ where θ is the angle of incidence. We assume the plasma is highly overdense, so that it behaves like a perfect conductor. The boundary conditions give the following amplitudes for the electric and magnetic fields close to the surface:

$$E_x = 2E_0 \sin\theta \tag{3.2}$$
$$E_y = E_z = 0 \tag{3.3}$$
$$B_x = B_y = 0 \tag{3.4}$$
$$B_z = 2E_0/c \tag{3.5}$$

where E_0 is the maximum amplitude of the incident electric field and c is the speed of light in vacuum.

On the one hand, the magnetic force can often be neglected in the non-relativistic regime $a_0 \ll 1$, and the electron dynamics is governed by the electric force, as described in reference [Brunel, 1987]. When the intensity increases ($a_0 \sim 1$), the magnetic force becomes comparable to the electric force, and magnetic effects should be considered. On the other hand, equation 3.2 shows that, when $\theta = 0$, the electric field cancels on the boundary and the magnetic field should play a dominant role for any laser intensity. Magnetic effects are important when $\omega_c \sim \omega_0$, where $\omega_c = eB/m_e$ is the cyclotron frequency. This condition is nevertheless too crude because the angle of incidence is not taken into account. Indeed, the cyclotron frequency is relevant for an electron in a magnetostatic field only, while there can be a non-zero electric field in the case we consider. To solve this issue, we hereafter move to a frame of reference where the fields are purely magnetostatic, and where this approximation holds.

As proposed in reference [Geindre *et al.*, 2006], let us do a quasistatic approximation and assume that the fields at the plasma surface are frozen to their peak value given by equations 3.2-3.5, and do not depend on the position. We hereafter apply a general method that moves this problem to a pure magnetostatic problem via a Lorentz transformation. This method is valid for uniform and orthogonal electrostatic E and magnetostatic B fields, with amplitudes verifying $B > E/c$. Here, $\boldsymbol{E} /\!/ \boldsymbol{e_x}$ and $\boldsymbol{B} /\!/ \boldsymbol{e_z}$.

We consider a Lorentz transformation with normalized velocity $\beta \boldsymbol{e_y}$ (see section 1.2 page 18). Let $\mathcal{R}$ and $\mathcal{R}'$ be the laboratory and boosted frames respectively. In what follows, the prime symbol stands for quantities in the boosted frame. The fields in $\mathcal{R}'$ are transformed via equations 1.53-1.56, and read

$$E'_x = \gamma(E + c\beta B) \tag{3.6}$$
$$E'_y = E'_z = 0 \tag{3.7}$$
$$B'_x = B'_y = 0 \tag{3.8}$$
$$B'_z = \gamma(B - \frac{\beta}{c}E) \tag{3.9}$$

where $\gamma = (1-\beta^2)^{-1/2}$. The problem is reduced to a magnetostatic problem by canceling the electrostatic field, *i.e.* choosing $\beta = -E/cB = -\sin\theta$. An electron at rest in the laboratory frame drifts in the boosted frame, and its Lorentz factor is γ. The magnetostatic field amplitude in $\mathcal{R}'$ and the relativistic cyclotron frequency are given by

$$B' = \frac{1}{\gamma}B \tag{3.10}$$

$$\omega_c' = \frac{eB'}{m_e\gamma} = \frac{eB}{m_e\gamma^2}. \tag{3.11}$$

Finally, the cyclotron angular frequency backtransformed to the laboratory frame $\mathcal{R}$ is given by:

$$\omega_c = \frac{\omega_c'}{\gamma} = \frac{eB}{\gamma^3 m_e}. \tag{3.12}$$

We apply these general expressions to the electric and magnetic fields at the boundary of a perfect conductor given in equations 3.2-3.5. They read $\beta = -\sin\theta$, $\gamma = 1/\cos\theta$, and the electron cyclotron frequency in the laboratory frame is given by

$$\omega_c = \frac{2\cos^3\theta eE_0}{m_e c}. \tag{3.13}$$

Magnetic effects become manifest when $\omega_c \sim \omega_0$. We define the gyromagnetic parameter

$$\mathcal{G} = \frac{\omega_c}{\omega_0} = 2a_0\cos^3\theta. \tag{3.14}$$

The gyromagnetic effect plays a role when $\mathcal{G} \gtrsim 1$. Note that this expression comes from the E/B ratio, and differentiates the electric-dominated regime $\mathcal{G} \lesssim 1$ from the magnetic-dominated regime $\mathcal{G} \gtrsim 1$. The electric field pulls electrons from the plasma towards vacuum, whereas the magnetic field makes them rotate, and brings them back to the plasma.

When a_0 becomes very large, $\omega_c \gg \omega_0$ and an electron circles in the magnetic field much faster than it moves in the electric field; magnetic effects are thus dominant, and $\mathcal{G}$ increases with a_0. When θ is very small, the electric force drops and the electron dynamics is governed by magnetic effects, which is expressed as $\mathcal{G} \propto \cos^3\theta$.

Figure 3.4 shows electron dynamics for $\mathcal{G} = 0.3$, 0.4 and 1 respectively. The different colors show trajectories for electrons with different starting time t_j. They were calculated by solving the relativistic equation of motion for electron number j, starting at time t_j, in the boosted frame:

$$\frac{d\boldsymbol{p}_j}{dt} = \frac{2eE_0}{\cos\theta}\sin(\omega_0' t_j)\boldsymbol{e}_x - 2eB_0\cos\theta\sin(\omega_0' t)\boldsymbol{v}_j \times \boldsymbol{e}_z \tag{3.15}$$

with $\omega_0' = \cos\theta\omega_0$. This is equivalent to Brunel's model presented in section 1.3.2, with two differences: first, magnetic and relativistic effects are added; second, these equations are solved in the boosted frame, the laser force $\alpha\sin(\omega_0' t)$ thus acts via the magnetic field. When $\mathcal{G}$ gets close to 1, the electron trajectories are strongly curved and confined close to the plasma surface.

This mechanism plays a major role for electron ejection: we anticipate that it prevents electrons from escaping the plasma for high intensities when the plasma is

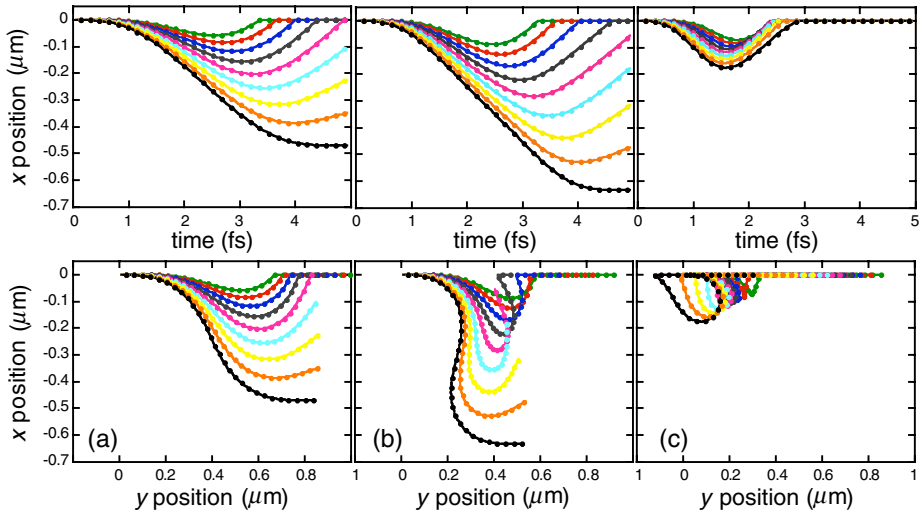


Figure 3.4: [Image from reference [Geindre *et al.*, 2006]] a) Electron trajectories $x(t)$ (top panel) and $x-y$ (bottom panel) for $\theta = 45°$ and $a_0 = 0.4$. Different trajectories, with different starting time, are superimposed. b) and c) show the same quantities for $a_0 = 0.7$ and $a_0 = 1.5$ respectively.

highly overdense with a step-like density profile. In section 3.2, we show how electrons can be ejected in the low-density step-like regime thanks to strong plasma fields.

When the plasma profile shows a relatively long density gradient, a strong plasma electrostatic field $\boldsymbol{E}_p /\!/ \boldsymbol{e}_x$ appears, which may drastically increase the E/B ratio. Hence, this field helps pulling electrons towards vacuum and favors electron ejection. When decreasing the gradient scale length, we observe that the electron ejection is strongly inhibited because of the gyromagnetic effect. A detailed analysis is presented in 3.3.

3.1.5 Electron ejection in 1D PIC simulations

Figure 3.5c) shows the magnetic field *vs.* time and space in a 1D simulation with physical conditions (given in the laboratory frame) $a_0 = 3$, $\tau = 5\,\mathrm{fs}$, $L = \lambda/8$, and a Gaussian time envelope. The overdense plasma fills the region $x > 4.7\lambda$. The incident and reflected fields are recorded as a function of time at $x = 0.5\lambda$ and plotted in figure 3.5 a) and b). The incident field shows a simple sine profile with an exponential envelope, while the reflected field is much distorted, which is a clear signature of high harmonic generation (see chapter 1).

The electron density is shown in figure 3.5d), using the same representation as the magnetic field. When the laser pulse reaches the target, the plasma surface oscillates at the laser frequency. Starting from $t \simeq 8.5T_L$ and $x \simeq 4.5\lambda$, an electron jet escapes the plasma and propagates in the $-x$ direction along the reflected field. We hereafter focus on a single oscillation of the plasma surface during one laser period.

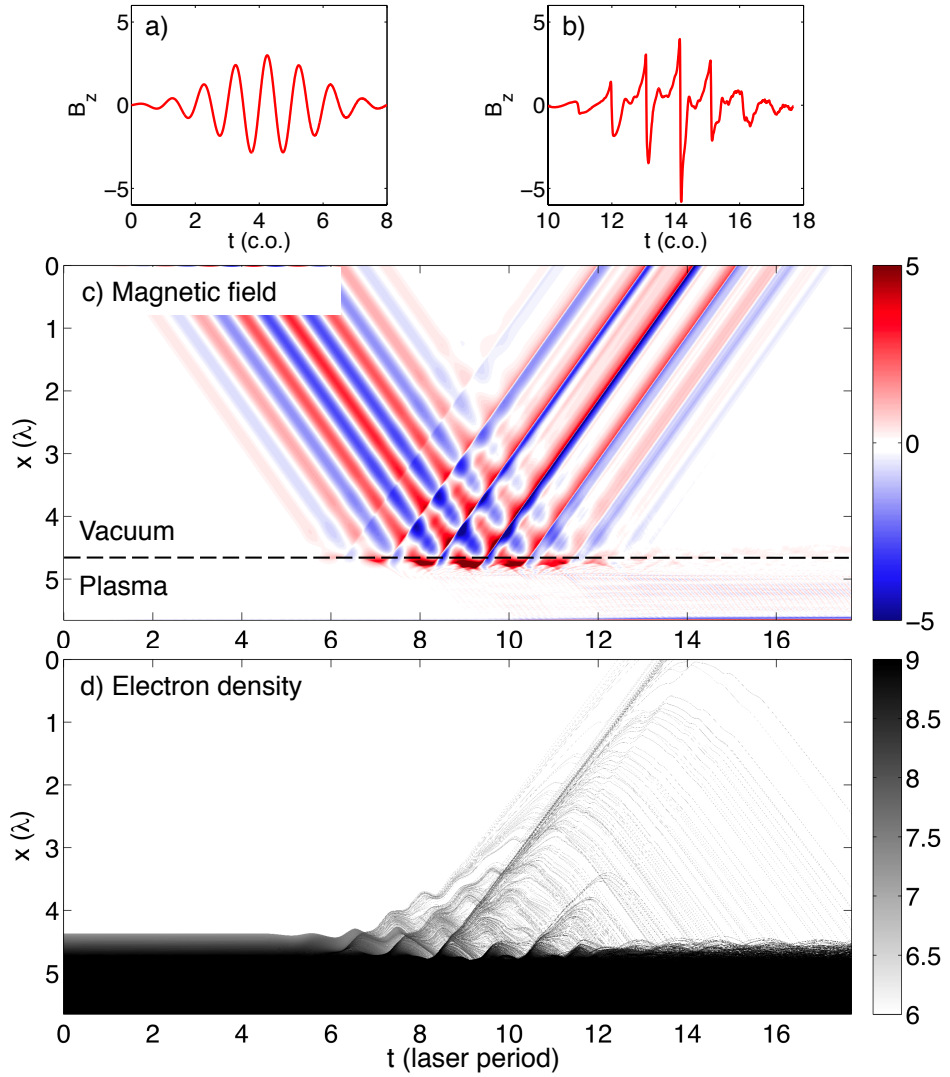


Figure 3.5: a) Magnetic field along time and space from a 1D PIC simulation performed in the boosted frame with physical conditions (given in the laboratory frame) $a_0 = 3$, $\tau = 5\,\mathrm{fs}$, $L = \lambda/8$. The area $x > 4.7\lambda$ is filled with the overdense plasma. b) Same representation for the electron density. A bunch of electrons propagates in vacuum towards the $x < 0$ direction, *i.e.* along the reflected pulse.

3.2 Electron ejection with a step-like density profile

In order to single-out the basic mechanism of backward electron ejection from plasma mirrors, this section focuses on a simplified configuration: a plane wave reflects off an overdense plasma with a step-like density profile, and the bulk density n_0 is an adjustable parameter. This approach was used in several articles (see section 3.1) and gives helpful insight into the underlying mechanisms.

We consider the relativistic regime, and study the role of two fundamental parameters: the laser amplitude a_0 and the plasma density n_0, in the typical range $a_0 = 2-20$ and $n_0 = 4-40n_c$. Low-density step-like plasma profiles are not very relevant in experiments because typical experiments involve a highly overdense plasma ($n_0 > 200n_c$) with a density gradient on its front side (see chapter 1). Yet the mechanisms are somewhat similar in both conditions.

As will be seen in this section and the following one, the laser pulse penetrates inside the density gradient during reflection. For a very sharp gradient ($L \ll \lambda$), the laser fields interact with high-density regions of the gradient ($n \gg n_c$). On the opposite, if the gradient is very smooth ($L \sim \lambda$), the electromagnetic fields are confined in the $n \gtrsim n_c$ region, and the reflection process occurs in a low-density region. Hence, a highly overdense plasma behaves in a similar way as a very sharp gradient, and a slightly overdense plasma resembles a very smooth gradient.

All the 1D PIC simulations are performed in the boosted frame, and all the physical quantities are given in the boosted frame from now on, unless otherwise specified. We use the following normalizations throughout this chapter:

$$t \equiv \omega_0 t \qquad v \equiv v/c \qquad x \equiv kx \tag{3.16}$$

$$y \equiv ky \qquad p \equiv p/m_e c \qquad n \equiv n/n_c^L \tag{3.17}$$

$$E \equiv \frac{eE}{m_e \omega_0 c} \qquad B \equiv \frac{eB}{m_e \omega_0} \tag{3.18}$$

Note that the plasma density is normalized with n_c^L, the critical density in the laboratory frame. For the sake of simplicity, n_c^L will be noted n_c throughout this chapter.

3.2.1 Phenomenology of electron ejection

Electric and magnetic fields

We performed a 1D simulation in the boosted frame with a monochromatic incident wave where the laser amplitude is $a_0 = 14$ (step-like laser envelope) and the plasma density is $n_0 = 10$ in the plasma bulk $x > 0$. We focus on the plasma dynamics during the first laser period. The electron density is shown as a function of time and space in figure 3.6 a) along with the magnetic field (b), the electric field along the target surface direction (c) and the electric field normal to the target (d). The ions are mobile in the simulation, but their motion is negligible on the scale of one laser period.

When the laser pulse reaches the plasma, it pushes the electron surface inside the plasma, up to a maximum distance of $x \simeq 0.5\lambda$. This creates a charge separation in the plasma because the ions are immobile, which results in plasma static fields that we discuss below. Afterwards, electrons travel along the $-x$ direction and some electrons propagate in vacuum.

In the boosted frame, as seen in section 1.2, the plasma electric field is along x whereas the laser electric fields is along y. The electrostatic (denoted with p for plasma)

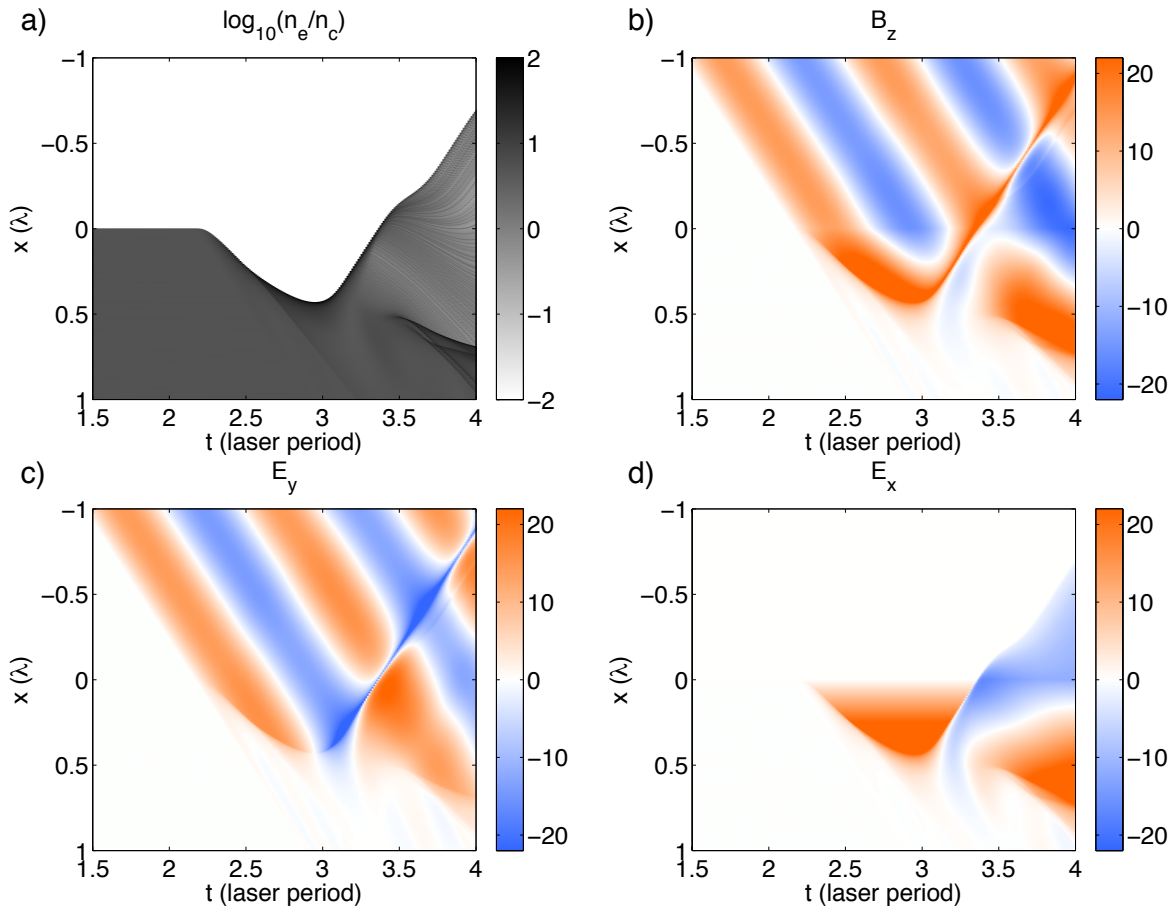


Figure 3.6: a) Electron density as a function of time and space in the 1D PIC simulation `these_step`. The incident wave is a monochromatic wave that reaches the plasma around $t = 2.2T_L$ with $a_0 = 14$ and $\theta = 45°$, the plasma has a step-like density profile with $n = 10$ for $x > 0$. $\Delta x = \lambda/2000$, ppc=1000. b), c) and d) are the magnetic field B_z and the tangential E_y and normal E_x electric fields respectively.

and electromagnetic (denoted with i for incident and r for reflected) contributions are decoupled in the electric field, while they are coupled in the magnetic field, which reads:

$$E = \begin{pmatrix} E_{ions} \\ E_{electromag} \\ 0 \end{pmatrix} = \begin{pmatrix} E_p \\ E_i + E_r \\ 0 \end{pmatrix} \tag{3.19}$$

$$B = \begin{pmatrix} 0 \\ 0 \\ B_{electromag} + B_{ions} \end{pmatrix} = \begin{pmatrix} 0 \\ 0 \\ B_i + B_r + B_p \end{pmatrix}. \tag{3.20}$$

These considerations help us understand the main fields: E_y in figure 3.6c) is the superposition of the incident and reflected fields, propagating in the $+x$ and $-x$ directions respectively. Figure 3.6d) shows the plasma electric fiels E_x. **When the laser pushes electrons, it builds a positive electrostatic field**, as can be seen in figure d) for $2.5T_L < t < 3T_L$. Afterwards, some electrons travel in vacuum and create a negative electrostatic field, as can be seen at $t \simeq 4T_L$ for $x < 0$. Finally, both contributions are superimposed in the B_z component of the magnetic field, shown in figure 3.6b).

Low density *vs.* high density

Even though this general process occurs for any $n_0 \gtrsim n_c$ and $a_0 > 1$ (and $\theta > 0$), it does not always lead to electron ejection. As an example, figure 3.7 shows the electron density along time and space from a PIC simulation with an initial density $n_0 = 10$ (a) and $n_0 = 30$ (b). One can clearly see a jet of electrons traveling in vacuum in the low-density case, whereas all electrons remain in the plasma for high-density. This section aims at understanding this difference in behavior.

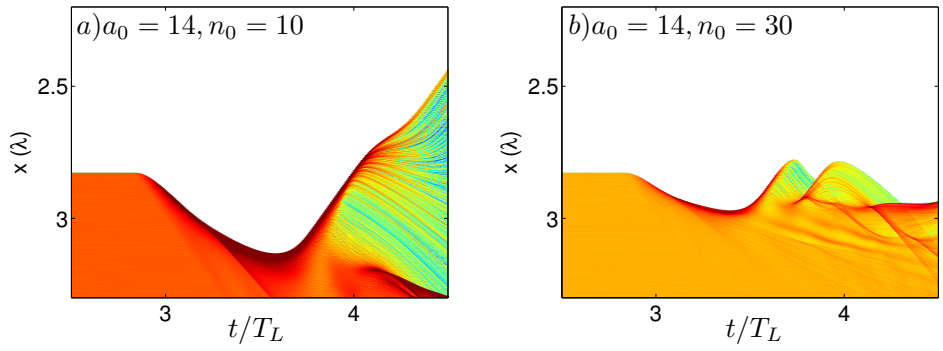


Figure 3.7: a) Log-scale electron density as a function of time and space for a step-like density profile and step-like temporal profile for the incident wave from a 1D PIC simulation ($a_0 = 14$ and $n_0 = 10$). b) Same representation for $n_0 = 30$.

3.2.2 Push-pull mechanism

Description of the mechanism

The plasma dynamics occurs as a push-pull mechanism. This is illustrated with the 1D PIC simulation `these_step` with a top-hat temporal shape for the incident wave. The incident driving fields read

$$\boldsymbol{E_i} = a_0 \sin(t - x)\boldsymbol{e_y} \qquad \boldsymbol{B_i} = a_0 \sin(t - x)\boldsymbol{e_z}$$

and the initial electron/ion speed is $\boldsymbol{\beta} = \boldsymbol{\beta}_d = -\sin\theta \boldsymbol{e_y}$. For $E_i > 0$, the electric force accelerates electrons in the $-y$ direction, allowing them to reach speed $\beta_y \gtrsim -1$ as soon as $a_0 > 1$ (see [Gonoskov *et al.*, 2011]). The $\boldsymbol{\beta} \times \boldsymbol{B_i}$ force is then directed towards the $+x$ direction, so that it pushes electrons which are bundled-up into a sharp density peak into the plasma.

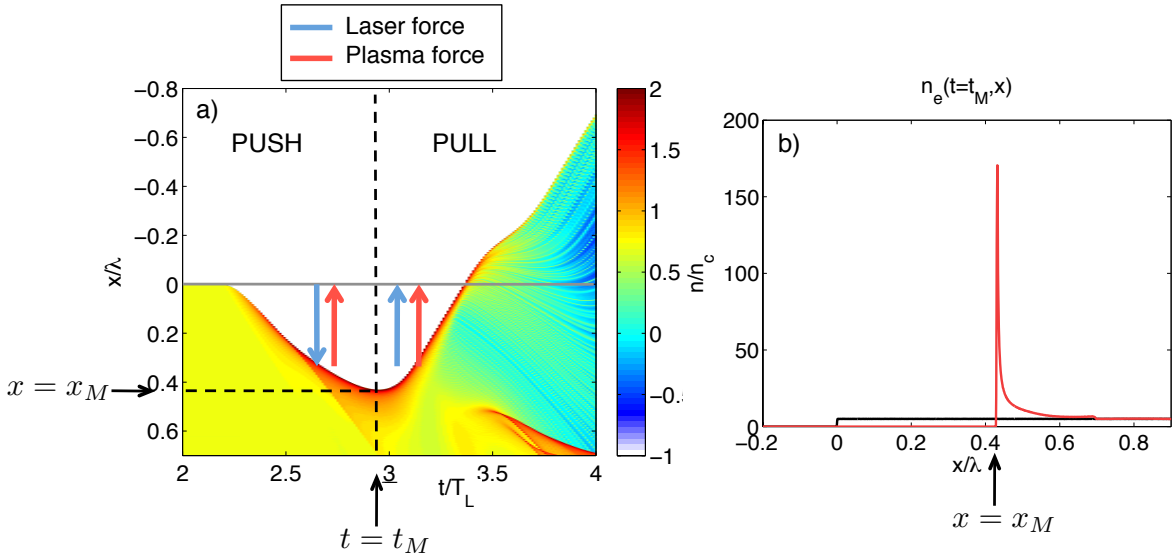


Figure 3.8: Illustration of the push-pull mechanism in a 1D PIC simulation. a) Electron density $\log_{10}(n_e)$ in a 1D PIC simulation with $a_0 = 14$ and $n_0 = 10$. The maximum depth $x = x_M$ is reached at $t = t_M$. b) Density profile $n_e(x)$ at $t = t_M$. The sharp peak, with width $< \lambda/100$, is located at $x = x_M$.

(i) Push phase: During the first half-period, the incident laser field pushes electrons inside the plasma while the ions are not displaced, which builds up an electrostatic plasma field $\boldsymbol{E_p} = E_p \boldsymbol{e}_x$. Because the ions are drifting, this charge separation also induces plasma currents which are the source of magnetostatic plasma field $\boldsymbol{B_p} = B_p \boldsymbol{e}_z$.

At $t = t_M$, the peak reaches a maximum position with $p_x = 0$. At this point, the forces due to the incident wave, the reflected wave and the plasma fields cancel out along the x direction. We hereafter derive the maximum peak position from the balance of forces as is done in [Gonoskov *et al.*, 2011]. Assuming all electrons have position x such that $x > x_M$, Gauss's and Ampère's laws read

$$\frac{\partial E_p}{\partial x}(x > 0) = \frac{n_i}{\cos^2\theta} = \frac{n_0}{\cos^3\theta} \tag{3.21}$$

$$\frac{\partial B_p}{\partial x}(x > 0) = \frac{-n_i v_{iy}}{\cos^2\theta} = \frac{n_0 \sin\theta}{\cos^3\theta} \tag{3.22}$$

where the $\cos^2\theta$ factor is due to the normalization with n_c and the additional $\cos\theta$ factor is due to the Lorentz transform of the charge density. The $\sin\theta$ term is the ion drift velocity in the boosted frame. Hence, the electrostatic and magnetostatic fields at position x are given by

$$E_p(x) = \frac{1}{\cos^3\theta} n_0 x \tag{3.23}$$

$$B_p(x) = \frac{\sin\theta}{\cos^3\theta} n_0 x. \tag{3.24}$$

We assume that the maximum peak depth x_M is an equilibrium position where the total force along x (incident and reflected waves plus plasma fields) is zero:

$$\beta_y(B_i + B_r + B_p) + E_p = 0. \tag{3.25}$$

Let us further assume that the electron velocity at x_M is $(\beta_x, \beta_y) = (0, -1)$. The laser reflects off the surface at x_M and we assume that the boundary conditions of a perfect conductor can be applied for the incident and reflected laser fields, giving $B_z = 2a_0$, hence,

$$2a_0 + \frac{\sin\theta}{\cos^3\theta} n_0 x_M - \frac{1}{\cos^3\theta} n_0 x_M = 0, \tag{3.26}$$

which gives the maximum depth

$$x_M = \frac{2a_0 \cos^3\theta}{n_0(1 - \sin\theta)}. \tag{3.27}$$

This expression gives a very good approximation within less than 10% error in a wide range of parameters $3 < a_0 < 20$ and $5 < n_0 < 40$. At $t = t_M$, the target surface is similar to a plasma capacitor where electrons are gathered in the density peak at $x = x_M$ and the half-space $x < x_M$ is filled with ions only.

(ii) Pull phase: During the following half-period, the incident field changes sign so that the $\beta_y B_i$ force pulls electrons towards vacuum, breaking the force balance along x. The electron peak is accelerated towards vacuum ($x < 0$), and radiates an attosecond electromagnetic bunch via the Relativistic Oscillating Mirror mechanism (see chapter 1). A small fraction ($< 1\%$) of electrons in the density peak escapes the plasma and travels along the reflected pulse, as can be seen in figure 3.8.

Peak dynamics

The dynamics of the electron density peak can be determined in a PIC simulation. Figure 3.9 a) shows the magnetic and electric forces on the density peak along time in the x direction, from a 1D PIC simulation. It starts around $t = 3T_L$ when the laser wave reaches the plasma and forms the density peak. One can see that the total force is almost zero during most of the laser period and becomes strongly negative right after the peak reaches its maximum depth. As can be seen on this image, the electric and magnetic forces components have similar amplitudes.

Figure 3.9b) shows the peak velocity β as a function of time. The first striking result is that the peak travels with relativistic speed $\beta \simeq 1$ along its motion. The initial electron velocity is due to the drift in the boosted frame: $(\beta_x, \beta_y) = (0, -\sin\theta)$. When the incident wave reaches the surface, the magnetic force pushes electrons inside the plasma ($\beta_x > 0$). The electric field $E_y > 0$ accelerates the bundled electrons towards $y < 0$. This phase lasts until the incident field sign changes and the peak reaches its maximum position at $t = t_M$. Then, $E_y = 0$ and $(\beta_x, \beta_y) = (0, -1)$. Afterwards, the $-\beta_y B_z < 0$ magnetic force strongly pulls the electron peak towards $-x$. Meanwhile, the electric field is now directed towards $+y$, and this phase stops at the emission time, when $(\beta_x, \beta_y) = (-1, 0)$.

The emission time is defined by $\beta_y(t_e) = 0$. Here, $t_e \simeq 3.7T_L$. At this time, $(\beta_x(t_e), \beta_y(t_e)) = (-1, 0)$ and the electron peak reaches its maximum speed towards vacuum. As a consequence, the Doppler effect is maximum, and an attosecond electromagnetic pulse is generated at time t_e. More details on the emission time can be found in section 1.4.3.

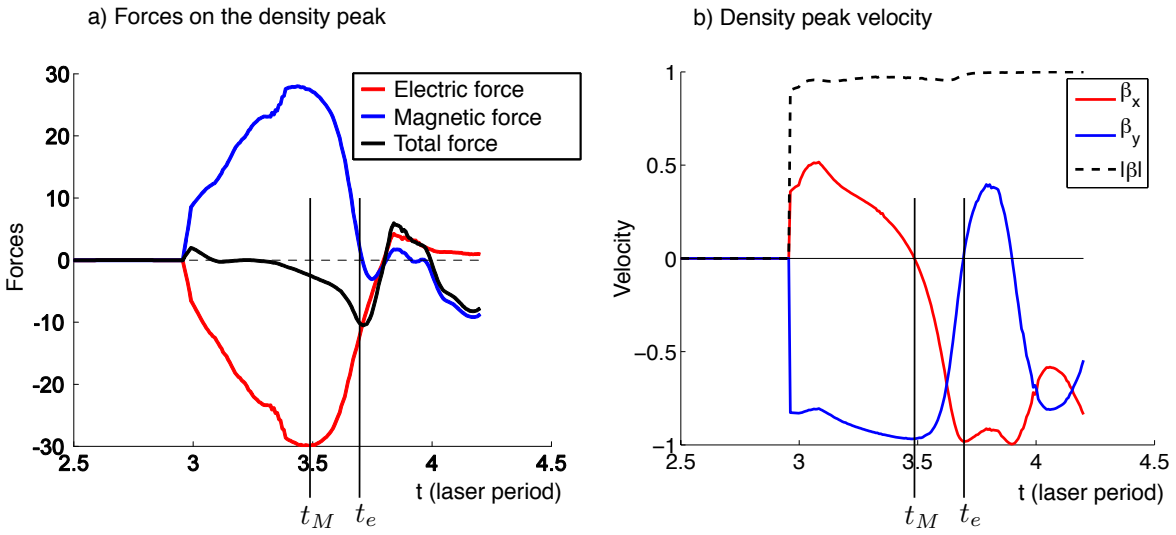


Figure 3.9: a) Forces along the density peak in 1D PIC simulation ($a_0 = 10$, $n_0 = 10n_c$). A balance builds up between the electric and magnetic forces as long as $\beta_y \simeq -1$, and breaks when $\beta_y = 0$ where the total force becomes negative, accelerating electrons towards vacuum. b) Speed of the density peak from the same simulation. Note that the velocity is only defined for $t \gtrsim 3T_L$ because the peak is not formed before.

This periodic mechanism results in high harmonic generation via the relativistic oscillating mirror (see 1.4.3). At this time, the electron peak has almost left the plasma.

The analysis mentioned above relies on the electron density peak dynamics. Nonetheless, the peak breaks during the pull phase because electrons inside the peak no longer have the same dynamics. This is shown in figure 3.10, which shows the electron density peak profile at several times during the peak acceleration towards vacuum, with a half-laser-period time-step (0 is the plasma border). After half a laser period, the number of electrons in the peak has dramatically decreased, and the distribution is strongly flattened. Moreover, at time $t_M + T_L$, a new peak is created deeper inside the plasma, which corresponds to the same mechanism at the following laser period. Note that this peak is not as sharp as the previous one, showing the complexity of the phenomenon with strong cycle-to-cycle memory effects.

Finally, the front edge of the density peak escapes the plasma and propagates in vacuum towards $-x$. The ejected electrons are part of the density peak along its acceleration towards vacuum. Finally, at the end of the pull phase, electrons in the density peak have strongly inhomogeneous velocities: the peak bursts.

3.2.3 Relativistic Electronic Spring by Gonoskov

Reference [Gonoskov *et al.*, 2011] presents a model for the surface dynamics, which aims at describing the temporal profile of the reflected field via a precise description of the density peak motion. The authors assume that the electron peak is defined at all time and derive its dynamics in an elegant way to calculate the reflected field.

Hypotheses of the model

Consider a plane wave that impinges on a homogeneous overdense plasma with initial density n_0. The target normal is along x and the plasma occupies the half-space $x > 0$. The incident wave is assumed to be ultrarelativistic ($a_0 \gg 1$) and the ions are immobile.

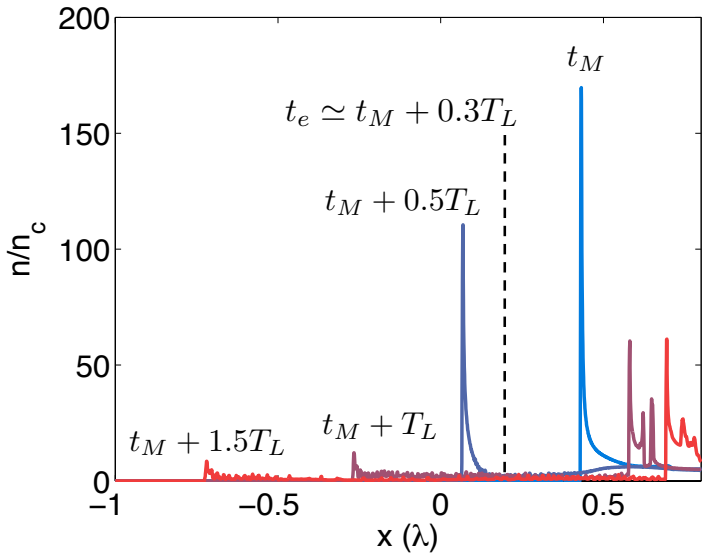


Figure 3.10: Propagation of the density peak towards vacuum ($-x$) during the acceleration phase from 1D PIC simulation `these_step`. The electron density is plotted in linear units along x in half-a-period timesteps, starting from the maximum depth t_M. At $t = t_M + T_L$, the peak amplitude has strongly decreased. Besides, a second peak has formed inside the plasma, which shows the repetition of the same mechanism during the following laser period. The peak travels with speed $\beta \simeq -1$. The dashed line shows the peak position at the emission time $t = t_e$.

The study is performed in the Bourdier boosted frame, where the physical quantities are modified according to the Lorentz transformation presented in 1.2.

When the laser reaches the target, the electrons are gathered in a high-density peak inside the plasma. This is shown in figure 3.8. The very sharp electron peak (width $\delta \ll \lambda$) oscillates in the plasma and radiates the reflected field.

The electron peak is characterized by its position $x_p(t)$ and normalized speed $\beta_x(t), \beta_y(t)$. The hypotheses of the model are:

- H1: All electrons between the plasma edge and $x_p(t)$ are gathered in the density peak, so that its total charge is $n_0 x_p(t)$. The peak is approximated by a Dirac distribution.

- H2: The peak velocity is ultrarelativistic at all time: $|\boldsymbol{\beta}| = 1$. This hypothesis is justified in our simulations (see figure 3.9). Note that it implies that the peak has infinite kinetic energy, so this model cannot rely on the equations of motion.

- H3: The total electric and magnetic fields inside the plasma behind the peak are zero, so that the plasma is neutral and unperturbed behind the density peak. Practically, this hypothesis can be written right behind the peak at $x_p^+(t)$ for any $t > 0$, and reads $\boldsymbol{E}(x_p^+(t), t) = 0$ and $\boldsymbol{B}(x_p^+(t), t) = 0$.

Peak dynamics

Let us derive the equation governing the peak dynamics using H3. The total magnetic field at position $x_p^+(t)$ right behind the peak is the sum of the laser and plasma contributions. The laser contribution is $a_0 \sin(t - x_p(t))$, and the ions contribution at time t is calculated through Maxwell-Ampère's equation 1.6, as done in equation 3.24. It

reads

$$B_p(x_p^+(t),t) = \frac{\sin\theta}{\cos^3\theta} n_0 x_p(t). \tag{3.28}$$

According to H1, the electron distribution is approximated to a Dirac distribution at position $x_p(t)$. At this point, we should remark that this statement is valid because we consider a unidimensional space. In a realistic 3D space, this means that electrons are gathered in a plane foil with surface charge $n_0 x_p(t)$ and speed β_x, β_y. The radiated field emitted by this foil in the $+x$ direction is

$$B_s(x_p^+(t),t) = \frac{n_0\beta_y}{1-\beta_x} x_p(t). \tag{3.29}$$

This electron foil screens the incident fields. Its dynamics is given by hypothesis H3, assuming that the sum of laser, ion and electron contributions behind the peak is zero:

$$B_i + B_p + B_s = 0. \tag{3.30}$$

This is shown in figure 3.11.

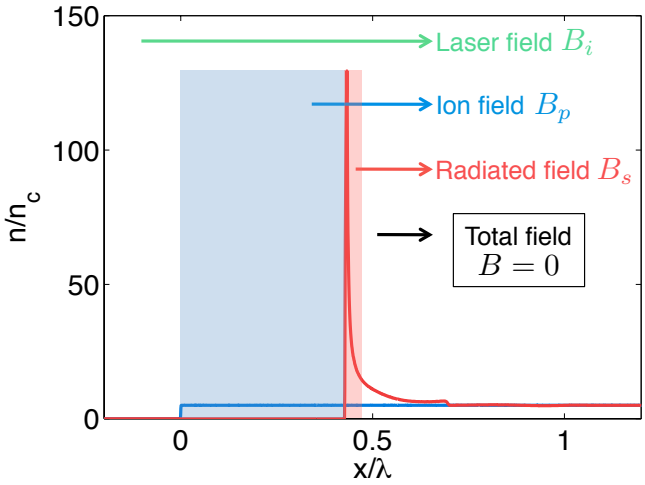


Figure 3.11: Illustration of the screening hypothesis (H3) in Gonoskov's model. The electron (red) and ion (blue) densities are plotted as a function of the position, for a given time. The total field in the plasma behind the density peak is assumed to be zero.

This gives equation 3.31 which, combined with hypothesis H2 and the definition of β_x, gives the following system

$$\sin(x_p - t) = \frac{n_0}{2a_0}\frac{x_p}{\cos^3\theta}\left(\sin\theta - \frac{\beta_y}{1-\beta_x}\right) \tag{3.31}$$

$$\beta_x^2 + \beta_y^2 = 1 \tag{3.32}$$

$$\frac{dx_p}{dt} = \beta_x. \tag{3.33}$$

The system of three equations 3.31–3.33 involves three variables (x_p, β_x, β_y) and can be solved numerically to determine the dynamics of the electron peak.

Reflected field

At this point, the three variables $x_p(t)$, $\beta_x(t)$ and $\beta_y(t)$ are known at all times. The fields radiated in vacuum $x < 0$, *i.e.* the reflected field B_r, can be calculated as the sum of the ion fields and the radiation emitted by the moving electron peak. The field on the left of the density peak $x_p^-(t)$ reads

$$B_r(x_p(t), t) = \frac{n_0}{2} \frac{x_p}{\cos^3\theta} \left(\frac{\beta_y}{1+\beta_x} + \sin\theta \right). \tag{3.34}$$

Equation 3.34 gives the reflected field on the peak position, which moves along time. A more practical observable is the reflected field at a given position, say $x = 0$, that can be calculated using the retarded time:

$$B_r(0, t + x_p(t)) = B_r(x_p(t), t). \tag{3.35}$$

Comparison with a PIC simulation

Hence, the model gives the electron peak position as well as the temporal profile of the reflected field. For very high laser intensities $a_0 > 10$, this model predicts very well the surface motion as well as the reflected field. Figure 3.12 shows a colormap of the magnetic field from a PIC simulation, compared with the magnetic field calculated from the model. The agreement is striking. Note that the total field behind the density peak is zero on the model, according to H3.

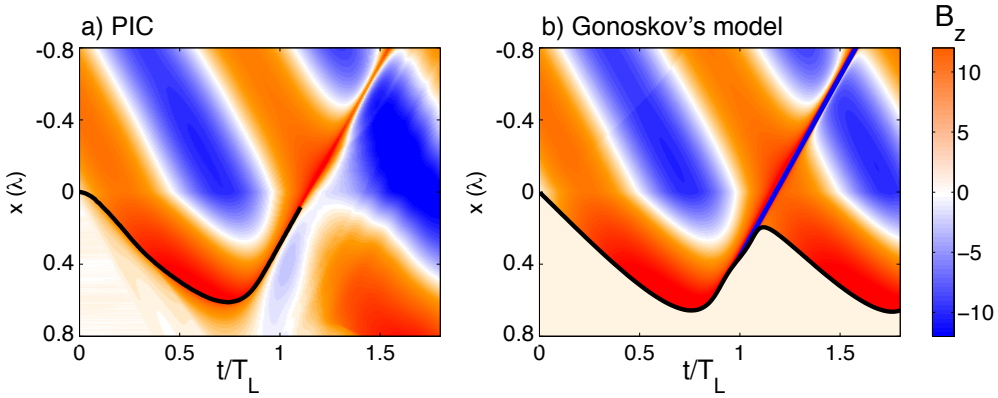


Figure 3.12: a) 2D map for the magnetic field along time and space for a 1D particle-in-cell simulation in the boosted frame. A step-like density profile was used, with a bulk density $n_0 = 5$ for $x > 0$. The laser amplitude is $a_0 = 10$. The reflected wave is created around $t = 0.8T_L$ at $x = 0.7\lambda$ and propagates as a very sharp burst along the $x < 0$ direction. The black line shows the electron density peak position. It stops after time $t > 1.1T_L$ because the density peak bursts at this time before it is formed again around time $t = 1.5T_L$. b) Same as a), calculated via Gonoskov's model. The attosecond bunch emission time and the surface dynamics are remarkably well reproduced.

Note that the system of equations 3.31–3.33 giving the peak dynamics does not depend independently on a_0 and n_0, but rather varies as a function of the parameter

$$S = \frac{n_0}{a_0}. \tag{3.36}$$

All the equations can be written as a function of this parameter (it also appears in equation 3.34 through x_p). As a consequence, a simulation with $2n_0$ and $2a_0$ gives

exactly the same result as a run with n_0 and a_0 (this is in agreement with the similarity theory developed in reference [Gordienko & Pukhov, 2005]).

Finally, the relativistic electronic spring model describes very well the peak dynamics as well as the temporal shape of the reflected field in spite of three major limitations: first, it works for very high intensities. Second, it assumes that the electron peak exists during the whole interaction, and remains in the plasma $x > 0$, which is debatable (see figure 3.10). Third, since the electron peak travels at the light velocity, its energy is infinite. As a consequence, there exists at least one instant at which the reflected field diverges (see equation 3.34), and the harmonic spectrum is not very well reproduced.

In spite of these rough assumptions, this provides an unprecedented description of the surface dynamics and the electric and magnetic fields. Yet it cannot be used directly for electron ejection because the peak is assumed to remain in the plasma at all time. Relying on this model, we derive a semi-analytical model for electron ejection in section 3.2.4.

As a summary, the maximum peak position x_M and the electrostatic field and electrostatic potential at this position read respectively

$$x_M = \frac{2a_0 \cos^3\theta}{n_0(1-\sin\theta)} \tag{3.37}$$

$$E_p(x_M) = \frac{2a_0 \cos^2\theta}{1-\sin\theta} \tag{3.38}$$

$$\phi_p(x_M) = \frac{2a_0^2 \cos^5\theta}{n_0(1-\sin\theta)^2} \tag{3.39}$$

where the electrostatic potential is calculated via its definition $E_p = -\partial_x \phi_p$ and normalized by $\phi_p \equiv e\phi_p/m_e c^2$.

3.2.4 Model for electron ejection with a step-like profile

The model described above provides the peak dynamics assuming it travels with constant speed $\beta = 1$, hence infinite kinetic energy, so we cannot write the equations of motion on the density peak. Besides, as shown in section 3.2.2, the ejected electrons are part of the density peak during the acceleration phase. However, Gonoskov's model assumes that the density peak remains in the plasma, while ejected electrons do have to travel in vacuum ($x < 0$). As a consequence, one step should be added to model electron ejection.

Model hypotheses

Our model consists in solving the equations of motion for an electron propagating in the fields calculated by Gonoskov's model. Following our observations from PIC simulations, we assume that the electron belongs to the density peak until the emission time t_e. At $t = t_e$, a test-particle is released, and its dynamics is calculated by solving the equations of motion in the fields derived from Gonoskov's model.

In principle, we could choose any time as the release time, provided the density peak is well defined (for example, $t \leq t_M + T_L$ in figure 3.10). Yet the initial conditions of the test-particle at the release time must be determined. Its position is given by the peak position, but its momentum components p_x and p_y are unknown, since the peak travels with infinite energy. This can be reduced to one single unknown at two specific

times: the time for maximum depth, where $p_x(t_M) = 0$, and the emission time, where $p_y(t_e) = 0$. We choose the emission time as the release time, and determine $p_x(t_e)$.

The attosecond pulse is emitted at t_e around the middle of the electron peak. As a consequence, the electromagnetic fields are extremely inhomogeneous inside the peak after t_e and the peak bursts after t_e. It is only well defined until the emission time.

The ion background forms an electrostatic potential ($\boldsymbol{E}_p = -\nabla\phi_p$) that reads

$$\phi_p(x) = \frac{n_0}{\cos^3\theta}\frac{x^2}{2}. \tag{3.40}$$

We define $\phi_e = \phi_p(x_e)$, and assume the initial electron momentum at t_e is given by

$$p_x(t_e) = \frac{\phi_e}{2}. \tag{3.41}$$

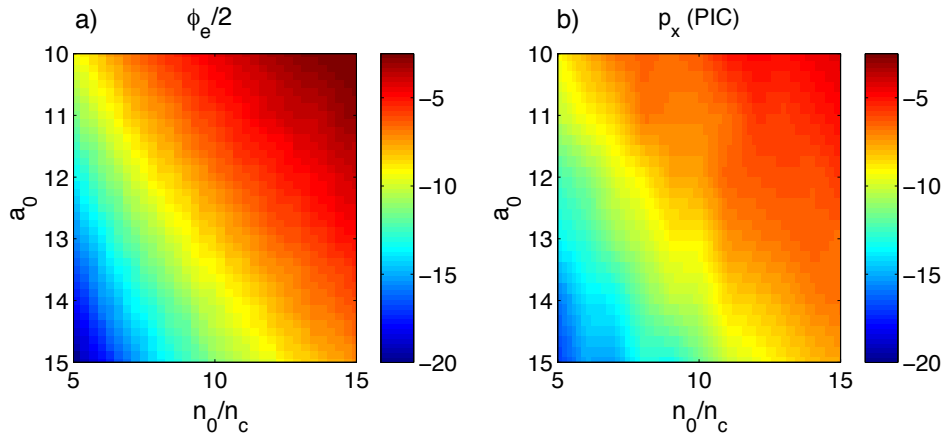


Figure 3.13: a) Half electrostatic potential $\phi_e/2$ at emission time t_e measured in a scan of PIC simulations as a function of a_0 and n_0. The incident wave has a top-hat temporal profile and the plasma has a step-like density profile, with bulk density n_0 given in units if n_c. The value was measured during the first plasma oscillation. b) p_x at emission time for the same set of simulations.

To verify this hypothesis, we measured $p_x(t_e)$ in the peak from a set of 1D simulations, and compared it to $\phi_e/2$. The result is shown in figure 3.13, which shows that hypothesis 3.41 is verified within $< 10\%$ error.

We finally get the maximum density n_0 above which no electron is ejected with the following procedure:

- For a given (a_0, n_0), calculate $S = n_0/a_0$;
- Compute the peak dynamics x_p, β_x and β_y via Gonoskov's model;
- Calculate the total electric and magnetic field via Gonoskov's model;
- Find the emission time t_e defined by $\beta_y(t_e) = 0$;
- Inject an electron at t_e with initial conditions $x = x_p(t_e)$, $p_x = \phi_e/2$, which reads $p_x = n_0 x_p(t_e)^2/4\cos^3\theta$ and $p_y = 0$ and solve the equation of motion in the space-time dependant electric and magnetic fields;
- An electron is considered to be ejected if $p_x < 0$ for any time $t_e < t < t_e + T_L$;

Validation of the model

This sequence was applied for $a_0 = 10$ with $n_0 = 5$ and $n_0 = 15$. The results are shown in figures 3.14 a) and b) respectively, where the solid line shows the peak position and the dashed line shows the electron position as a function of time, superimposed to the magnetic field map. The electron is only ejected in the low-density case, in agreement with figure 3.7.

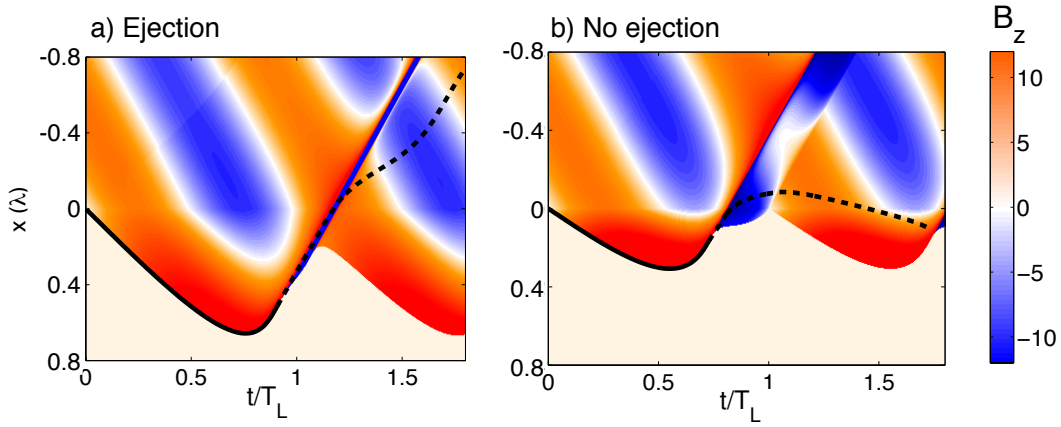


Figure 3.14: a) Time-space map of the magnetic field for $a_0 = 10$ and $n_0 = 5$ calculated from Gonoskov's model. The line shows the electron trajectory: It coincides with the peak trajectory (solid black line) until the emission time t_e. For $t > t_e$, the electron propagates away from the peak position (black dashed line), and escapes the plasma. b) shows the same representation for $n_0 = 15$. The electron is sent back to the plasma bulk.

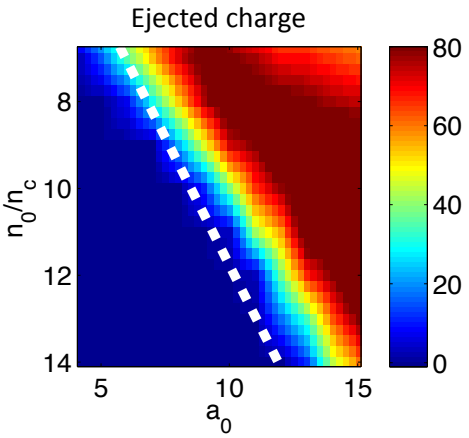


Figure 3.15: Ejected charge in pC/μm^{-2} as a function of a_0 and n_0 from a scan of 1D PIC simulations. The incident wave had a 3-laser-period duration with a step-like envelope, and electrons were detected 1λ away from the plasma surface. The white dashed line shows the threshold $n_0 = f(a_0) = 0.8a_0$ (*i.e.* $S = 0.8$) above which no electron can escape, according to the model. It agrees fairly well with the PIC scan results.

We finally ran our model for different values of S, and observed that there is no ejected electrons for $S > S_{th}$ where S_{th} is the threshold value. We measured this value as $S_{th} = 0.8$. These predictions were confronted to a set of 1D PIC simulations, with $4 < a_0 < 15$ and $7 < n_0 < 14$. The ejected charge from PIC simulation is shown in figure 3.15. As expected, the ejected charge depends on $S = n_0/a_0$ instead of a_0 and n_0 independently. As we could conjecture from figure 3.7, the ejected charge drops to

zero when S increases because of the gyromagnetic effect. S_{th} was measured in this set of simulations, and reads $S_{th} = 0.85$, which is very close to the value given by our model. The white dashed line in figure 3.15 stands for the threshold $S_{th} = 0.8$ given by our model, showing very good agreement with PIC results.

3.2.5 Discussion

Physical picture: For a given value of a_0, the ejected charge drops to zero when increasing n_0 above a threshold. We hereafter propose two physical explanations for this behavior.

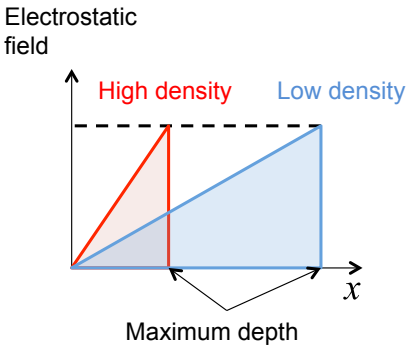


Figure 3.16: Illustration of the electrostatic potential formation for a low-density and a high-density step-like plasma. In both cases, the maximum electrostatic field reaches the same value that screens the incident field. In the low-density case, the electron density peak is pushed further, so the electrostatic potential is higher and the plasma provides more energy to the electrons in the peak.

The first one relies on the energy provided to the electron by the plasma field E_p in the ion capacitor (see 3.8). As can be seen from equation 3.27, the maximum depth varies as $x_M \propto 1/n_0$. The electrostatic field and potential read

$$\frac{E_p(x_M)}{a_0} = \frac{2\cos^2\theta}{1-\sin\theta} \tag{3.42}$$

$$\frac{\phi_p(x_M)}{a_0} = \frac{2a_0\cos^5\theta}{n_0(1-\sin\theta)^2}. \tag{3.43}$$

The maximum electrostatic field, at $x = x_M$ does not depend on the plasma density, while the potential $\phi_p(x_M) \propto 1/n_0$. As a consequence, the plasma capacitor provides more energy to the electrons for a low plasma density, and helps electron ejection. This is illustrated in figure 3.16.

The second explanation is more phenomenological. The temporal profile of the reflected pulse depends on the plasma density, as shown in image 3.17. When the density is high, the magnetic field is strongly negative at the rear of the pulse. This field bends the trajectories of ejected electrons travelling in this zone and brings them back to the plasma. There is no such zone in the low-density cases, which also favors electron ejection.

Gyromagnetic effect: In the limit $n_0 \to +\infty$, $\phi_p(x_M) \to 0$ and the plasma fields have negligible effect. As a consequence, the gyromagnetic effect is dominant and prevents electron ejection. Note that electron ejection in this section is made possible because of the presence of strong plasma fields when the density is sufficiently low, breaking the picture of the gyromagnetic effect given in section 3.1.4.

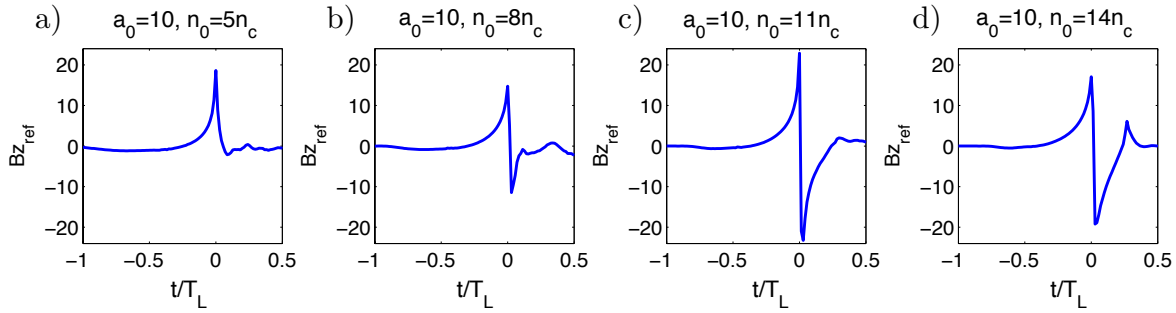


Figure 3.17: a) Magnetic field in the reflected wave as a function of time during a single laser period, in a low-density case. Other panels show the same data for increasing plasma density. A large area with negative magnetic field that efficiently brings ejected electrons back to the plasma appears for higher initial densities.

Conclusion: As a conclusion, during the wave reflection, the electrons are gathered in a sharp density peak that oscillates in the plasma. The Relativistic Electronic Spring model describes the peak dynamics as a function of the single parameter $S = n_0/a_0$. During each laser period, when the density peak is accelerated towards vacuum, a small fraction escapes and can propagate far away from the plasma.

Above a certain threshold $S > S_{th}$, no electrons are ejected from the plasma. We presented a model that reproduces this trend, and found a value $S_{th} = 0.8$, close to that extracted from PIC simulations $S_{th} = 0.85$. This behavior has two causes: the energy that electrons can acquire from the plasma, and the temporal shape of the reflected field.

However, this model relies on one hypothesis, $p_x(t_e) = \phi_e/2$, which is verified in PIC simulations but is not justified physically, and is a phenomenological observation, which is not satisfying. The next section is dedicated to the plasma mirror regime with a density gradient.

3.3 Electron ejection with an exponential density gradient

As described in section 1.1, most experiments consist in the reflection of a laser pulse on a highly overdense plasma with a density gradient on its front side. This section is dedicated to this plasma profile, shown in figure 3.18. The bulk density is typically in the range $n_0 = 100 - 300n_c$, and the exponential density gradient scale length is $L = 0.01 - 1\lambda$. This study involves the same mechanisms as for a step-like density profile presented in previous section 3.2.

The model presented in the case of a step-like profile and based on Gonoskov's model reproduces the whole surface dynamics. As a consequence, we initially intended to extend it to the case of a density gradient. Yet, it relies on a strong unproved hypothesis which, furthermore, is no longer valid in presence of a density gradient. Strong efforts were done to extend this model nonetheless, which still remains unsuccessful.

As a consequence, we used a different approach which led us to a simpler, trimmed model which, though showing less precision on the description of the surface dynamics, still yields a correct picture of the electron trajectories. This model is presented in the following section.

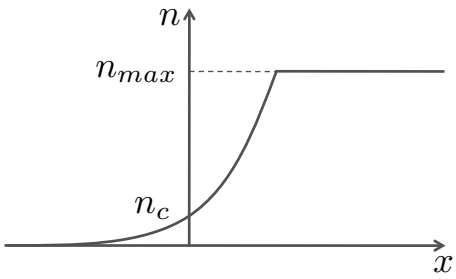


Figure 3.18: Exponential density gradient $n = n_c \exp(x/L)$ in the gradient, and $n = n_{max}$ in the plasma bulk. Typically $L = \lambda/10$ and $n_{max} = 200 n_c$.

3.3.1 Surface dynamics

Short gradient *vs.* long gradient

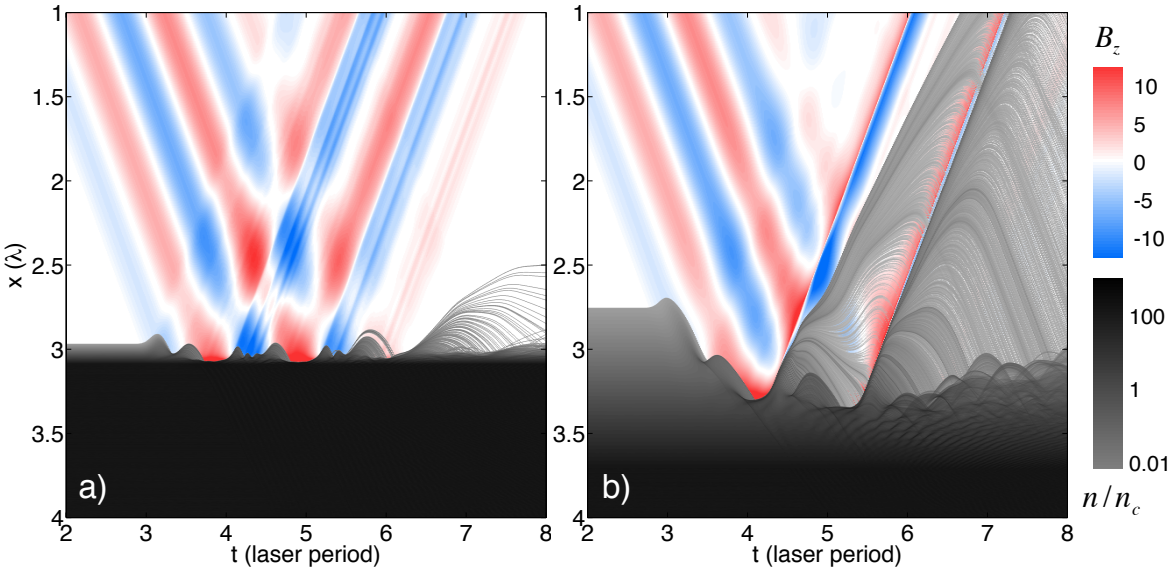


Figure 3.19: a) Electron density $\log_{10}(n_e/n_c)$ as a function of time and space from the 1D PIC simulation `these_grad1s64`. The magnetic field is shown in red-blue colors. The conditions of the simulation are: $a_0 = 5$, $\tau = 4T_L$, sine-square temporal envelope ($2T_L$ FWHM), $L = \lambda/64$, $n_{max} = 200 n_c$ (lab frame). The ions are immobile. Numerical conditions are 500 ppc and $\Delta x = \lambda'/2000$. The critical density is located at $x = 3\lambda$; b) is the same for $L = \lambda/8$, in simulation `these_grad1s8`.

Figure 3.19 a) shows a time-space map of the electron density and magnetic field from a 1D PIC simulation in the boosted frame for a two-laser-period FWHM incident wave with $a_0 = 5$ and $\theta = 45°$ on an overdense plasma with $n_{max} = 100 n_c$ and a density gradient of scale length $L = \lambda/64$ on its front side. During each laser period, the plasma surface shows many fast oscillations, and finally no electron escapes the plasma. This is a consequence of the gyromagnetic effect (see section 3.1.4).

Figure 3.19b) shows the result of a similar simulation for $L = \lambda/8$. The surface oscillates once per laser period, and two strong jets of ejected electrons can be seen escaping the plasma and propagating in vacuum. This section aims at explaining this difference, and describes quantitatively the role of the density gradient length.

Train of attosecond electron bunches

The simulations shown in figure 3.19 shows the reflection of a few-cycle laser pulse ($\tau_L = 5.2\,\mathrm{fs}$ FWHM), with only two electron jets ejected in the long-gradient case. For a longer pulse duration ($\tau_L = 25\,\mathrm{fs}$ FWHM), an electron bunch is ejected during each laser period, resulting in a train of attosecond bunches. This is shown in figure 3.20, where the reflected field and the density of ejected electrons are plotted along time at the plasma edge (at a distance $d_{probe} = 0.03\lambda$ from the critical density). The simulation conditions are the same as in the few-cycle case. Each electron bunch is emitted at a node of the reflected field, when $B_{zr} = 0$ and $E_{yr} = 0$. Note that the reflected magnetic field is extremely distorted, and the sharp peaks indicate a rich harmonic content, as expected from high harmonic generation by the ROM mechanism (see section 1.4.3 and reference [Thaury & Quéré, 2010]). Besides, the charge contained in each attosecond electron bunch can vary strongly between two consecutive periods, showing that the ejection during one period may affect subsequent periods.

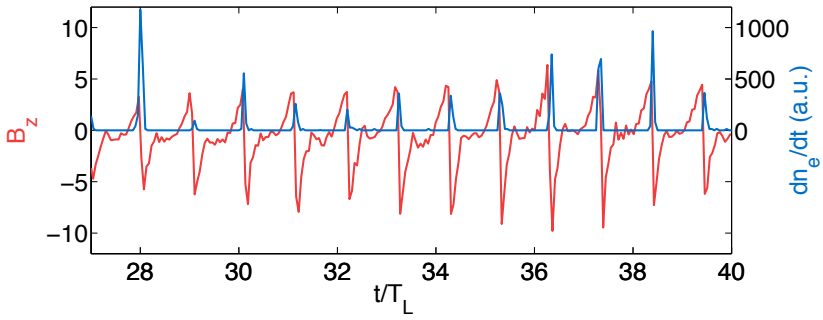


Figure 3.20: 1D PIC simulation result for $a_0 = 5$ and $L = \lambda/8$. Red line: reflected magnetic field at the initial plasma edge as a function of time (a Fourier filter was applied to remove the incident field). Blue line: density of ejected electrons as a function of time at the same position.

Push-pull mechanism and maximum peak depth x_M

We hereafter follow the same steps as in previous section 3.2 and focus on the mechanism that takes place during a single laser period. To this purpose, we performed a 1D PIC simulation with a top-hat temporal shape for the incident wave. The incident driving fields read

$$\boldsymbol{E_i} = a_0 \sin(t - x)\boldsymbol{e_y} \qquad \boldsymbol{B_i} = a_0 \sin(t - x)\boldsymbol{e_z}$$

and the initial electron/ion speed is $\boldsymbol{\beta} = -\sin\theta \boldsymbol{e_y}$. The same push-pull mechanism occurs as in the case of a step-like density profile:

(i) Push phase: During the first half-period, the incident laser field pushes electrons inside the plasma while the ions are not displaced, which builds up an electrostatic plasma field $\boldsymbol{E_p}$ along x and a magnetostatic plasma field $\boldsymbol{B_p}$ along z.

At $t = t_M$, the peak reaches a maximum position with $p_x = 0$. We hereafter derive the maximum peak position from this balance as is done in previous section (see also [Gonoskov *et al.*, 2011; Vincenti *et al.*, 2014]). Assuming all electrons are located at $x > x_M$, Gauss's and Ampère's laws give the electrostatic and magnetostatic fields

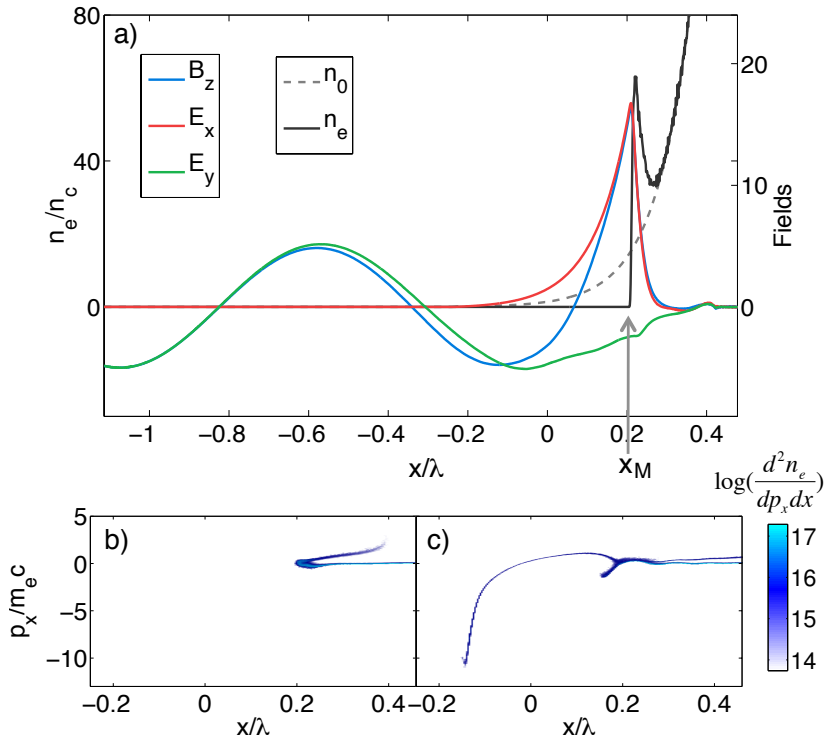


Figure 3.21: a) Density and fields at maximal depth ($t = t_M = 2.3T_L$) from a 1D PIC simulation with $a_0 = 5$ and $L = \lambda/8$. The black and dashed grey line stand for the electron and ion densities respectively. Color lines are magnetic field B_z (blue), electrostatic field E_x (red) and electric field E_y (green). b) & c) Phase space (x,p_x) at $t = t_M$ and $t = t_M + 0.4T_L$ respectively.

at position x:

$$E_p(x) = \frac{1}{\cos^3\theta} L e^{x/L} \tag{3.44}$$

$$B_p(x) = \frac{\sin\theta}{\cos^3\theta} L e^{x/L}. \tag{3.45}$$

The equilibrium equation 3.26 becomes, in the case of a density gradient,

$$2a_0 + \frac{\sin\theta}{\cos^3\theta} L e^{x_M/L} - \frac{1}{\cos^3\theta} L e^{x_M/L} = 0. \tag{3.46}$$

Solving for x_M, we obtain

$$x_M = L \log\left[\frac{2a_0\cos^3\theta}{L(1-\sin\theta)}\right]. \tag{3.47}$$

This equation gives an estimate for the surface position at maximum depth that fits within less than 20% error in the worst case in the whole parameter range ($0.5 < a_0 < 10$, $0.01\lambda < L < \lambda$) when compared with PIC simulations.

As a summary, the maximum peak position x_M and the ion density, the electrostatic field and the electrostatic potential at the maximum peak position read respectively

$$x_M = L \log\left(\frac{2a_0\cos^3\theta}{L(1-\sin\theta)}\right) \qquad n_i(x_M) = \frac{2a_0}{L(1-\sin\theta)} \tag{3.48}$$

$$E_p(x_M) = \frac{2a_0}{1-\sin\theta} \qquad \phi_p(x_M) = \frac{2a_0 L}{1-\sin\theta} \tag{3.49}$$

Note that $E_p(x_M)$ has exactly the same expression as in the case of a step-like density profile.

(ii) Pull phase: During the following half-period, the $v_y B_i$ force pulls electrons towards vacuum, breaking the force balance along x. The electron peak is accelerated towards vacuum ($x < 0$), and radiates an attosecond electromagnetic bunch via the Relativistic Oscillating Mirror mechanism. A small fraction ($< 1\%$) of electrons in the density peak escapes the plasma and travels along the reflected pulse. This is shown in figure 3.21b) and c), where the phase space is represented at $t = t_M$ and $t > t_M$ respectively. For $t > t_M$, one can see a jet of electrons travelling towards vacuum with $x < 0$ and $p_x < 0$.

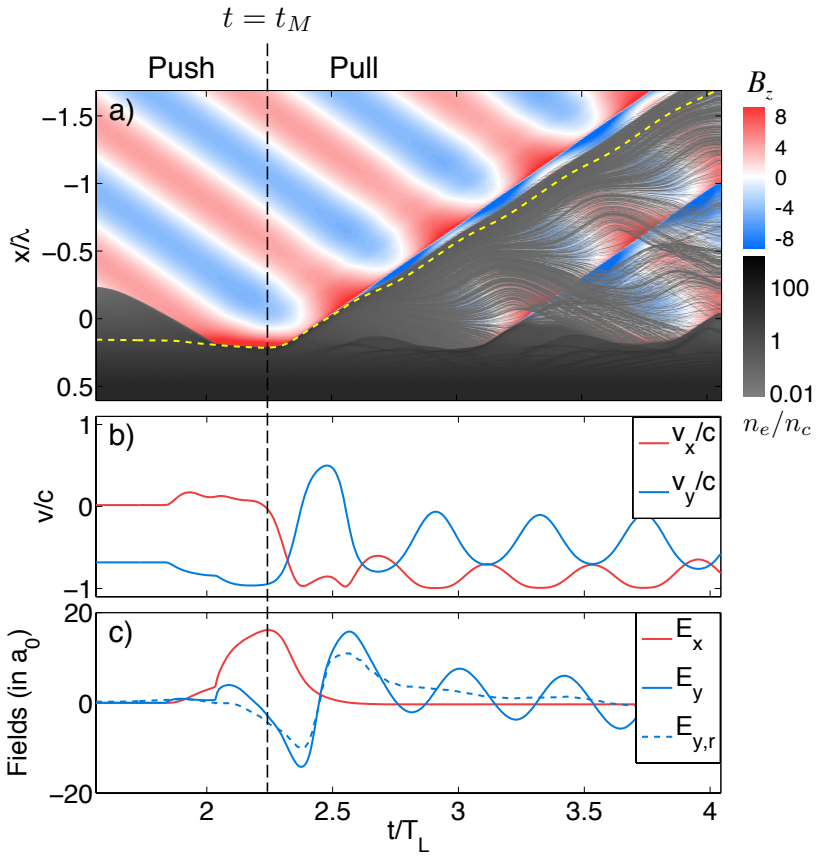


Figure 3.22: Dynamics of an ejected electron for parameters $a_0 = 5$, $L = \lambda/8$ a) Greyscale: electron density $n_e(x,t)$. Color scale: magnetic field $B_z(x,t)$. The yellow dashed line represents the trajectory of an ejected electron. b) Velocity components of the ejected electron. c) Electric fields experienced by the ejected electron along its trajectory.

Dynamics of an ejected electron

The orbit of such an electron is shown in figure 3.22. Panel a) shows the magnetic field B_z (color scale) and the electron density n_e (grey scale) versus time and space. The electron trajectory is plotted as a dashed yellow line in figure 3.22 a). It originates from deep inside the plasma around $x = x_M$, and is released in the plasma capacitor at $t = t_M$.

The electron starts with speed $(\beta_x, \beta_y) = (0, -\sin\theta)$ (see figure 3.22b)) because of the plasma drift, and is accelerated in the $-y$ direction until $t = t_M$ where $(\beta_x, \beta_y) \simeq$

$(0, -1)$.

At $t = t_M$, represented by the vertical black dashed line in figure 3.22, the electron is part of the density peak, and is released in the ion plasma capacitor. This can be seen in figure 3.22c), where the red line stands for the plasma electric field E_x at the electron position along time. E_x increases for $t < t_M$ while the charge separation is built, and reaches a maximum value at $t = t_M$. For $t > t_M$, the electron propagates towards $-x$, converting the electrostatic potential of the ion capacitor into kinetic energy. At time $t \simeq 2.6T_L$, the electron leaves the plasma and $E_x \sim 0$.

After leaving the plasma, the electron propagates in vacuum where the incident wave ($\boldsymbol{k}_i /\!\!/ \boldsymbol{e_x}$) and the reflected wave ($\boldsymbol{k}_r /\!\!/ -\boldsymbol{e_x}$) are superimposed. Its speed is close to $(\beta_x, \beta_y) \sim (-1, 0)$, so its motion is the superposition of fast oscillations around $\omega_{elec} \simeq 2\omega_0$ due to the incident field with slower variations $\omega_{elec} \ll \omega_0$ in the reflected field. This is shown in figure 3.22c), where the blue dashed line shows the reflected electric field along the electron trajectory. It varies very smoothly, indicating that the electron slowly dephases with respect to the reflected field.

Note that figure 3.22 shows the general case of an electron in the density peak. It is quite clear that after $t = t_M$ (see $t = 3.5T_L$), there are electrons before the test-electron shown in yellow: the plasma in the $x > x_{elec}(t)$ area is non-neutral and exerts a recall force on the test electron.

Plasma fields *vs.* electromagnetic fields

Finally, the acceleration after $t = t_M$ occurs as follows: first, the plasma capacitor discharges, and its potential energy is transferred to electrons in the density peak as kinetic energy, giving the electron a relativistic speed $\beta_x \simeq -1$ towards vacuum. Afterwards, the electron propagates and oscillates in the incident + reflected fields. To confirm that this scenario is valid for all ejected electrons, we compute the work of the electric fields along the trajectories of ejected electrons. The total electric field reads $\boldsymbol{E} = E_p \boldsymbol{e_x} + (E_i + E_r)\boldsymbol{e_y}$ where E_p, E_i and E_r stand for the plasma, incident and reflected electric fields respectively. The work in x and y yields

$$\Gamma_x = -\int_0^t E_p \beta_x dt \tag{3.50}$$

$$\Gamma_y = -\int_0^t (E_i + E_r)\beta_y dt \tag{3.51}$$

where $\Gamma_{x,y}$ are normalized by $\Gamma_{x,y} \equiv \Gamma_{x,y}/m_e c^2$. Γ_x is the energy gain due to the plasma fields while Γ_y is due to electromagnetic fields. These works are shown for a large number of ejected electrons in figure 3.23 from a PIC simulation with $a_0 = 10$ and gradient length $L = \lambda/8$. At the plasma edge (a), the work is along x, so electrons are accelerated by the plasma electrostatic field. Further away from the plasma (b), the dominant work is along y, due to laser fields. At a distance of 2λ away from the plasma edge (c), the mean plasma work Γ_x decreases. This is because electrons are slowed down by the non-neutral plasma restoring force. This effect is probably enhanced in 1D PIC simulations.

3.3.2 Scan $a_0 - L$ with 1D PIC simulations

The main parameters affecting the emission of backward electrons are (i) the laser amplitude a_0, (ii) the plasma density gradient length L, (iii) the angle of incidence θ

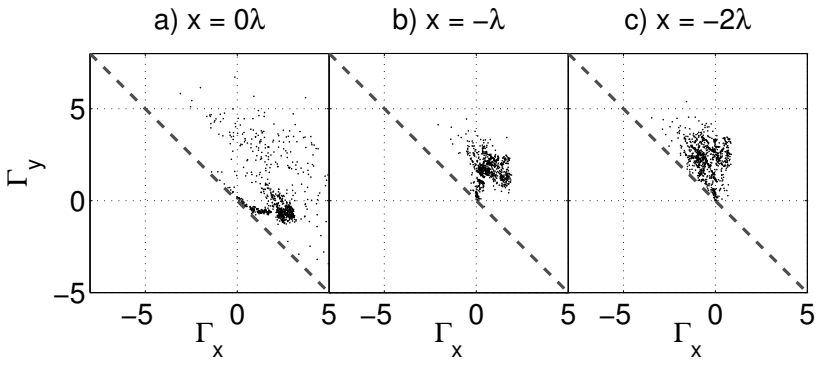


Figure 3.23: Electric force work from a 1D PIC simulation with $a_0 = 10$ and $L = \lambda/8$. The work is calculated when electrons reach $x = 0$, $x = -\lambda$ and $x = -2\lambda$ respectively. Γ_x is due to plasma fields while the Γ_y is due to the transverse laser field.

and (iv) the pulse duration. In this study, we restrict ourselves to the case of femtosecond pulse durations, typically $20 - 30$ fs, as used in current high-intensity experiments. In order to study the role of the main parameters a_0 and L, we performed a set of one hundred 1D Particle-In-Cell (PIC) simulations, each requiring little computer resources. The scan name is `PARAM_harmv9`, and simulations in this scan are named `harmv9_a*_L1s*`, for example `harmv9_a80_L1s32` uses $a_0 = 8$ and $L = \lambda/32$.

In the laboratory frame, a 800 nm, 25 fs laser pulse impinges on a solid-density plasma with angle of incidence $\theta = 45°$. Its amplitude is varied from $a_0 = 0.2$ to $a_0 = 10$. The plasma bulk density is $250n_c$, corresponding to an ionized SiO_2 target, and the gradient length is varied from $\lambda/100$ to λ. We assume that the density gradient has an exponential shape $n_0(x) = n_c e^{x/L}$, so that $n_0(x = 0) = n_c$. The density gradient is artificially cut at the plasma boundary x_b defined as $n_0(x_b) = 0.2n_c$, to avoid filling the whole box with particles. This cutoff verifies $n_0(x_b) < \cos^2\theta n_c$, where $\cos^2\theta n_c$ is the density at which the obliquely incident laser is reflected in the low-intensity regime (see section 1.3.1 on page 22). The simulations were performed in the boosted frame, hence numerical conditions are given in this frame: the numerical space-step was $\delta x = \lambda/4000$, and we used 1000 particles-per-cell for good statistics. The simulation box was $\Delta x = 20\lambda$ large. Ions were mobile (we took oxygen ions as the lightest ions in a Silica target) but simulations with immobile ions yielded very similar results.

When simulating the ejection of electrons with 1D simulations, two effects must be considered. First, the laser does not diffract, so that the laser intensity is greatly overestimated as soon as the propagation distance is larger than a Rayleigh length. Second, charged particles are represented by charged surfaces. Therefore, the electrostatic force between two charged particles does not depend on the distance r between them, while it decreases in $1/r^2$ in a 3D geometry. As electrons leave the target, the plasma surface becomes positively charged and exerts a restoring force that does not depend on the electron position. If one runs a 1D simulation long enough, all electrons eventually return to the plasma and the ejected charge tends towards zero. In order to obtain realistic results, we chose to consider electrons to be ejected if they cross a plane located at a distance $d = 7\lambda$ from the plasma edge. This distance was chosen to be (i) much smaller than the Rayleigh length of most current experiments, so that the 1D approximation remains valid, and (ii) much larger than the gradient lengths we studied, for electrons to be detected far from the plasma surface. This point is crucial as detecting electrons too close to the plasma surface considerably overestimates the ejected charge, while detecting them too far leads to wrong results due to the invalidity

of the 1D approximation.

Optimal gradient scale length L

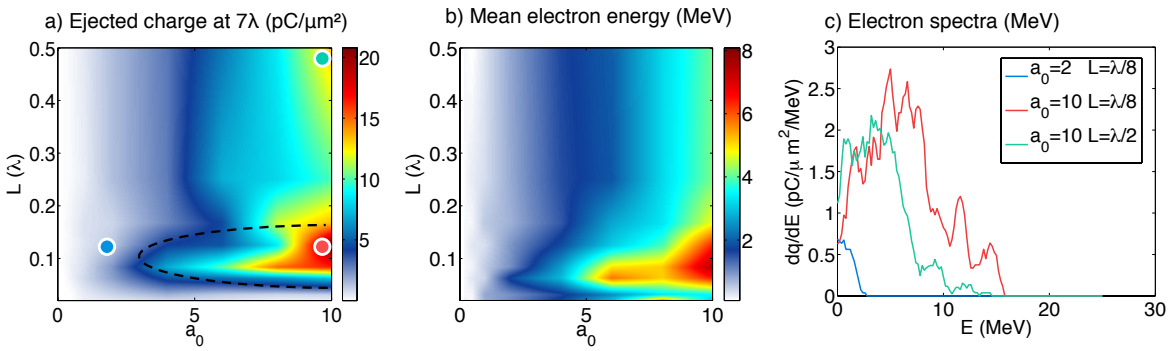


Figure 3.24: Results of a 1D PIC simulation scan (a_0,L) with $n_{max} = 250n_c$ – a) Ejected charge. Particles were detected at a distance $d = 7\lambda$ from the target, and the charge was integrated all along the simulation. – b) Mean energy of the ejected electrons – c) Electron spectra from 3 simulations with parameters indicated by the color circles in panel a).

Figure 3.24 a) shows the ejected charge as a function of a_0 and L. First, it is clear from figure 3.24 that there are no ejected electrons when the gradient scale length is $L = 0\lambda$. This was explained by the gyromagnetic effect (see section 3.1.4). This effect is neutralized with longer gradients. For a given value of a_0, the ejected charge increases with L, reaches a maximum for $L = L_{max} \simeq \lambda/10$, and then slowly decreases. We find that the value of the optimum gradient L_{max} depends little on a_0 in this range. The increase in ejected charge with L for $L < L_{max}$ is due to the increase in the maximum electrostatic potential $\phi_p(x_M) \propto a_0 L$ in the ion capacitor, as described in section 3.2 Evidently, the results also show that the ejected charge increases with the laser amplitude a_0.

In figure 3.24b), the mean energy of ejected electrons is plotted in the same parameter space. It varies in a similar fashion as the ejected charge: the higher the ejected charge, the more energetic the electrons. The electron spectrum is plotted on panel c), for three different simulations represented by the color circles in figure 3.24 a). The red and green curve stand for $a_0 = 10$ and a gradient length respectively $L \simeq L_{max}$ and $L \gg L_{max}$. The electron spectra are quite broad and electron energies are in the few-MeV to 10 MeV range.

Ejected charge drop for very long gradient

The PIC scan shows that the ejected charge drops significantly for very long gradients. When the hypothesis $kL < 1$ ($L < \lambda/2\pi$) is broken, in particular when $kL \gg 1$, this ejection scenario is not valid anymore. Indeed, the formation of a large density peak does not occur for larger gradients, as shown in figures 3.25 a) and b), where the electron density profile is plotted at $t = t_M$ for a short and a long gradient respectively. It is readily seen that for the long gradient case, the density in the peak is ten times lower and the width of the peak is also much larger. Consequently, the plasma capacitor does not form and electrons cannot be accelerated efficiently by the plasma field. The limit $kL = 1$ reads $L = \lambda/2\pi$ in units of laser wavelengths, which is comparable to $L_{max} = \lambda/10$.

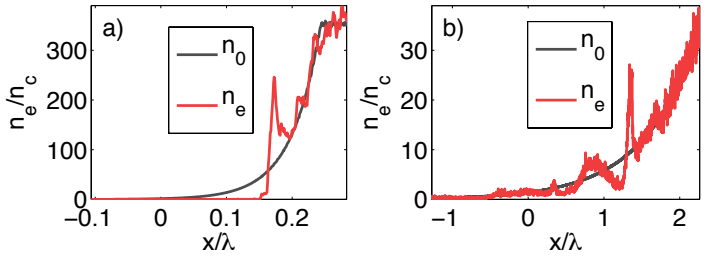


Figure 3.25: a) Electron density at $t = 0$ (black) and $t = t_M$ for $a_0 = 8$ and $L = \lambda/16$. b) Same as a) for $L = \lambda$.

3.3.3 Toy model for the electron ejection

In the previous discussion, we found that the energy gain in the plasma capacitor scaled as $\propto a_0 L$, explaining qualitatively why the ejected charge increases with L and a_0, in the limit of small gradients. However, a more quantitative model would be useful to estimate the ejected charge and typical ejected energy. Several models have been developed for high harmonic generation [Baeva *et al.*, 2006; Lichters *et al.*, 1996], surface motion [Debayle *et al.*, 2015; Gonoskov *et al.*, 2011; Sanz *et al.*, 2012] or electron jets inside the plasma [Ruhl, 1996]. However, reference [Baeva *et al.*, 2006] does not describe electron dynamics and reference [Lichters *et al.*, 1996] assumes that all electrons are gathered on an oscillating surface which cannot escape the plasma border. The model developed in reference [Debayle *et al.*, 2015] assumes a high density step $n_e \gg n_c$, which is not compatible with a density gradient. Hence, none of them is suitable for describing backward electron acceleration under oblique incidence with a density gradient.

The model developed by Gonoskov in reference [Gonoskov *et al.*, 2011] describes very well the peak dynamics at very large intensity ($a_0 \gg 1$) under oblique incidence and for a step-like density profile. However, the density peak is assumed to always travel at the speed of light $|\boldsymbol{\beta}| = 1$, *i.e.* infinite energy, so the model cannot be used to solve the equations of motion. We tried to follow the same procedure as we did in the case of a step-like density profile, but it was not conclusive.

We now propose a simple numerical model to illustrate the ejection process during one optical cycle. The incident laser wave is approximated by a monochromatic plane wave with $a_0 > 1$. Ions are immobile. We assume $kL \ll 1$ so that electrons are gathered in a density peak of width $d \ll L$. In the boosted frame, the ion density profile reads $n_i(x) = n_0(x) = n_c e^{x/L}/\cos\theta$. We consider an electron in the density peak, and describe its motion starting from $t = t_M$:

- first, the equations of motion for an electron in the density peak are derived;
- second, we find the appropriate initial conditions;
- third, this set of equations is solved numerically and compared with results of PIC simulations.

Electrons are driven by (i) electromagnetic fields and (ii) plasma fields. We describe the motion of electrons in the density peak during the pull phase, during which the reflected field is generated. The incident laser electric field is written $\boldsymbol{E_i} = +a_0 \sin(t - x + \phi_{M,i})\boldsymbol{e_y}$, where the phase $\phi_{M,i} = x_M - t_M + \pi$ is chosen so that the laser field changes sign at (t_M, x_M). For the reflected field, we neglect the harmonic content of the field and simply write $\boldsymbol{E_r} = a_0 \sin(t + x + \phi_{M,r})\boldsymbol{e_y}$ with $\phi_{M,r} = -x_M - t_M$.

Concerning the plasma field, it is crucial to include electron screening in the density peak in order to model the ejected charge. Indeed, when an electron j is located on the front edge of the peak ($x_j = x_M$), it experiences the full plasma field $\boldsymbol{E_p}$ (see figure 3.26). On the contrary, an electron located at $x_j > x_M$ experiences a screened plasma field $\boldsymbol{E_p} - \boldsymbol{E_s}$, where $\boldsymbol{E_s} = E_s \boldsymbol{e_x}$ stands for the electronic screening field, and is less likely to escape the plasma. As seen before, the plasma fields amplitude at the position of electron j, $x_j(t)$ can be obtained by integrating Maxwell-Gauss's equation, giving

$$E_p - E_s = \frac{1}{\cos^2\theta}\left(\int_{-\infty}^{x_j(t)} n_i(x)dx - \int_{-\infty}^{x_j(t)} n_e(x)dx\right). \tag{3.52}$$

The first term E_p is the unscreened plasma electric field already calculated in equation 3.44, while the second term is the screening electric field coming from electrons in the density peak.

Since the shape of the density peak cannot be calculated analytically, the second integral cannot be evaluated easily. Therefore, the screening field E_s is derived by assuming that there is no trajectory crossing, as in [Brunel, 1987]: if electrons j and k in the density peak verify $x_j(t_M) < x_k(t_M)$, then $x_j(t) < x_k(t)$ at any time $t \geq t_M$. With this assumption, the number of electrons on the left of electron j, *i.e.* at $x < x_j(t)$, is constant along time, see figure 3.26.

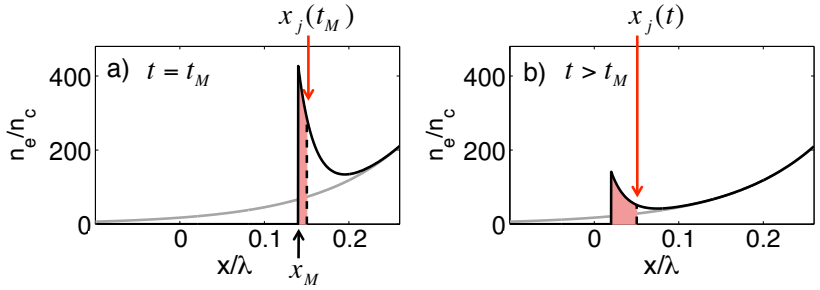


Figure 3.26: a) Sketch of the electron density at $t = t_M$. The black dotted line stands for x_{j0}, the position of electron j at $t = t_M$, the initial time for our model. The red area shows the initial charge on the left of electron j. b) Same as a) for $t > t_M$. In agreement with the hypothesis of no trajectory crossing, the charge on the left of electron j is conserved along time: the surface of the red area is the same for all $t \geq t_M$.

Hence, the integral of the electron contribution in the Maxwell-Gauss equation is conserved,

$$\begin{aligned} E_s &= \int_{-\infty}^{x_j(t)} \frac{n_e(x,t)}{\cos^2\theta} dx \\ &= \int_{-\infty}^{x_j(t_M)} \frac{n_e(x,t_M)}{\cos^2\theta} dx \\ &= \sigma_j \end{aligned} \tag{3.53}$$

where σ_j is the initial surface charge on the left of electron j. Therefore, the screening field E_s is simply determined by the surface charge σ_j, and there is no need to know the details of the shape of the density peak. This electronic surface charge screens the plasma field E_p and reduces the acceleration of electrons. Note that this screening field is constant in time and therefore has a considerable effect on the electron trajectories. As the electron peak moves along x and y, it radiates a magnetic field B_s through

Ampère's law, which is responsible for the reflected field. Neglecting the high harmonics, this radiation comes down to a monochromatic plane wave that we include in the equation of motion. Finally, taking these effects into account, the equation of motion for electron j reads

$$\begin{aligned}\frac{d\boldsymbol{p_j}}{dt} &= -a_0 \sin(t - x_j(t) + \phi_{M,i})\Big[\boldsymbol{e_y} + \boldsymbol{\beta}_j(t) \times \boldsymbol{e_z}\Big] \\ &\quad -a_0 \sin(t + x_j(t) + \phi_{M,r})\Big[\boldsymbol{e_y} - \boldsymbol{\beta}_j(t) \times \boldsymbol{e_z}\Big] \\ &\quad -\frac{L}{\cos^3\theta} e^{x_j(t)/L}\Big[\boldsymbol{e_x} + \sin\theta \boldsymbol{\beta}_j(t) \times \boldsymbol{e_z}\Big] \\ &\quad +\sigma_j \boldsymbol{e_x}. \end{aligned} \tag{3.54}$$

The first and second lines on the RHS express the incident and reflected waves, the third line is for the plasma capacitor fields and the last line is the screening field. The initial conditions are taken at $t_0 = t_M$, when electrons in the density peak are located at $x_M < x < x_M + \delta_s$. Since $\delta_s \ll L$, we assume that all electrons start at $x = x_M$ and use the expression of x_M given above.

The initial momentum of electrons is: $p_{x0} = 0$ because at t_M the peak position is maximum. The transverse momentum p_y is derived from the conservation of the canonical momentum $P_y = p_y - a_y = P_{y0}$. The density peak reaches its maximum depth when the incident field changes sign, *i.e.* $a(t_M, x_M) = a_0$. The initial conditions are the same for all electrons and read

$$\begin{cases} x_0 &= x_M \\ p_{x0} &= 0 \\ p_{y0} &= -\tan\theta - a_0 \end{cases}$$

Finally, the only difference between electrons j and k is the initial charge on the left side of the electron, *i.e.* the term σ_j in equation 3.54. These equations are solved numerically for different values of σ_j. The ejected charge can be determined by increasing σ_j until a threshold value σ_{max} above which the electron is not ejected; the ejected charge is then simply σ_{max}. An example is given in figure 3.27, where electron trajectories are plotted for $a_0 = 8$ and $L = \lambda/8$, from a PIC simulation (a) and using the model (b). There is no trajectory crossing in the PIC simulation before $t = 1.5T_L$, which validates our hypothesis. The global dynamics is very well reproduced.

The following ejection criterion was adopted in the model: an electron is considered to be ejected if p_x is negative during 3 periods. This criterion is different from the one we adopted for PIC simulations because we assumed that electrons do not cross, which is wrong for large timescales.

Figures 3.27c) and d) show the ejected charge plotted versus L and a_0 respectively. The model reproduces the global trends: the charge increases with a_0 and L. It overestimates the ejected charge because the ejection criterion is much more stringent for the PIC simulation than for the model. The linear scaling of ejected charge with a_0 is well reproduced. The scaling with the density gradient does not fit as well, which can be explained by the fact that as kL approaches 1, the plasma capacitor model collapses. Besides, for very large intensities, the ion motion becomes significant and may affect the interaction. Remarkably, our simple model also reproduces the trends and the order of magnitude of the mean energy of ejected electrons. This is shown in figure 3.27e) and f).

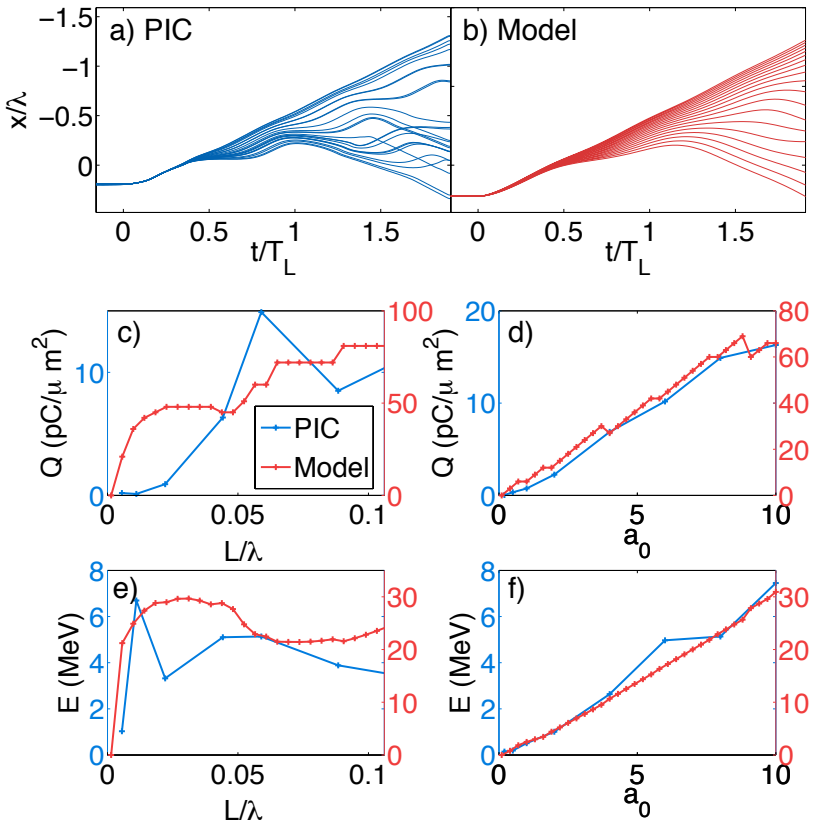


Figure 3.27: a) Electron trajectories from PIC simulation with $a_0 = 8$ $L = \lambda/8$. b) Electron trajectories from the model, with the same parameters. In both cases, $t = 0$ stands for t_M. c) Ejected charge versus L for $a_0 = 8$ from PIC simulations and our model. d) Ejected charge versus a_0 for $L = \lambda/12$ from PIC simulations and our model. e) Same comparisons between the PIC simulations and the model but for the average energy of the ejected electrons.

To illustrate the role of plasma effects, the model was run with no ion plasma fields (removing the third line in equation 3.54), in the same conditions as figure 3.27c). The ejected charge never exceeded 1 pC/μm^2, which clearly validates the plasma capacitor model for electron ejection. When we run the model with no reflected field, we find that the ejected charge increases linearly with the gradient scale length L instead of saturating at longer gradients. This shows that the reflected field also plays a role in the details of the ejection.

3.3.4 Comparison with 2D PIC simulations

We now show the results of 2D PIC simulations in order to confirm the validity of the 1D study in the laboratory frame. Simulations are named `injectorv4_L1s*`.

A 800 nm, laser pulse impinges on the solid-density plasma with a $\theta = 45°$ incidence angle. The pulse duration is 25 fs, its spot size is 3.4 μm FWHM and its amplitude is $a_0 = 3$. We performed simulations for the following gradient scale lengths: $L = \lambda/32, \lambda/8, \lambda/4, \lambda/2, \lambda$. Ejected electrons are detected with two electron probes. The first one is parallel to the plasma surface and located 25λ away from the plasma surface to record electrons emitted around the specular direction. The second one is perpendicular to the plasma surface and 25λ away from the reflection point, to record electrons ejected along the plasma surface.

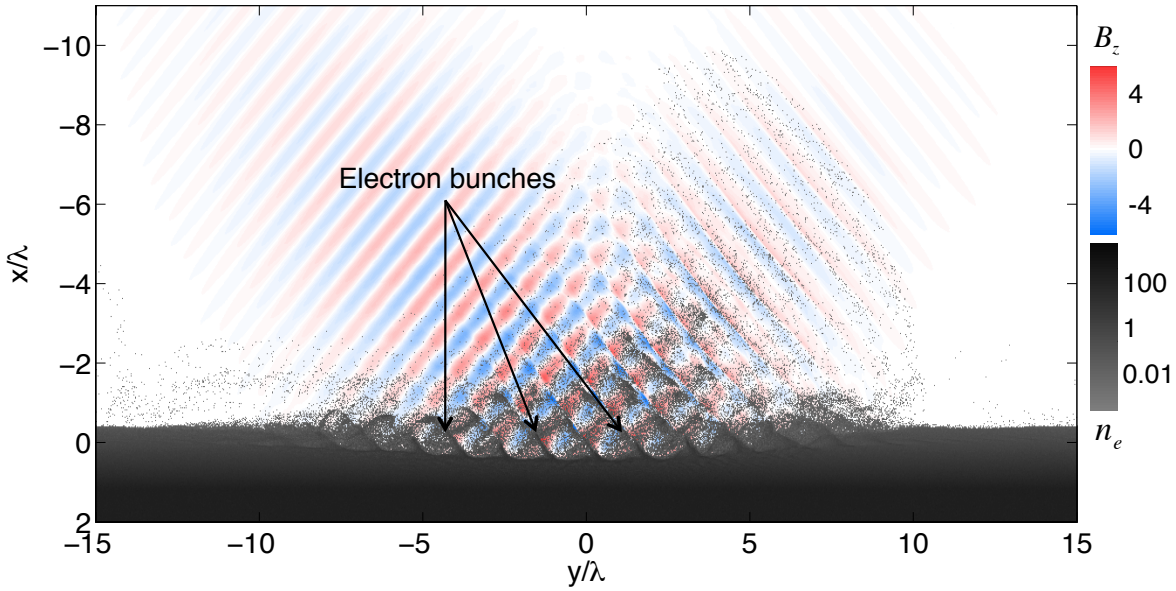


Figure 3.28: Snapshot of a 2D PIC simulation with $a_0 = 3$ and $L = \lambda/8$ during the pulse reflection. Electron jets propagate in vacuum.

Figure 3.28 shows a snapshot of a 2D PIC simulation. Jets of electrons are ejected at precise phases of the reflected laser field (at zeros of the electric field) and further propagate in the interference pattern and afterwards in the reflected field. The 2D simulations reproduce the main phenomena depicted in the 1D PIC simulations: at each laser period, electrons are pushed and form a sharp density peak. This gives rise to a plasma capacitor in which electrons gain energy and are ejected.

More qualitative results are shown in figure 3.29. The black line shows the total ejected charge (*i.e.* on both electron probes) as a function of the gradient length. As previously, the ejected charge increases with the gradient scale length until it reaches a maximum for $L \simeq \lambda/4$. This qualitatively confirms the observations from the 1D PIC

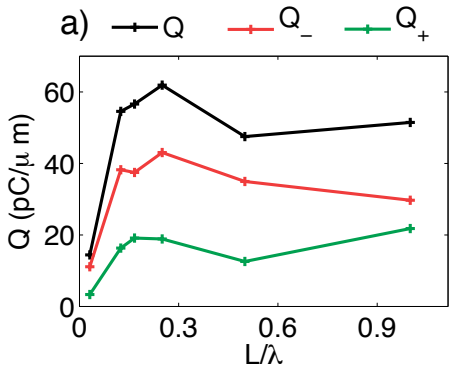


Figure 3.29: Results of 2D PIC simulations for $a_0 = 3$ and various gradient lengths. Ejected charge as a function of the gradient length. Electrons are sorted depending on their final emission angle: Q_+ is the charge for electrons with $\theta > 45°$, and Q_- is the charge for electrons with $\theta < 45°$, so that $Q = Q_- + Q_+$

simulations, although the optimal gradient length L_{max} is longer: $L_{max} \simeq \lambda/4$ instead of $L_{max} \simeq \lambda/10$ in 1D.

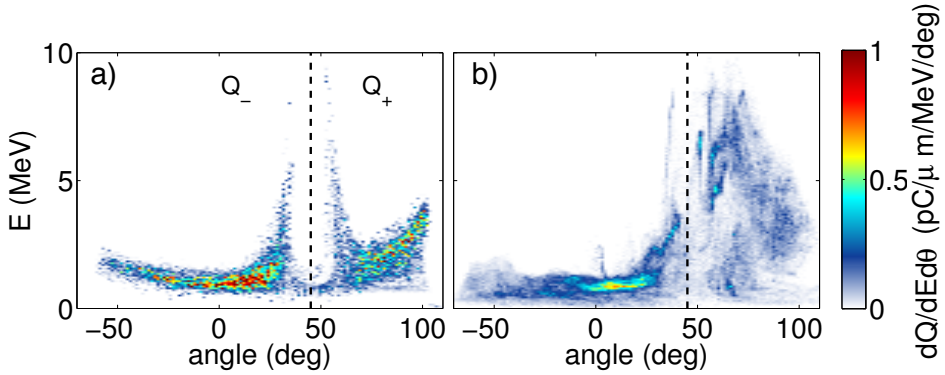


Figure 3.30: Final angle-energy distribution for a)$L = \lambda/8$ and b)$L = \lambda$. The vertical dashed black line shows the specular direction. Q_- and Q_+ are shown as the total charge on the left and on the right of the dashed line.

Previous experiments showed that for short gradients, electrons are emitted between the normal and specular direction, so that the electron beam is not symmetric around the specular direction. This asymmetry can be explained by the dynamics of electrons in the reflected field while they undergo vacuum laser acceleration, as explained in chapter 4.

To take into account this asymmetric emission, the ejected electrons are sorted as a function of their final emission angle. We define Q_-, the ejected charge of electrons with angles $< 45°$ (*i.e.* between the normal and specular direction) and Q_+ as the charge for electrons emitted with angles $> 45°$ (*i.e.* between the specular and grazing directions). This is shown in figure 3.29, where Q_- decreases for gradients above $L \simeq \lambda/4$, while Q_+ increases for long gradients. The behaviour of Q_- is consistent with the plasma capacitor scenario while the opposite behaviour of Q_+ indicates a different ejection mechanism which dominates for longer gradients. These two regimes give rise to significantly different angular distributions, as seen in figure 3.30 a) and b). Panel c) shows the angle-energy distribution in the case of a short gradient ($L = \lambda/8$) for which the majority of electrons are ejected with angle $\theta < 45°$. In this case, the ponderomotive force bores a hole close to the specular direction as it pushes electrons

away from the laser pulse, see chapter 4. Panel d) shows the case of a longer gradient ($L = \lambda$): more electrons are ejected along the target, indicating a different emission process.

Conclusion: This chapter presents a description of the backward electron ejection mechanism in the relativistic regime. Plasma fields are shown to play a major role. This periodic emission leads to a train of attosecond electron bunches injected in the reflected field.

In the case of a step-like density profile, the ejection mechanism is described as a push-pull mechanism occurring at each laser period, where electrons are gathered in a sharp density peak that oscillates around the plasma surface. A small fraction of the electrons contained in the peak escape the plasma along the reflected field. A numerical study was performed using 1D PIC simulations in the range $1 < a_0 < 20$ and $5 < n_0/n_c < 15$. The ejected charge depends on the $S = n_0/a_0$ parameter, and PIC simulations showed that no electrons are ejected above a threshold value $S_{th}^{[PIC]} \sim 0.85$. We developed a model, based on Gonoskov's relativistic electronic spring model, that reproduces this threshold $S_{th}^{[model]} = 0.8$. Above this threshold, plasma effects are not strong enough to counter the gyromagnetic effect, which inhibits electron ejection.

This analysis is extended to the case of a largely overdense plasma $n_{bulk} \sim 200 n_c$ with an exponential density gradient on its front side, which is the configuration of most experiments. The ejection process is similar to the case of a step-like density gradient. A scan of 1D PIC simulations is performed as a function of two major parameters, a_0 and the gradient length L, showing an optimal value for the gradient length $L_{max} \simeq \lambda/8$. The regime $L \ll \lambda$ shows no ejection of electrons because it is dominated by the gyromagnetic effect. On the opposite, $L \gg \lambda/2\pi$ shows a drop in ejected charge because the density peak description breaks.

Finally, ion fields due to charge-separation in the plasma are shown to play a dominant role for electron ejection. The electron density peak is pushed inside the plasma, creating an ion capacitor. The maximum depth x_M is derived for the step-like profile and the gradient profile assuming $L < \lambda/2\pi$, and the corresponding electrostatic potentials, normalized by the incident wave amplitude, read

$$\frac{\phi_{\text{step}}(x_M)}{a_0} = \frac{2\cos^5\theta}{S(1-\sin\theta)^2} \qquad \frac{\phi_{\text{gradient}}(x_M)}{a_0} = \frac{2L}{1-\sin\theta}. \tag{3.55}$$

The higher this potential, the more energy is transferred from the plasma to the electrons, and the higher the ejected charge. While ϕ_{step}/a_0 depends on a_0 and n_0 via the S parameter, $\phi_{\text{gradient}}/a_0$ is simply proportional to the gradient length, showing the importance of this parameter.

Chapter 4

Vacuum Laser Acceleration

Contents

4.1 Basics of vacuum laser acceleration 115

4.1.1 Particle acceleration 115

4.1.2 Lawson-Woodward theorem 117

4.2 Electron in a laser pulse: typical behaviors 120

4.2.1 Introduction 120

4.2.2 *Ponderomotive* behaviour 121

4.2.3 *VLA* behaviour 123

4.2.4 *VLA/ponderomotive* ratio 128

4.3 Vacuum laser acceleration using a plasma mirror injector 131

4.3.1 Experimental attempts for vacuum laser acceleration 131

4.3.2 Principle 133

4.3.3 Experiment by Adrien Leblanc (UHI100 at CEA) 134

4.3.4 Model 136

4.3.5 Interpretation of the experimental results 139

Introduction

As shown in chapter 3, the reflection of an ultraintense laser pulse off a plasma mirror leads to injection of attosecond electron bunches in the reflected field. In this chapter, we demonstrate that these electron bunches can afterwards be accelerated in the reflected field via vacuum laser acceleration (VLA), as illustrated in figure 4.1.

Over the past decades, direct acceleration of electrons by light *in vacuum* has attracted considerable interest and has been extensively studied theoretically, see references [Dodin & Fisch, 2003; Esarey *et al.*, 1995; Hartemann *et al.*, 1995; Maltsev & Ditmire, 2003; Pang *et al.*, 2002; Salamin & Keitel, 2002; Stupakov & Zolotorev, 2001; Varin & Piché, 2006; Yu *et al.*, 2000]. The underlying idea is to inject free electrons into an ultraintense laser field so that they always remain within a given half optical cycle of the field, where they constantly gain energy until they leave the focal volume. During this process, the Lorentz factor γ_0 can be increased by $4a_0^2\gamma_0$ for electrons with relativistic initial energy in a monochromatic plane wave.

Yet very few experiments were performed in this regime because VLA occurs efficiently only for electrons injected in the laser field with specific initial conditions that are extremely challenging to fulfill experimentally (see [Dodin & Fisch, 2003]). Indeed, in order to stay in phase with the laser field, electrons need to have initial velocities close to c along the laser propagation axis. In addition, they should start interacting with the intense laser beam already close to its spatial and temporal maxima, and even be injected at appropriate phases of this field. Electrons that do not satisfy these stringent requirements tend to explore many different optical cycles and undergo ponderomotive scattering, resulting in a low energy gain (see section 2.2.4).

In this chapter, we show how plasma mirrors can be used as electron injectors in the reflected laser field, providing a simple experimental solution to study the interaction of free electrons with intense lasers in vacuum. This chapter is organized as follows: section 4.1 describes the basic mechanisms for vacuum laser acceleration. The fundamental Lawson-Woodward theorem is demonstrated, and its limits are pointed out. Section 4.2 describes the two typical dynamics for an electron travelling in a laser pulse: *ponderomotive* when electrons oscillate many times before leaving the laser pulse, and *VLA* when electrons undergo sub-cycle acceleration before escaping the pulse in the polarization plane. Finally, the use of plasma mirror injectors for vacuum laser acceleration is presented in section 4.3. We present experimental results backed with a model, showing that the use of a plasma mirror allows for a considerable amount of electrons to undergo vacuum laser acceleration.

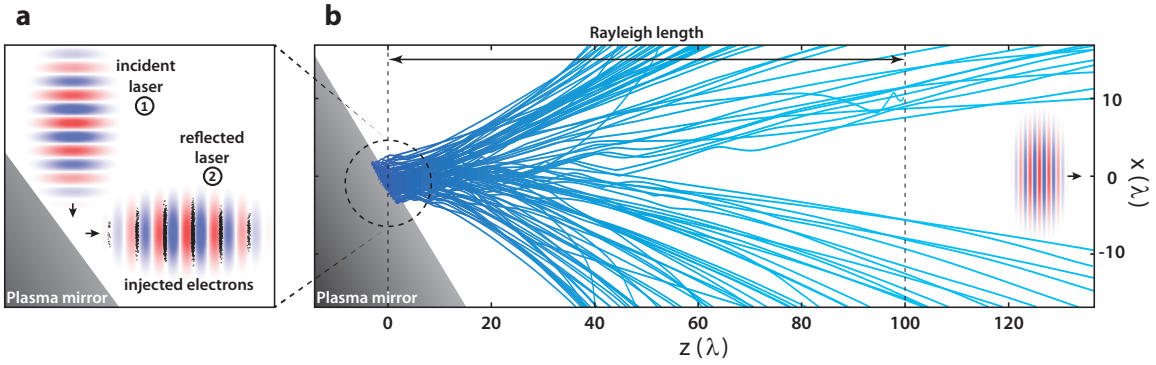
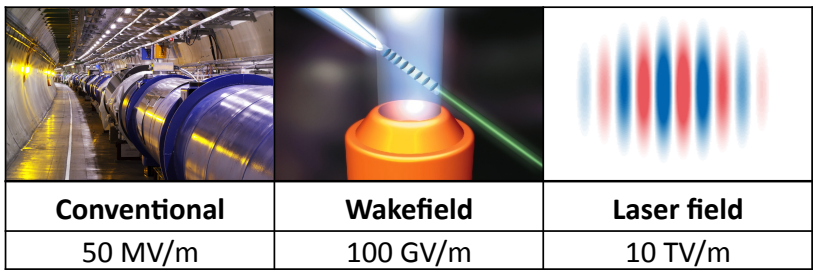


Figure 4.1: Injection of relativistic electrons in ultraintense laser fields using plasma mirrors. a) Injection of electron bunches from the plasma mirror in the reflected field. b) Electron trajectories in the reflected field (blue lines). The pulse on the right is an aid to the eye.

4.1 Basics of vacuum laser acceleration

4.1.1 Particle acceleration



Conventional	Wakefield	Laser field
50 MV/m	100 GV/m	10 TV/m

Figure 4.2: Picture of the Large Hadron Collider at CERN, schematic of a laser wakefield accelerator and electric field in a laser pulse, with the corresponding typical electric fields.

In a particle accelerator, charged particles are accelerated by an electric field E over a certain distance D. In the case of a static homogeneous field, the final particle energy varies as $\mathcal{E} \propto E \times D$. Conventional accelerators rely on a weak electric field $E \sim$ MV/m and a long accelerating distance $D \sim$ km, making them extremely large facilities. The most famous of its kind, the Large Hadron Collider at CERN, has the shape of a ring with a perimeter of 27 km.

The cost of these facilities led physicists to search for more compact accelerators. Plasma-based accelerators allow the generation of much higher electrostatic fields $E \sim 100\,\mathrm{GV/m}$ that accelerate particles to relativistic energies within a short distance $D = 100\,\mu\mathrm{m} - 1\,\mathrm{m}$. This is summarized in figure 4.2. To go further, the highest electrostatic fields one can make in a laboratory are those inside a laser pulse, where they can reach $E \sim 10\,\mathrm{TV/m}$. The conversion with normalized units reads

$$E = 4a_0\ \mathrm{TV/m}. \tag{4.1}$$

This is the underlying idea of vacuum laser acceleration, which was studied in references [Esarey *et al.*, 1995; Hartemann *et al.*, 1995]. Note that the energy gain via VLA scales as $\Delta\mathcal{E}[MeV] \simeq 35\sqrt{P[TW]}$ where P is the power of the laser beam, as shown in reference [Mori & Katsouleas, 1995]. The maximum energy gain is much higher for laser wakefield accelerators, so VLA does not compete with these accelerators when the aim is to get the fastest electrons.

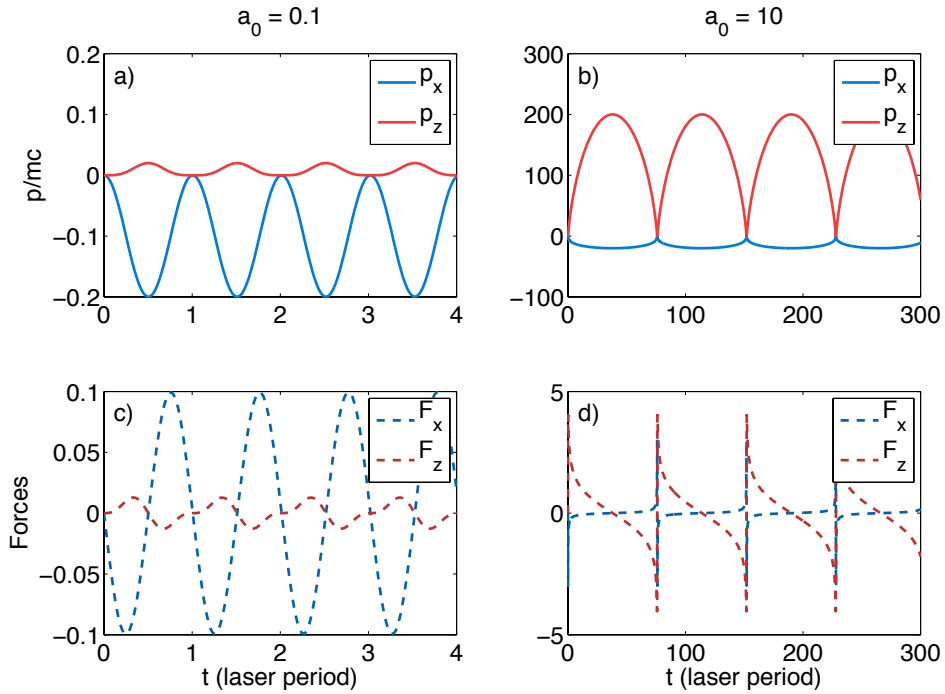


Figure 4.3: a) Electron dynamics in a monochromatic plane wave with $a_0 = 0.1$. The electron starts with speed $v = 0$ at a field node $z = 0$. Note that there is no time-envelope, so the electron starts inside the wave. c) Forces on the electron. b) and d) shows the same quantities for $a_0 = 10$. There is no motion along y in these cases.

We consider an electron propagating in a linearly-polarized laser pulse. The wave propagates along z and is polarized along x. In the monochromatic plane wave approximation, the electric and magnetic fields and the equation of motion for an electron are given in chapter 2 on page 66 and read

$$\boldsymbol{E} = E_0 \sin(\omega_0 t - kz)\boldsymbol{e_x} \tag{4.2}$$

$$\boldsymbol{B} = \frac{E_0}{c} \sin(\omega_0 t - kz)\boldsymbol{e_y} \tag{4.3}$$

$$\frac{d\boldsymbol{p}}{dt} = -e\left(\boldsymbol{E} + \boldsymbol{v} \times \boldsymbol{B}\right) \tag{4.4}$$

so that the electron oscillates in the x direction because of the electric field and its velocity direction is bent towards the propagation direction z by the $v_x B_y$ magnetic force. Figure 4.3 shows the electron momentum along time for $a_0 = 0.1$ and $a_0 = 10$. The electron is initially immobile at $t = 0$ and $z = 0$.

In the non-relativistic case – panels a) and c) – the magnetic force is negligible and $F_z \ll F_x$ where F_z and F_x are the z and x components of the total force respectively. The electron is driven by the electric field and oscillates almost exclusively in the polarization direction x. The displacement along z is negligible ($\Delta z \ll \lambda$), so that the electron oscillates at the laser period ($T_{elec} \simeq T_L$). In this regime, $|\boldsymbol{p}|/m_e c \simeq |p_x|/m_e c \simeq a_0$, and very little acceleration occurs.

On the contrary, in the highly relativistic case $a_0 = 10$ – panels b) and d) – the electron momentum is mostly directed towards the propagation direction z because of the magnetic force and the z component of the total force is dominant: $F_z \gg F_x$. The displacement along z is very large $\Delta z \gg \lambda$, and the electron dephases very slowly in the laser field. Hence, the period of its oscillations is much longer ($T_{elec} \simeq 80 T_L$). In

this regime, $|\boldsymbol{p}|/m_e c \simeq |p_z|/m_e c \gg a_0$, and one can expect very high energy gain if the electron can escape the pulse when its energy is maximum. **This is the regime we call vacuum laser acceleration**.

In this regime, the electron remains for a long time in the same phase of the laser field, so that the electric field effectively transfers energy to the electron. The magnetic force does no work, but instead bends the electron trajectory towards the propagation direction. Assuming $\beta_z \to 1$, the equation of motion gives

$$\frac{dp_x}{dt} \sim -\frac{eE_0}{2\gamma^2} \tag{4.5}$$

$$\frac{dp_z}{dt} \sim -eE_0 \tag{4.6}$$

so that the total force along z is much higher than that along x when the electron has a relativistic speed along z, hence $\gamma \gg 1$. In what follows, we derive the conditions under which the electron effectively gains energy.

4.1.2 Lawson-Woodward theorem

The most famous theorem dealing with particle acceleration by electromagnetic fields in vacuum is the Lawson-Woodward theorem [Lawson *et al.*, 1979; Woodward, 1946] (see also [Esarey *et al.*, 1995]), which states that in a 3D configuration, under some hypotheses, a particle cannot gain energy from an electromagnetic wave. It is massively invoked as a deadly argument against particle acceleration in vacuum by a laser pulse, though its scope of validity is, at the least, limited. In this paragraph, we present the theorem, its proof and its limits.

Theorem

Consider an electron propagating in an electromagnetic wave with propagation and polarization directions both in the $x-z$ plane, for example a laser pulse propagating along z (respectively x) and polarized along x (respectively z). Let us assume

(H1) no boundaries: The wave is in vacuum, there are no boundaries;
(H2) no external field: There is no electrostatic or magnetostatic external field;
(H3) electron travels at the speed of light: The electron propagates with velocity $\boldsymbol{v} = c\boldsymbol{e_z}$, hence infinite energy;
(H4) infinite interaction region: The interaction takes place from $t = -\infty \to +\infty$, and $z = -\infty \to +\infty$.
(H5) no non-linear forces: The $v \times B$ force, ponderomotive force etc. are neglected.

Result: An electron interacting with an electromagnetic wave under these conditions does not gain energy between $t = -\infty$ and $t = +\infty$.

Proof

We consider the field component with angular frequency ω. The Helmholtz equation – using (H1) and (H2) – and the subsequent dispersion relation read

$$\Delta \boldsymbol{E} = -\frac{\omega^2}{c^2}\boldsymbol{E} \tag{4.7}$$

$$\frac{\omega^2}{c^2} = k_x^2 + k_y^2 + k_z^2. \tag{4.8}$$

Starting from the definition of the Fourier transform in space $\tilde{\boldsymbol{E}}$ of $\boldsymbol{E}$ and injecting the dispersion relation, we get, for the E_z component:

$$E_z = \int\int \tilde{E}_z(k_x, k_y) e^{i(k_x x + k_y y + k_z z - \omega t)} dk_x dk_y, \tag{4.9}$$

where we used

$$k_z = \sqrt{\frac{\omega^2}{c^2} - k_x^2 - k_y^2} \tag{4.10}$$

for convenience. Gauss's law in vacuum reads $\nabla \cdot \boldsymbol{E} = 0$, giving the relation between the Fourier-transformed components of the electric field:

$$k_z \tilde{E}_z + k_x \tilde{E}_x = 0. \tag{4.11}$$

According to (H3), the electron velocity is along z, so only the electric force $-eE_z$ can work. This shows how strong the hypothesis $\boldsymbol{v} = c\boldsymbol{e}_z$ is: no oscillation due to the electromagnetic wave is allowed. Besides, we can set $x(t) = 0$ and $y(t) = 0$ for the electron at any time, and $z(t) = ct$. The final energy gain for the electron is given by the work of the force due to E_z, proportional to

$$\begin{aligned}
\Gamma_z &= c\int_{-\infty}^{+\infty} dt E_z(x(t), y(t), z(t)) \text{ (H4)} && (4.12)\\
&= \int_{-\infty}^{+\infty} dz E_z(0, 0, z) && (4.13)\\
&= -\int_{-\infty}^{+\infty} dz \int\int dk_x dk_y \frac{k_x}{k_z} \tilde{E}_x(k_x, k_y) e^{i(k_z - \omega/c)z} && (4.14)\\
&= -\int\int dk_x dk_y \frac{k_x}{k_z} \tilde{E}_x(k_x, k_y) \int_{-\infty}^{+\infty} dz e^{i(k_z - \omega/c)z} && (4.15)\\
&= -\frac{1}{2\pi}\int\int \frac{k_x}{k_z} dk_x dk_y \tilde{E}_x(k_x, k_y)\delta(k_z - \omega/c), && (4.16)
\end{aligned}$$

by virtue of $2\pi \int_{-\infty}^{+\infty} e^{i\alpha x} dx = \delta(\alpha)$. Let us finally switch to cylindrical coordinates $k_x = k_\perp \cos\phi$ and $k_y = k_\perp \sin\phi$:

$$\Gamma_z = \int\int \frac{k_\perp}{k_z} \cos\phi \tilde{E}_x(k_\perp \cos\phi, k_\perp \sin\phi)\delta(k_z - \omega/c) d\phi dk_\perp. \tag{4.17}$$

The integration is not trivial because the integrand diverges for $k_z = \sqrt{\omega^2/c^2 - k_\perp^2} = 0$, *i.e.* $k_\perp = \omega/c$. Yet it varies as $1/\sqrt{\pm(k_\perp - \omega/c)}$, and is integrable. Hence, we can apply the Dirac function which is non-zero for $k_\perp = 0$, giving the final result

$$\Gamma_z = 0. \tag{4.18}$$

Limits

In spite of its presumed general scope of application, this theorem shows severe limits. While there is little restrictive condition on the electromagnetic wave (provided it is linearly polarized), there are strong assumptions on the electron dynamics:

(H3) electron travels at the speed of light This hypothesis assumes $v_z = c$ during the whole interaction. It has the following consequences: first, the electron has infinite energy. Second, only E_z can do non-zero work. Yet in the plane wave approximation (see figure 4.3 a) for example), the electron travels essentially along z and the only field with non-zero work is E_x. Besides, it obviously states that the laser field does not perturb the electron trajectory.

(H5) no non-linear forces The $v \times B$ force is neglected. Figure 4.3b) and equations 4.6 show that the dynamics of a relativistic electron can be mostly driven by the magnetic force, especially when the electron travels along the propagation direction.

These are general limits to the Lawson-Woodward theorem. Besides, our setup brings specific limits:

Boundaries In our case, we will set an external boundary and external fields using a plasma mirror, hence breaking hypotheses (H1) and (H2) – and (H4).

Electron driven by electromagnetic fields The electron travels in the laser pulse with initial speed smaller than c, and its dynamics is strongly deteriorated by these fields, breaking hypotheses (H3) and (H5) in the relativistic regime.

When trying to accelerate electrons in a laser wave, one has to justify that at least one hypothesis is broken. In our case, at least four hypotheses are violated, and the results are presented in section 4.3.3.

Plettner's experiment

A remarkable experimental work was performed in reference [Plettner *et al.*, 2005]. Though the authors claim a new acceleration mechanism, they bring even more noteworthy results on the Lawson-Woodward theorem and its limits.

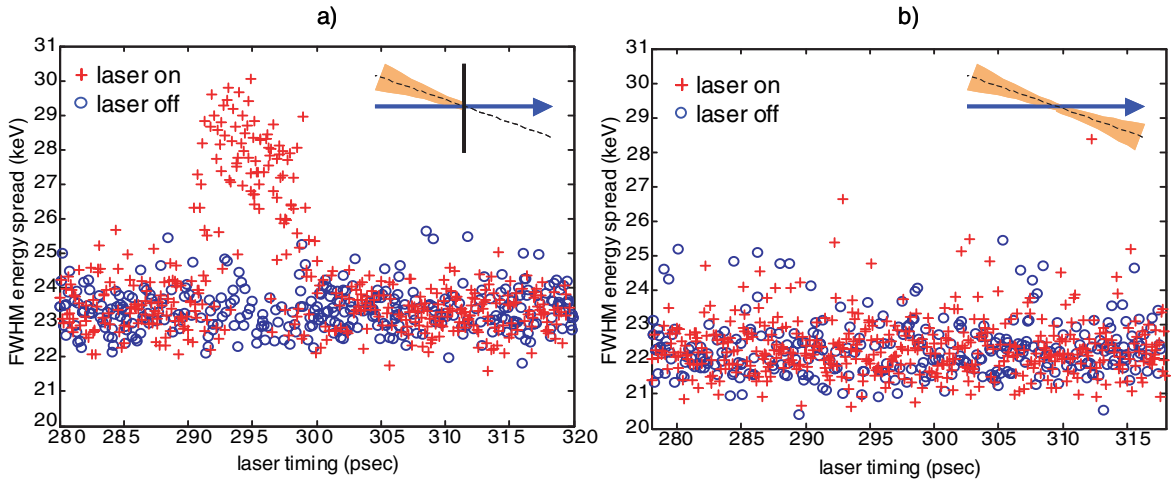


Figure 4.4: [Image from reference [Plettner *et al.*, 2005]] a) Final energy spread of the electron beam as a function of delay between electron beam and laser pulse, in presence of a boundary. The experimental configuration is shown in the inset, where the electron beam propagates along the blue line and the laser pulse is represented by the yellow area. b) shows the same as a) with no boundary.

A 30 MeV electron bunch propagates in the z direction, and meets a laser pulse at focus ($z = 0$), with a small angle to the z direction. The laser pulse is 4 ps-long with energy of 2 μJ, giving a peak field strength $a_0 < 0.1$. Note that the normalized initial electron momentum $p_0/mc \simeq 60$ is much higher than the laser peak amplitude $p_0/mc \gg a_0$, so that the electrons are expected to show little deviation by the laser – (H3) and (H4) are verified. The authors measure the energy spread of the electron bunch after the interaction. In these conditions, all the hypotheses (H1-H5) are verified,

and the final energy spread is the same with and without the laser pulse, as shown in figure 4.4b).

Then, a boundary parallel to the $x-y$ plane at $z=0$ was added. This boundary is a thin tape that reflects the laser pulse without troubling significantly the electron bunch, hence breaking hypothesis (H1). They observe that the energy spread of the electron beam is increased during this interaction, as shown in figure 4.4b). Some electrons in the beam gain or lose energy during this interaction.

This experiment shows an illustration of the Lawson-Woodward theorem when all its hypotheses are verified, as well as the possibility to break (H1) to accelerate electrons. Yet their setup is not meant for electron acceleration, since it finally degrades an externally-generated high-quality 30 MeV monoenergetic electron beam.

4.2 Electron in a laser pulse: typical behaviors

4.2.1 Introduction

The dynamics of electrons in a laser pulse can be extremely diverse and strongly depend on their initial position and momentum. Yet any trajectory can be compared with two archetypal orbits. First, **ponderomotive** dynamics stands for electrons that see many oscillations in the laser field and undergo the average ponderomotive force (see chapter 2) until they leave the pulse. Second, **VLA** dynamics designates electrons travelling close to the speed of light along the propagation direction z, which remain in the same phase of the laser pulse. They are accelerated in the polarization plane $z-x$ until they escape the pulse. The laser field at the electron position remains positive (respectively negative) while the electron is in the laser pulse, so that the electron finally escapes the pulse with $p_x<0$ (respectively $p_x>0$).

We consider the dynamics of an electron in a linearly polarized laser pulse with Gaussian space and time profiles, in the relativistic regime. The laser parameters are $\lambda=0.8\,\mu$m, $a_0=4$, $w_0=5\,\mu\text{m}=6.25\lambda$, pulse duration $\tau_L=30\,$fs and the pulse is focused in the plane $z=0$ at $t=0$. All the simulations in this chapter are performed with the `test-particle code`, using first-order field corrections (see section 2.2.3, page 70). The laser phase is such that, around $x=0, y=0$, the electric field reads

$$\boldsymbol{E}\propto+\sin(kz-\omega_0 t)\boldsymbol{e}_x. \tag{4.19}$$

Note that, with this notation, the electric and magnetic fields are zero at $t=0$ and $z=0$. The electron is characterized by its position $\boldsymbol{R}=(x,y,z)$ and momentum $\boldsymbol{P}=(p_x,p_y,p_z)$. The simulation starting time is called t_{st}.

The ponderomotive and VLA dynamics are studied in sections 4.2.2 and 4.2.3 respectively. As an illustration, a typical ponderomotive trajectory is plotted in figure 4.6 (page 122), and a typical VLA trajectory is shown in figure 4.9 (page 124). Both were obtained using the laser parameters described above, for an electron starting with $\boldsymbol{P}_{st}=(0,0,1)m_ec$, *i.e.* with kinetic energy $\mathcal{E}_k\simeq 200\,$keV. The only difference is the initial electron position with respect to the laser pulse.

Figure 4.5 a) shows the configuration for the ponderomotive dynamics. The electron starts outside the pulse with $t_{st}<0$, and is overtaken by the laser pulse around $t=0$ and $z=0$. This configuration leads to a ponderomotive electron trajectory.

Figure 4.5b) illustrates the configuration we use to investigate the VLA dynamics. The electron starts inside the pulse around the focal spot with $t_{st}=0$. This configuration gave the VLA electron trajectory.

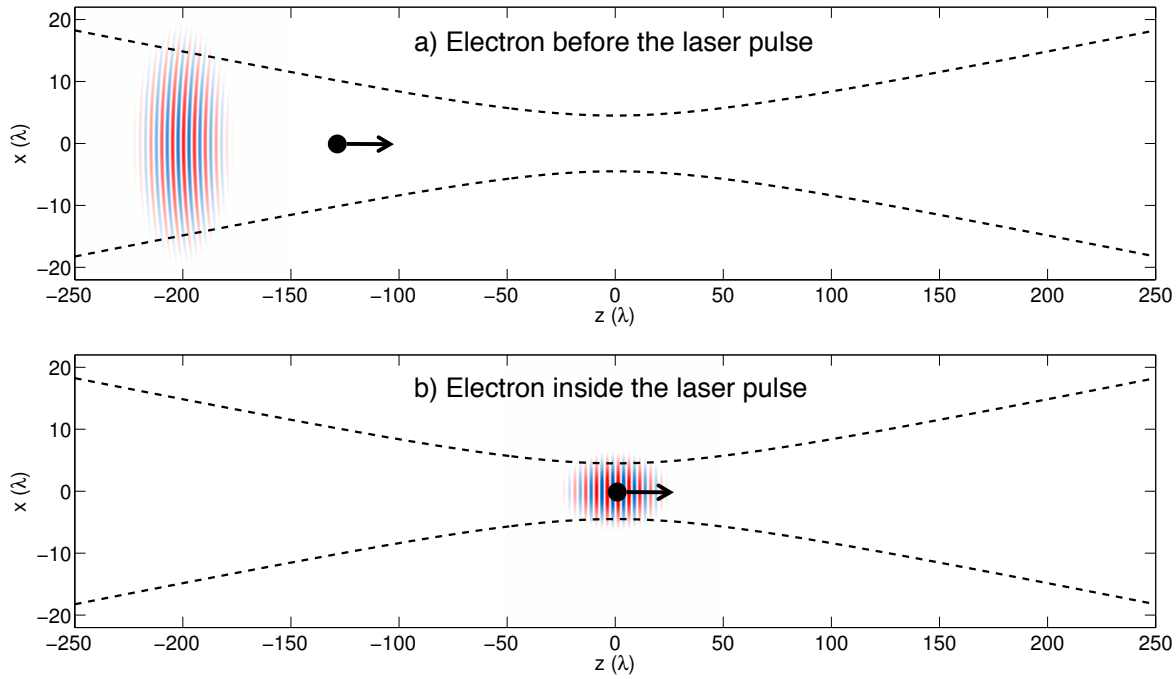


Figure 4.5: Two initial configurations for electron dynamics. In configuration a), the electron motion starts before the laser pulse, where the pulse envelope is zero, and is overtaken at $t = 0$ and $z = 0$. This disposition mostly leads to ponderomotive scattering. In configuration b), the electron starts at focus in the center of the pulse with initial speed along z. With ultraintense tightly-focused laser beams, this can lead to vacuum laser acceleration.

The Lawson-Woodward theorem does not apply to these configurations because the electron shows strong oscillations in the laser polarization directions – (H3) and (H5) are violated. Besides, the second configuration – figure 4.5b) – also breaks hypothesis (H4) because the electron motion starts at $t_{st} = 0$ inside the laser pulse, and may result in a high energy gain.

A major difference between these two cases is the initial transverse canonical momentum. When the electron starts before the laser pulse, the laser vector potential is zero, so that the transverse canonical momentum $\boldsymbol{P}_{\perp 0} = \boldsymbol{p}_{\perp 0} = \boldsymbol{0}$. On the opposite, an electron inside the laser pulse at $t_{st} = 0$ with $z_{st} = 0$ starts at a field node (see equation 4.19), *i.e.* with a maximum vector potential, and $\boldsymbol{P}_{\perp 0}/m_e c = a_0 \boldsymbol{e}_x$.

4.2.2 *Ponderomotive* behaviour

Electron trajectory

The electron starts with $\boldsymbol{R}_{st} = (-1.5, 1.1, -68.4)\lambda$ and $\boldsymbol{P}_{st} = (0, 0, 1)m_e c$ and the simulation starts at $t_{st} = -98T_L$ so that both the maximum of the pulse envelope and the electron reach $z = 0$ at $t = 0$.

The result of this run (`these_traj_1`) is shown in figure 4.6 a). When the electron is overtaken by the laser pulse, it oscillates in the laser field – see panel c) – and is ejected with little energy gain ($\gamma = 3$ at the end). The electron undergoes the average ponderomotive force, as discussed in section 2.2.4 page 71, and is ejected transversely – see panel a).

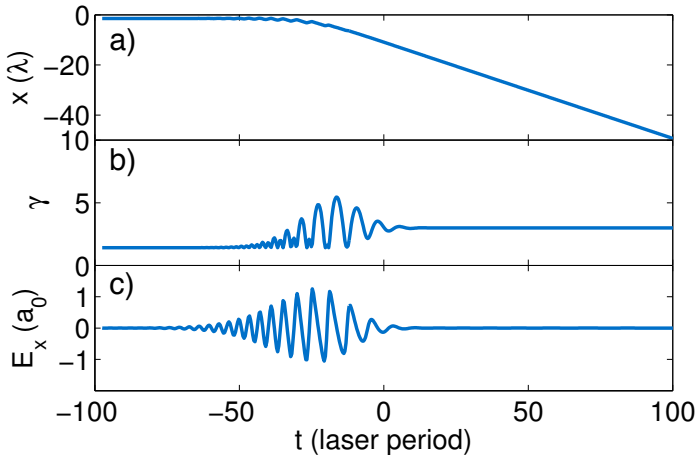


Figure 4.6: a-c) Dynamics of a *ponderomotive* electron. The electron starts with $p_z = 1$ before the laser pulse, and is overtaken around $t = 0$. Its transverse position x, Lorentz factor γ and the electric field at the electron position are plotted as a function of time in a), b) and c) respectively.

Axisymmetric hole

A simulation in this configuration was run with 100 000 electrons, with the same laser parameters. The initial electron distribution is $\boldsymbol{R_{st}} \pm \sigma_R = (0, 0, -68.4) \pm (3.1, 3.1, 0.1)\lambda$ and $\boldsymbol{P_{st}} \pm \sigma_P = (0, 0, 1) \pm (0.1, 0.1, 1) m_e c$. σ stands for the standard deviation of the initial Gaussian distribution for both quantities. The simulation starts at $t_{st} = -98 T_L$. The run name is `these_compvlapond_1`.

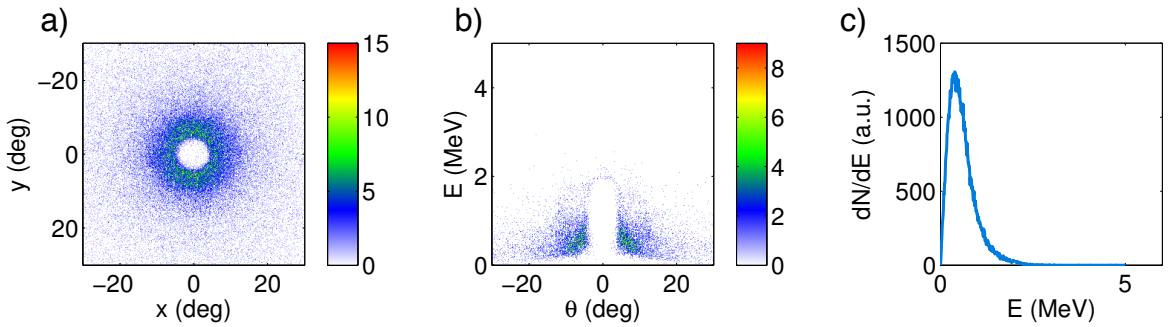


Figure 4.7: Final electron distribution for run `these_compvlapond_1` in the first configuration –figure 4.5 a)– far after all electrons have left the pulse. a) angular distribution. $(0, 0)$ is the propagation direction. b) Angle-energy distribution. c) Final spectrum for the total electron population.

The final angular distribution is shown in figure 4.7 a), where one can see a clear hole in the laser propagation direction. Besides, the distribution is axisymmetric, even though the laser fields are not because of the linear polarization. This is a clear signature of ponderomotive scattering. The final energy remains below $1 - 2\,\mathrm{MeV}$, as shown in figure 4.7b) and c).

The initial energy is $\mathcal{E} \simeq 200\,\mathrm{keV}$, so the electrons show little energy gain. Note that the maximum energy gain is comparable with the ponderomotive potential $\phi_p = m_e c^2 a_0^2/4 = 2\,\mathrm{MeV}$ for $a_0 = 4$.

Scaling laws: angle-energy correlation

Relying on Hartemann's calculations presented in chapter 2, we derive a general formula that links the final propagation angle $\theta = \operatorname{atan} \beta_r/\beta_z$ (with $\beta_r^2 = \beta_x^2 + \beta_y^2$) and the Lorentz factor of the electrons. This derivation is done in reference [Hartemann *et al.*, 1995].

Consider an electron propagating in a monochromatic plane wave, starting with initial phase $\phi = 0$ and speed $\boldsymbol{v}/c = (0, 0, \beta_{z0})$, as in section 2.2.1 (page 66). The definition of the Lorentz factor gives

$$\frac{\beta_x^2}{\beta_z^2} = \frac{\gamma^2 - 1 - \gamma^2\beta_z^2}{\gamma^2\beta_z^2} \tag{4.20}$$

and the conservation equation 2.53 reads

$$\gamma(1 - \beta_z) = \gamma_0(1 - \beta_{z0}). \tag{4.21}$$

Using again $\gamma_0(1-\beta_{z0}) = 1/\gamma_0(1+\beta_{z0})$ and the conservation equation, we remark that

$$\gamma^2 - 1 - \gamma^2\beta_z^2 = -1 + 2\gamma\gamma_0(1 - \beta_{z0}) - \gamma_0^2(1 - \beta_{z0})^2 \tag{4.22}$$

$$= \frac{2}{1 + \beta_{z0}}\left(\frac{\gamma}{\gamma_0} - 1\right), \tag{4.23}$$

and equation 4.20 gives the following equation between the electron propagation direction θ and its Lorentz factor

$$\tan^2(\theta) = \frac{\left(\frac{2}{1+\beta_{z0}}\right)\left(\frac{\gamma}{\gamma_0} - 1\right)}{[\gamma - \gamma_0(1 - \beta_{z0})]^2}. \tag{4.24}$$

This relation was also derived by Brice Quesnel in reference [Quesnel & Mora, 1998] relying on the ponderomotive force.

This result was confronted with a scan of simulations with the `test-particle code`. The laser pulse parameters are $a_0 = 4$, $w_0 = 5\,\mu$m, pulse duration 30 fs, $\lambda = 0.8\,\mu$m, focused on $z = 0$ at $t = 0$. The initial conditions for the electron distribution are $\boldsymbol{R}_{st} = (0 \pm 3, 0 \pm 3, z_0 \pm 1)\lambda$ and $\boldsymbol{P}_{st} = (0, 0, p_{z0})$. The electron bunch starts before the main pulse, and z_0 is set as a function of p_{z0}, so that the electron bunch and the laser pulse meet at focus at $t = 0$.

The scan consists in five simulations `these_pond_thetagamma_(1-5)` with $p_{z0}/m_ec = 0, 1, 2, 3, 4$. Figure 4.8 shows the final angular distribution for these simulations. The distribution is axisymmetric and shows a clear hole in the propagation direction, which are characteristic features of the ponderomotive force. The black dashed line was calculated using equation 4.24, and shows excellent agreement with the simulation results.

Note that the final distribution in figure 4.8 a) ($p_{z0} = 1$) is perfectly axisymmetric while figures 4.8d) and e) show a slight asymmetry: two bulbs can be seen in the polarization direction x, on the left and on the right of the central hole. When p_{z0} is higher, the quiver velocity of the electrons increases, and few electrons escape the pulse via the VLA mechanism.

4.2.3 *VLA* behaviour

Electron trajectory

In the configuration shown in figure 4.5b), the electron starts inside the laser pulse. Simulation `these_traj_2` was run with $t_{st} = 0$ and $R_{st} = (0.6, 0, -0.1)\lambda$. The phase

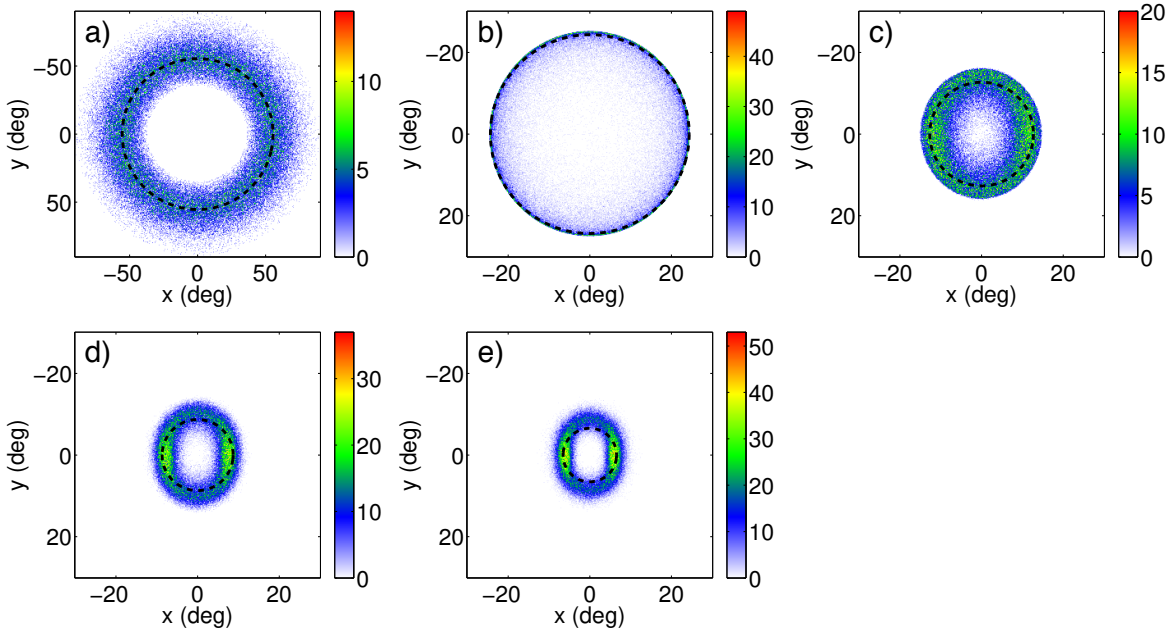


Figure 4.8: Final electron angular distributions in the first configuration shown in figure 4.5 a). The doughnut-shaped axisymmetric profile is a signature of ponderomotive scattering. The black dashed circle stands for the application of equation 4.24. The initial electron momentum $p_z/m_e c$ for each image is a) 0; b) 1; c) 2; d) 3; e) 4.

is $\phi_{st}/2\pi = -0.1$ (with $E_x = E_0 \sin\phi$, see equation 4.19), so that the electron starts close to a field node. All other parameters are the same as in figure 4.6, in particular $\boldsymbol{P_{st}} = (0, 0, 1)m_e c$.

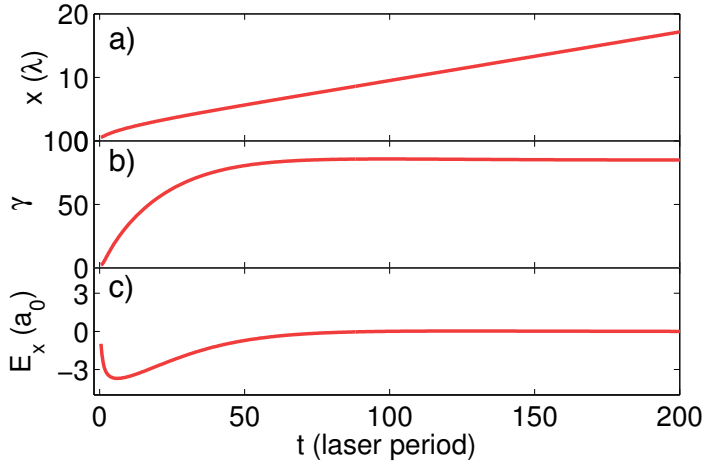


Figure 4.9: a-c) Dynamics of a *VLA* electron. The electron starts with $p_z/m_e c = 1$ inside the laser pulse, at $t = 0$ and $z = 0$. Its transverse position x, Lorentz factor γ and the electric field at the electron position are plotted along time in a), b) and c) respectively.

The electron trajectory is shown in figure 4.9, and is dramatically different from the ponderomotive case. The electron does not oscillate in the laser pulse, but rather remains in the same phase of the laser field: $E_x < 0$ all along its trajectory, as shown in panel c). Hence, it is accelerated all along its propagation by the electric field in the polarization direction, and escapes with a high energy ($\gamma = 100$). This satisfies our previous definition of VLA.

Spot in the polarization plane

As for the ponderomotive case, a simulation in the second configuration – figure 4.5b) – was run with 100 000 electrons, with the same laser parameters. The initial electron distribution is $\boldsymbol{R_{st}} \pm \sigma_R = (0,0,0) \pm (3.1, 3.1, 0.1)\lambda$ and $\boldsymbol{P_{st}} \pm \sigma_P = (0,0,1) \pm (0.1, 0.1, 1) m_e c$. This gives $\phi_{st}/2\pi = 0 \pm 0.1$ (see equation 4.19). The simulation starts at $t_{st} = 0$ The run name is `these_compvlapond_2`.

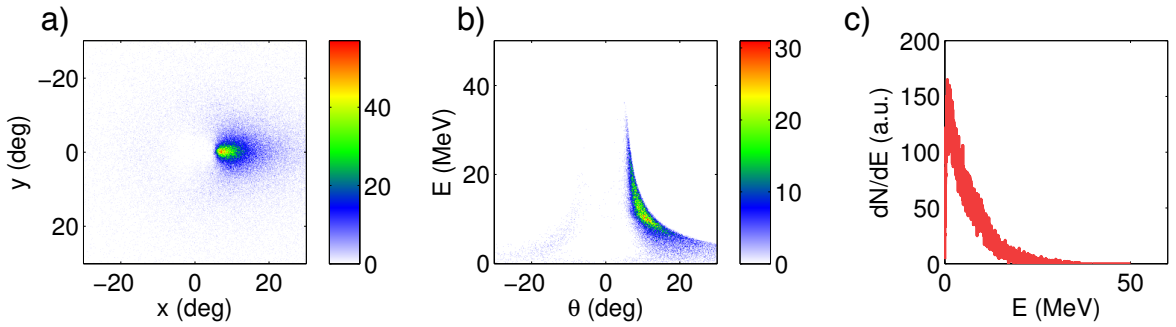


Figure 4.10: Final electron distribution for run `these_compvlapond_2` in the second configuration – figure 4.5b) – far after all electrons have left the pulse. a) angular distribution. $(0,0)$ is the propagation direction. b) Angle-energy distribution. c) Final spectrum for the total electron population.

The final angular distribution is shown in figure 4.10 a), where there is an electron spot in the polarization direction. In figure 4.10b) one can see a clear correlation between the final angle and energy of the electrons. The closer from the propagation axis, the higher the energy. The spectrum shown in figure 4.10c) extends up to tens of MeV, so the final energy of fast electrons has been multiplied by a factor of approximately 100.

Scaling laws: angle and energy

In this section, we derive an estimate of the ejection angle and energy of electrons that start moving inside a laser pulse and undergo vacuum laser acceleration. We first consider the dynamics of an electron in a plane wave.

The dynamics of an electron in a low-intensity ($a_0 = 0.1$) plane wave is shown in figure 4.11 a). The electron oscillates mostly in the polarization direction x at the laser frequency. The electron displacement along z is negligible ($< p_z >_t \ll m_e c$), so the field phase at the electron position varies linearly $\phi \simeq \omega_0 t$, as shown in figure 4.11c). $p(\phi)$ is plotted in figure 4.11e), and shows no difference with $p(t)$, see figure 4.11 a).

The dynamics differs significantly when the wave intensity becomes largely relativistic $a_0 = 10$, as shown in panel b). $< p_z >_t \gg m_e c$, so the electron experiences a very slow phase shift, as can be seen on panel d). The electron experiences a 2π phase shift within ~ 80 laser periods.

In both cases, $E_x = E_0 \sin\phi = E_0 \sin(\omega_0 t - kz)$, so the electric and magnetic fields are positive for $0 < \phi < \pi$ and negative for $\pi < \phi < 2\pi$. The electron starts with $\phi_{st} = 0$ and is accelerated towards $-x$ until $\phi = \pi$ and then decelerated, where the electron gets dephased.

Dephasing length: When $\phi > \pi$, the electron starts being decelerated, so its maximum energy is reached for $\phi = \pi$. The dephasing length is given by $z(\phi = \pi)$ for an

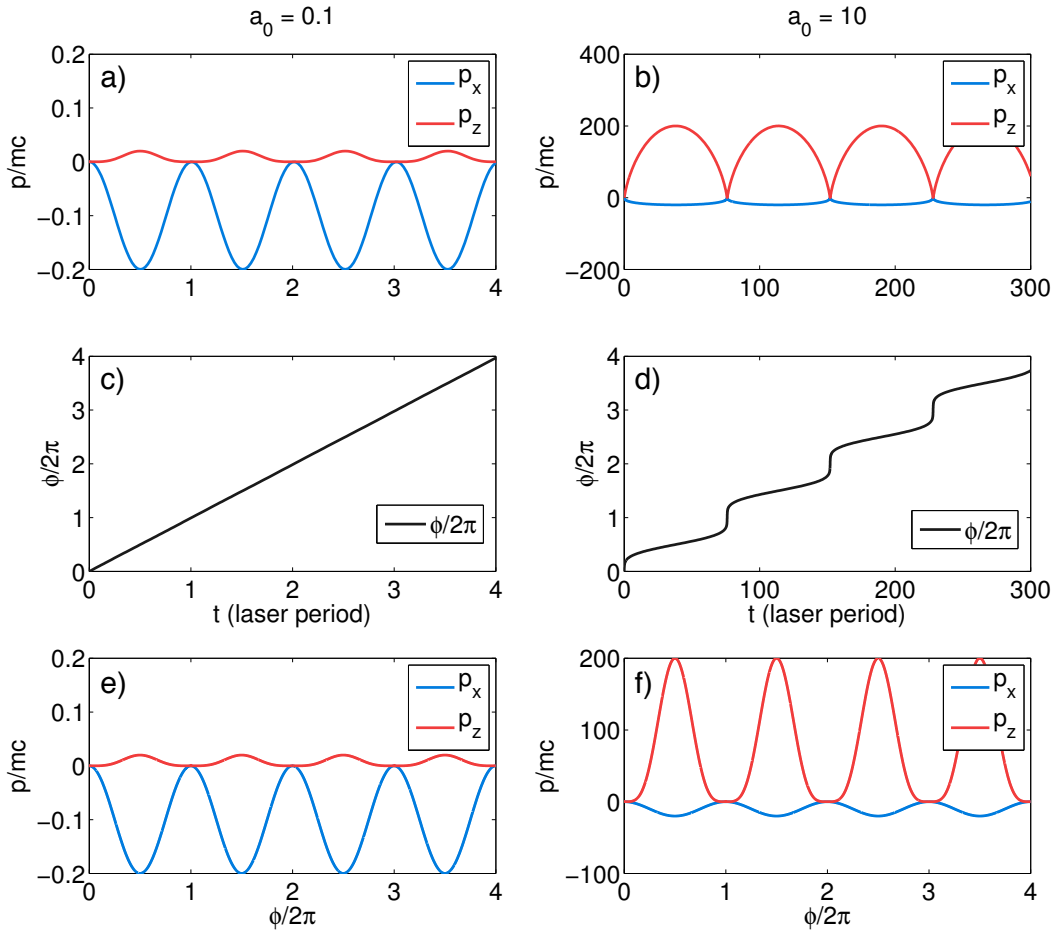


Figure 4.11: Dynamics of an electron in a plane wave in the non-relativistic ($a_0 = 0.1$) and relativistic ($a_0 = 10$) cases. a) Momentum components along the polarization (p_x) and propagation (p_z) directions as a function of time. c) Phase $\phi = \omega_0 t - kz(t)$ of the wave at the electron position as a function of time. $\phi \simeq \omega_0 t$. e) Momentum as a function of the electron phase in the wave. b), d) and f) are the same as a), c) and e) for $a_0 = 10$. $\phi \neq \omega_0 t$. In both cases, the electron starts at rest at a field node, and the time span correspond to a 8π phase shift in the wave.

electron starting at $z = 0$ with $\phi_{st} = 0$ and $\boldsymbol{v}_{st} = (0, 0, \beta_{z0}c)$. It is readily obtained from equation 2.64 (page 67), and reads

$$kL_{deph} = \pi \frac{\beta_{z0} + \frac{3}{4}a_0^2(1+\beta_{z0})}{1-\beta_{z0}}. \tag{4.25}$$

This estimate is valid as long as $L_{deph} \lesssim z_R$, otherwise the plane wave approximation does not hold. The limits around $\beta_{z0} = 0$ and 1 read

$$kL_{deph} \longrightarrow \frac{3\pi}{4}a_0^2 \qquad \text{when } \beta_{z0} \longrightarrow 0 \tag{4.26}$$

$$kL_{deph} \longrightarrow 2\pi\gamma_0^2\left(1+\frac{3}{2}a_0^2\right) \qquad \text{when } \beta_{z0} \longrightarrow 1 \tag{4.27}$$

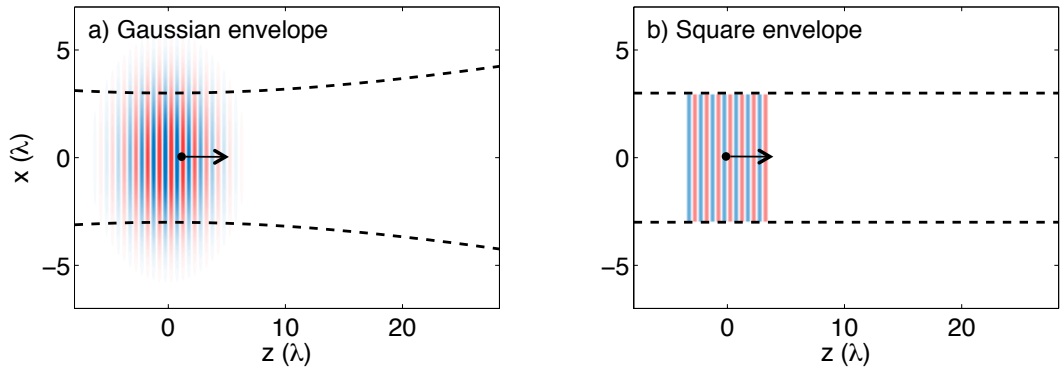


Figure 4.12: Model for side ejection: the Gaussian pulse (a) is approximated by a square-envelope plane wave.

A Gaussian pulse is approximated by a plane wave with a square envelope, as shown in figure 4.12. This is a 2D extension to the plane wave approximation, so that we can use Hartemann's analytical results and model the electron ejection.

Side ejection: A Gaussian pulse with peak amplitude a_0 is approximated by a square-envelope pulse with total width $2w_0$ constant amplitude a_{0s}. We assume the energy in the volume $0 < z < z_R$ is the same for both envelopes, giving $a_{0s} \simeq a_0/2$, and study the dynamics of an electron in this square-envelope pulse. Vacuum laser acceleration is optimal if the electron is accelerated all along its propagation until it leaves the pulse. In other words, the electron undergoes VLA if it escapes the pulse ($x = \pm w_0$) before it gets dephased ($\phi = \pi$). Using equation 2.63, this condition reads

$$kx(\phi = \pi) = \frac{\pi a_{0s}}{\gamma_0(1-\beta_{z0})} > kw_0, \tag{4.28}$$

giving the following condition for VLA:

$$\gamma_0(1+\beta_{z0})a_{0s} > \frac{2w_0}{\lambda}. \tag{4.29}$$

Estimate for angle and energy at ejection: Let us assume $x(\phi = \pi) = w_0$, so that the electron escapes the pulse with its highest energy. Equations 2.60-2.62 (page 67)

simulation	a_0	w_0	p_{z0}	$\sigma(p_{z0})$
a)`these_enervla_1`	4	$6.25\lambda = 5\,\mu$m	4	2
b)`these_enervla_3`	4	$12.5\lambda = 10\,\mu$m	8.4	4.2
c)`these_enervla_4`	2	$6.25\lambda = 5\,\mu$m	3.5	1.75

Table 4.1: Simulation conditions in the scan for VLA scaling laws. All simulations were run with the `test-particle code`, with 10 000 electrons, $\tau_L = 30$ fs. The electrons started in the pulse center, at a field node, with $\phi_{st} = 0$ and Gaussian distribution $(x_0, y_0) = (0 \pm 5, 0 \pm 5)\lambda$ and $(p_{x0}, p_{z0}) = (0 \pm 1, 0 \pm 1)m_e c$.

give the following estimates for the ejection angle and energy, expressed directly as a function of a_0, (not a_{0s}):

$$\gamma_{ej} = \gamma_0 \left[1 + 2a_0(1 + \beta_{z0})\right] \tag{4.30}$$

$$\theta_{ej} = \text{atan}\left[\frac{2a_0}{\gamma_0 \left[\beta_{z0} + 2a_0^2(1 + \beta_{z0})\right]}\right]. \tag{4.31}$$

A set of simulations was performed with the `test-particle code` where the condition $L_{deph} = z_R$ was always satisfied. The simulation parameters and results are shown in Table 4.1, and the results can be found in figure 4.13. The final energy-angle distribution is shown, along with the estimate values from equations 4.30 and 4.31. This simple extended 1D model reproduces remarkably the trends observed in numerical simulations.

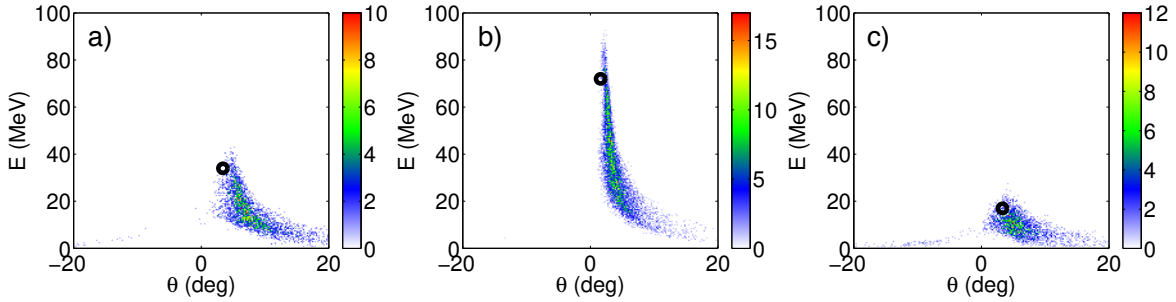


Figure 4.13: Angle-energy electron distribution from a test-scan for in the second configuration – figure 4.5b). The simulation parameters are given in table 4.1. The black ring stands for theoretical values from equations 4.30 and 4.31.

4.2.4 *VLA/ponderomotive* ratio

The previous sections illustrated how electrons starting before the laser pulse could be scattered by the ponderomotive force, and how electrons starting inside the laser pulse could undergo vacuum laser acceleration. Yet the dynamics can be fairly more complex, and both configurations can lead to both dynamics.

First, when an electron is overtaken by the laser pulse, it oscillates in the polarization direction. If the amplitude of this quiver motion is higher than the beam waist, the electron can escape in the polarization direction, with a higher energy gain. As an example, this occurs for some electrons in figure 4.8e), forming the two bright spots along x, on both sides of the propagation direction.

Second, an electron starting in the laser pulse may oscillate in the laser fields and be scattered by the ponderomotive force. For an electron starting with velocity $\boldsymbol{v} /\!\!/ \boldsymbol{e_z}$, ponderomotive scattering occurs preferably when the electron starts at a field maximum, where its transverse canonical momentum is zero $\boldsymbol{P}_{\perp 0} = \boldsymbol{p}_{\perp 0} + \boldsymbol{a}_{\perp 0} = \boldsymbol{0}$, whereas VLA happens when the electron starts with a maximum canonical momentum $\boldsymbol{P}_{\perp 0} = \boldsymbol{p}_{\perp 0} + \boldsymbol{a}_{\perp 0} = a_0 \boldsymbol{e}_x$. A detailed example can be found in section 4.3.5.

This section is dedicated to general trends of electron dynamics in a laser pulse. Starting with a large initial electron distribution, we focus on average effects and find a criterion that discriminates VLA and ponderomotive behaviours. The electron distribution starts inside the laser pulse because it is more relevant for section 4.3. The ratio of VLA electrons is shown to depend on a single parameter $\mathit{\Pi}$.

Because the number of free parameters for the electron distribution is extremely large, we restrict ourselves to $\boldsymbol{R}_{st} = (0, 0, 0)$ and $\boldsymbol{P}_{st} = (0, 0, p_{z0} \pm \sigma_p)$. The role of the laser parameters and p_{z0}, which we consider to be the dominant parameters, are identified. The probability density function for the electron Lorentz factor f_{γ_0} is Gaussian with mean value μ and standard deviation $\mathit{\Gamma}_0$, with $\mu \gg 1$.

$$f_{\gamma_0}(x) = \frac{1}{\sqrt{2\pi {\mathit{\Gamma}_0}^2}} \exp\left(-\frac{(x-\mu)^2}{2{\mathit{\Gamma}_0}^2}\right). \tag{4.32}$$

Let us rely once again on the square-envelope approximation used before: the laser pulse has a square envelope with total width $2w_0$ and amplitude $a_{0s} = a_0/2$. The escape time t_{esc} is defined as $x(t_{esc}) = \pm w_0$. Consider an electron with initial velocity $\boldsymbol{v}/c = \beta_{z0}\boldsymbol{e_z}$ and associated Lorentz factor γ_0 starting with $\phi_0 = 0$ in a laser pulse. The quiver amplitude x_{quiv} for an electron is calculated in section 2.2.1 and reads

$$k x_{quiv} = a_{0s}\gamma_0(1 + \beta_{z0}). \tag{4.33}$$

The electron undergoes VLA provided $x_{quiv} > w_0$. For the initial distribution given in equation 4.32, the probability for an electron to satisfy this condition is given by

$$\mathbb{P}[VLA] = \mathbb{P}\left[\gamma_0(1+\beta_{z0}) > \frac{k w_0}{a_{0s}}\right] \tag{4.34}$$

$$= \mathbb{P}\left[\gamma_0 > \frac{k w_0}{2a_{0s}}\right], \text{ assuming } \gamma_0 \gg 1 \tag{4.35}$$

After integration, this probability reads, as a function of a_0,

$$\mathbb{P}[VLA] = \frac{1}{2}\mathrm{erfc}(\mathit{\Pi}) \tag{4.36}$$

$$\text{where } \mathit{\Pi} = \frac{\frac{k w_0}{a_0} - \mu}{\sqrt{2}\mathit{\Gamma}_0} \tag{4.37}$$

and erfc is the complementary error function defined on $\mathbb{R}$ as

$$\mathrm{erfc}(x) = \frac{2}{\sqrt{\pi}} \int_x^{+\infty} e^{-t^2} dt. \tag{4.38}$$

This function is depicted in figure 4.14.

The smaller $\mathit{\Pi}$, the higher the VLA ratio. The global trends are intuitive: VLA is favored by a higher mean Lorentz factor μ or a smaller beam waist w_0.

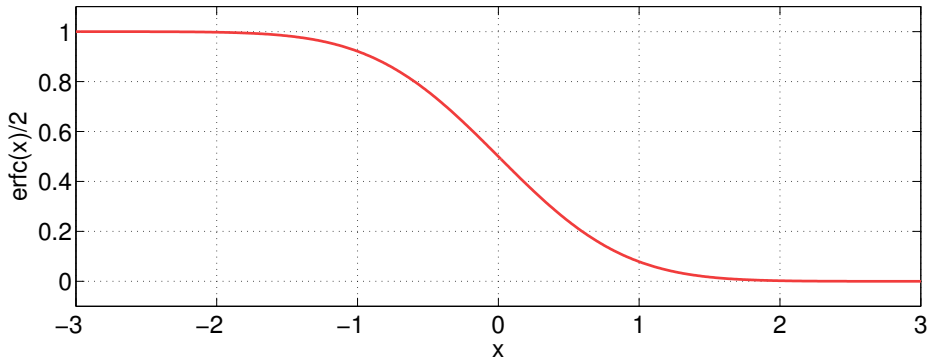


Figure 4.14: Complementary error function erfc.

simulation	a_0	w_0	μ	Π	%VLA
these_vla_1	8	$8\,\mu\text{m} = 10\lambda$	8	0	77%
these_vla_2	8	$5.3\,\mu\text{m} = 6.6\lambda$	8	$-1/2$	88%
these_vla_3	8	$11\,\mu\text{m} = 13.8\lambda$	8	$+1/2$	66%
these_vla_4	12	$8\,\mu\text{m} = 10\lambda$	8	$-1/2$	86%
these_vla_5	5.8	$8\,\mu\text{m} = 10\lambda$	8	$+1/2$	68%
these_vla_6	8	$8\,\mu\text{m} = 10\lambda$	10.7	$-1/2$	88%
these_vla_7	8	$8\,\mu\text{m} = 10\lambda$	5	$+1/2$	57%

Table 4.2: Simulation condition for a scan in Π parameter. All simulations were run with the `test-particle code`, with 10 000 electrons, $\Gamma_0 = 4$, $\tau_L = 30\,\text{fs}$. The electrons start in the pulse center, at a field node, with $\phi_0 = 0$ and Gaussian distribution $(x_0, y_0) = (0 \pm w_0/2, 0 \pm w_0/2)$ and $(p_{x0}, p_{z0}) = (0 \pm 1, 0 \pm 1)m_e c$.

We performed a set of numerical runs to illustrate this result. The simulation conditions are shown on table 4.2. Simulation `these_vla_1` was run for $\Pi = 0$. Simulations `these_vla_2,4,6` were run with $\Pi = -1/2$ varying w_0, a_0 and μ respectively. Simulations `these_vla_3,5,7` were run with $\Pi = +1/2$ varying w_0, a_0 and μ respectively. The result is shown in figure 4.15, where the ratio of VLA electrons is plotted as a function of the Π parameter.

The simulations run until all electrons have left the pulse. Electrons are considered to have a VLA dynamics if they remain in the same optical cycle (see ≤ 1 sign change of the electric field) until they leave the pulse. An electron is considered out of the pulse if the laser amplitude at the electron position is smaller than $a_0/100$.

Expression 4.36 gives $\mathbb{P}[VLA](\Pi = 0) = 50\%$, $\mathbb{P}[VLA](\Pi = -1/2) = 76\%$ and $\mathbb{P}[VLA](\Pi = +1/2) = 24\%$. The absolute values do not match the simulation results because of the rough approximations we have made (plane wave, $\sigma_x = \sigma_y = 0$ and $\sigma_{px} = \sigma_{py} = 0$ for the initial distributions in the derivation), but the trends are very well reproduced, and Π appears to be the relevant parameter. Note that, for $\mu = 5$, hypothesis $\gamma_0 \gg 1$ is a bit weak because $\gamma_0 = 5 \pm 4$.

In this section, for a given initial electron distribution inside a laser pulse, we derived a parameter Π that discriminates whether vacuum laser acceleration or ponderomotive scattering is the dominant mechanism. We showed that VLA was dominant for $\Pi < 0$. On the opposite, when $\Pi \gg 1$, most electrons have ponderomotive dynamics.

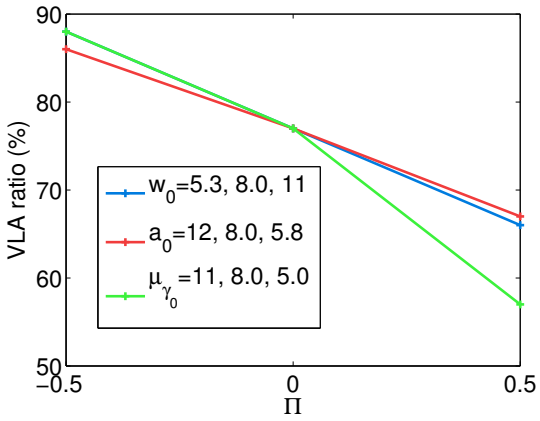


Figure 4.15: Ratio of VLA electrons as a function of the Π parameter. Simulations were run with 10000 particles. The laser parameters are described in table 4.2.

4.3 Vacuum laser acceleration using a plasma mirror injector

4.3.1 Experimental attempts for vacuum laser acceleration

Though vacuum laser acceleration may lead to energy gains up to a factor of several orders of magnitude, few experimental results meet theoretical expectations. The most efficient acceleration is expected for initially relativistic electrons propagating along with the laser in the second configuration – figure 4.5b). Yet this configuration is extremely challenging to fulfil, as it requires to inject electrons in a few cubic microns with femtosecond precision. The main published results in the field are listed below.

Experiments with electrons starting before the laser pulse

The first idea for electron acceleration in vacuum is to focus an intense laser pulse into a low-temperature electron cloud. This was first performed in reference [Malka & Miquel, 1996]. A prepulse is focused onto a thin solid target to generate a cloud of free electrons behind the target. The energy of electrons in the cloud is around a few tenths of keV. The main laser pulse is focused in the electron cloud. The laser parameters are $\lambda = 1.056\,\mu$m, $w_0 = 10\,\mu$m, the pulse duration is 500 fs and the normalized amplitude is $a_0 = 3$.

Electrons up to 1 MeV energy were detected at an angle $\theta \simeq 45°$ with respect to the propagation direction in the polarization plane $(\boldsymbol{k}, \boldsymbol{E})$, and the effect of the laser fields was clearly demonstrated. Yet their explanation remained controversial, as they modeled the experimental results without describing the ponderomotive force, which is supposed to play a dominant role in this interaction, as explained in the comment [Mora & Quesnel, 1998].

From Hartemann's analysis, we expect the acceleration to be more efficient for electrons with a strong longitudinal velocity, according to the formula

$$\gamma_{max} = \gamma_0 \left[1 + 2(1 + \beta_{z0})a_0^2\right]. \tag{4.39}$$

Hence, focusing a laser beam onto a copropagating relativistic electron beam is likely to result in a higher energy gain for the electrons. This idea was presented in reference [Esarey *et al.*, 1995], where the authors propose to focus a laser beam with

a parabolic mirror with a small hole. An externally-accelerated electron bunch goes through the hole and meets the laser beam at focus, as shown in figure 4.16.

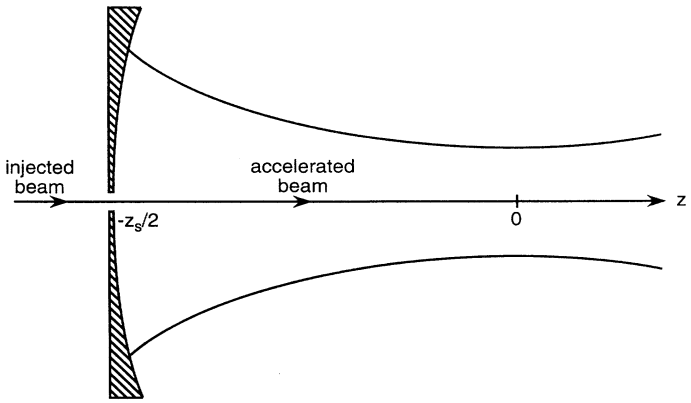


Figure 4.16: [Image from reference [Esarey *et al.*, 1995]] Schematic of a parabolic mirror with a hole for vacuum acceleration.

However this setup is extremely difficult to build. One attempt is presented in reference [Cline *et al.*, 2013] with a CO_2 laser with $a_0 \simeq 2$. The electron bunch energy was 20 MeV. The effect of the laser was to increase the energy spread from 1.8% to 3.3%. Even though this result shows that electrons can be accelerated in vacuum with a laser pulse with relativistic intensity, their setup can clearly not be used as an electron accelerator since it degrades an externally-generated high-quality electron beam, as in reference [Plettner *et al.*, 2005]. Besides, the energy gain is extremely low. Another attempt is presented in reference [Carbajo *et al.*, 2015], with a radially-polarised laser beam. The acceleration remains below the keV range, and the accelerated charge is of the order of a femtocoulomb (10^4 electrons).

Experiments with electrons starting inside the laser pulse

A much higher energy gain is expected when electrons are injected inside the laser pulse, where they undergo vacuum laser acceleration. Several experiments lead to low-energy electrons (see reference [McNaught *et al.*, 1998]). Let us focus on reference [Moore *et al.*, 1999], which presents experimental results in a very low-density gas. The laser parameters are $\lambda = 1\,\mu$m, $a_0 = 1.5$ ($I = 3 \times 10^{18}\,\mathrm{W \cdot cm^{-2}}$), and the pulse duration is $\tau_L = 400$ fs.

Electrons are injected in the laser pulse via ionization. The laser pulse is focused into a chamber filled with 1 Torr Krypton gas. While outermost electrons are ionized at the very front edge of the laser pulse, the eighteenth ionization (Kr^{18+}) occurs via barrier-suppression ionization when the intensity reaches the threshold $I_{th} = 2 \times 10^{18}\,\mathrm{W \cdot cm^{-2}}$. Electrons are freed in the laser around a maximum of the electric field, with low energy ($p_0 \ll a_0$). This clearly violates hypothesis (H4) of the Lawson-Woodward theorem. Electrons up to 300 keV were observed in this experiment in the plane of polarization. Yet the weakness of this configuration is that electrons are injected with zero velocity around a field maximum, *i.e.* with transverse canonical momentum $\boldsymbol{P}_{\perp 0} = 0$, which is definitely not optimal for VLA.

According to equation 4.39, the highest final energies can be obtained with electrons starting inside the laser pulse with high speed along the propagation direction. We hereafter show how a plasma mirror can make electron injection in these conditions possible.

As described in chapter 1, several experiments deal with the acceleration of electrons during the reflection of a laser pulse off an overdense plasma. In particular, a 1 MeV electron bunch around the specular direction is observed in reference [Mordovanakis *et al.*, 2009] using a $\lambda = 800\,\text{nm}$, $a_0 \simeq 1.5$, 30 fs-long laser pulse. Yet the electron acceleration is not identified as vacuum laser acceleration, and the acceleration mechanism is not discussed in great detail and remains hazy.

4.3.2 Principle

As shown in chapter 3, the reflection of a laser pulse from a plasma mirror results in ejection of electrons from the plasma surface into the reflected pulse once per laser period. These electrons are injected at zeros of the reflected field with a relativistic velocity. Hence, plasma mirrors can be used as electron injectors in the reflected laser field, providing a simple experimental solution to study the interaction of free electrons with intense lasers in vacuum.

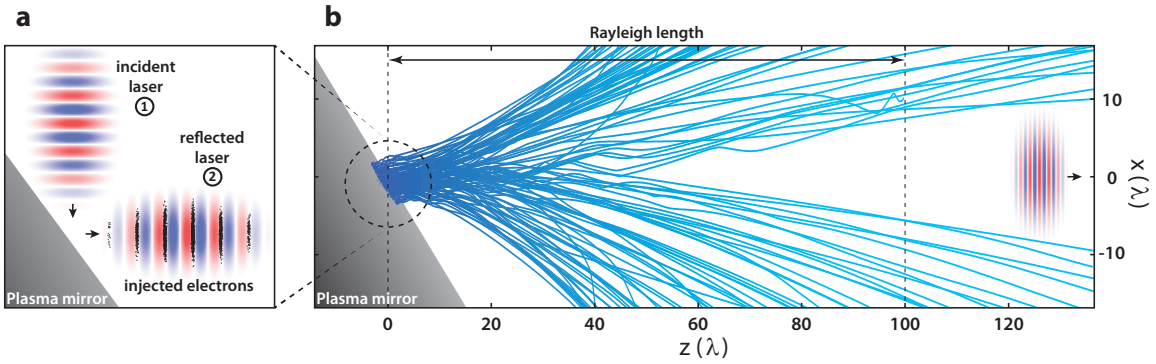


Figure 4.17: **Injection of relativistic electrons in ultraintense laser fields using plasma mirrors**. Panel a): principle of a plasma mirror injector. As an ultraintense laser pulse (E-field sketched in red and blue) reflects off a plasma mirror and expels relativistic electrons (black dots) at specific phases of the field. Panel b) shows electron trajectories (blue lines) computed from a 2D PIC simulation. Once expelled from the surface, they copropagate and interact with the reflected laser field over a distance of the order of the Rayleigh length ($z_R = 100\lambda$). This interaction clearly modifies the electron angular distribution as electrons are expelled to the sides of the focal volume.

This principle is illustrated in figure 4.17. Panel a) shows injection of attosecond bunches during the pulse reflection on the plasma mirror. Panel b) shows a snapshot of electron trajectories from a 2D PIC simulation. The simulation was performed with $a_0 = 5$ and $w_0 = 5\,\mu\text{m}$, the pulse duration is 25 fs. The plasma bulk density is $n = 100 n_c$ and the density gradient scale length is optimal for electron ejection $L = \lambda/8$. The reflected pulse on the right is an aid to the eye. Electrons are ejected from the plasma surface in the focal spot and propagate along the reflected pulse. They form a spray that propagates along the reflected pulse. After a distance of the order of the laser Rayleigh length, they spread on both sides of the laser pulse.

In the following sections, experimental results for vacuum laser acceleration using a plasma mirror injector are detailed. A numerical model is derived, that reproduces the experimental results. Finally, this model is used for discriminating VLA and ponderomotive behaviours in the final electron distribution from the experiment.

4.3.3 Experiment by Adrien Leblanc (UHI100 at CEA)

The experimental setup is shown in figure 4.18. The spatial profile of electron beams emitted by a plasma mirror exposed to an ultraintense laser pulse is measured, as well as their energy distributions at different emission angles. It was performed with the UHI100 laser of CEA/IRAMIS, a 100 TW laser system that delivers 800 nm, 25 fs pulses. Once the temporal contrast is improved by 4 orders of magnitude with a plasma-based temporal filtering system (see reference [Lévy *et al.*, 2007]), the laser pulses are focused on a flat fused silica target with an incidence angle of 55° and p-polarization, at a peak intensity of 2.10^{19} W $\cdot$ cm^{-2} ($a_0 \simeq 3.1$). The focal spot is 5.5 μm FWHM and the Rayleigh length is about 80 μm. To optimize the electron signal, the scale length of the plasma density gradient at the surface was accurately controlled by preionizing the target with a weaker prepulse ($\approx 10^{16}$ W $\cdot$ cm^{-2}) at an adjustable delay of a few hundred femtoseconds before the main pulse (see reference [Kahaly *et al.*, 2013]). The target ionization by the prepulse and the plasma expansion are described in section 1.1.2, page 13. The electron beam spatial profile was measured using a LANEX phosphor screen placed 15 cm away from the target, perpendicularly to the specular direction, imaged on a CCD camera. A magnetic spectrometer can be inserted before this LANEX screen in order to measure the electron energy distribution.

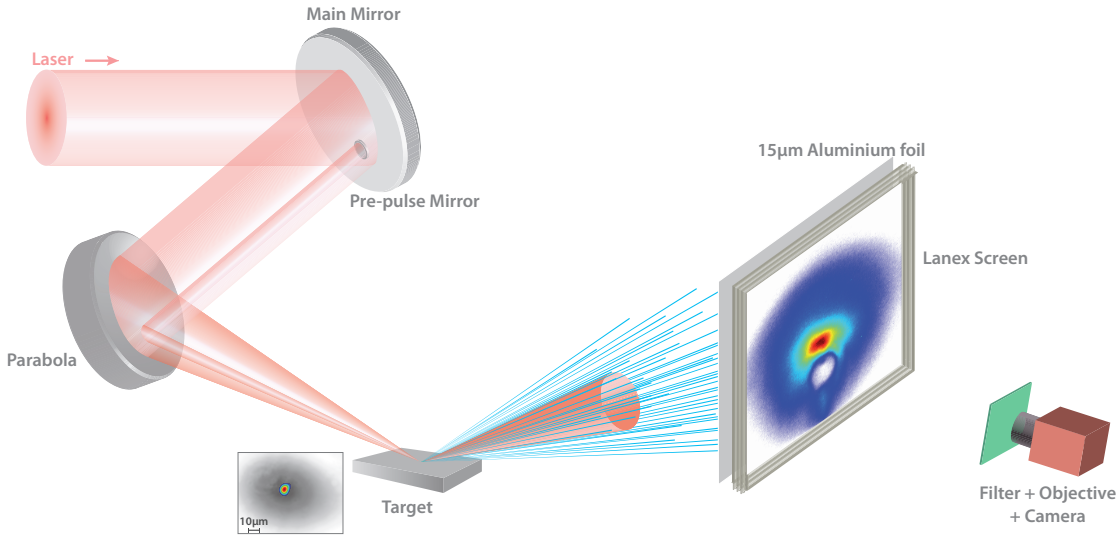


Figure 4.18: [Courtesy of A. Leblanc] Experimental setup on the UHI100 laser at CEA.

A typical electron angular distribution is shown in Fig. 4.19 a). The measured electron emission spreads over a broad cone of ≈ 600 mrad angular width, but is spatially very inhomogeneous within this cone. A pronounced hole is observed in the propagation direction of the reflected beam, with a cylindrical symmetry around this axis. The total angular width of this hole is about 200 mrad, comparable to the divergence of the reflected beam. The other dominant feature is a bright electron peak on one edge of this hole, along the direction of the laser polarization (horizontal axis in Fig. 4.19) and located between the specular and the normal directions. Its divergence is about 100 mrad, much smaller than that of the total electron beam. From the signal measured on the calibrated LANEX screen (see reference [Glinec *et al.*, 2006]), the overall charge in the electron beam is about 12 nC, with 3 nC within the bright spot. These patterns were clearly observed at high intensity $I > 10^{19}$ W $\cdot$ cm^{-2} and optimized for experimental gradient scale lengths of $L \simeq \lambda/15$.

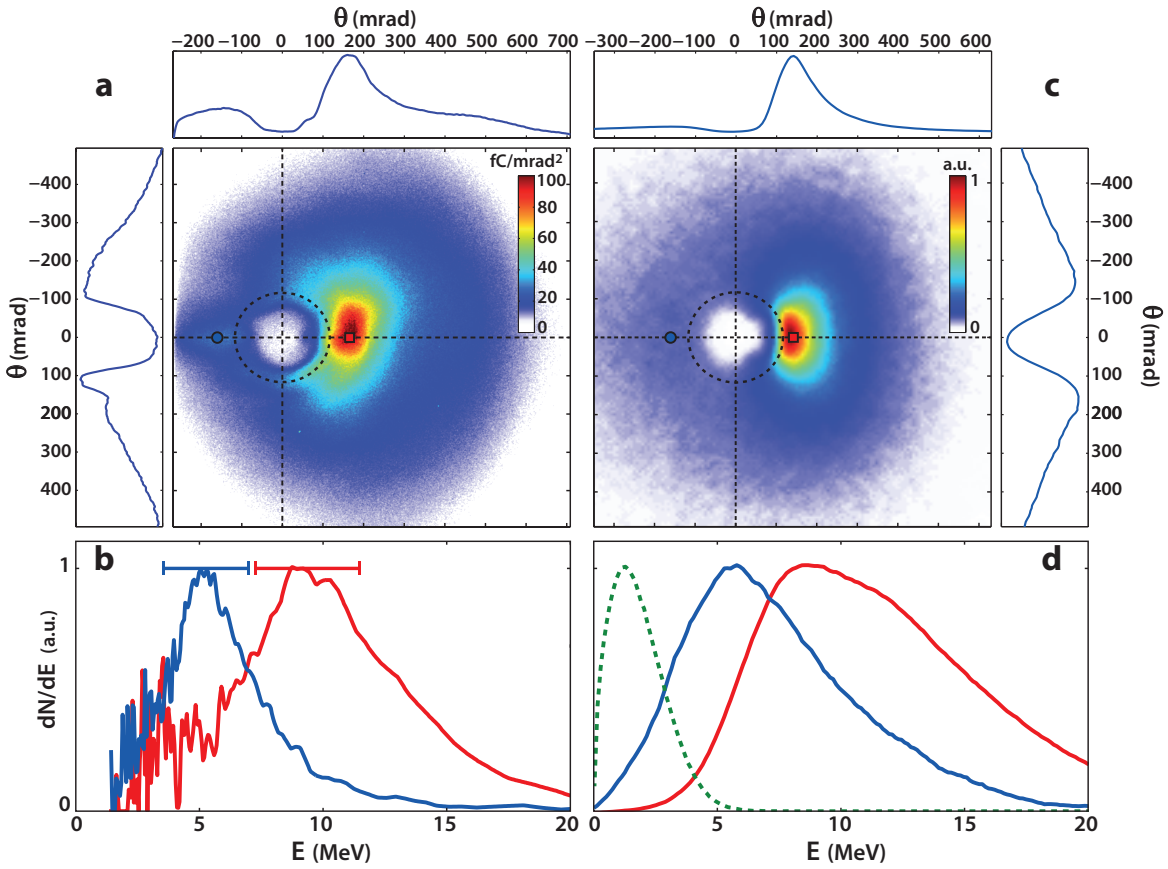


Figure 4.19: **Experimental evidence of vacuum laser acceleration.** Panel a) shows a typical experimental angular distribution of electrons emitted from plasma mirrors into vacuum, measured with the LANEX screen. It consists of a broad emission cone (blue disk), which is strongly modulated by two patterns: a hole around the specular direction due to ponderomotive scattering and a bright spot due to vacuum laser acceleration. Line-outs of the distribution along the dashed lines are plotted in the side panels, and the direction normal to the plasma mirror surface corresponds to $\theta \simeq 960\,\mathrm{mrad}$ (not shown). Panel b) shows the electron spectra measured at two different locations in the beam, indicated by the blue circle and the red square in panel a), that respectively correspond to the blue and red curves of panel b). Panel c) and d) show the same quantities, from numerical simulations with the `test-particle code`. The dashed green curve in panel d) shows the initial electron energy distribution used in this model. As can be seen from the green and red spectra in panel d), the model shows that electrons are accelerated by VLA from 1.5 MeV to 10 MeV, resulting in an energy gain of 7.

Figure 4.19b) shows the spatially-resolved electron spectra measured at two different locations in the beam, on opposite sides of the hole along the laser polarization direction. Broad peaked spectra are observed, with a central energy of a few MeV. The key feature here is that the central energy is twice higher in the bright electron peak (10 MeV) than on the opposite side of the hole (5 MeV). This difference in energy suggests a straightforward interpretation for the spatial pattern of the electron beam. The bright spot in the polarization plane could correspond to electrons which have gained energy by VLA due to appropriate injection conditions in the field. The other electrons in the beam would have experienced isotropic ponderomotive scattering, leading to the symmetrical hole around the laser axis. We now validate this interpretation, by first studying the conditions of injection of electrons from plasma mirrors into the vacuum, and then their subsequent dynamics in the reflected field.

4.3.4 Model

Practical coordinate systems

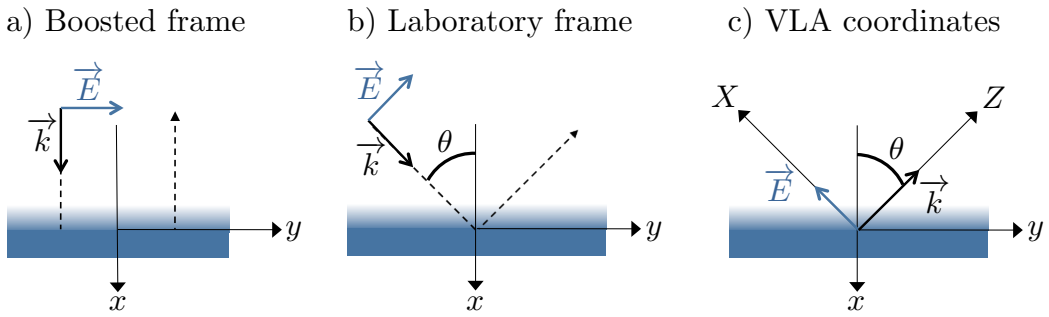


Figure 4.20: a) Configuration in the boosted frame for 1D PIC simulation. b) Configuration in the laboratory frame. c) Coordinate system adapted to the study of VLA in the reflected pulse.

The properties of electrons ejected from the plasma mirror into the vacuum are taken from PIC simulations. Classic notations were used for 1D PIC simulations in the boosted frame in all this work, as shown in figure 4.20 a). Yet most practical notations for VLA use Z as the laser propagation direction and X as the polarization direction. The initial conditions are injected in the `test-particle code` after (i) a Lorentz transform to go back to the laboratory frame (see chapter 2) and (ii) a rotation to deal with VLA. These steps are illustrated in figure 4.20. The Lorentz factor and normalized velocity for the *Bourdier* $\rightarrow$ *Laboratory* transformation read

$$\gamma_0 = \frac{1}{\cos\theta} \qquad\qquad \beta_{y0} = -\sin\theta. \tag{4.40}$$

These transformations read

$$\left\{\begin{array}{l}\gamma^B\\ p_x^B\\ p_y^B\end{array}\right. \longrightarrow \left\{\begin{array}{lcl}\gamma^L &=& \gamma_0\gamma^B - \gamma_0\beta_{y0}\frac{p_y^B}{m_e c}\\ p_x^L &=& p_x^B\\ p_y^L &=& -\gamma_0\beta_{y0}\gamma^B m_e c + \gamma_0 p_y^B\end{array}\right. \longrightarrow \left\{\begin{array}{lcl}\gamma^L & & \\ p_X^L &=& -\sin\theta p_x^L - \cos\theta p_y^L\\ p_Z^L &=& -\cos\theta p_x^L + \sin\theta p_y^L\end{array}\right. \tag{4.41}$$

where exponents B and L stand for coordinates in the Boosted frame and Laboratory frame respectively. The first arrow stands for the Lorentz transformation, the second

λ	a_0	n_{max}	L	T_e	ions	Δx	ppc
800 nm	2.1	$400n_c$	$\lambda/8$	1 keV	immobile	$\lambda/1000$	4000

Table 4.3: Simulation conditions for the `p-CI1D` 1D PIC simulation performed with EPOCH. They are all given in the laboratory frame for easy comparison with the experiments.

one is a simple rotation around $Y = y$. Here, Z and X stand for the propagation and polarization directions respectively, for the reflected pulse.

From now on, all quantities will be considered in the (X, Y, Z) coordinates in the laboratory frame and will be noted with lower case letters (x, y, z) for the sake of simplicity. These transformations are performed via the script `CIBouOlle.m`.

Injection from the plasma mirror: 1D PIC simulation

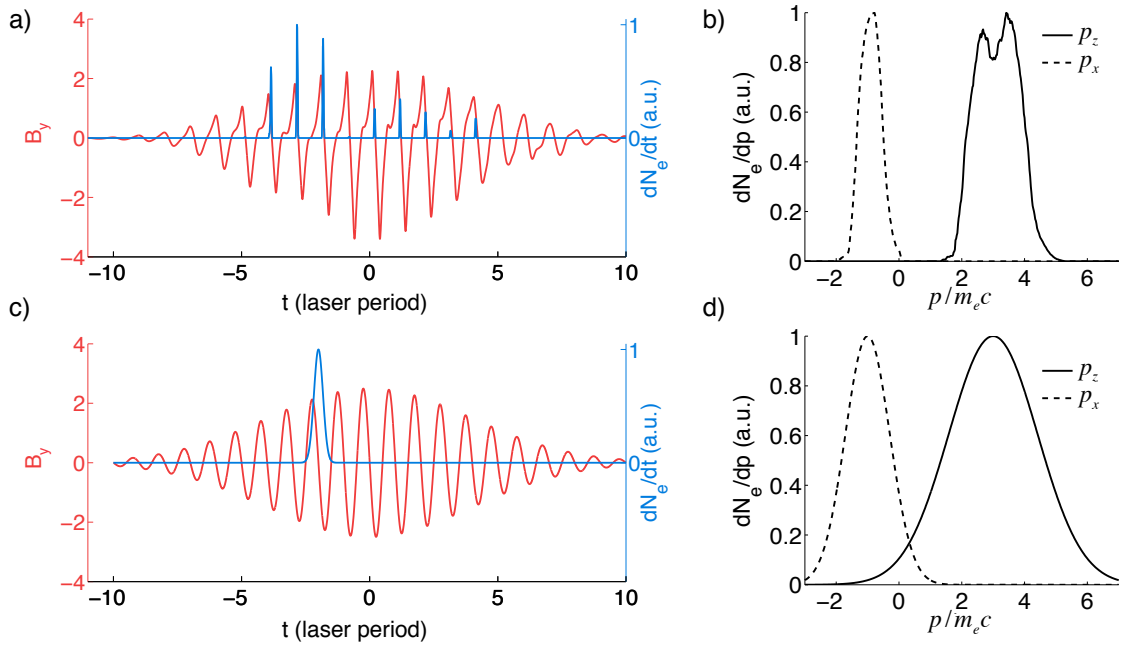


Figure 4.21: **Initial conditions of electrons ejected from plasma mirrors.** Panel a): waveform of the laser magnetic field B_y reflected by the plasma mirror (red line), and temporal density profile of the ejected high-energy electrons (blue line), obtained from PIC simulations. Both quantities were sampled at $z = 750$ nm from the plasma mirror surface. Panel b) shows the corresponding momentum distribution of these electrons, along the specular direction (p_z) and along the polarization direction of the reflected laser (p_x), taken from the 1D PIC simulation `p-CI1D`. c) and d) show the initial conditions as injected in the `test-particle code`.

The simulation parameters for the 1D PIC simulation `p-CI1D` are shown in table 4.3. The laser is assumed to deliver a pulse with Gaussian envelope and maximum amplitude $a_0 = 3$ in the experiment. We took $a_0 = 2.1$ as its mean value on the focal spot. Figure 4.21 a) shows the density of ejected electrons as a function of time, together with the waveform $B_y(t)$ of the reflected field for interaction conditions corresponding to the experiment. These quantities were both sampled very close to the plasma mirror surface ($d \ll w_0$), when electrons escape the plasma and are injected into the vacuum

λ	a_0	w_0	$\boldsymbol{R}_{st}/\lambda$	σ_R/λ	$\boldsymbol{P}_{st}/m_e c$	$\sigma_P/m_e c$
800 nm	2.5	5 μm	$(0,0,0)$	$(2,2,0.1)$	$(-1,0,3)$	$(1,1,3)$

Table 4.4: Simulation conditions for run `p-VLA-2015` with the `test-particle code`. The wavelength is $\lambda = 800\,\text{nm}$. We chose $a_0 = 2.5$ to account for the $\sim 70\%$ reflectivity. The initial distribution in position (momentum) is a Gaussian distribution with center $\boldsymbol{R}_{st}$ ($\boldsymbol{P}_{st}$) and standard deviation σ_R (σ_P).

in the core of the reflected field. Once again, electrons are observed to be emitted in the form of attosecond bunches at laser field nodes.

The waveform of the reflected field deviates from a pure sine wave because of high harmonic generation. While this can quantitatively affect the exact outcome of the subsequent laser-electron interaction in vacuum, we will show that this does not qualitatively alter the physics involved. Note that due to the gyromagnetic effect or cycle-to-cycle effects, the electron injection significantly drops around the peak of the laser pulse and most electrons are injected slightly before the pulse maximum.

Figure 4.21b) shows the momentum distributions of these electrons right after their ejection, along the specular direction (p_z) and along the laser polarization direction (p_x). Electrons start their motion in vacuum in the reflected laser pulse with relativistic velocities, corresponding to an average energy of 1.5 MeV ($\gamma_0 \simeq 3$), and are ejected with an average angle of 20° away from the specular direction. These initial conditions are close to being ideal for the observation of VLA, and definitely much more favorable than those achieved in all previous experimental attempts to observe this effect (see references [Carbajo *et al.*, 2015; Cline *et al.*, 2013; Moore *et al.*, 1999]).

Propagation in the reflected pulse: test-particle code

To study the subsequent interaction of these electrons with the laser field in vacuum, we turn to the `test-particle code` to calculate the trajectories of two million electrons injected in the field. The set of initial conditions from the PIC simulation `p-CI1D` is shown in figures 4.21 a) and b). The initial conditions injected in the `test-particle code` are shown in figures 4.21c) and d). For the sake of simplicity, a single electron bunch is injected in the reflected field, corresponding to ejection at a single laser period. Besides, larger distributions were taken for the initial phase and momentum (p_x, p_z).

This choice is justified by the following arguments: (i) the 1D PIC simulation gives the initial conditions for a given value of the incident laser intensity I, while the intensity actually varies between 0 and I_0 in the laser focal spot. (ii) When electrons are ejected from the plasma, they travel through a zone where the incident field and the reflected field are superimposed. As shown in figure 3.22, the incident field results in oscillations in the electron trajectories, which we expect to blur the distribution after a short distance $d < w_0/2$. Except for this blurring effect, we neglect the role of the incident field after the electron ejection. Hence, we took initial conditions from figure 4.21 as initial conditions in the `p-VLA-2015` run with the `test-particle code`. The simulation parameters for this run are gathered in table 4.4.

Figure 4.19c) shows the angular electron distribution obtained from these simulations, for physical conditions corresponding to the experiment. The agreement of this distribution with the experimental one is striking: the two main features observed in the experiment – the hole around the laser axis and the bright peak shifted along the laser polarization – are both well reproduced. The final energy spectra calculated on

each side of the hole are shown in figure 4.19d) and also compare well with the experimental observations. Despite its simplicity, this model thus captures the essential physics of the interaction in vacuum. This shows that effects such as space charge or the nonsinusoidal waveform of the reflected field, not taken into account in these simulations, do not play a major role once electrons are in vacuum.

4.3.5 Interpretation of the experimental results

Considering this good agreement, the 3D model can now be exploited to analyze the trajectories of electrons contributing to the different patterns observed in the electron beam. To this end, we sort the electrons into different groups, depending on the number of laser optical cycles N_{oc} that they have crossed along their trajectories. This provides a quantitative criterion for distinguishing electrons that experienced vacuum laser acceleration from those scattered by the ponderomotive force. It is illustrated in figure 4.22 a) which shows two trajectories $(x, z - ct)$, representative of these two regimes: $N_{oc} \leq 1$ (full line) and $N_{oc} = 3$ (dashed line). The corresponding temporal evolutions of the electron Lorentz factor are shown in figure 4.22 b).

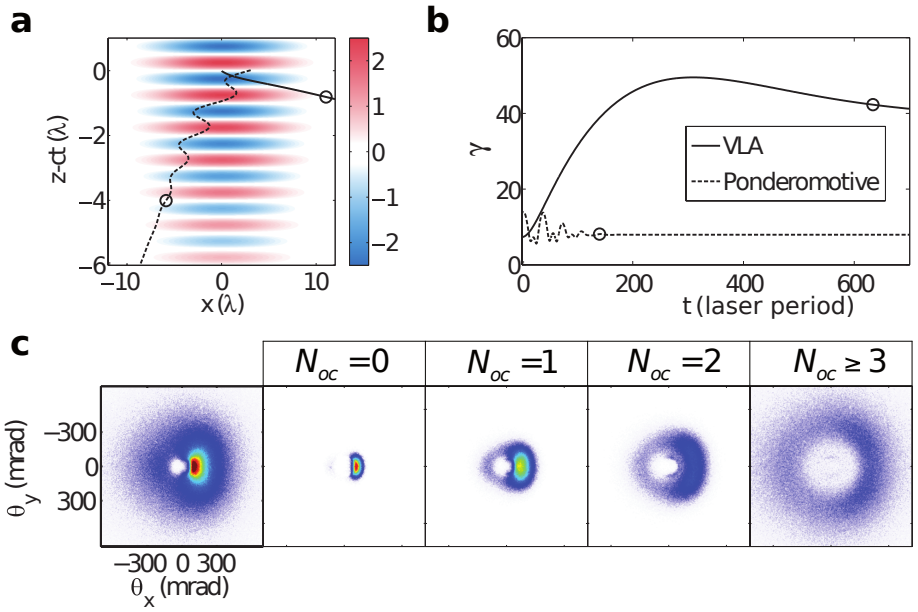


Figure 4.22: **Final distribution from run `p-VLA-2015` with initial conditions from the PIC simulation `p-CI1D`** Panel a) shows two types of electron trajectories, corresponding to electrons that have respectively explored $N_{oc} \leq 1$ (full line) and $N_{oc} = 3$ (dashed line) optical cycles before escaping the laser beam. The trajectories are displayed in a coordinate system moving with the laser beam, and the colourmap sketches the laser field in this frame. The circles represent the positions for which we consider that these electrons escape the laser pulse, *i.e.* when the pulse envelope at the electron position is less than $a_0/100$. Panel b) shows the temporal evolution of the electron Lorentz factor $\gamma(t)$ along these two trajectories. Panel c) shows the angular distribution of various electron populations which are sorted according to the number of optical cycles they experience.

In the first case, the VLA electron does not oscillate in the field, but rather surfs the laser wavefront in which it was injected, along the polarization direction. It gains energy almost all along its trajectory, until it escapes the focal volume sideways after an interaction distance of the order of the Rayleigh length. In contrast, the ponderomotive electron oscillates as it explores several optical cycles of the laser field, and gets quickly

expelled out of the laser beam with a low energy gain – akin to a surfer that has missed the wave – as illustrated in figure 4.22 b), where the circles stand for the ejection time.

In practice, there is a continuous transition between these two extreme types of trajectories, depending on the exact electron injection conditions in the field. This is illustrated by the images in figure 4.22 c), showing the beam patterns produced by several sub-ensembles of electrons in the simulations, corresponding to N_{oc} varying from $N_{oc} = 0$ (VLA electrons) to $N_{oc} \geq 3$ (ponderomotive electrons). Ponderomotive electrons form a doughnut-shaped beam centered on the laser propagation axis, while VLA electrons tend to concentrate in a bright peak on the edge of the ponderomotive hole, along the polarization direction, as seen in section 4.2 (page 120).

This analysis confirms our interpretation of the electron beam patterns observed in experiments, and provides clear proof that the bright peak in these patterns is due to VLA. According to our simulations, these electrons are accelerated from 1.5 MeV to 10 MeV (figure 4.19 d)) over a distance of less than 100 μm, corresponding to an energy gain by VLA of about 7 in this experiment. In addition, a remarkable feature of VLA is that the position of the peak in figure 4.22 c) depends on the phase of injection of electrons in the laser field: if we artificially vary this phase by π (half a laser period) in the simulation, this bright spot shifts to the other side of the ponderomotive hole. The experimental observation of this peak *on one side only* of the hole is thus a clear indication that electrons are ejected out of the plasma mirror at a specific phase of the laser field, in the form of sub-laser cycle (attosecond) bunches.

Conclusion: Accelerating electrons directly in a laser pulse has been a long-standing issue, in particular because of its simplicity. The available intense electromagnetic fields give hope that electrons could be accelerated up to highly relativistic energies within a few microns.

In spite of this apparent simplicity, efficiently accelerating a bunch of electrons has proved difficult. There is a lot of variety in the dynamics of an electron into an intense laser, and the conditions for obtaining a high energy gain are stringent.

In this chapter, we identified the two most archetypal dynamics: (i) **ponderomotive** when electrons oscillate many times in the laser field and (ii) **VLA** when they do not oscillate but remain in the same laser period until they escape the pulse. We presented scaling laws for the final angle and energy in both cases. Besides, for a given electron distribution, we derived a criterion stating whether the VLA or the ponderomotive dynamics is dominant.

We show that a high energy gain can be expected for electrons via the VLA mechanism provided the electrons start inside a high-intensity laser pulse with an initial relativistic speed along the pulse propagation direction. This condition is extremely challenging to fulfill experimentally, and most experiments to date lead to ponderomotive scattering with low energy gain.

This problem can be solved using a plasma mirror injector: during the reflection of a laser pulse upon a plasma mirror, electrons are ejected from the plasma towards vacuum and can undergo VLA in the reflected pulse. The experiment was performed on the UHI100 laser at CEA, and resulted in a 3 nC 10 MeV electron bunch accelerated via VLA. Finally, we present a model to interpret the experimental electron distribution as the superposition of a doughnut due to ponderomotive electrons and a bright spot of VLA electrons.

Chapter 5

Electron acceleration and high harmonic generation

Contents

5.1 Anticorrelation CWE/electrons in the low-intensity regime $a_0 < 1$ 143

5.1.1 Experimental results from the *Salle Noire* laser (LOA) by Maïmouna Bocoum 143

5.1.2 Dynamics of ejected electrons 148

5.2 Correlation ROM/electrons in the high-intensity regime $a_0 > 1$ 149

5.2.1 Expected correlation 150

5.2.2 Experimental results from the UHI100 laser (CEA) by Adrien Leblanc 150

5.2.3 Confirmation from PIC simulations 152

Introduction

As presented in chapter 1, the reflection of an ultraintense laser pulse upon an overdense plasma is an extremely rich interaction that can lead to particle acceleration as well as high harmonic generation via two distinct processes. The coherent wake emission process (CWE) is optimal for relatively low laser intensities ($a_0 < 1$) and very short density gradients ($L < \lambda/40$) whereas the relativistic oscillating mirror (ROM) mechanism prevails for high intensities ($a_0 > 1$) and longer gradients $L \sim \lambda/10 - \lambda/5$. Both mechanisms occur once per laser period and result in a train of attosecond bunches in the reflected field, giving rise to harmonics of the laser frequency in the spectral domain. They are detected in experiments by measuring the spectrum of the reflected field, and ejected electrons can also be detected in the backward direction. Comparing these mechanisms gives significant insight into the plasma surface dynamics.

Figure 5.1 shows the electron density map and the generation of attosecond bunches from the 1D PIC simulation `these_cwerom`. The first laser period leads to the ejection of an electron bunch (elec1), a ROM attosecond bunch (rom1) and a CWE attosecond bunch (cwe1), showing the simultaneity of these mechanisms. The first bunch rom1 is generated by electrons accelerated towards $-x$ whereas cwe1 starts deeper inside the plasma, due to plasma oscillations in the overdense region. The relative strength of both mechanisms depends on the intensity and gradient conditions. The physical conditions $a_0 = 1$ and $L = \lambda/60$ were chosen with care so that both HHG mechanisms occur with a comparable strength.

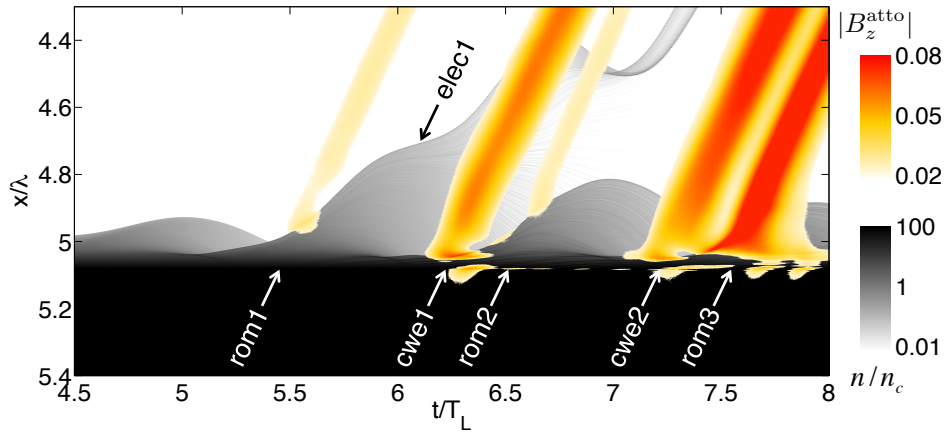


Figure 5.1: Attosecond bunches from ROM and CWE mechanisms from 1D PIC simulation `these_cwerom` with $a_0 = 1$, $L = \lambda/60$, $n_{max} = 100n_c$ and $\tau_L = 4T_L$ FWHM with a $\sin^2$ envelope, during the rising edge of the pulse. $n(x = 5\lambda) = n_c$. The grey scale represents the electron density, and the yellow-red scale the envelope of the attosecond reflected field (a Fourier filter was applied to keep harmonics order above 4).

Section 5.1 focuses on the low-intensity regime where CWE is dominant. It is shown that harmonic generation and electron emission occur for distinct gradient lengths. The electron ejection and acceleration mechanisms in the low-intensity regime are compared to the push-pull and VLA mechanisms that take place at high intensity. Section 5.2 is dedicated to the high-intensity regime, and a clear correlation between ROM harmonics and electron emission is demonstrated. Both sections strongly rely on experimental results obtained on cutting-edge laser systems at LOA and CEA. In either case, the optimal gradient is observed and measured to be around $L = \lambda/10$, confirming our theoretical predictions.

5.1 Anticorrelation CWE/electrons in the low-intensity regime $a_0 < 1$

The dominant mechanism for high harmonic generation in the low-intensity regime is the CWE mechanism, as detailed in chapter 1. It relies on bunches of electrons, called Brunel electrons, propagating towards the plasma bulk ($+x$), as shown in figure 5.2 a).

Electron ejection in this regime occurs via the same push-pull mechanism as in the high-intensity regime, described in chapter 3: electrons are pushed towards the plasma bulk, forming a plasma capacitor with the immobile ions. This plasma capacitor accelerates an electron bunch towards vacuum, and some escape the plasma, as shown in figure 5.2b).

This discussion gives clues that these processes should not be simultaneous: CWE is dominant when many electrons travel towards $+x$ whereas a bunch of electrons may be ejected if a strong acceleration occurs towards $-x$. In addition, they are expected to take place for very different gradient lengths: $L \simeq \lambda/50$ (see chapter 1) and $L \simeq \lambda/10$ (see chapter 3) respectively.

In section 5.1.1, through a controlled pump-probe experiment using sub-relativistic femtosecond laser pulses, we directly observe the transition from a confined plasma that can efficiently emit laser harmonics – figure 5.2 a) – to an extended plasma structure that accelerates fast electrons into vacuum up to a few hundred keV – figure 5.2b).

Section 5.1.2 is dedicated to the electron ejection and acceleration processes. It is shown that the same push-pull mechanism occurs as in the high-intensity regime. Yet no vacuum laser acceleration occurs in this regime: the final energy of ejected electrons is the energy they obtain from the plasma capacitor.

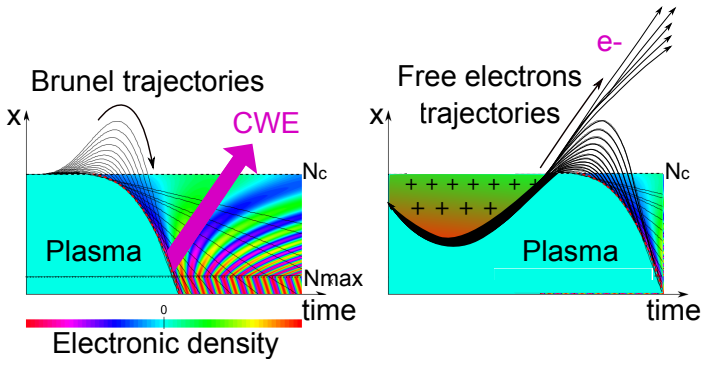


Figure 5.2: Diagrams of plasma mirror surface structures leading to a) CWE and b) electron acceleration on the sub-laser-cycle time scale: electrons are accelerated in the density gradient and escape from the plasma.

5.1.1 Experimental results from the *Salle Noire* laser (LOA) by Maïmouna Bocoum

Experimental setup and results

The experiment was carried out on the *Salle Noire* laser system at Laboratoire d'Optique Appliquée (LOA) delivering 3 mJ energy, 30 fs (FWHM in intensity) pulses at 1kHz repetition rate with high temporal contrast (better than $> 10^{-10}$, see reference [Jullien *et al.*, 2014]). This experimental work was performed by M. Bocoum during her Ph.D.

The p-polarized pulse is focused down to 1.7 μm FWHM spot size onto an optically flat fused silica target ($\sim 250 n_c$), leading to peak intensities on target $\simeq 10^{18}\,\mathrm{W/cm^2}$ ($a_0 \simeq 0.7$) for an incidence angle $\theta_L = 49.3°$, with repetition rate of 1 kHz (see reference [Borot *et al.*, 2014]). 5% of the main beam is picked off and focused down to 5 times the main beam spot size on target in order to induce homogeneous plasma expansion at the surface. The plasma scale length L can then be varied by changing the relative delay between this prepulse and the main high-intensity pulse. Spatial Domain Interferometry (SDI), presented in reference [Bocoum *et al.*, 2015], was used to estimate the plasma expansion velocity c_s and we find $c_s = dL/dt = 10.8 \pm 1.1, \mathrm{nm/ps}$ for a prepulse intensity of $\simeq 3.5 \times 10^{14}\,\mathrm{W/cm^2}$ ($a_0 \simeq 0.013$).

Harmonics emitted in the specular direction are sent into a home-made XUV spectrometer where the harmonic spectrum is resolved in the horizontal plane and the harmonic beam divergence in the vertical direction using a coupled MCP and phosphor screen detector. At the same time, a $6 \times 17\,\mathrm{cm}$ Lanex scintillator was positioned 10 cm away parallel to the target surface without blocking the specular direction. The angular electron emission profile in this geometry was recorded as a function of $\theta \in [-20°\ 30°]$, the angle with respect to target normal in the plane of incidence and $\phi \in [-20°\ 20°]$, the angle with respect to target normal in the tangential plane. Note that the Lanex screen only detects electrons with energies larger than 150 keV, see reference [Glinec *et al.*, 2006]. The Lanex screen could also be replaced by an electron spectrometer to characterize the electron energy distribution.

Figure 5.3 a) shows the harmonic spectrum and the electron signal as a function of pump-probe delay, hence the gradient length. The harmonic signal was integrated along the divergence angle. The plasma scale length calculated from the plasma expansion velocity is indicated on the bottom axis.

The first striking result is that harmonics are generated efficiently for pump-probe delays below 4 ps, corresponding to $L \leq 0.05\lambda$. The spectrum extends up to the plasma frequency cutoff $\omega_{max} = 16\omega_0$, which is the typical signature of CWE (see reference [Kahaly *et al.*, 2013] and chapter 1). The plasma frequency cutoff confirms that Brunel electrons efficiently generate coherent wake emission. This also indicates that the temporal contrast close to the pulse peak does not allow us to explore arbitrarily small plasma scale lengths. The drop in CWE emission efficiency with increasing density gradient has already been observed experimentally and is theoretically predicted to be in the range $0.02 < L/\lambda < 0.1$ in references [Kahaly *et al.*, 2013; Tarasevitch *et al.*, 2007] depending on laser intensity [Thaury & Quéré, 2010].

The second striking result is that a maximum electron signal is reached for a delay of 8 ps ($L \sim 0.1\lambda$), where harmonic emission is negligible. The ejected electrons form a large spot between 10° and 20° and drop at the edge of the Lanex at $\sim 30°$. This drop in signal is a geometrical artifact due to the anisotropic emission of the Lanex screen, see reference [Glinec *et al.*, 2006]. Figure 5.3b) shows the full electron angular distribution for a delay of ~ 7 ps, obtained by moving the Lanex screen perpendicular to the specular direction. The distribution shows a hole close to the specular direction, presumably formed by the ponderomotive force of the reflected laser pulse, see chapter 4. Using the Lanex calibration, we estimate that the ejected charge reaches a maximum of ~ 11 pC compared with ~ 2 pC at zero delay. Figure 5.3c) shows electron spectra without prepulse, for the optimal delay for electronic emission, and after 20 ps respectively. Hence, electrons can be effectively accelerated up to ~ 600 keV at the optimal density gradient.

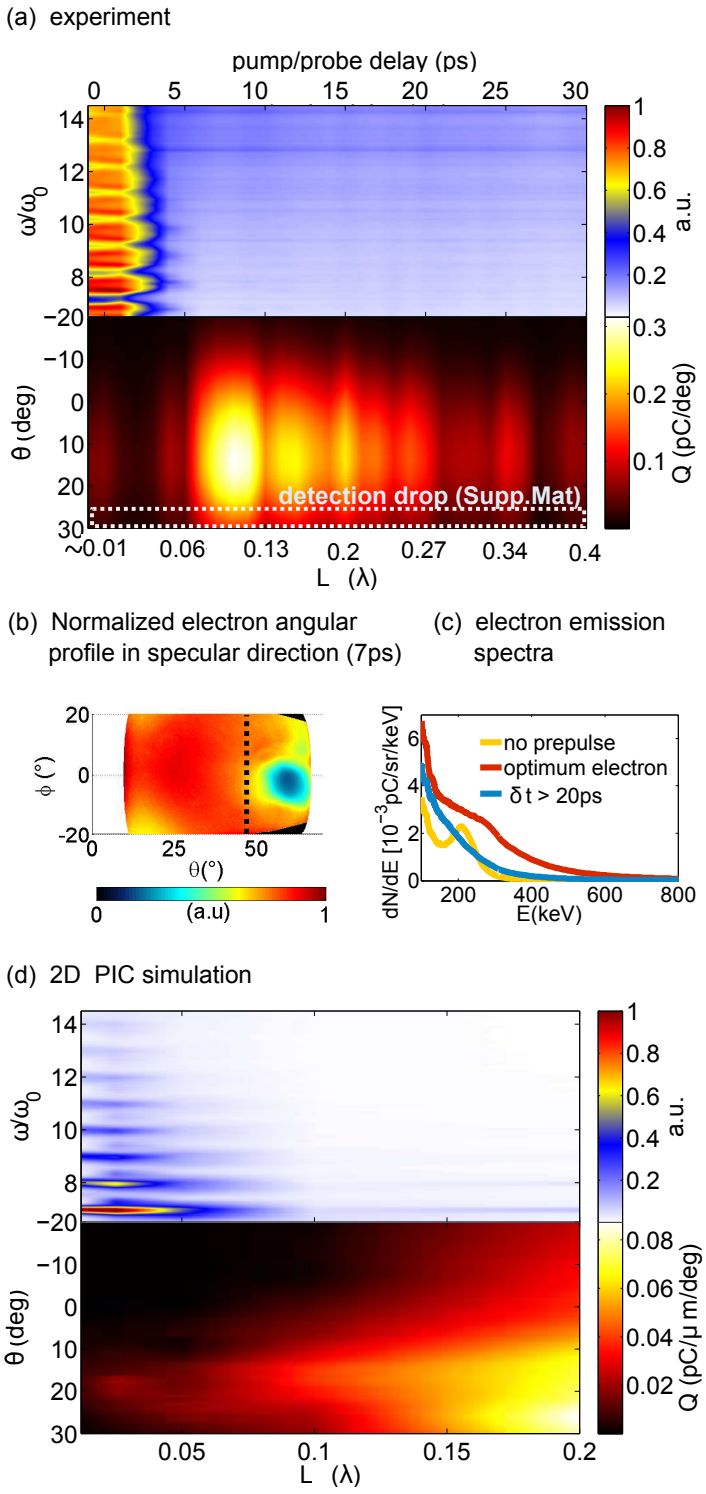


Figure 5.3: (a) Experimental harmonic spectra and electron angular emission profiles as a function of pump-probe delay (top axis) between the prepulse and the main pulse. The electron signal was integrated along the tangential coordinate ϕ. The corresponding plasma scale length L (bottom axis) was extracted from the plasma expansion velocity $c_s = 10.8\,\mathrm{nm/ps}$ measured by SDI; b) Electron angular distribution when the Lanex is placed perpendicular to the specular direction and after deconvolution; c) Electron energy spectra for three typical delays; d) Same as a) for 2D PIC simulations with $a_0 = 0.4$, and gradient length $L \in [0.01\lambda; 0.2\lambda]$.

PIC simulations

Experimentally, we observe that the emission of harmonics and electrons is anti-correlated when changing the gradient scale length. These experimental results were confronted to 2D particle-in-cell simulations (`CWEv5_largewaist_L1s40-CWEv5_largewaist_L1s5`), in which a $\lambda = 800\,\text{nm}$, 30 fs (intensity FWHM) pulse is focused onto an overdense plasma ($n_{max} = 250 n_c$) with immobile ions. The plasma density decreases exponentially with various scale lengths, from $L = 0.01\lambda$ to 0.2λ. The plasma density is cut at $n_b = n_c/5$, so that the plasma boundary is defined by $x_b = -\log(5)L$. The laser amplitude is $a_0 = 0.4$ and the incidence angle 45°. A good spatial resolution is required for simulating CWE harmonics, so we use $\Delta x = \lambda/420$ with 80 particles per cell. In the simulations, electrons are detected at 9λ away from the critical surface and only electrons with energies > 150 keV are recorded. As illustrated in figure 5.3d), the PIC simulations qualitatively reproduce our experimental observations: the CWE emission efficiency decreases for $L > 0.05\lambda$ and the effective ejected electron charge increases up to ~ 3 pC.μm^{-1} for $L = 0.2\lambda$ compared to 0.12 pC.μm^{-1} when $L = 0.01\lambda$ (*i.e.* $\simeq 10$ pC and 0.7 pC respectively, for a 3.4 μm spot size FWHM).

The electron angular distribution was plotted over the range $\theta \in [-20°\ 30°]$ for a direct comparison with experiment. Note that PIC simulations were first performed with the experimental vacuum laser amplitude $a_0 = 0.8$, but a strong harmonic emission attributed to the ROM emission mechanism persisted for longer gradients. This indicates that the laser intensity at focus is not high enough to support ROM emission in the experiments (see chapter 1). Therefore, in the simulations, the beam spot size was doubled without changing the pulse energy, i.e. a_0 was decreased to 0.4, to reproduce the anticorrelated behaviour. Note that our overestimation of the experimental intensity on target may be due to a slight defocusing of the laser on target or debris reducing the overall reflectivity of the focusing optic, a standard problem with high repetition rate laser-plasma interaction experiments using tight focusing.

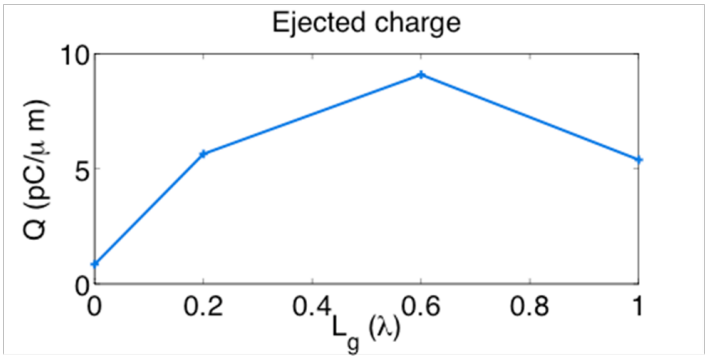


Figure 5.4: Ejected charge as a function of the gradient length, from 2D PIC simulations with $a_0 = 0.4$, $n_{max} = 250 n_c$. The name of the scan was `largewaist_electronsv2_L*`. Keeping the numerical space step $\Delta x = \lambda/420$ and 80 particles per cell as in figure 5.3 results in a dramatic increase of the computational cost. We changed both conditions and ran simulations with a larger box. These conditions were not sufficient to describe high harmonic generation, so we did not investigate CWE in this scan.

The scan `CWEv5_largewaist*` shown in figure 5.3 was not extended up to very long gradients because of its computational cost. Besides, electrons are detected at a distance smaller than the Rayleigh length in this scan, and should be detected further. In order to observe the optimal gradient in 2D PIC simulations, we re-ran this scan with

only 10 particles per cell. These runs are `largewaist_electronsv2_L0p0 - largewaist_electronsv2_L1`. The box size was $30\lambda \times 90\lambda$, and electrons were detected 25λ away from the plasma surface. The result is shown in figure 5.4, where the optimal gradient length is found between $L = \lambda/5$ and $L = \lambda$.

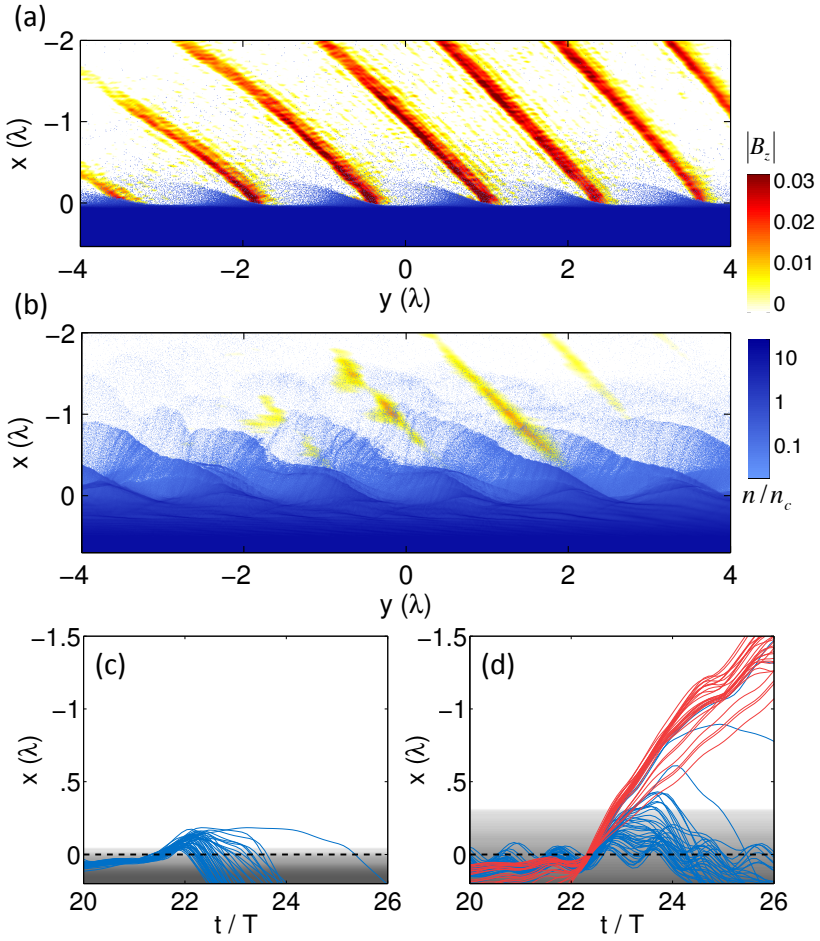


Figure 5.5: a) Snapshot from the 2D PIC simulation for $L = \lambda/40$. Blue: electron density (log-scale). Yellow-red: reflected harmonic field. A Fourier filter was applied to keep only harmonic orders $\geq 5\omega_0$. The harmonic field comes out as a train of attosecond pulses; b) Same as a) for $L = \lambda/5$ (same instant, same colour scale); c) and d) typical electron trajectories for $L = \lambda/40$ and $L = \lambda/5$ respectively. x is the coordinate normal to the plasma surface. The grey scale stands for the plasma initial density and the black dotted line ($x = 0$) shows the position of the critical density. The electrons represented here interact with the laser around its maximum ($t = 22T_L$). Red trajectories stand for ejected electrons.

Figure 5.5 shows a comparison of 2D PIC simulations with a gradient length optimized for harmonic emission ($L = \lambda/40$) and electron emission ($L = \lambda/5$), respectively. In panels a) and b), one can clearly see oscillations of the electron surface at the laser frequency. This is very similar to what happens at high intensity (see figure 3.28, page 109). Strong harmonic generation can be seen in panel a). The corresponding electron trajectories are shown in panel c), where the x coordinate (normal to the target) of electrons is plotted along time. For clarity, a single bunch of electrons is represented here. It interacts with the laser around its temporal maximum ($t = 22T_L$, where T_L is the optical period) in the center of the interference pattern. One can clearly see Brunel-like trajectories: electrons make a short excursion in vacuum before being driven back to the plasma where they trigger plasma waves. In panel b), the

amplitude of these oscillations is greater and layers of electrons are ejected from the plasma surface. The corresponding electron trajectories are plotted in panel d). Once again, a bunch of electrons was selected for clarity. A fraction of these electrons (in red) escape from the plasma and propagate into vacuum in the interference pattern with a velocity $\simeq c/2$.

5.1.2 Dynamics of ejected electrons

Electron ejection: push-pull mechanism

In the low-intensity regime, the ejection process is the same push-pull mechanism as the one occurring at high intensity, described in chapter 3. Oscillations of the plasma surface can be seen in figure 5.5a-b). As in the high-intensity regime, no electron is ejected when the density gradient is too short (see figure 5.5c)), whereas some escape the plasma in the case of a long gradient (see figure 5.5d).

To highlight the role of the plasma capacitor, figure 5.6 shows the spectrum of ejected electrons when they cross the plasma boundary at x_b for a short (blue) and a long (red) density gradient. The average energy is much higher for longer gradients, thus confirming our predictions: the plasma capacitor provides more energy to the ejected electrons in the case of a long density gradient, and serves as an injector of electrons into the reflecting laser.

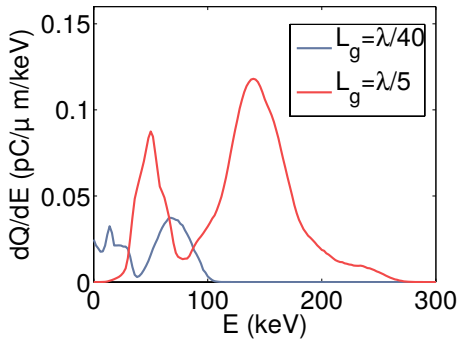


Figure 5.6: Simulated ejected electron spectra at the plasma boundary x_b for $L = \lambda/40$ (grey) and $L = \lambda/5$ (red) as they cross the plasma critical surface.

Electron acceleration: prevailing role of the plasma capacitor

The ejected electrons travel through the interference field created by the incident and reflected laser beams and it was still under debate whether plasma waves (see [Bastiani *et al.*, 1997]), interference fields (as in [Mordovanakis *et al.*, 2009; Naumova *et al.*, 2004b; Tian *et al.*, 2012]) or vacuum laser acceleration predominantly accounted for final electron energies and angular spread for these intensities. As shown in chapter 3, enhanced electron generation is observed typically for $0.1 < L/\lambda < 0.5$.

To answer this question, we plot the simulated electron spectra at the plasma border, at 3.3λ and 9λ away from the plasma in figure 5.7b). Within this range, no net energy gain can be observed from the electromagnetic wave in vacuum, **we conclude that the energy gain in this low-intensity experiment is mostly due to acceleration inside the plasma gradient**.

However, further away from the plasma (9λ), the electron spectrum broadens and the tail of the distribution reaches 400 keV, which could be the signature of ponderomo-

tive and/or stochastic heating in the interference pattern, as claimed in reference [Sheng *et al.*, 2002]. The observation of a hole formation in the experimental electron density profile, that can be seen in figure 5.3b), and the absence of a strong collimated beam is another evidence that the interaction between the accelerated electrons and the laser is purely ponderomotive. Finally, from simulations and experiments, we also conclude that electrons are not accelerated by plasma waves related to the CWE mechanism, as suggested in reference [Bastiani *et al.*, 1997], otherwise electron and harmonic emission would be simultaneously optimal.

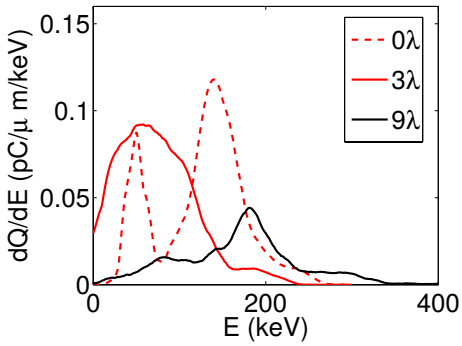


Figure 5.7: Ejected electron spectra for $L = \lambda/5$ as they cross the plasma surface (dotted line), 3λ and 9λ away from the plasma surface (respectively red and black solid line).

These results show the transition from high harmonic emission to fast electron ejection as the electronic density gradient increases at the surface of a plasma mirror driven by a sub-relativistic laser pulse. Experiments reveal that both processes do not occur simultaneously for the same density gradient. For sharp gradients ($L < \lambda/30$), electrons are driven across the confined plasma, leading to efficient CWE. For softer gradients, some electrons are efficiently accelerated out of the plasma by the space charge field created for $L \sim 0.1\lambda$.

Although the interaction with the reflected laser field thermalizes the electron spectra and reshapes the spatial emission profile via ponderomotive interactions, the majority of the acceleration occurs inside the plasma density gradient. **When the gradient length becomes higher than $L \sim 40\,\mathrm{nm}$, the plasma mirror behaviour switches from a collection of efficient XUV resonators to a nanoscale electron accelerator**.

5.2 Correlation ROM/electrons in the high-intensity regime $a_0 > 1$

The Relativistic Oscillating Mirror mechanisms is dominant for high harmonic generation in the high-intensity regime. When the electron density peak is accelerated towards vacuum during the pull phase, it radiates an attosecond electromagnetic bunch with a broad spectrum. This process is developed in chapter 1.

As demonstrated in chapter 3, a fraction of this peak can be ejected from the plasma surface. More electrons are likely to escape the surface if they are accelerated faster by the plasma fields during the pull phase. As a consequence, one can expect the ROM efficiency and electron ejection to be correlated, as part of the same mechanism.

This consideration is investigated in more details in the next section, and the correlation is demonstrated in experiments in section 5.2.2 and in 1D and 2D PIC simulations

in section 5.2.3.

5.2.1 Expected correlation

Figure 5.8 a) shows the electron density from PIC simulation `these_rom1` as well as attosecond bunches. One can see that the electron dynamics is clearly very anharmonic. As discussed in chapter 3, during each laser period, electrons are gathered in a sharp density peak. This density peak can be seen as the oscillating mirror in Lichters' model. Once per laser period, the peak is strongly accelerated towards vacuum (see $t/T_L = 7$ in this example), and generates high frequencies in the reflected field. Both Lichters' model and the BGP theory relate the harmonic efficiency with the maximum speed of electrons: the faster the density peak, the higher the harmonic efficiency.

The current density J_x is depicted in figure 5.8b). The emission of the attosecond bunch in the reflected field at $(t/T_L = 7, x/\lambda = 5.2)$ occurs when J_x is maximum. More details can be found in section 1.4.3, page 43.

As described in chapter 3, a small fraction of the electrons contained in the density peak are ejected from the plasma. They form the electron jets propagating towards $-x$ in figure 5.8. As a consequence, we expect the electron ejection and harmonic generation via the ROM mechanism to vary in a similar fashion.

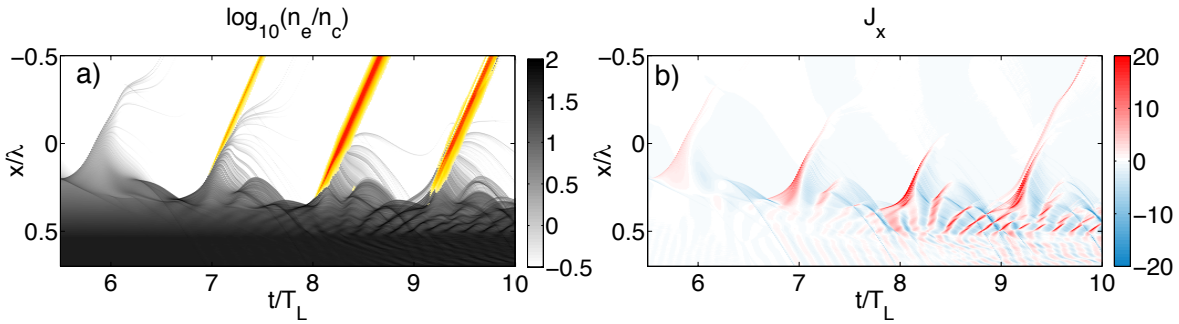


Figure 5.8: Surface dynamics in simulation `these_rom1`. a) Log-scale electron density. One electron jet travels towards vacuum once per laser period. Colours represent attosecond bunches. A Fourier filter was applied to the magnetic field to keep only high frequencies. b) Transverse current J_x.

5.2.2 Experimental results from the UHI100 laser (CEA) by Adrien Leblanc

The experiment was performed on the UHI100 laser at CEA by A. Leblanc and his coworkers during his Ph.D. The experimental setup is the same one as used to study VLA, and a detailed description can be found in chapter 4. Additional diagnostics were used in order to measure the reflected field spectrum. The experimental conditions are $a_0 = 3$, $\theta = 55°$, the beam spot size is $5.5\,\mu$m and the pulse duration is 30 fs. Both the electromagnetic spectrum of the reflected field and the angular distribution for the ejected electrons are recorded during the same laser shots.

The experimental results are shown in figure 5.9. Panel a) shows the harmonic spectra as a function of the gradient length. Panel b) shows the angular distribution for the ejected electrons. The black dashed line shows the optimal gradient, which is the same for harmonic generation and electron ejection. These data were integrated to get figure 5.9 c), where the total ejected charge and the harmonic efficiency are plotted

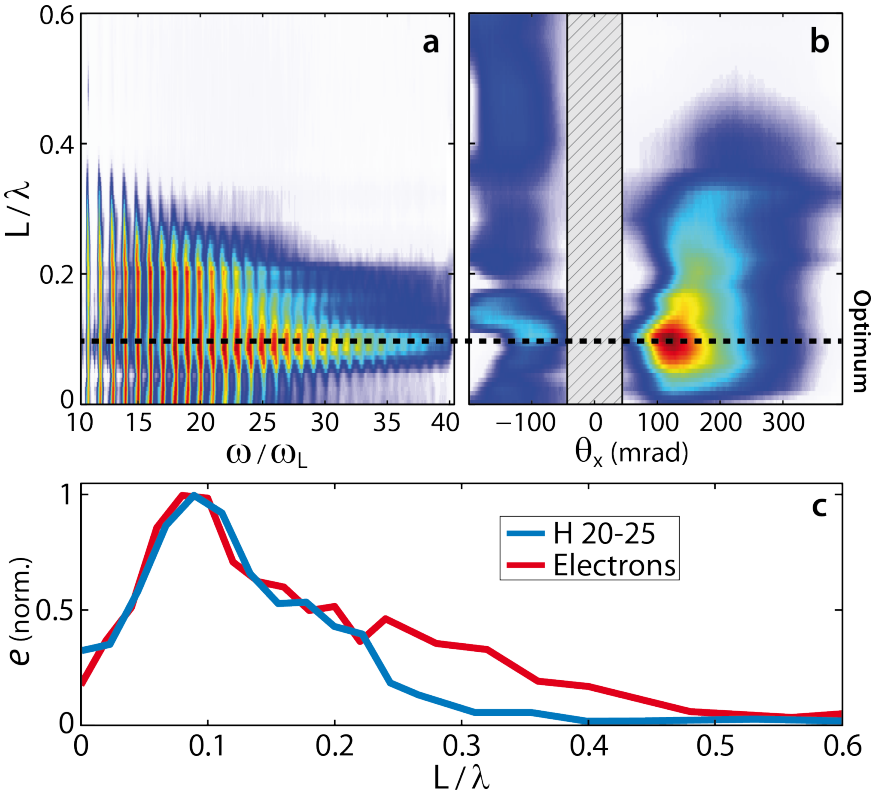


Figure 5.9: [Image from A. Leblanc's thesis]a) Experimental harmonic spectra as a function of the gradient length L. b) Electron angular emission profile as a function of the gradient length. The electron signal was integrated along the direction perpendicular to the polarization plane. c) Total harmonic efficiency e in harmonic orders H20-H25, along with electron emission.

as a function of the gradient length. They clearly vary in a similar fashion and are clearly correlated.

5.2.3 Confirmation from PIC simulations

2D PIC scan

We expect the ejected charge and the harmonic efficiency to be correlated. In order to further investigate this correlation, we performed a scan of 2D PIC simulations, and measured at once the ejected charge and the harmonic generation efficiency. We used the scan `injectorv4_L1s*`, already seen in chapter 3. The result is shown in figure 5.10 b), where the Q_- charge defined in section 3.3.4 is plotted with the harmonic signal as a function of the gradient length. The total charge is shown in figure 5.10 a). Both the harmonic signal and the relevant electron signal Q_- peak for the same value, showing a clear correlation.

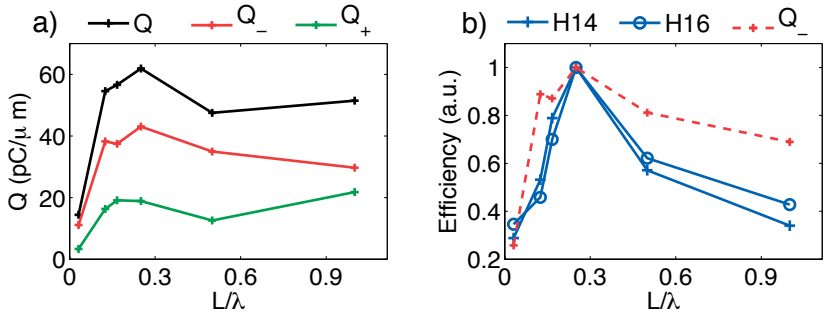


Figure 5.10: Ejected charge as a function of the gradient length from scan `injectorv4` (see chapter 3). a) Total ejected charge Q and ejected charge with angle $< 45°$ (Q_-) and $> 45°$ (Q_+). b) Ejected charge Q_- along with harmonics efficiency for H14 and H16.

1D PIC scan

The harmonics efficiency can also be compared with the electron ejected charge in the 1D PIC scan `harmv9_a*_L1s*` shown in chapter 3. Figure 5.11 shows the ejected charge as well as the efficiency of two harmonic orders as a function of a_0 and the gradient length L. As expected, HHG via the ROM mechanism and ejected charge vary in a similar fashion indeed. However, the decrease in harmonics efficiency is not as clear as in 2D PIC simulations and experiments. Note that a small bulb with non-zero harmonic signal can be seen in panels b) and c) for $a_0 < 1$ and $L < 0.05$. These are harmonics generated via the CWE mechanism.

Conclusion: Electron emission and harmonic generation were simultaneously studied. We investigated two regimes: the sub-relativistic regime and the relativistic regime, corresponding to the two laser systems that provided the experimental results, the *Salle Noire* laser at LOA and the UHI100 laser at CEA respectively. Both lead to backward electron acceleration by the mechanism described in chapter 3, and high harmonic generation via two distinct mechanisms.

In the sub-relativistic regime ($a_0 < 1$), coherent wake emission (CWE) is the dominant mechanism for high harmonic generation, which is substantial for short gradients $L \sim \lambda/50$. Electron emission is still optimal for a longer gradient length $L_{max} \simeq \lambda/10$. Hence, scanning the L parameter, we observed no correlation, or even anti-correlation

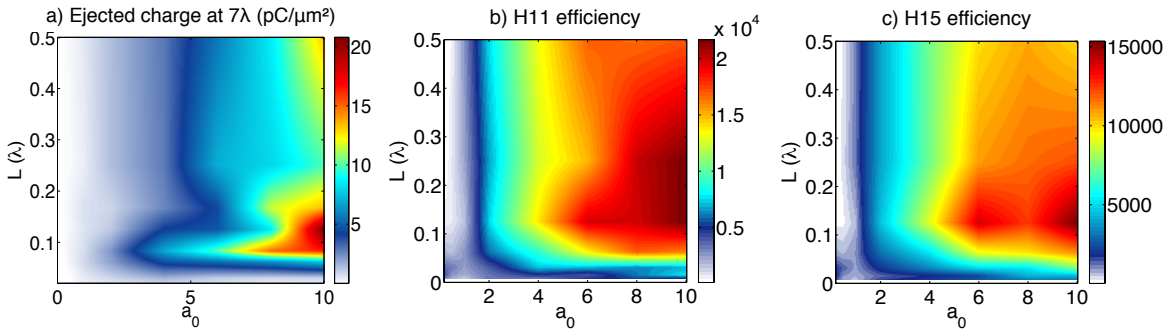


Figure 5.11: a) Ejected charge from scan `PARAM_harmv9` (see chapter 3) b) H11 efficiency. c) H15 efficiency.

between CWE efficiency and electron ejection. The density gradient acts as a plasma capacitor that accelerates electrons. The final energy of ejected electrons is comparable to their energy when they leave the plasma. They do not experience VLA because they have sub-relativistic speed and because the Rayleigh length in this experiment is extremely short. **In the low-intensity experiment, electrons are mostly accelerated by the plasma capacitor**.

In the relativistic regime ($a_0 > 1$), high harmonics are generated via the relativistic oscillating mirror (ROM). Electrons are gathered in a sharp density peak which radiates as it is accelerated towards vacuum. A small fraction of this peak escapes the plasma, and composes the ejected electrons, as described in chapter 3. Therefore, ejected electrons are part of the sheet that radiates high frequencies, and these two mechanisms are clearly correlated. The final energy of the ejected electrons can be seven times higher than when they leave the plasma because electrons experience VLA. Indeed, they have relativistic speed and the laser Rayleigh length is relatively long. **In the high-intensity regime, electrons can be mostly accelerated in the reflected field via the VLA mechanism**.

These results are summarized in figure 5.12, where the ejected charge and harmonics efficiency are shown as a function of the gradient length on the *Salle Noire* laser at LOA (a) and on the UHI100 laser at CEA (b). Signals are anti-correlated in the first case and correlated in the second case, and the ejected charge peaks around $L = \lambda/10$ in both regimes. In agreement with our predictions in chapter 3, for our range of parameters, **the optimal gradient length is nearly independent of the laser intensity**.

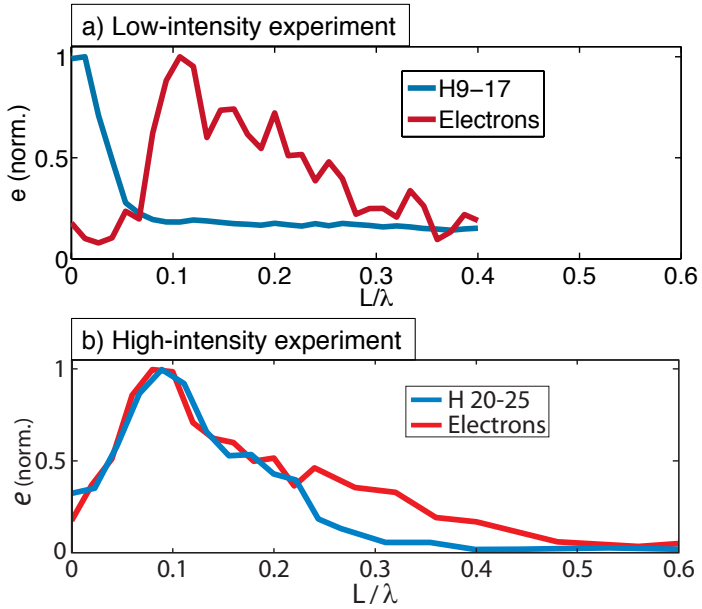


Figure 5.12: a) Harmonics efficiency e and ejected charge as a function of the density gradient in experiments on the *Salle Noire* laser at LOA. These signals were calculated by integration from results shown in figure 5.3, to show the general trends. b) Same as a) from the UHI100 laser at CEA. All signals were normalized with respect to their maximum value.

Conclusion

Outcome

The first part of my PhD work consisted in identifying the backward electron ejection process when a laser pulse reflects off a plasma mirror. In a simplified configuration, where a monochromatic wave with $1 < a_0 < 20$ impinges under oblique incidence $\theta = 45°$ on an overdense plasma with a step-like density profile with density $5 < n_0/n_c < 15$, a bunch of electrons is ejected at every laser period via a push-pull mechanism. Electrons at the plasma surface are gathered in a sharp density peak that oscillates inside the plasma. The ions create a plasma capacitor which accelerates the electron peak towards vacuum during the pull phase, and a fraction of the electrons contained in the peak can escape the plasma and propagate along the reflected field. The ejected charge depends on the $S = n_0/a_0$ parameter, and PIC simulations showed that no electrons were ejected above a threshold value $S_{th}^{[PIC]} \sim 0.85$. For $S > S_{th}^{[PIC]}$, the potential of the plasma capacitor is no longer strong enough to counter the gyromagnetic effect, and all electrons are brought back to the plasma. Based on Gonoskov's model, we propose a toy model that reproduces this threshold, and find $S_{th}^{[model]} \sim 0.8$. This analysis is extended to the configuration of most experiments, namely a largely overdense plasma $n_{bulk} \sim 200 n_c$ with an exponential density gradient on its front side. The same push-pull mechanism occurs as in the case of a step-like profile. We show that there is an optimal gradient scale length $L_{max} \simeq \lambda/8$ for electron ejection: when $kL \to 0$, plasma fields vanish and the gyromagnetic effect prevents electron ejection, as in the $n_0 \to \infty$ step-like case. When $kL \to \infty$, the mechanism breaks and the ejected charge drops. The optimal gradient length was measured to be $L_{max}^{[exp]} \simeq \lambda/10$ in experiments in two very different regimes, thus confirming our predictions. These considerations showed the key role played by the plasma fields, and nourished the other topics investigated in this work.

The second theme I investigated was the vacuum laser acceleration scheme (VLA), and the possibility to use a plasma mirror as an electron injector. When studying the dynamics of an electron in a laser pulse, most studies consist in scanning the electron initial conditions and plotting the resulting energy gain. This procedure gives the optimal initial conditions to accelerate an electron inside a laser pulse. My work in this domain was inspired by experiments, and aimed at underlining general trends and scaling laws. Two archetypal behaviors were highlighted: first, the ponderomotive dynamics when electrons oscillate in the laser pulse and are scattered by the ponderomotive force, resulting in a doughnut-shape distribution with a low energy gain. Second, the VLA dynamics when electrons are accelerated in the same phase of the laser field all along their propagation until they leave the pulse, forming a spot in the polarization plane with a high energy gain. In a simplified configuration where the electrons start at a field node with speed along the propagation direction, a single

parameter Π, which links the laser parameters a_0, z_R and the energy of the electrons, governs the balance between these two cases. As shown in chapter 3, an attosecond electron bunch is ejected from the plasma for every laser period when the reflected field is zero. These electrons have relativistic energies and travel in a direction close to the specular direction, *i.e.* the propagation direction for the reflected pulse. These conditions are close to be optimal for VLA. An experiment performed on the UHI100 laser at CEA ($a_0 = 3$, 5.5 μm spot size and 30 fs duration) showed that a plasma mirror could actually serve as an electron injector for VLA. This proof-of-concept experiment resulted in a 3 nC, 10 MeV electron beam, and both ponderomotive and VLA dynamics were identified using a model.

One of the interests of plasma mirrors resides in the possibility to generate attosecond bunches via high harmonic generation. Hence, the third and last theme of this work was naturally the correlation between high harmonic generation and electron ejection. This study strongly relies on experimental results on the two laser systems UHI100 and *Salle Noire*, that allow a precise control of the experimental parameters, in particular the gradient length, and provide extremely valuable results. Two regimes were thus investigated, corresponding to the parameters accessible with these two systems. On the one hand, experiments on the *Salle Noire* laser in the sub-relativistic regime ($a_0 \simeq 0.5$) showed an anti-correlation between harmonic generation and electron emission. This is because the dominant mechanism in this regime, coherent wake emission, is optimal for very short gradients $L \sim \lambda/50$ and relies on electrons that return to the plasma, whereas electron emission takes place when electrons are accelerated out of the plasma. Hence, when increasing the gradient length for $a_0 \simeq 0.5$, the plasma behavior switches from a collection of nanoscale resonators to a nanoscale accelerating capacitor. On the other hand, experiments performed on the UHI100 laser in the relativistic regime $a_0 \simeq 3$ showed a strong correlation between harmonic generation and electron emission. Knowing the ejection process, the reason is straightforward: ejected electrons belong to the density peak that radiates an attosecond bunch. As a consequence, the faster the density peak, the higher the harmonic efficiency and the higher the ejected charge. Finally, this chapter also demonstrated that the electron acceleration mechanism is different in the two abovementioned regimes: in the low-intensity regime, electrons are mostly accelerated in the plasma capacitor whereas in the high-intensity regime, the electron energy can be multiplied by seven via VLA in the reflected pulse after ejection from the plasma mirror. The two laser parameters responsible for this discrepancy are the laser intensity and the Rayleigh length.

Based on two distinct topics, high harmonic generation and electron emission, this study aimed at bringing insight into the plasma surface dynamics during the reflection of a laser pulse upon a plasma mirror. The jets of ejected electrons are a signature of the ROM mechanism, which provides a macroscopic observable of a nanoscale phenomenon. Besides, even though this study did not aim at providing a new source of electrons, one can be interested in characterizing the electron bunch accelerated via VLA. Using the toy model proposed in chapter 4, we can see that this source provides a very high charge electron bunch with a large angle-energy correlation: the closer from the specular direction, the higher the electron energy. Let us assume we put a pinhole to select a $\Delta\theta = 1°$ disk of the ejected electrons in the polarization plane. If the pinhole is located in the electron spot at an angle $\theta_{select} = 6°$ with respect to the specular direction, the resulting electron bunch has a 10 MeV peak energy with 100% energy spread FWHM. Then, $\theta_{select} = 8°$ gives a 7 MeV peak energy with a 60% energy spread and $\theta_{select} = 10°$ gives a 5 MeV peak energy with a 60% energy spread. In all cases, the ejected charge

is around 30 pC. This is not yet a competitive source for applications like ultrafast electron diffraction, which requires a $\sim 1\%$ energy spread, but these very first results stimulate further studies, where the role of the angle of incidence, for exemple, could be clarified.

Perspectives

The VLA experiment performed on the UHI100 laser served as a proof-of-principle for vacuum laser acceleration with a linearly-polarized gaussian beam. In a short term, two ideas can be put into practice: first, this scheme can be extended to a radially-polarized laser beam, for which a significant amount of theoretical studies show that it could result in an energetic collimated electron bunch [Bochove *et al.*, 1992; Fortin *et al.*, 2009; Marceau *et al.*, 2013; Salamin, 2006]. When focused down to a few microns spot size, such a beam has a strong component of the electric field along the propagation direction, which is perfectly suited to accelerate electrons. Besides, the radial electric field vanishes on the axis. When injected at the appropriate phase, electrons can propagate in fields that are both accelerating and focusing, which is the optimal configuration (as in laser wakefield accelerators). This could result in a few-MeV electron bunch much more collimated than with a linear polarization. Yet as shown in chapter 3, the plasma mirror injector does not allow for a control of the injection phase. But our first brief investigations on VLA with a radially-polarized beam using a plasma mirror injector showed that a significant charge could actually be injected in the optimal phase. Besides, in this case, the push-pull mechanism can also be at play in normal incidence because the longitudinal electric component would be normal to the target.

Second, when dealing with high harmonic generation, the attosecond lighthouse scheme [Wheeler *et al.*, 2012] allows the generation of isolated attosecond light pulses, instead of a train of pulses. Introducing a wave-front rotation at the laser focal spot, the attosecond light pulses propagate in slightly different directions, and can be separated via angular gating. This elegant technique could be applied to electron emission. During each laser period, a short electron bunch is ejected and accelerated via VLA, resulting in a broad spectral and angular distribution with a strong correlation between energy $\mathcal{E}$ and angle θ_e: $\mathcal{E} = f(\theta_e)$. Using the lighthouse technique, this function f could be drastically different for consecutive cycles. As a consequence, when looking at a given angle theta, one could see several electron bunches with distinct energies, coming from distinct laser periods. This makes it possible to select easily a single bunch, generated during a single laser period, with potential few-fs duration. Moreover, even without this angular gating technique, a single short electron bunch can be generated using a single-cycle laser pulse: experiments with a 3.4 fs pulse with relativistic intensity are currently being carried out on the *Salle Noire* system at LOA, and the distribution of the ejected electrons will be characterized soon. In this case, the carrier-envelope phase, namely the phase between the optical cycle and the pulse envelope, could play an important role. This parameter is well-controlled on the *Salle Noire* system, allowing a precise study of the physics involved.

On the long term, one can think of three applications for these VLA electron bunches. First, their properties are perfectly suited for non-destructive X-ray control: an electron beam with relativistic energies (~ 10 MeV), high charge (> 1 nC) and large divergence (10°) propagates through a tantalum foil, where electrons are stopped

and emit X-rays via the bremsstrahlung mechanism. This bright X-ray source with a large divergence can be used to probe matter, and may find industrial application in the crack detection in the structure of a plane, in particular in the landing gear. VLA electrons would very well meet the needs for this application, as soon as the laser system can be compact and work at a high repetition rate.

Another long-term application consists in combining this VLA electron bunch with other accelerating schemes, like laser wakefield accelerators. The high ejected charge and the strong energy-angle correlation allows for a strong filtering, and can result in a $5 - 10\,\mathrm{MeV}$ electron bunch perfectly synchronized with the laser pulse. Combining a plasma mirror with a gas jet can provide a new injection technique, which is a hot topic for laser wakefield accelerators.

Finally, the strongest property of plasma mirrors is their capability to generate simultaneously high harmonics of the laser and bunches of relativistic electrons with a very large charge. Combined with the rotating target system already implemented on the *Salle Noire* laser system, this could provide a $1\,\mathrm{kHz}$ source of relativistic electrons. Also, the high charge allows a fine filtering in the electron distribution. As a consequence, plasma mirrors with future laser systems could provide a double source of isolated soft X-ray attosecond pulses and ultrashort relativistic electron bunches. These perfectly synchronized sources could be used for pump-probe experiments, with an X-ray pump and an electron probe, leading to ultrafast electron diffraction with extreme time and space resolutions.

List of figures

1 Tokita's electron diffraction image 2

1.1 General setup for plasma mirrors 11
1.2 Plasma dynamics and BBGKY hierarchy 12
1.3 Photoinduced ionization mechanisms 14
1.4 Boosted frame by Bourdier 18
1.5 Boosted frame: pros and cons 20
1.6 Example of a 1D PIC simulation 21
1.7 Resonance absorption 23
1.8 Vacuum heating 25
1.9 Extended Brunel model 27
1.10 $J \times B$ heating 28
1.11 Overview of angular distribution for electron jets 29
1.12 Experimental electron distributions 30
1.13 Train of attosecond pulses *vs.* high harmonic generation 34
1.14 The CWE mechanism 35
1.15 CWE and electrons in PIC simulations 37
1.16 CWE harmonic spectrum 37
1.17 CWE in PIC simulations 38
1.18 CWE: peak propagation in the plasma 39
1.19 CWE: gradient length and shape of the spectrum 40
1.20 ROM and electrons in PIC simulations 41
1.21 ROM harmonic spectrum 41
1.22 Doppler effect 42
1.23 Liénard-Wiechert potentials and attosecond bunch generation 44
1.24 Lichters' model: electron and ion density 45
1.25 Retarded time and integration area in J 46
1.26 Lichters' model: illustration 49
1.27 ROM in PIC simulations 50

2.1 Diagram for Vlasov simulations 54
2.2 Diagram for PIC simulations 55
2.3 Weight functions 56
2.4 2D Yee grid 57
2.5 Villasenor current deposition 59
2.6 Influence of numerical parameters in PIC simulations 62
2.7 2D PIC simulations: example 64
2.8 Electron dynamics in a monochromatic plane wave 68
2.9 Gaussian mode 69
2.10 Ponderomotive force and electron trajectory 71

2.11 First-order correction in laser fields 72

3.1 Attosecond electron bunches in PIC simulations 77
3.2 Importance of the density gradient scale length 78
3.3 Electron acceleration in vacuum from 1D PIC simulations 79
3.4 Gyromagnetic effect 82
3.5 Laser reflection and backward electron ejection 83
3.6 Reflection process: focus on one laser period 85
3.7 Low-density *vs.* High-density 86
3.8 Step-like profile: Push-pull mechanism 87
3.9 Dynamics of the electron density peak 89
3.10 Electron density peak acceleration towards vacuum 90
3.11 Diagram for the Relativistic Electron Spring model 91
3.12 RES model *vs.* PIC simulation 92
3.13 Hypothesis $p_x = \phi_e/2$ in PIC simulations 94
3.14 Ejection model: low density *vs.* high density 95
3.15 1D PIC scan: ejected charge as a function of a_0 and n_0 95
3.16 Electrostatic potential and plasma density 96
3.17 Temporal shape of the reflected field 97
3.18 Exponential gradient 98
3.19 Electron ejection: short gradient *vs.* long gradient 98
3.20 Electron bunches escape the plasma 99
3.21 Density peak formation 100
3.22 Electron dynamics in a 1D PIC simulation 101
3.23 Forces work on ejected electrons 103
3.24 1D PIC scan: ejected charge as a function of a_0 and L 104
3.25 Density peak breaking for very long gradient $kL \gg 1$ 105
3.26 Ejection model: Non-crossing hypothesis and Gauss's law 106
3.27 Density gradient and electron ejection: model *vs.* PIC simulations . . . 108
3.28 Attosecond electron bunches in 2D PIC simulations 109
3.29 2D PIC scan: ejected charge with L 110
3.30 Large-angle ejection for very long gradients 110

4.1 Schematic of a plasma mirror injector 115
4.2 Conventional, plasma-wakefield and vaccum laser accelerators 115
4.3 Electron in a plane wave: low- *vs.* high-intensity regime 116
4.4 Lawson-Woodward theorem and Plettner's experiment 119
4.5 *Ponderomotive* and *VLA* configurations 121
4.6 Ponderomotive trajectory 122
4.7 Ponderomotive scattering: electron distribution 122
4.8 Role of p_z in ponderomotive scattering 124
4.9 VLA trajectory 124
4.10 VLA dynamics: electron distribution 125
4.11 Electron in a plane wave for $a_0 = 0.1$ and $a_0 = 10$ 126
4.12 Gaussian pulse and square envelope model 127
4.13 Scaling laws for VLA electrons in simulations 128
4.14 Complementary error function 130
4.15 VLA ratio with respect to the Π parameter 131
4.16 Injection scheme for VLA 132
4.17 Schematic of a plasma mirror injector 133

4.18 Experimental setup for VLA . . . 134
4.19 VLA: model *vs.* experimental results . . . 135
4.20 Frame of reference for VLA . . . 136
4.21 Initial conditions for the VLA model . . . 137
4.22 Ponderomotive and VLA electron trajectories . . . 139

5.1 Simultaneous ROM and CWE attosecond bunches . . . 142
5.2 CWE *vs.* electron ejection: basic mechanism . . . 143
5.3 CWE *vs.* electron ejection: experimental and PIC results . . . 145
5.4 Ejected charge as a function of the gradient length . . . 146
5.5 CWE *vs.* electron ejection: 2D PIC snapshots . . . 147
5.6 Energy obtained in the plasma capacitor . . . 148
5.7 Plasma *vs.* laser acceleration . . . 149
5.8 ROM *vs.* electron ejection in PIC simulations . . . 150
5.9 ROM vs. electron ejection in experiments . . . 151
5.10 ROM *vs.* electron ejection: role of the gradient length . . . 152
5.11 ROM *vs.* electron ejection in 1D PIC simulations . . . 153
5.12 Experimental results: low- *vs.* high-intensity . . . 154

List of Tables

1.1 Conversion table . . . 9
1.2 Laser systems UHI100 and *Salle Noire* . . . 10
1.3 Collisional and non-collisional regimes . . . 13
1.4 Ionization intensities for silica . . . 15
1.5 Preplasma expansion . . . 18
1.6 Experimental review . . . 32

2.1 Scan on numerical parameters: run conditions . . . 61
2.2 Cost of numerical simulations . . . 62
2.3 Physical and numerical parameters for PIC simulations . . . 63

3.1 Geindre's study on the gradient length . . . 78
3.2 PIC and Vlasov simulation parameters in Ruhl's study . . . 79

4.1 Simulation parameters for VLA scaling tests . . . 128
4.2 VLA/ponderomotive ratio . . . 130
4.3 VLA from plasma mirror: 1D PIC simulation . . . 137
4.4 VLA from plasma mirror: test-particle code . . . 138

A.1 Physical parameters for 1D PIC simulations . . . II
A.2 Numerical parameters for 1D PIC simulations . . . II
A.3 Physical parameters for 2D PIC simulations . . . III
A.4 Numerical parameters for 2D PIC simulations . . . IV

Bibliography

Agrawal, GP, & Pattanayak, DN. 1979. Gaussian beam propagation beyond the paraxial approximation. *J. Opt. Soc. Am.*, **69**(4), 575–578. 70

Alder, Berni J, & Wainwright, TE. 1959. Studies in molecular dynamics. I. General method. *The Journal of Chemical Physics*, **31**(2), 459–466. 3

Arber, T D, Bennett, K, Brady, C S, Lawrence-Douglas, A, Ramsay, M G, Sircombe, N J, Gillies, P, Evans, R G, Schmitz, H, & Bell, A R. 2015. Contemporary particle-in-cell approach to laser-plasma modelling. *Plasma Phys. Control. Fusion*, **57**(11), 113001. 56

Baeva, T, Gordienko, S, & Pukhov, A. 2006. Theory of high-order harmonic generation in relativistic laser interaction with overdense plasma. *Phys. Rev. E*, **74**(4), 046404. 40, 48, 105

Bastiani, S, Rousse, A, Geindre, J P, Audebert, P, Quoix, C, Hamoniaux, G, Antonetti, A, & Gauthier, J C. 1997. Experimental study of the interaction of subpicosecond laser pulses with solid targets of varying initial scale lengths. *Phys. Rev. E*, **56**(6), 7179. 32, 148, 149

Beg, F N, Bell, A R, Dangor, A E, Danson, C N, Fews, A P, Glinsky, M E, Hammel, B A, Lee, P, Norreys, P A, & Tatarakis, M A. 1997. A study of picosecond laser–solid interactions up to 1019 W cm- 2. *Phys. Plasmas*, **4**(2), 447–457. 32

Bergmann, A, & Mulser, P. 1993. Breaking of resonantly excited electron plasma waves. *Phys. Rev. E*, **47**(5), 3585. 24

Birdsall, Charles K, & Langdon, A Bruce. 2004. *Plasma physics via computer simulation*. CRC Press. 60

Bochove, EJ, Moore, GT, & Scully, MO. 1992. Acceleration of particles by an asymmetric Hermite-Gaussian laser beam. *Phys. Rev. A*, **46**(10), 6640. 157

Bocoum, Maïmouna, Böhle, Frederik, Vernier, Aline, Jullien, Aurélie, Faure, Jérôme, & Lopez-Martens, Rodrigo. 2015. Spatial-domain interferometer for measuring plasma mirror expansion. *Opt. Lett.*, **40**(13), 3009–3012. 31, 144

Borot, A, Douillet, D, Iaquaniello, G, Lefrou, T, Audebert, P, Geindre, J-P, & Lopez-Martens, R. 2014. High repetition rate plasma mirror device for attosecond science. *Rev. Sci. Instrum.*, **85**(1), 013104. 144

Borot, Antonin. 2012. *Génération d'impulsions attosecondes sur miroir plasma à très haute cadence*. Ph.D. thesis, Ecole Polytechnique X. 16

Bourdier, A. 1983. Oblique incidence of a strong electromagnetic wave on a cold inhomogeneous electron plasma. Relativistic effects. *Phys. Fluids*, **26**(7), 1804–1807. 18

Boyd, T J M, & Ondarza-Rovira, R. 2008. Anomalies in universal intensity scaling in ultrarelativistic laser-plasma interactions. *Phys. Rev. Lett.*, **101**(12), 125004. 49

Brandl, F, Hidding, B, Osterholz, J, Hemmers, D, Karmakar, A, Pukhov, A, & Pretzler, G. 2009. Directed acceleration of electrons from a solid surface by sub-10-fs laser pulses. *Phys. Rev. Lett.*, **102**(19), 195001. 32

Brunel, F. 1987. Not-so-resonant, resonant absorption. *Phys. Rev. Lett.*, **59**(1), 52. 24, 26, 80, 106

Bulanov, So V, Naumova, N M, & Pegoraro, F. 1994. Interaction of an ultrashort, relativistically strong laser pulse with an overdense plasma. *Phys. Plasmas*, **1**(3), 745–757. 42, 43

Burnett, NH, Baldis, HA, Richardson, MC, & Enright, GD. 1977. Harmonic generation in CO2 laser target interaction. *Appl. Phys. Lett.*, **31**(3), 172–174. 2, 40

Cai, D F, Gu, Y Q, Zheng, Z J, Wen, T S, Chunyu, S T, Wang, Z B, & Yang, X D. 2003. Experimental study for angular distribution of the hot electrons generated by femtosecond laser interaction with solid targets. *Phys. Plasmas*, **10**(8), 3265–3269. 31, 32, 79

Cai, D F, Gu, Y Q, Zheng, Z J, Zhou, W M, Yang, X D, Jiao, C Y, Chen, H, Wen, T S, & Chunyu, S T. 2004. Double-peak emission of hot electrons generated by femtosecond laser interaction with solid targets. *Phys. Rev. E*, **70**(6), 066410. 32

Carbajo, Sergio, Nanni, Emilio A, Wong, Liang Jie, Miller, RJ, & Kärtner, Franz X. 2015. Direct laser acceleration of electrons in free-space. *ArXiv*. 132, 138

Carter, William H. 1970. Bandlimited angular spectrum approximation to a scalar dipole field. *Opt. Comm.*, **2**(3), 142–148. 70

Cavalieri, Adrian L, Müller, Norbert, Uphues, Th, Yakovlev, Vladislav S, Baltuška, Andrius, Horvath, Balint, Schmidt, B, Blümel, L, Holzwarth, R, Hendel, S, *et al.* 2007. Attosecond spectroscopy in condensed matter. *Nature*, **449**(7165), 1029–1032. 2

Chen, L M, Zhang, J, Dong, Q L, Teng, H, Liang, T J, Zhao, L Z, & Wei, Z Y. 2001. Hot electron generation via vacuum heating process in femtosecond laser–solid interactions. *Phys. Plasmas*, **8**(6), 2925–2929. 32

Chen, L M, Kando, Masaki, Xu, M H, Li, Y T, Koga, J, Chen, M, Xu, H, Yuan, X H, Dong, Q L, & Sheng, Z M. 2008. Study of X-ray emission enhancement via a high-contrast femtosecond laser interacting with a solid foil. *Phys. Rev. Lett.*, **100**(4), 045004. 16

Cheng, Chio-Zong, & Knorr, Georg. 1976. The integration of the Vlasov equation in configuration space. *J. Comp. Phys.*, **22**(3), 330–351. 54

Cicchitelli, Lorenzo, Hora, H, & Postle, R. 1990. Longitudinal field components for laser beams in vacuum. *Phys. Rev. A*, **41**(7), 3727. 70

Cline, David, Shao, Lei, Ding, Xiaoping, Ho, Yukun, Kong, Qing, & Wang, Pingxiao. 2013. First Observation of Acceleration of Electrons by a Laser in a Vacuum. *J. Mod. Phys.* 132, 138

Corkum, Paul B. 1993. Plasma perspective on strong field multiphoton ionization. *Phys. Rev. Lett.*, **71**(13), 1994. 2

Debayle, A, Sanz, J, & Gremillet, L. 2015. Self-consistent theory of high-order harmonic generation by relativistic plasma mirror. *Phys. Rev. E*, **92**(5), 053108. 105

Delcroix, Jean-Loup, & Bers, Abraham. 1994. *Physique des plasmas*. Les Ulis (Essonne): EDP sciences. 13

Dendy, Richard O. 1995. *Plasma physics: an introductory course*. Cambridge University Press. 13

Denisov, NG. 1957. On a singularity of the field of an electromagnetic wave propagated in an inhomogeneous plasma. *Sov. Phys. JETP*, **4**(4), 544–553. 23

Dodin, IY, & Fisch, NJ. 2003. Relativistic electron acceleration in focused laser fields after above-threshold ionization. *Phys. Rev. E*, **68**(5), 056402. 114

Drescher, Markus, Hentschel, Michael, Kienberger, R, Uiberacker, Matthias, Yakovlev, Vladislav, Scrinzi, Armin, Westerwalbesloh, Th, Kleineberg, U, Heinzmann, Ulrich, & Krausz, Ferenc. 2002. Time-resolved atomic inner-shell spectroscopy. *Nature*, **419**(6909), 803–807. 2

Dromey, B, Zepf, M, Gopal, A, Lancaster, K, Wei, M S, Krushelnick, K, Tatarakis, M, Vakakis, N, Moustaizis, S, Kodama, R, *et al.* 2006. High harmonic generation in the relativistic limit. *Nat. Phys.*, **2**(7), 456–459. 40

Einstein, A. 1905a. Zur elektrodynamik bewegter körper [adp 17, 891 (1905)]. *Annalen der Physik*, **14**(S1), 194–224. 43

Einstein, Albert. 1905b. On the electrodynamics of moving bodies. 43

Emma, Paul, Akre, R, Arthur, J, Bionta, R, Bostedt, C, Bozek, J, Brachmann, A, Bucksbaum, P, Coffee, Ryan, Decker, F-J, *et al.* 2010. First lasing and operation of an ångstrom-wavelength free-electron laser. *Nat. Photonics*, **4**(9), 641–647. 1

Esarey, E, Schroeder, CB, & Leemans, WP. 2009. Physics of laser-driven plasma-based electron accelerators. *Rev. Mod. Phys.*, **81**(3), 1229. 2, 76

Esarey, Eric, Sprangle, Phillip, & Krall, Jonathan. 1995. Laser acceleration of electrons in vacuum. *Phys. Rev. E*, **52**(5), 5443. 114, 115, 117, 131, 132

Esirkepov, T Zh. 2001. Exact charge conservation scheme for particle-in-cell simulation with an arbitrary form-factor. *Comput. Phys. Comm.*, **135**(2), 144–153. 59

Estabrook, K G, Valeo, E J, & Kruer, W L. 1975. Two-dimensional relativistic simulations of resonance absorption. *Phys. Fluids*, **18**(9), 1151–1159. 23

Faure, Jérôme, Glinec, Yannick, Pukhov, A, Kiselev, S, Gordienko, S, Lefebvre, E, Rousseau, J-P, Burgy, F, & Malka, Victor. 2004. A laser–plasma accelerator producing monoenergetic electron beams. *Nature*, **431**(7008), 541–544. 2

Filbet, Francis, Sonnendrücker, Eric, & Bertrand, Pierre. 2001. Conservative numerical schemes for the Vlasov equation. *J. Comp. Phys.*, **172**(1), 166–187. 54

Forslund, D W, Kindel, J M, Lee, Kenneth, Lindman, E L, & Morse, R L. 1975. Theory and simulation of resonant absorption in a hot plasma. *Phys. Rev. A*, **11**(2), 679. 23, 24

Forslund, DW, Kindel, JM, & Lee, K. 1977. Theory of hot-electron spectra at high laser intensity. *Phys. Rev. Lett.*, **39**(5), 284. 24

Fortin, Pierre-Louis, Piché, Michel, & Varin, Charles. 2009. Direct-field electron acceleration with ultrafast radially polarized laser beams: scaling laws and optimization. *J. Phys. B*, **43**(2), 025401. 157

Geddes, CGR, Toth, Cs, Van Tilborg, J, Esarey, E, Schroeder, CB, Bruhwiler, D, Nieter, C, Cary, J, & Leemans, WP. 2004. High-quality electron beams from a laser wakefield accelerator using plasma-channel guiding. *Nature*, **431**(7008), 538–541. 2

Geindre, J-P, Audebert, P, & Marjoribanks, R S. 2006. Relativistic A C Gyromagnetic Effects in Ultraintense Laser-Matter Interaction. *Phys. Rev. Lett.*, **97**(8), 085001. 80, 82

Geindre, J-P, Marjoribanks, R S, & Audebert, P. 2010. Electron vacuum acceleration in a regime beyond brunel absorption. *Phys. Rev. Lett.*, **104**(13), 135001. 77, 78, 79

Geindre, JP, Mysyrowicz, A, Dos Santos, A, Audebert, P, Rousse, A, Hamoniaux, G, Antonetti, A, Falliès, F, & Gauthier, JC. 1994. Frequency-domain interferometer for measuring the phase and amplitude of a femtosecond pulse probing a laser-produced plasma. *Opt. Lett.*, **19**(23), 1997–1999. 31

Gibbon, Paul. 1996. Harmonic generation by femtosecond laser-solid interaction: A coherent water-window light source. *Phys. Rev. Lett.*, **76**(1), 50. 16

Gibbon, Paul. 2004. *Short pulse laser interactions with matter*. World Scientific Publishing Company. 14, 16

Ginzburg, VL. 1964. *The Properties of Electromagnetic Waves in Plasma*. 23

Glinec, Yannick, Faure, Jérôme, Guemnie-Tafo, A, Malka, Victor, Monard, H, Larbre, JP, De Waele, V, Marignier, JL, & Mostafavi, M. 2006. Absolute calibration for a broad range single shot electron spectrometer. *Rev. Sci. Instrum.*, **77**(10), 103301. 134, 144

Gonoskov, Arkady A, Korzhimanov, Artem V, Kim, Arkady V, Marklund, Mattias, & Sergeev, Aleksander M. 2011. Ultrarelativistic nanoplasmonics as a route towards extreme-intensity attosecond pulses. *Phys. Rev. E*, **84**(4), 046403. 40, 87, 89, 99, 105

Gordienko, S, & Pukhov, A. 2005. Scalings for ultrarelativistic laser plasmas and quasimonoenergetic electrons. *Phys. Plasmas*, **12**(4), 043109. 93

Grassi, Anna, Fedeli, Luca, Sgattoni, Andrea, & Macchi, Andrea. 2016. Vlasov simulation of laser-driven shock acceleration and ion turbulence. *Plasma Phys. Control. Fusion*, **58**(3), 034021. 54

Haaland, Carsten M. 1995. Laser electron acceleration in vacuum. *Opt. Comm.*, **114**(3), 280–284. 3

Hartemann, FV, Fochs, SN, Le Sage, GP, Luhmann Jr, NC, Woodworth, JG, Perry, MD, Chen, YJ, & Kerman, AK. 1995. Nonlinear ponderomotive scattering of relativistic electrons by an intense laser field at focus. *Phys. Rev. E*, **51**(5), 4833. 66, 114, 115, 123

Jackson, John David. 1999. *Classical electrodynamics*. Wiley. 44

Jullien, Aurélie, Ricci, Aurélien, Böhle, Frederik, Rousseau, Jean-Philippe, Grabielle, Stéphanie, Forget, Nicolas, Jacqmin, Hermance, Mercier, Brigitte, & Lopez-Martens, Rodrigo. 2014. Carrier-envelope-phase stable, high-contrast, double chirped-pulse-amplification laser system. *Opt. Lett.*, **39**(13), 3774–3777. 143

Kahaly, S, Monchocé, S, Vincenti, H, Dzelzainis, T, Dromey, B, Zepf, M, Martin, Ph, & Quéré, F. 2013. Direct observation of density-gradient effects in harmonic generation from plasma mirrors. *Phys. Rev. Lett.*, **110**(17), 175001. 31, 134, 144

Kibble, TWB. 1966. Refraction of electron beams by intense electromagnetic waves. *Phys. Rev. Lett.*, **16**(23), 1054. 9

Kruer, W L, & Estabrook, Kent. 1985. J× B heating by very intense laser light. *Phys. Fluids*, **28**(1), 430–432. 27

Kruer, William L. 1988. *The physics of laser plasma interactions*. Addison-Wesley Publishing Co. 13, 16, 23

Langdon, A Bruce, & Birdsall, Charles K. 1970. Theory of Plasma Simulation Using Finite-Size Particles. *Phys. Fluids*, **13**(8), 2115–2122. 60

Lawson, JD, *et al.* 1979. Lasers and accelerators. *IEEE Trans. Nucl. Sci.*, **26**(3), 4217–4219. 117

Lévy, Anna, Ceccotti, Tiberio, D'Oliveira, Pascal, Réau, Fabrice, Perdrix, Michel, Quéré, Fabien, Monot, Pascal, Bougeard, Michel, Lagadec, Hervé, Martin, Philippe, *et al.* 2007. Double plasma mirror for ultrahigh temporal contrast ultraintense laser pulses. *Opt. Lett.*, **32**(3), 310–312. 134

Li, Y T, Yuan, X H, Xu, M H, Zheng, Z Y, Sheng, Z M, Chen, M, Ma, Y Y, Liang, W X, Yu, Q Z, Zhang, Y, *et al.* 2006a. Observation of a fast electron beam emitted along the surface of a target irradiated by intense femtosecond laser pulses. *Phys. Rev. Lett.*, **96**(16), 165003. 31, 32

Li, Z, Daido, H, Fukumi, A, Sagisaka, A, Ogura, K, Nishiuchi, M, Orimo, S, Hayashi, Y, Mori, M, Kado, M, *et al.* 2006b. Measurements of energy and angular distribution of hot electrons and protons emitted from a p-and s-polarized intense femtosecond laser pulse driven thin foil target. *Phys. Plasmas*, **13**(4), 3104. 29, 30, 32, 79

Lichters, Roland, Meyer-ter-Vehn, J, & Pukhov, A. 1996. Short-pulse laser harmonics from oscillating plasma surfaces driven at relativistic intensity. *Phys. Plasmas*, **3**(9), 3425–3437. 40, 45, 105

Lorenz, Edward N. 1963. Deterministic nonperiodic flow. *J. Atm. Sci.*, **20**(2), 130–141. 3

Malka, G, & Miquel, JL. 1996. Experimental confirmation of ponderomotive-force electrons produced by an ultrarelativistic laser pulse on a solid target. *Phys. Rev. Lett.*, **77**(1), 75. 31, 32, 131

Maltsev, A, & Ditmire, T. 2003. Above threshold ionization in tightly focused, strongly relativistic laser fields. *Phys. Rev. Lett.*, **90**(5), 053002. 114

Malvache, Arnaud. 2011. *Optique non-linéaire à haute intensité: Compression d'impulsions laser Interaction laser-plasma*. Ph.D. thesis, Ecole Polytechnique X. 34, 38

Mangles, SPD, Murphy, CD, Najmudin, Z, Thomas, AGR, Collier, JL, Dangor, AE, Divall, EJ, Foster, PS, Gallacher, JG, Hooker, CJ, *et al.* 2004. Monoenergetic beams of relativistic electrons from intense laser–plasma interactions. *Nature*, **431**(7008), 535–538. 2

Marceau, Vincent, Varin, Charles, Brabec, Thomas, & Piché, Michel. 2013. Femtosecond 240-keV electron pulses from direct laser acceleration in a low-density gas. *Phys. Rev. Lett.*, **111**(22), 224801. 157

McNaught, SJ, Knauer, JP, & Meyerhofer, DD. 1998. Photoelectron initial conditions for tunneling ionization in a linearly polarized laser. *Phys. Rev. A*, **58**(2), 1399. 132

Moore, CI, Ting, A, McNaught, SJ, Qiu, J, Burris, HR, & Sprangle, P. 1999. A laser-accelerator injector based on laser ionization and ponderomotive acceleration of electrons. *Phys. Rev. Lett.*, **82**(8), 1688. 132, 138

Mora, P, & Quesnel, B. 1998. Comment on ?Experimental observation of electrons accelerated in vacuum to relativistic energies by a high-intensity laser? *Phys. Rev. Lett.*, **80**(6), 1351. 131

Mordovanakis, Aghapi G, Easter, James, Naumova, Natalia M, Popov, Konstantin, Masson-Laborde, Paul-Edouard, Hou, Bixue, Sokolov, Igor, Mourou, Gérard, Glazyrin, Igor V, Rozmus, Wojciech, *et al.* 2009. Quasimonoenergetic electron beams with relativistic energies and ultrashort duration from laser-solid interactions at 0.5 kHz. *Phys. Rev. Lett.*, **103**(23), 235001. 29, 30, 32, 33, 133, 148

Mori, WB, & Katsouleas, T. 1995. Laser acceleration. *Pages 112–130 of: AIP Conference Proceedings*, vol. 335. 115

Naumova, N M, Sokolov, I, Nees, J, Maksimchuk, A, Yanovsky, V, & Mourou, G. 2004a. Attosecond electron bunches. *Phys. Rev. Lett.*, **93**(19), 195003. 76, 77

Naumova, N M, Nees, J A, Sokolov, I V, Hou, B, & Mourou, GA. 2004b. Relativistic generation of isolated attosecond pulses in a λ 3 focal volume. *Phys. Rev. Lett.*, **92**(6), 063902. 148

Pang, J, Ho, YK, Yuan, XQ, Cao, N, Kong, Q, Wang, PX, Shao, L, Esarey, EH, & Sessler, AM. 2002. Subluminous phase velocity of a focused laser beam and vacuum laser acceleration. *Phys. Rev. E*, **66**(6), 066501. 114

Plettner, T, Byer, RL, Colby, E, Cowan, B, Sears, CMS, Spencer, JE, & Siemann, RH. 2005. Visible-laser acceleration of relativistic electrons in a semi-infinite vacuum. *Phys. Rev. Lett.*, **95**(13), 134801. 119, 132

Quéré, F, Thaury, Cédric, Monot, P, Dobosz, S, Martin, Ph, Geindre, J-P, & Audebert, P. 2006. Coherent wake emission of high-order harmonics from overdense plasmas. *Phys. Rev. Lett.*, **96**(12), 125004. 2, 34

Quesnel, Brice. 1998. *Effets relativistes dans l'interaction laser-plasma à très haut flux: instabilités paramétriques électroniques et force pondéromotrice*. Ph.D. thesis, Ecole Polytechnique X. 70

Quesnel, Brice, & Mora, Patrick. 1998. Theory and simulation of the interaction of ultraintense laser pulses with electrons in vacuum. *Phys. Rev. E*, **58**(3), 3719. 70, 71, 123

Ruhl, H. 1996. Electron jets produced by ultrashort laser pulses. *J. Opt. Soc. Am. B*, **13**(2), 388–394. 28, 105

Ruhl, H, Sentoku, Y, Mima, K, Tanaka, K A, & Kodama, R. 1999. Collimated electron jets by intense laser-beam–plasma surface interaction under oblique incidence. *Phys. Rev. Lett.*, **82**(4), 743. 33, 78, 79

Salamin, Yousef I. 2006. Electron acceleration from rest in vacuum by an axicon Gaussian laser beam. *Phys. Rev. A*, **73**(4), 043402. 157

Salamin, Yousef I, & Keitel, Christoph H. 2002. Electron acceleration by a tightly focused laser beam. *Phys. Rev. Lett.*, **88**(9), 095005. 114

Santala, M I K, Zepf, M, Watts, I, Beg, F N, Clark, E, Tatarakis, M, Krushelnick, K, Dangor, A E, McCanny, T, Spencer, I, *et al.* 2000. Effect of the plasma density scale length on the direction of fast electrons in relativistic laser-solid interactions. *Phys. Rev. Lett.*, **84**(7), 1459. 31, 32

Sanz, J, Debayle, A, & Mima, K. 2012. Model for ultraintense laser-plasma interaction at normal incidence. *Phys. Rev. E*, **85**(4), 046411. 105

Sheng, Z-M, Mima, K, Sentoku, Y, Jovanović, MS, Taguchi, T, Zhang, J, & Meyer-ter Vehn, J. 2002. Stochastic heating and acceleration of electrons in colliding laser fields in plasma. *Phys. Rev. Lett.*, **88**(5), 055004. 149

Siegman, Anthony E. 1986. Lasers University Science Books. *Mill Valley, CA*, **37**, 208. 8, 69

Strickland, Donna, & Mourou, Gerard. 1985. Compression of amplified chirped optical pulses. *Opt. Comm.*, **56**(3), 219–221. 1

Stupakov, GENNADY V, & Zolotorev, MS. 2001. Ponderomotive laser acceleration and focusing in vacuum for generation of attosecond electron bunches. *Phys. Rev. Lett.*, **86**(23), 5274. 114

Tajima, T, & Dawson, JM. 1979. Laser electron accelerator. *Phys. Rev. Lett.*, **43**(4), 267. 2

Tarasevitch, Alexander, Lobov, Konstantin, Wünsche, Clemens, & von der Linde, Dietrich. 2007. Transition to the relativistic regime in high order harmonic generation. *Phys. Rev. Lett.*, **98**(10), 103902. 144

Thaury, Cédric. 2008. *Génération d'harmoniques d'ordres élevés sur miroir plasma.* Ph.D. thesis, Université Paris Sud-Paris XI. 36, 44

Thaury, Cédric, & Quéré, F. 2010. High-order harmonic and attosecond pulse generation on plasma mirrors: basic mechanisms. *J. Phys. B*, **43**(21), 213001. 34, 38, 40, 45, 99, 144

Thaury, Cédric, Quéré, F, Geindre, J-P, Levy, A, Ceccotti, T, Monot, P, Bougeard, M, Réau, F, D'Oliveira, P, Audebert, P, *et al.* 2007. Plasma mirrors for ultrahigh-intensity optics. *Nat. Phys.*, **3**(6), 424–429. 34, 36, 40

Thomas, AGR, Tzoufras, M, Robinson, APL, Kingham, RJ, Ridgers, CP, Sherlock, M, & Bell, AR. 2012. A review of Vlasov–Fokker–Planck numerical modeling of inertial confinement fusion plasma. *J. Comp. Phys.*, **231**(3), 1051–1079. 54

Tian, Ye, Liu, Jiansheng, Wang, Wentao, Wang, Cheng, Deng, Aihua, Xia, Changquan, Li, Wentao, Cao, Lihua, Lu, Haiyang, Zhang, Hui, *et al.* 2012. Electron Emission at Locked Phases from the Laser-Driven Surface Plasma Wave. *Phys. Rev. Lett.*, **109**(11), 115002. 32, 148

Tokita, Shigeki, Hashida, Masaki, Inoue, Shunsuke, Nishoji, Toshihiko, Otani, Kazuto, & Sakabe, Shuji. 2010. Single-shot femtosecond electron diffraction with laser-accelerated electrons: experimental demonstration of electron pulse compression. *Phys. Rev. Lett.*, **105**(21), 215004. 2

Tommasini, Riccardo, Fill, Ernst E, Bruch, Reinhard, & Pretzler, Georg. 2004. Generation of monoenergetic ultrashort electron pulses from a fs laser plasma. *Appl. Phys. B*, **79**(8), 923–926. 32

Uiberacker, Matthias, Uphues, Th, Schultze, Martin, Verhoef, Aart Johannes, Yakovlev, Vladislav, Kling, Matthias F, Rauschenberger, Jens, Kabachnik, Nicolai M, Schröder, Hartmut, Lezius, Matthias, *et al.* 2007. Attosecond real-time observation of electron tunnelling in atoms. *Nature*, **446**(7136), 627–632. 2

Varin, Charles, & Piché, Michel. 2006. Relativistic attosecond electron pulses from a free-space laser-acceleration scheme. *Phys. Rev. E*, **74**(4), 045602. 114

Varin, Charles, Piché, Michel, & Porras, Miguel A. 2005. Acceleration of electrons from rest to GeV energies by ultrashort transverse magnetic laser pulses in free space. *Phys. Rev. E*, **71**(2), 026603. 73

Villasenor, John, & Buneman, Oscar. 1992. Rigorous charge conservation for local electromagnetic field solvers. *Comput. Phys. Comm.*, **69**(2-3), 306–316. 58

Vincenti, H, Monchocé, S, Kahaly, S, Bonnaud, G, Martin, Ph, & Quéré, F. 2014. Optical properties of relativistic plasma mirrors. *Nat. Commun.*, **5**, 3403. 16, 99

Wharton, K B, Hatchett, S P, Wilks, S C, Key, M H, Moody, J D, Yanovsky, V, Offenberger, A A, Hammel, B A, Perry, M D, & Joshi, C. 1998. Experimental measurements of hot electrons generated by ultraintense (> 10 19 W/cm 2) laser-plasma interactions on solid-density targets. *Phys. Rev. Lett.*, **81**(4), 822. 32

Wheeler, Jonathan A, Borot, Antonin, Monchocé, Sylvain, Vincenti, Henri, Ricci, Aurélien, Malvache, Arnaud, Lopez-Martens, Rodrigo, & Quéré, Fabien. 2012. Attosecond lighthouses from plasma mirrors. *Nat. Photonics*, **6**(12), 829–833. 2, 157

Wilks, SC. 1993. Simulations of ultraintense laser–plasma interactions. *Phys. Fluids B*, **5**(7), 2603–2608. 28

Woodward, PM. 1946. A method of calculating the field over a plane aperture required to produce a given polar diagram. *J. Inst. Electr. Eng.*, **93**(10), 1554–1558. 117

Yee, Kane S, *et al.* 1966. Numerical solution of initial boundary value problems involving Maxwellss equations in isotropic media. *IEEE Trans. Antennas Propag*, **14**(3), 302–307. 53, 56

Yu, Wei, Yu, MY, Ma, JX, Sheng, ZM, Zhang, J, Daido, H, Liu, SB, Xu, ZZ, & Li, RX. 2000. Ponderomotive acceleration of electrons at the focus of high intensity lasers. *Phys. Rev. E*, **61**(3), R2220. 114

Ziman, John M. 1960. *Electrons and phonons: the theory of transport phenomena in solids*. Oxford University Press. 1

Appendix A

Parameters for numerical simulations

name	a_0	τ_L	n_{bulk}	n_{min}	L	T_e[eV]	ions	T_i[eV]
these_cwe2	0.3	∞	$100n_c$	$0.2n_c$	$\lambda/60$	0	immobile	0
these_cwe	0.1	∞	$250n_c$	$0.2n_c$	$\lambda/50$	0	immobile	0
these_rom2	0.8	∞	$100n_c$	$0.2n_c$	$\lambda/50$	0	immobile	0
these_rom1	5	∞	$50n_c$	$0.2n_c$	$\lambda/8$	0	immobile	0
these_step	10	∞	$5n_c$	$0.1n_c$	0	0	immobile	0
these_grad1s64	5	$2T_L$ FWHM $\sin^2$	$200n_c$	$0.1n_c$	$\lambda/64$	0	immobile	0
these_grad1s8	5	$2T_L$ FWHM $\sin^2$	$200n_c$	$0.1n_c$	$\lambda/8$	0	immobile	0
harmv9_a*_L1s*	*	$10T_L$ FWHM $\mathcal{G}$	$250n_c$	$0.2n_c$	*	500	3672	50
these_cwerom	1	$4T_L$ FWHM $\sin^2$	$100n_c$	$0.2n_c$	$\lambda/60$	0	immobile	0

Table A.1: Physical parameters for 1D PIC simulations. All simulations were performed with EPOCH. The angle of incidence was $\theta = 45°$. The second column indicates the duration and the temporal profile of the laser envelope, where $\sin^2$ stands for an arch of a $\sin^2$ function and $\mathcal{G}$ stands for a gaussian function. When ions are not immobile, the second last column contains the ion's m/q ratio with respect to the electron's m/q ratio.

name	Δx	ppc	x_{crit}	L_{bulk}	N_{part}	N_{cell}	N_{step}
these_cwe2	$\lambda/3000$	500	5λ	3λ	2×10^6	2×10^4	6×10^4
these_cwe	$\lambda/5000$	500	1λ	3λ	10^6	8×10^3	2×10^4
these_rom2	$\lambda/1000$	50	5λ	3λ	10^5	10^4	2×10^4
these_rom1	$\lambda/1000$	500	5λ	3λ	10^6	10^4	2×10^4
these_step	$\lambda/2000$	1000	3λ	3λ	4×10^6	10^4	2×10^4
these_grad1s64	$\lambda/1000$	500	3λ	3λ			
these_grad1s8	$\lambda/1000$	500	3λ	3λ			
harmv9_a*_L1s*	$\lambda/3000$	1000	20λ	4λ	2×10^6	8×10^4	2×10^4
these_cwerom	$\lambda/3000$	500	5λ	2.2λ			

Table A.2: Numerical parameters for 1D PIC simulations. All simulations were performed with EPOCH. L_{bulk} stands for the width of the dense region of plasma with $n = n_{bulk}$.

name	a_0	w_0	τ_L	n_{bulk}	n_{min}	L	T_e[eV]	ions	T_i[eV]
injectorv2_L1s32	3	3.6λ	$9.7T_L$ FWHM $\mathcal{G}$	$100n_c$	$0.2n_c$	$\lambda/32$	0	3672	0
injectorv2_L1s8	3	3.6λ	$9.7T_L$ FWHM $\mathcal{G}$	$100n_c$	$0.2n_c$	$\lambda/8$	0	3672	0
injectorv2_L1s1	3	3.6λ	$9.7T_L$ FWHM $\mathcal{G}$	$100n_c$	$0.2n_c$	λ	0	3672	0
injectorv3_L1s32	3	3.6λ	$9.7T_L$ FWHM $\mathcal{G}$	$100n_c$	$0.2n_c$	$\lambda/32$	100	3672	10
injectorv3_L1s8	3	3.6λ	$9.7T_L$ FWHM $\mathcal{G}$	$100n_c$	$0.2n_c$	$\lambda/8$	100	3672	10
injectorv3_L1s1	3	3.6λ	$9.7T_L$ FWHM $\mathcal{G}$	$100n_c$	$0.2n_c$	λ	100	3672	10
injectorv4_L1s32	3	3.6λ	$9.7T_L$ FWHM $\mathcal{G}$	$100n_c$	$0.2n_c$	$\lambda/32$	100	3672	10
injectorv4_L1s8	3	3.6λ	$9.7T_L$ FWHM $\mathcal{G}$	$100n_c$	$0.2n_c$	$\lambda/8$	100	3672	10
injectorv4_L1s1	3	3.6λ	$9.7T_L$ FWHM $\mathcal{G}$	$100n_c$	$0.2n_c$	λ	100	3672	10
CWEv5_largewaist_L1s40	0.4	3.4λ	$9.7T_L$ FWHM $\mathcal{G}$	$250n_c$	$0.2n_c$	$\lambda/40$	50	immobile	0
CWEv5_largewaist_L1s5	0.4	3.4λ	$9.7T_L$ FWHM $\mathcal{G}$	$250n_c$	$0.2n_c$	$\lambda/5$	50	immobile	0
largewaist_electronsv2_L0p0	0.4	3.4λ	$9.7T_L$ FWHM $\mathcal{G}$	$100n_c$	$0.2n_c$	0	500	3672	50
largewaist_electronsv2_L0p2	0.4	3.4λ	$9.7T_L$ FWHM $\mathcal{G}$	$100n_c$	$0.2n_c$	0.2λ	500	3672	50
largewaist_electronsv2_L0p6	0.4	3.4λ	$9.7T_L$ FWHM $\mathcal{G}$	$100n_c$	$0.2n_c$	0.6λ	500	3672	50
largewaist_electronsv2_L1	0.4	3.4λ	$9.7T_L$ FWHM $\mathcal{G}$	$100n_c$	$0.2n_c$	λ	500	3672	50

Table A.3: Physical parameters for 2D PIC simulations. All simulations were performed with EPOCH. The second column shows the beam waist. The angle of incidence was $\theta = 45°$. The second column indicates the duration and the temporal profile of the laser envelope, where $\sin^2$ stands for an arch of a $\sin^2$ function and $\mathcal{G}$ stands for a gaussian function. When ions are not immobile, the second last column contains the ion's m/q ratio with respect to the electron's m/q ratio.

name	Δx	ppc	x_{crit}	L_{bulk}	N_{part}	N_{cell}	N_{step}	time
injectorv2_L1s32	$\lambda/200$	10	25λ	4λ	10^8	10^8	2.8×10^4	1 900h
injectorv2_L1s8	$\lambda/200$	10	25λ	4λ	1.3×10^8	1.1×10^8	2.8×10^4	1 900h
injectorv2_L1s1	$\lambda/200$	10	25λ	4λ	2.7×10^8	1.1×10^8	2.8×10^4	4 000h
injectorv3_L1s32	$\lambda/200$	10	25λ	4λ	10^8	10^8	2.8×10^4	1 900h
injectorv3_L1s8	$\lambda/200$	10	25λ	4λ	1.3×10^8	1.1×10^8	2.8×10^4	1 900h
injectorv3_L1s1	$\lambda/200$	10	25λ	4λ	2.7×10^8	1.1×10^8	2.8×10^4	4 000h
injectorv4_L1s32	$\lambda/300$	10	25λ	4λ	2.7×10^8	2.3×10^8	4.1×10^4	6 000h
injectorv4_L1s8	$\lambda/300$	10	25λ	4λ	2.9×10^8	2.3×10^8	4.1×10^4	6 000h
injectorv4_L1s1	$\lambda/300$	10	25λ	4λ	6×10^8	2.6×10^8	4.1×10^4	18 000h
CWEv5_largewaist_L1s40	$\lambda/420$	80	10λ	5λ	2.9×10^8	1.1×10^8	4×10^4	3 000h
CWEv5_largewaist_L1s5	$\lambda/420$	80	10λ	5λ	9×10^8	1.3×10^8	4×10^4	9 000h
largewaist_electronsv2_L0p0	$\lambda/400$	10	25λ	5λ	2.8×10^8	4.3×10^8	6×10^4	14 000h
largewaist_electronsv2_L0p2	$\lambda/400$	10	25λ	5λ	3.7×10^8	4.3×10^8	6×10^4	22 000h
largewaist_electronsv2_L0p6	$\lambda/400$	10	25λ	5λ	3.9×10^8	4.3×10^8	6×10^4	25 000h
largewaist_electronsv2_L1	$\lambda/350$	10	25λ	5λ	4×10^8	3.3×10^8	6×10^4	23 000h

Table A.4: Numerical parameters for 2D PIC simulations. All simulations were performed with EPOCH. The space step Δx is the same in both directions. L_{bulk} stands for the width of the dense region of plasma with $n = n_{bulk}$.

Appendix B

Extended Brunel model

Figure 1.9 shows electron trajectories calculated with a simplified model. We start from Brunel's hypotheses (see section 1.3.2), and relax the following hypotheses:

Low-intensity: Relativistic and magnetic corrections are included in the equation of motion;

Small displacement: We no longer assume that the electron displacement around the target surface is small ($|\delta x| \ll \lambda$), so that the space dependence is taken into account in the equations.

All other assumptions from Brunel's model, including the perfectly reflecting mirror and the plasma fields, are conserved. Besides, the equations are solved in the Bourdier boosted frame (see 1.2), where the incident, reflected and plasma fields on electron number j are respectively:

$$\boldsymbol{E}'_i = -E_0 \cos\theta \sin(\omega' t' - k' x')\boldsymbol{e}_y \tag{B.1}$$

$$\boldsymbol{B}'_i = -\frac{E_0}{c} \cos\theta \sin(\omega' t' - k' x')\boldsymbol{e}_z \tag{B.2}$$

$$\boldsymbol{E}'_r = +E_0 \cos\theta \sin(\omega' t' + k' x')\boldsymbol{e}_y \tag{B.3}$$

$$\boldsymbol{B}'_r = -\frac{E_0}{c} \cos\theta \sin(\omega' t' + k' x')\boldsymbol{e}_z \tag{B.4}$$

$$\boldsymbol{E}'_{pj} = -2E_0 \sin\theta \cos\theta \sin(\omega' t'_j)\boldsymbol{e}_x \tag{B.5}$$

$$\boldsymbol{B}'_{pj} = -2\frac{E_0}{c} \sin^2\theta \cos\theta \sin(\omega' t'_j)\boldsymbol{e}_z \tag{B.6}$$

where x is the electron position and t_j is its release time in the fields. The electron speed is $\boldsymbol{v}$. Solving

$$\frac{d\boldsymbol{p}'_j}{dt'} = -e(\boldsymbol{E}' + \boldsymbol{v}' \times \boldsymbol{B}') \tag{B.7}$$

$$\text{with } \boldsymbol{E}' = \boldsymbol{E}'_i + \boldsymbol{E}'_r + \boldsymbol{E}'_{pj} \tag{B.8}$$

$$\text{and } \boldsymbol{B}' = \boldsymbol{B}'_i + \boldsymbol{B}'_r + \boldsymbol{B}'_{pj} \tag{B.9}$$

for different release times t_j with $0 < t_j < T'_L/2$ gives trajectories in figure 1.9.

Appendix C

Summary in French

Lorsqu'une impulsion laser est focalisée à une intensité relativiste sur une cible solide, le matériau est instantanément ionisé et forme un miroir plasma, c'est-à-dire un plasma surdense présentant un court gradient de densité sur sa face avant. La réflexion de l'impulsion laser génère alors des harmoniques élevées dans l'impulsion réfléchie, et des électrons peuvent être accélérés hors de la cible. Si la génération d'harmoniques est bien comprise, l'accélération des électrons reste, à ce jour, mal expliquée. Or, de nombreuses expériences font état d'électrons éjectés de la cible, parfois à des énergies relativistes. Basé sur des résultats expérimentaux obtenus avec deux lasers femtosecondes ultraintenses (le laser *Salle Noire* au LOA et le laser UHI100 au CEA), ce travail théorique et numérique a pour but d'identifier les mécanismes d'éjection et d'accélération des électrons hors de la cible. Les simulations numériques ont été réalisées avec le code particle-in-cell EPOCH.

On considère une impulsion laser ultracourte (25 fs, avec $1\,\mathrm{fs} = 10^{-15}\,\mathrm{s}$) et ultraintense ($I \sim 10^{18}\,\mathrm{W \cdot cm^{-2}}$) focalisée en incidence oblique ($\theta \simeq 45°$) et polarisation P sur un miroir plasma. La longueur d'onde du laser est de l'ordre de $\lambda = 800\,\mathrm{nm}$ et la tache focale mesure quelques microns. Le corps du plasma est largement sur-dense et le gradient de densité en face avant a un profil exponentiel avec une longueur caractéristique inférieure à la longueur d'onde du laser. Expérimentalement, ce profil de plasma est obtenu en focalisant une pré-impulsion sur une cible solide (un morceau de plastique avec une qualité de surface optique) avant l'impulsion principale. Cette pré-impulsion ionise la cible, et le plasma sur-dense ainsi créé s'étend dans le vide en formant un profil exponentiel. L'impulsion principale est envoyée sur la cible quelques picosecondes après la pré-impulsion. La longueur de gradient est ainsi déterminée par l'intervalle de temps entre la pré-impulsion et l'impulsion principale.

Lorsque l'impulsion principale se réfléchit sur le miroir plasma, certains électrons initialement présents dans le gradient de densité sont éjectés du plasma. Le premier axe de recherche a été d'identifier le mécanisme d'éjection, qui a lieu à l'échelle du gradient de densité ($< \lambda$). Nous avons démontré qu'il s'agit d'un mécanisme de type push-pull périodique : pendant chaque cycle optique, les électrons sont successivement poussés dans le plasma pendant un demi-cycle, puis tirés vers le vide pendant le demi-cycle suivant. Ces oscillations forcées génèrent des champs plasma très intenses. Nous avons expliqué le rôle déterminant de ces champs plasma et montré que la longueur caractéristique du gradient de densité est un paramètre fondamental de cette interaction. En particulier, les simulations numériques et les expériences révèlent qu'il existe une longueur de gradient optimale pour l'éjection d'électrons (de l'ordre de $\lambda/10$), et nous proposons une explication à cette observation.

Après l'éjection du plasma, les électrons peuvent être accélérés par les champs laser de l'impulsion réfléchie. Cette étape a constitué mon deuxième axe de recherche. Ce processus, appelé *accélération laser dans le vide*, avait été peu étudié expérimentalement en raison de la difficulté d'injecter des électrons directement au centre d'une impulsion laser intense. Le miroir plasma constitue une solution à ce problème, et sert d'injecteur à électrons. Grâce à un modèle présenté dans cette thèse, nous avons pu interpréter les résultats expérimentaux obtenus sur le laser UHI100 du CEA. En particulier, nous démontrons que ces expériences ont conduit pour la première fois à l'accélération dans le vide d'un faisceau d'électrons de charge élevée (3 nC) jusqu'à des énergies relativistes (10 MeV).

Enfin, la génération d'harmoniques lors de cette interaction peut se produire suivant deux mécanismes : l'émission cohérente de sillage (CWE) à faible intensité et le miroir oscillant relativiste (ROM) à haute intensité. La comparaison entre l'éjection d'électrons et chacun de ces mécanismes bien connus constitue le troisième axe de recherche de cette thèse. Nous avons interprété les expériences réalisées sur le laser de la *Salle Noire* du LOA, qui ont révélé une anti-corrélation entre la génération d'harmoniques par CWE et l'éjection d'électrons à basse intensité. A l'inverse, dans le régime de haute intensité, la génération d'harmoniques par le mécanisme ROM et l'éjection d'électrons évoluent de façon très similaire lorsqu'on fait varier la longueur de gradient. Nous montrons que ces grandeurs sont corréléess car elles témoignent toutes deux du même mécanisme. La comparaison entre la génération d'harmoniques et l'éjection d'électrons nous a permis de valider notre compréhension du mouvement des électrons et d'apporter de nouvelles connaissances sur la dynamique nanométrique de la surface du miroir plasma.

Appendix D

Publications

- **Vacuum laser acceleration of relativistic electrons using a plasma mirror injector**, M. Thévenet, A. Leblanc, S. Kahaly, H. Vincenti, A. Vernier, F. Quéré, J. Faure, *Nature Physics* **12**, 355-360 (2016)
- **Anticorrelated emission of high-harmonics and fast electron beams from plasma mirrors**, M. Bocoum, M. Thévenet, F. Böhle, B. Beaurepaire, A. Vernier, A. Jullien, J. Faure, R. Lopez-Martens, *Physical Review Letters* **116**, 185001 (2016)
- **On the physics of electron ejection from laser-irradiated overdense plasmas**, M. Thévenet, H. Vincenti, J. Faure, *Physics of Plasmas* **23**, 063119 (2016)

nature physics

ARTICLES

PUBLISHED ONLINE: 21 DECEMBER 2015 | DOI: 10.1038/NPHYS3597

Vacuum laser acceleration of relativistic electrons using plasma mirror injectors

M. Thévenet[1†], A. Leblanc[2†], S. Kahaly[2], H. Vincenti[1], A. Vernier[1], F. Quéré[2*] and J. Faure[1*]

Accelerating particles to relativistic energies over very short distances using lasers has been a long-standing goal in physics. Among the various schemes proposed for electrons, vacuum laser acceleration has attracted considerable interest and has been extensively studied theoretically because of its appealing simplicity: electrons interact with an intense laser field in vacuum and can be continuously accelerated, provided they remain at a given phase of the field until they escape the laser beam. But demonstrating this effect experimentally has proved extremely challenging, as it imposes stringent requirements on the conditions of injection of electrons in the laser field. Here, we solve this long-standing experimental problem by using a plasma mirror to inject electrons in an ultraintense laser field, and obtain clear evidence of vacuum laser acceleration. With the advent of petawatt lasers, this scheme could provide a competitive source of very high charge (nC) and ultrashort relativistic electron beams.

Femtosecond lasers at present achieve light intensities at focus that far exceed 10^{18} W cm^{-2} at near infrared wavelengths[1]. One of the great prospects of these extreme intensities is the laser-driven acceleration of electrons to relativistic energies within very short distances. At present, the most advanced scheme consists of using ultraintense laser pulses to excite large-amplitude wakefields in underdense plasmas, providing extremely high accelerating gradients of the order of 100 GV m^{-1} (ref. 2). However, over the past decades, the direct acceleration of electrons by light in vacuum has also attracted considerable interest and has been extensively studied theoretically[3–11]. These investigations have been driven by the fundamental interest of this most elementary interaction, and by its potential for extreme electron acceleration through electric fields greater than tens of TV m^{-1} that ultraintense laser pulses provide.

The underlying idea is to inject free electrons into an ultraintense laser field so that they always remain within a given half optical cycle of the field, where they constantly gain energy until they leave the focal volume. One-dimensional (1D) analytical calculations[3] show that, for relativistic electrons, the maximum energy gain from this process is $\Delta E \propto mc^2\gamma_0 a_0^2$, where γ_0 is the electron initial Lorentz factor, a_0 is the normalized laser vector potential, m the electron mass, and c the vacuum light velocity. Reaching high energy gains thus requires high initial energies $\gamma_0 \gg 1$ and/or ultrahigh laser amplitudes ($a_0 \gg 1$).

In contrast with the large body of theoretical work published on this vacuum laser acceleration (VLA) of electrons to relativistic energies, experimental observations have largely remained elusive[12–17]—sometimes even controversial[18,19]—and have so far not demonstrated significant energy gains. This is because VLA occurs efficiently only for electrons injected in the laser field with specific initial conditions that are extremely challenging to fulfil experimentally[9]. Indeed, to stay in phase with the laser field, electrons need to have initial velocities close to c along the laser propagation axis. In addition, they should start interacting with the intense laser beam already close to its spatial and temporal maxima, and even be injected at appropriate phases of this field.

Electrons that do not satisfy these stringent requirements tend to explore many different optical cycles as they interact with the laser field, leading to an oscillatory motion where they are successively accelerated and decelerated, so that their final energy gain is low. When averaged over several cycles, this typically results in a drift motion where electrons are isotropically expelled away from high-intensity regions, an effect which can be accounted for by the relativistic ponderomotive force[20–22].

Here, we present clear evidence of VLA of bunches of $\sim 10^{10}$ electrons, corresponding to charges in the nC range, up to relativistic energies around 10 MeV. Our experimental results clearly discriminate for the first time electrons that have experienced subcycle acceleration, from those whose dynamics has mostly been determined by ponderomotive scattering. To solve the long-standing experimental problem of electron injection in the laser field, we demonstrate a new approach based on the use of plasma mirrors[23], that specularly reflect ultraintense laser fields while simultaneously injecting relativistic electrons in the core of these reflected fields, co-linearly with the propagation direction.

Plasma mirrors as electron injectors

Plasma mirrors are dense plasmas resulting from the ionization of initially solid targets irradiated by intense femtosecond laser pulses[23]. Because their density is comparable to the initial solid density ($\sim 10^{23}$ electrons cm^{-3}), their reflectivity can be as high as 80% (ref. 24). An essential feature of plasma mirrors is that to a large extent they behave like ordinary mirrors: the laser field is specularly reflected with hardly any alteration of its spatial properties[25], even at extremely high laser intensities. This is because plasma expansion is very limited on subpicosecond timescales: the plasma–vacuum interface remains optically flat (flatness $\delta L \ll \lambda$, with λ the laser wavelength) while the femtosecond laser pulse reflects, thus leaving the beam wavefront essentially unaffected. Owing to these remarkable properties, plasma mirrors are now largely used in ultrafast optics as a single-shot high-intensity optical device, for example, to improve the temporal contrast of femtosecond pulses[24],

[1]LOA, ENSTA ParisTech, CNRS, Ecole polytechnique, Université Paris-Saclay, 828 bd des Maréchaux, 91762 Palaiseau cedex, France. [2]Lasers, Interactions and Dynamics Laboratory (LIDyL), Commissariat à l'Energie Atomique, Université Paris-Saclay, DSM/IRAMIS, CEN Saclay, 91191 Gif sur Yvette, France. †These authors contributed equally to this work. *e-mail: fabien.quere@cea.fr; jerome.faure@ensta.fr

© 2015 Macmillan Publishers Limited. All rights reserved

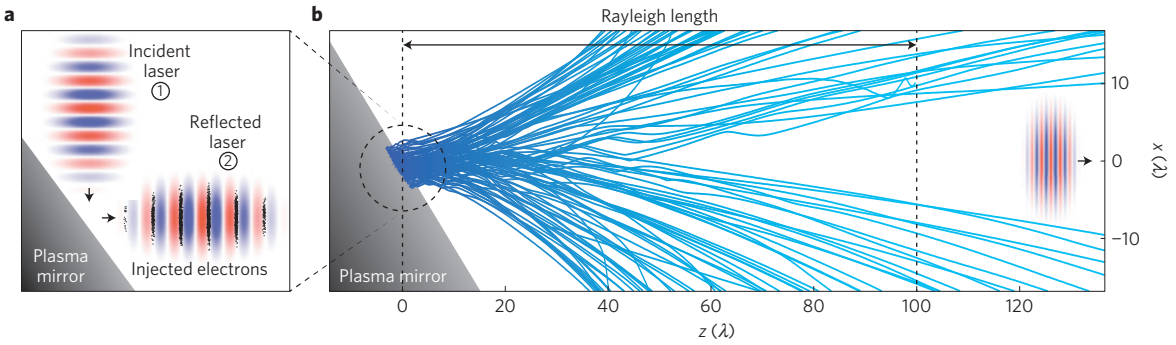


Figure 1 | Injection of relativistic electrons in ultraintense laser fields using plasma mirrors. a, Principle of a plasma mirror injector. As an ultraintense laser pulse (E-field sketched in red and blue) reflects on a plasma mirror, it expels relativistic electrons (black dots) at specific phases of the field. These electrons then interact with the reflected pulse in vacuum. **b**, Electron trajectories (blue lines) computed from a 2D PIC simulation of the laser–plasma interaction (see Methods). Electrons were initially located in the vicinity of the surface of the plasma mirror. Once expelled from the surface, they co-propagate and interact with the reflected laser field over a distance of the order of the Rayleigh length ($z_R = 100\lambda$). This interaction clearly modifies the electron angular distribution as electrons are expelled to the side of the focal volume (see also Supplementary Movie).

for the tight focusing of ultraintense beams[26], or for the generation of high-order harmonics and attosecond pulses[27,28].

During reflection on a plasma mirror, an ultraintense laser pulse can also expel relativistic electrons in a direction close to the specular angle, as seen in particle-in-cell simulations (PIC)[29,30]. Thus, the key idea of this work is that plasma mirrors can be used as electron injectors in the reflected laser field, providing a simple experimental solution to study the interaction of free electrons with intense lasers in vacuum (Fig. 1). These electrons are emitted at given phases of the laser field[30,31], as depicted in Fig. 1a, and then interact with this field in vacuum over the Rayleigh length, as shown in Fig. 1b. Although there have been some observations of electron ejection from solid surfaces[31–35], the experimental parameters did not permit the attainment of the VLA regime we have identified in this work.

Experimental results

Our experiment consisted in measuring the spatial profile of electron beams emitted by plasma mirrors exposed to ultraintense laser pulses, as well as their energy distributions at different emission angles. It was performed on the UHI100 laser at CEA/IRAMIS, a 100 TW laser system that delivers 800 nm, 25 fs pulses. Once their temporal contrast is improved by four orders of magnitude with a plasma-based temporal filtering system[36], the laser pulses are focused on a flat fused silica target at an incidence angle of 55° in the p-polarization, at a peak intensity of 2×10^{19} W cm^{-2} ($a_0 \simeq 3.1$). The focal spot is 5.5 μm full-width at half-maximum (FWHM) and the Rayleigh length is about 80 μm. To optimize the electron signal, the scale length of the plasma density gradient at the surface was accurately controlled by preionizing the target with a weaker prepulse ($\sim 10^{16}$ W cm^{-2}) at an adjustable delay of a few hundreds of femtoseconds before the main pulse[37] (see Supplementary Information for the full data). The electron beam spatial profile was measured using a LANEX phosphor screen placed 15 cm away from the target, perpendicularly to the specular direction, imaged on a charged-coupled device (CCD) camera. A magnetic spectrometer can be inserted before this LANEX screen to measure the electron energy distribution.

A typical electron angular distribution is shown in Fig. 2. The measured electron emission spreads over a broad cone of ∼600 mrad angular width, but is spatially very inhomogeneous within this cone. A pronounced hole is observed around the propagation direction of the reflected beam, with a cylindrical symmetry around this axis. The total angular width of this hole is about 200 mrad, comparable to the divergence of the reflected beam. The other dominant feature is a bright electron peak on one edge of this hole, along the direction of the laser polarization (horizontal axis in Fig. 2) and located between the specular and the normal directions. Its divergence is about 100 mrad, much smaller than that of the total electron beam. From the signal measured on the calibrated LANEX screen[38], the overall charge in the electron beam is about 12 nC, with 3 nC within the bright spot. Note that these patterns were clearly observed at high intensity $I > 10^{19}$ W cm^{-2} and optimized for gradient scale lengths of $L \simeq \lambda/15$ (see Supplementary Information).

Figure 2b shows the spatially resolved electron spectra measured at two different locations in the beam, on opposite sides of the hole along the laser polarization direction. Broad peaked spectra are observed, with a central energy of a few MeV. The key feature here is that the central energy is two times higher in the bright electron peak (10 MeV) than on the opposite side of the hole (5 MeV). This difference in energy suggests a straightforward interpretation for the spatial pattern of the electron beam. The bright peak along the laser polarization could correspond to electrons which have gained energy by VLA owing to appropriate injection conditions in the field. The other electrons in the beam would have experienced isotropic ponderomotive scattering, leading to the symmetrical hole around the laser axis. We now validate this interpretation, by first studying the conditions of injection of electrons from plasma mirrors into the vacuum, and then their subsequent dynamics in the reflected field.

Modelling of the experimental results

Given the complexity of the coupling between intense laser fields and plasma mirrors, we turn to PIC simulations to determine the properties of electrons ejected in the vacuum. Figure 3a shows the density of ejected electrons as a function of time, together with the waveform $B_y(t)$ of the reflected field for interaction conditions corresponding to our experiment. These quantities were both sampled very close to the plasma mirror surface ($d \leq \lambda$), when electrons escape the plasma and are injected into the vacuum in the core of the reflected field. Electrons are observed to be emitted in the form of attosecond bunches at very precise phases close to the nodes of the laser field. We note that the waveform of the reflected field is distorted on reflection, and strongly deviates from a pure sine wave. This is due to the generation of high-order harmonics of the laser frequency on the plasma mirror[39], which is unavoidable at these intensities in the p-polarization. Although this can quantitatively affect the exact outcome of the subsequent laser–electron interaction in vacuum, we will show that this does not qualitatively alter the physics involved. Figure 3b shows the momentum distributions of these electrons immediately after their

© 2015 Macmillan Publishers Limited. All rights reserved

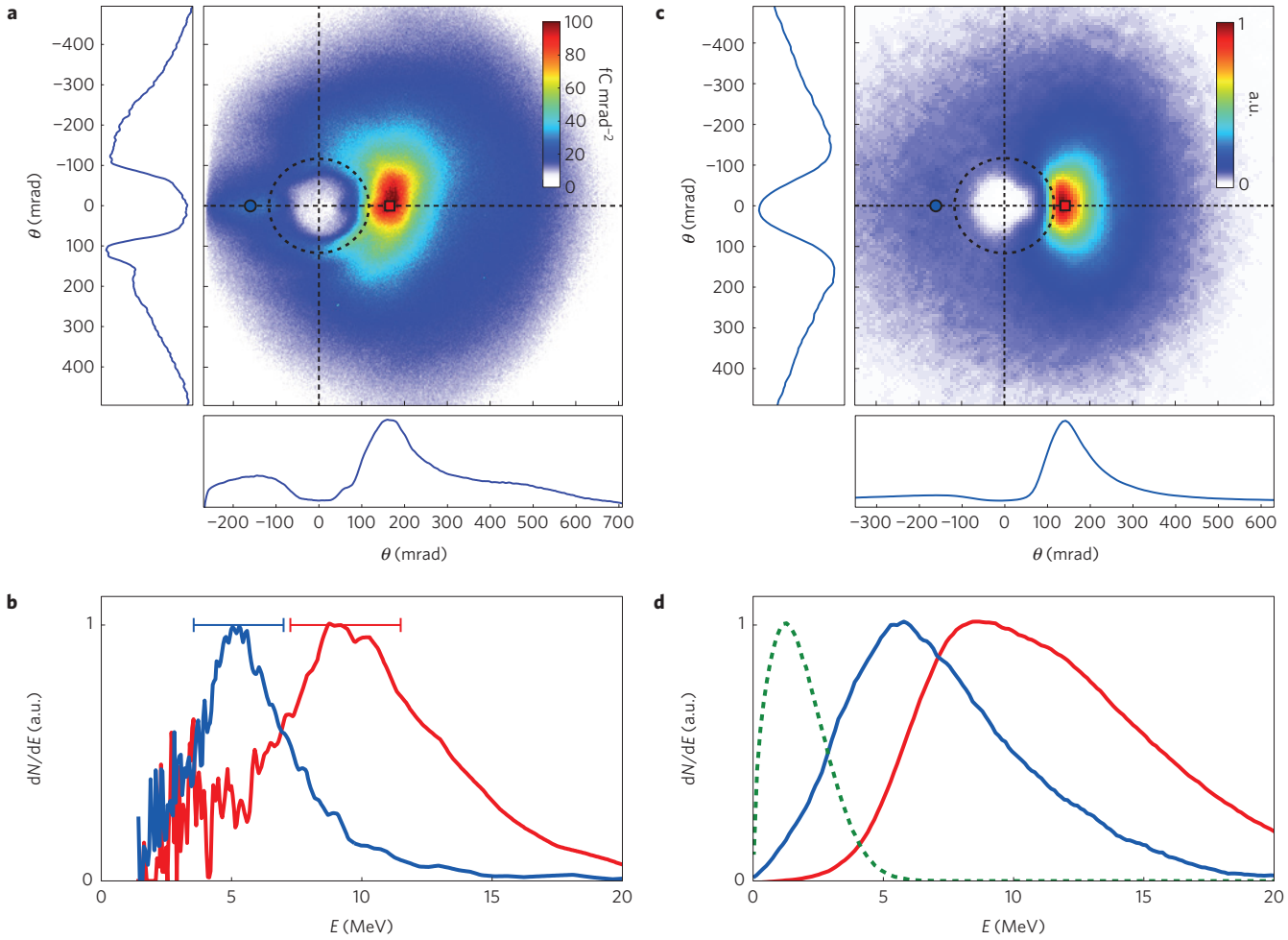


Figure 2 | Experimental evidence of vacuum laser acceleration. Panel **a**, Typical experimental angular distribution of electrons emitted from plasma mirrors into the vacuum, measured with the LANEX screen. It consists of a broad emission cone (blue disk), which is strongly modulated by two main patterns. One is a well defined hole (in white) around the reflected laser beam (whose size and position in the detection plane are indicated by the dashed circle), due to the ponderomotive scattering of electrons after their ejection from the plasma mirror. The other is a bright peak (in red), right on the edge of this hole, due to VLA of a fraction of these electrons. Line-outs of the distribution along the dashed lines are plotted in the side panels, and the direction normal to the plasma mirror surface corresponds to $\theta \simeq 960$ mrad (not shown). **b**, Electron spectra measured at two different locations in the beam (the horizontal error bars represent the spectrometer resolution). These locations are indicated by the blue circle and the red square in **a**, that respectively correspond to the blue and red curves of **b**. All the features of **a**,**b** were very robust experimentally, being observed on all shots performed in similar experimental conditions (see Supplementary Information). **c**,**d**, Same quantities as in **a**,**b**, now obtained from numerical simulations based on a 3D test particle model. The dashed curve in **d** shows the initial electron energy distribution used in this model. As can be seen from the green and red spectra in **d**, the model shows that electrons are accelerated by VLA from 1.5 to 10 MeV, resulting in a sevenfold energy gain.

ejection, along the specular direction (p_z) and along the laser polarization direction (p_x). Electrons start their motion in vacuum with relativistic velocities, corresponding to an average energy of 1.5 MeV ($\gamma_0 \simeq 3$), and are ejected with an average angle of 20° away from the specular direction.

These initial conditions are close to being ideal for the observation of VLA, and definitely much more favourable than those achieved in all previous experimental attempts to observe this effect[13,14,16,17]. In experiments based on electron injection by ionization of core atomic levels, electrons started the interaction at rest and could not reach relativistic energies[13,14]. In those relying on electron beams produced by conventional accelerators, combined with an intense laser through a drilled mirror, the phase of injection in the field covers a full optical period, so that only a very small fraction of the electrons actually gains energy by VLA (refs 16,17).

To study the subsequent interaction of these electrons with the laser field in vacuum, we turn to a simple 3D test particle model, similar to the one used in ref. 22 (see Methods). In this model, the relativistic equations of motion are solved for electrons injected in a sinusoidal laser field, assumed to be Gaussian in space and time, and known analytically at every time and position. This is computationally much less demanding than the 3D PIC simulations that would be required to account for the isotropic effect of the ponderomotive force.

Using this model, we calculate the trajectories of millions of electrons injected in the field. The set of initial conditions for these electrons is derived from the output of PIC simulations, such as those shown in Fig. 3 (see Methods). Figure 2c shows the angular electron distribution obtained from these simulations, for physical conditions corresponding to our experiment. The agreement of this distribution with the experimental one is striking: the two main features observed in the experiment—the hole around the laser axis and the bright peak along the laser polarization—are both well reproduced. The final energy spectra calculated on each side of the hole are shown in Fig. 2d and also compare well with the experimental observations. Despite its simplicity, this model

© 2015 Macmillan Publishers Limited. All rights reserved

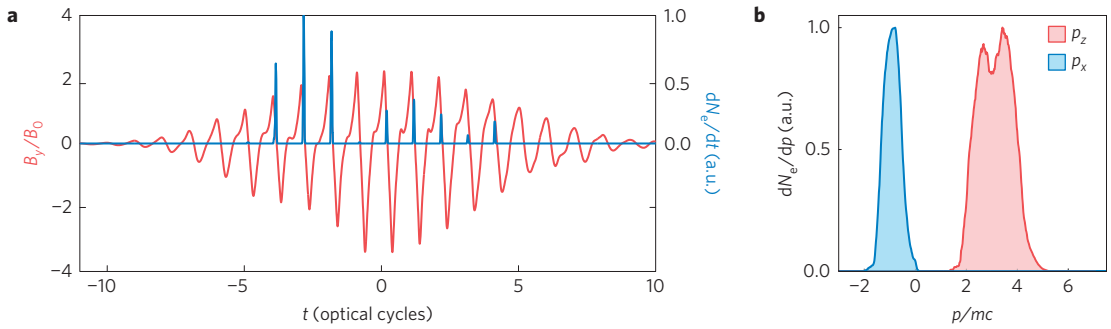


Figure 3 | Initial conditions of electrons ejected from plasma mirrors. a, Waveform of the laser magnetic field B_y reflected by the plasma mirror (red line), and temporal density profile of the ejected high-energy electrons (blue line), obtained from PIC simulations. Both quantities were sampled at $z = 750$ nm from the plasma mirror surface. Note that owing to the complex coupling of the laser field with the plasma surface[43], the electron injection drops significantly around the peak of the laser pulse and most electrons are injected slightly before the pulse maximum. **b**, Corresponding momentum distribution of these electrons, along the specular direction (p_z) and along the polarization direction of the reflected laser (p_x).

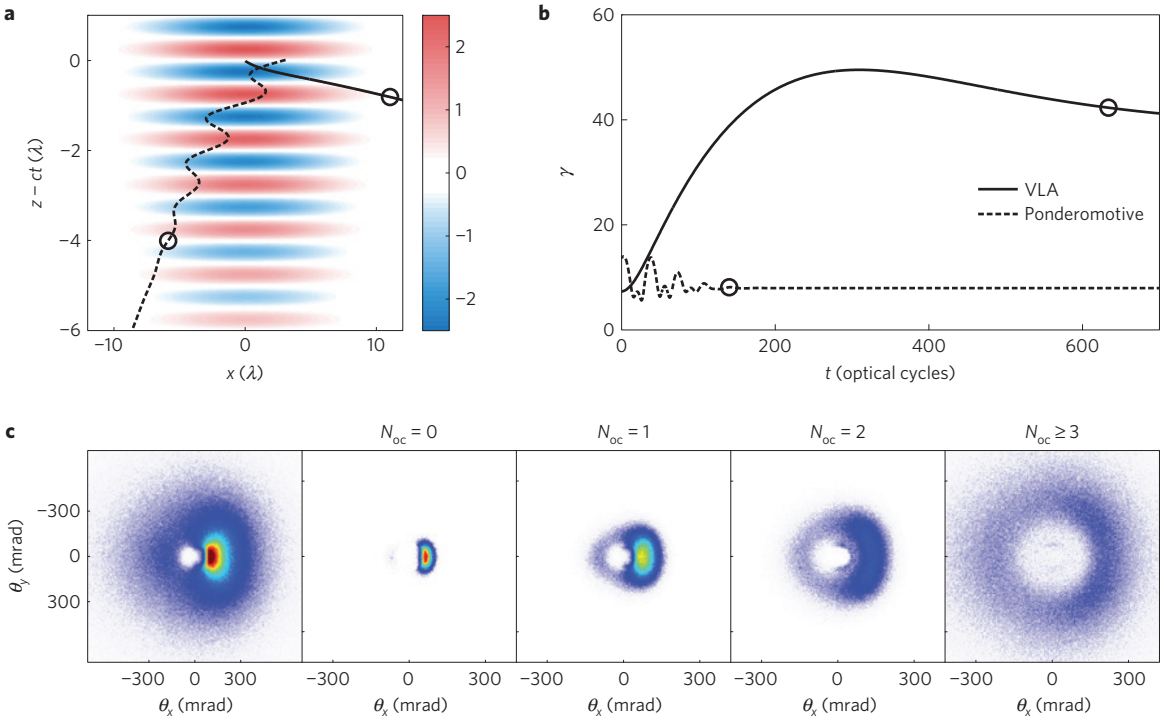


Figure 4 | 3D modelling of laser–electron interaction in vacuum. a, Two types of electron trajectories, corresponding to electrons that have respectively explored $N_{oc} \leq 1$ (full line) and $N_{oc} = 3$ (dashed line) optical cycles before escaping the laser beam. The trajectories are shown in a frame moving with the laser beam, and the colour map sketches the laser field in this frame. The circles represent the positions for which we consider that these electrons escape the laser pulse (see Methods). **b**, Temporal evolution of the electron Lorentz factor $\gamma(t)$ along these two trajectories. **c**, Angular distribution for various electron populations, sorted according to the number of optical cycles they experience. VLA electrons clearly form the bright spot, whereas ponderomotive electrons form a doughnut-shaped distribution.

thus captures the essential physics of the interaction in vacuum. This shows that effects such as space charge or the non-sinusoidal waveform of the reflected field, not taken into account in these simulations, do not play a major role once electrons are in vacuum.

Interpretation of the experimental results

Considering this good agreement, this 3D model can now be exploited to analyse the trajectories of electrons contributing to the different patterns observed in the electron beam. To this end, we sort the electrons into different groups, depending on the number of laser optical cycles N_{oc} that they have crossed along their trajectory. This provides a quantitative criterion for distinguishing electrons that experienced VLA, from those scattered by the ponderomotive force. This is illustrated in Fig. 4a, which shows two trajectories (x, $z - ct$), representative of these two regimes: $N_{oc} \leq 1$ (full line) and $N_{oc} = 3$ (dashed line). The corresponding temporal evolutions of the electron Lorentz factor is shown in Fig. 4b.

In the first case, the 'VLA electron' does not oscillate in the field, but rather 'surfs' the laser wavefront in which it was injected, along the polarization direction. It thus gains energy almost along its entire trajectory, until it escapes the focal volume sideways after an interaction distance of the order of the Rayleigh length. In contrast, the 'ponderomotive electron' oscillates as it explores several optical cycles of the laser field, and gets quickly expelled from the laser beam with a low energy gain—akin to a surfer that has missed the wave—as illustrated in Fig. 4b, where the circles stand for the ejection time.

© 2015 Macmillan Publishers Limited. All rights reserved

In practice, there is a continuous transition between these two extreme types of trajectories, depending on the exact electron injection conditions in the field. This is illustrated by the images in Fig. 4c showing the beam patterns produced by several subensembles of electrons in the simulations, corresponding to N_{oc} varying from $N_{oc} = 0$ (VLA electrons) to $N_{oc} \geq 3$ (ponderomotive electrons). Ponderomotive electrons form a doughnut-shaped beam centred on the laser propagation axis, whereas VLA electrons tend to concentrate in a bright peak on the edge of the ponderomotive hole, along the polarization direction.

This analysis confirms our interpretation of the electron beam patterns observed in experiments, and provides clear proof that the bright peak in these patterns is due to VLA. According to our simulations, these electrons are accelerated from 1.5 to 10 MeV (Fig. 2d) over a distance of less than 100 μm, corresponding to an approximate sevenfold energy gain by VLA in this experiment. In addition, a remarkable feature of VLA is that the position of the peak in Fig. 4c depends on the phase of injection of electrons in the laser field: if we artificially vary this phase by π (half a laser period) in the simulation, this bright spot shifts to the other side of the ponderomotive hole. The experimental observation of this peak on one side only of the hole is thus a clear indication that electrons are ejected out of the plasma mirror at a specific phase of the laser field, in the form of sub-laser cycle (attosecond) bunches.

Even though several experiments have been performed on electron ejection from solid surfaces[31–35] during the past decade, the VLA regime had never been reached before. With laser intensities lower by one to three orders of magnitude compared to our experiment, electrons were accelerated rather via ponderomotive effects in the interference pattern at the surface of the solid target[33], or by stochastic heating[34]. This was due in particular to the lower injection energies, which did not allow electrons to stay in phase with the laser field. Using ultrahigh intensities in excess of 10^{19} W cm^{-2}, we were able to move from these processes to VLA and to generate electron beams with energies one to two orders of magnitude higher, with a charge at least three orders of magnitude higher than these previous works.

Outlook

We have obtained the first unambiguous experimental evidence of VLA of relativistic electrons by ultraintense laser fields, using a new concept for injecting electrons. This simple scheme, based on the remarkable properties of plasma mirrors, is flexible and can, in principle, be extended to much higher laser intensities and to more complex laser beams. From a fundamental point of view, it opens the way to the extensive experimental investigation of the interaction of free electrons with ultraintense lasers in various experimental conditions. Using petawatt lasers and intensities in excess of 10^{21} W cm^{-2}, electrons could be exposed to accelerating gradients approaching 100 TV m^{-1} over tens of micrometres, and should thus reach energies in the GeV range[7,10], making VLA a promising scheme for the production of high charge (nC) ultra-relativistic beams. In addition, spatial shaping of the laser beam, providing doughnut beam shapes, as in radially polarized laser beams[4,6,11] or Laguerre–Gauss beams[40], has the potential to further improve the beam quality and to provide more collimated electron beams. Similarly, temporal shaping of the field through the use of two-colour lasers[41,42] could also be a path towards the subcycle control of the injection phase in the laser field.

Methods

Methods and any associated references are available in the online version of the paper.

Received 27 May 2015; accepted 12 November 2015; published online 21 December 2015

References

1. Yu, T. J. *et al.* Generation of high-contrast, 30 fs, 1.5 PW laser pulses from chirped-pulse amplification Ti:sapphire laser. *Opt. Express* **20,** 10807–10815 (2012).
2. Esarey, E., Schroeder, C. B. & Leemans, W. P. Physics of laser-driven plasma-based electron accelerators. *Rev. Mod. Phys.* **81,** 1229–1285 (2009).
3. Hartemann, F. V. *et al.* Nonlinear ponderomotive scattering of relativistic electrons by an intense laser field at focus. *Phys. Rev. E* **51,** 4833–4843 (1995).
4. Esarey, E., Sprangle, P. & Krall, J. Laser acceleration of electrons in vacuum. *Phys. Rev. E* **52,** 5443–5453 (1995).
5. Yu, W. *et al.* Ponderomotive acceleration of electrons at the focus of high intensity lasers. *Phys. Rev. E* **61,** R2220–R2223 (2000).
6. Stupakov, G. V. & Zolotorev, M. S. Ponderomotive laser acceleration and focusing in vacuum for generation of attosecond electron bunches. *Phys. Rev. Lett.* **86,** 5274–5277 (2001).
7. Salamin, Y. I. & Keitel, C. H. Electron acceleration by a tightly focused laser beam. *Phys. Rev. Lett.* **88,** 095005 (2002).
8. Pang, J. *et al.* Subluminous phase velocity of a focused laser beam and vacuum laser acceleration. *Phys. Rev. E* **66,** 066501 (2002).
9. Dodin, I. Y. & Fisch, N. J. Relativistic electron acceleration in focused laser fields after above-threshold ionization. *Phys. Rev. E* **68,** 056402 (2003).
10. Maltsev, A. & Ditmire, T. Above threshold ionization in tightly focused, strongly relativistic laser fields. *Phys. Rev. Lett.* **90,** 053002 (2003).
11. Varin, C. & Piché, M. Relativistic attosecond electron pulses from a free-space laser-acceleration scheme. *Phys. Rev. E* **74,** 045602 (2006).
12. Malka, G., Lefebvre, E. & Miquel, J. L. Experimental observation of electrons accelerated in vacuum to relativistic energies by a high-intensity laser. *Phys. Rev. Lett.* **78,** 3314–3317 (1997).
13. McNaught, S. J., Knauer, J. P. & Meyerhofer, D. D. Photoelectron initial conditions for tunneling ionization in a linearly polarized laser. *Phys. Rev. A* **58,** 1399–1411 (1998).
14. Moore, C. I. *et al.* A laser-accelerator injector based on laser ionization and ponderomotive acceleration of electrons. *Phys. Rev. Lett.* **82,** 1688–1691 (1999).
15. Payeur, S. *et al.* Generation of a beam of fast electrons by tightly focusing a radially polarized ultrashort laser pulse. *Appl. Phys. Lett.* **101,** 041105 (2012).
16. Cline, D. *et al.* First observation of acceleration of electrons by a laser in a vacuum. *J. Mod. Phys.* **4,** 1–6 (1, 2013).
17. Carbajo, S. *et al.* Direct laser acceleration of electrons in free-space. Preprint at http://arXiv.org/abs/1501.05101 (2015).
18. Mora, P. & Quesnel, B. Comment on "Experimental observation of electrons accelerated in vacuum to relativistic energies by a high-intensity laser". *Phys. Rev. Lett.* **80,** 1351 (1998).
19. McDonald, K. T. Comment on "Experimental observation of electrons accelerated in vacuum to relativistic energies by a high-intensity laser". *Phys. Rev. Lett.* **80,** 1350 (1998).
20. Schmidt, G. & Wilcox, T. Relativistic particle motion in nonuniform electromagnetic waves. *Phys. Rev. Lett.* **31,** 1380–1383 (1973).
21. Startsev, E. A. & McKinstrie, C. J. Multiple scale derivation of the relativistic ponderomotive force. *Phys. Rev. E* **55,** 7527–7535 (1997).
22. Quesnel, B. & Mora, P. Theory and simulation of the interaction of ultra-intense laser pulses with electrons in vacuum. *Phys. Rev. E* **58,** 3719–3732 (1998).
23. Thaury, C. *et al.* Plasma mirrors for ultrahigh-intensity optics. *Nature Phys.* **3,** 424–429 (2007).
24. Doumy, G. *et al.* Complete characterization of a plasma mirror for the production of high-contrast ultraintense laser pulses. *Phys. Rev. E* **69,** 026402 (2004).
25. Vincenti, H. *et al.* Optical properties of relativistic plasma mirrors. *Nature Commun.* **5,** 3403 (2014).
26. Nakatsutsumi, M. *et al.* Fast focusing of short-pulse lasers by innovative plasma optics toward extreme intensity. *Opt. Lett.* **35,** 2314–2316 (2010).
27. Dromey, B. *et al.* High harmonic generation in the relativistic limit. *Nature Phys.* **2,** 456–459 (2006).
28. Wheeler, J. A. *et al.* Attosecond lighthouses from plasma mirrors. *Nature Photon.* **6,** 829–833 (2012).
29. Naumova, N. *et al.* Attosecond electron bunches. *Phys. Rev. Lett.* **93,** 195003 (2004).
30. Geindre, J. P., Marjoribanks, R. S. & Audebert, P. Electron vacuum acceleration in a regime beyond Brunel absorption. *Phys. Rev. Lett.* **104,** 135001 (2010).
31. Tian, Y. *et al.* Electron emission at locked phases from the laser-driven surface plasma wave. *Phys. Rev. Lett.* **109,** 115002 (2012).
32. Cai, D. F. *et al.* Experimental study for angular distribution of the hot electrons generated by femtosecond laser interaction with solid targets. *Phys. Plasmas* **10,** 3265–3269 (2003).
33. Mordovanakis, A. G. *et al.* Quasimonoenergetic electron beams with relativistic energies and ultrashort duration from laser-solid interactions at 0.5 kHz. *Phys. Rev. Lett.* **103,** 235001 (2009).

© 2015 Macmillan Publishers Limited. All rights reserved

34. Brandl, F. *et al.* Directed acceleration of electrons from a solid surface by sub-10-fs laser pulses. *Phys. Rev. Lett.* **102,** 195001 (2009).
35. Wang, W. *et al.* Angular and energy distribution of fast electrons emitted from a solid surface irradiated by femtosecond laser pulses in various conditions. *Phys. Plasmas* **17,** 023108 (2010).
36. Lévy, A. *et al.* Double plasma mirror for ultrahigh temporal contrast ultraintense laser pulses. *Opt. Lett.* **32,** 310–312 (2007).
37. Kahaly, S. *et al.* Direct observation of density-gradient effects in harmonic generation from plasma mirrors. *Phys. Rev. Lett.* **110,** 175001 (2013).
38. Glinec, Y. *et al.* Absolute calibration for a broad range single shot electron spectrometer. *Rev. Sci. Instrum.* **77,** 103301 (2006).
39. Thaury, C. & Quéré, F. High-order harmonic and attosecond pulse generation on plasma mirrors: Basic mechanisms. *J. Phys. B* **43,** 213001 (2010).
40. Zhang, X. *et al.* Field properties and vacuum electron acceleration in a laser beam of high-order Laguerre–Gaussian mode. *Opt. Commun.* **281,** 4103–4108 (2008).
41. Mauritsson, J., Dahlström, J. M., Mansten, E. & Fordell, T. Sub-cycle control of attosecond pulse generation using two-colour laser fields. *J. Phys. B* **42,** 134003 (2009).
42. Edwards, M. R., Platonenko, V. T. & Mikhailova, J. Enhanced attosecond bursts of relativistic high-order harmonics driven by two-color fields. *Opt. Lett.* **39,** 6823–6826 (2014).
43. Geindre, J. P., Audebert, P. & Marjoribanks, R. S. Relativistic AC gyromagnetic effects in ultraintense laser–matter interaction. *Phys. Rev. Lett.* **97,** 085001 (2006).

Acknowledgements

We are grateful to P. d'Oliveira, F. Réau, C. Pothier and D. Garzella for operating the UHI100 laser source. This work was funded by the European Research Council under Contract No. 306708, ERC Starting Grant FEMTOELEC, the Agence Nationale pour la Recherche under contract ANR-14-CE32-0011-03 APERO and LASERLAB-EUROPE (grant agreement no. 284464, EC's Seventh Framework Programme) through the CHARPAC Joint Research Action. We acknowledge the support of GENCI for access on super computer Curie. Simulations were run using EPOCH, which was developed as part of the UK EPSRC funded projects EP/G054940/1.

Author contributions

A.L. performed the experiment with S.K. and F.Q.; A.L. analysed the data; A.V. and J.F. calibrated the electron spectrometer. H.V. modified EPOCH for 1D boosted frame simulations. H.V. and M.T. performed the PIC simulations and developed the associated post-processing tools. M.T. developed and exploited the test particle model. All authors participated in the interpretation of the results. A.L. and M.T made the figures. F.Q. and J.F. designed and directed the project with equal contributions, and wrote the paper with inputs from the other authors.

Additional information

Supplementary information is available in the online version of the paper. Reprints and permissions information is available online at www.nature.com/reprints. Correspondence and requests for materials should be addressed to F.Q. or J.F.

Competing financial interests

The authors declare no competing financial interests.

© 2015 Macmillan Publishers Limited. All rights reserved

Methods

PIC simulations. 2D particle-in-cell (PIC) simulations were carried out to gain insight into the injection and acceleration process (see Fig. 1b and Supplementary Movie). A p-polarized laser pulse ($\lambda = 800$ nm, $\tau = 25$ fs FWHM, waist $w_0 = 5\,\mu$m, $a_0 = 3.5$, where $a_0 = eE_0/m\omega c$ is the normalized laser vector potential, with e and m the electron charge and mass, ω and E_0 the laser frequency and peak amplitude, and c the light velocity in vacuum) impinges on an overdense plasma ($n_0 = 100n_c$, where $n_c = 1.6 \times 10^{21}$ cm^{-3} is the critical plasma density for $\lambda = 800$ nm) with an exponential density gradient on its front side of decay length $L = \lambda/10$. The incidence angle is 45°. Simulation parameters were as follows: space step $\Delta x = \lambda/2{,}000$, 40 particles per cell, box size: $40\lambda \times 45\lambda$. To follow the electron trajectories far away from the target, a moving simulation box is used: after the laser pulse reflects from the target, the box begins to move at the speed of light and follows the reflected pulse, thus making it possible to follow the dynamics of energetic electrons along a path length of many wavelengths (typically 100 μm).

To determine the injection conditions of electrons in the reflected field, we performed 1D PIC simulations in the boosted frame[44], with $\lambda = 800$ nm, $a_0 = 3$, $L = \lambda/8$, $\tau = 25$ fs FWHM. The numerical parameters were $\Delta x = \lambda/1{,}000$, box length 4λ, 4,000 particles per cell. The magnetic field and electron density plotted in Fig. 3 were recorded at the front edge of the plasma mirror, at $z = 750$ nm from the bulk density region (that is, where $n = 100n_c$). A filter was used to remove low-energy electrons ($E < 0.5$ MeV), which typically return to the plasma within one optical cycle. Both 1D and 2D PIC simulations were performed with the code EPOCH.

Model. The 3D particle model consists in solving the relativistic equations of motion for electrons in a laser pulse. The Gaussian pulse propagates along the $+z$ direction and is polarized along x. The fields E_x and B_y are those given by the paraxial approximation. To properly model the ponderomotive force[22,45], a first-order development with respect to the parameter $\epsilon = 1/kw_0$ is used to ensure that the laser field satisfies Maxwell's equations, at least to the first order of ϵ. This introduces new components B_z and E_z, proportional to ϵ. A derivation of these fields can be found in ref. 22. Omitting these components leads to incorrect trajectories (as in refs 12,31), by artificially restricting all forces to the polarization plane. We used PIC simulations to determine the reflectivity of the plasma mirror, which was about 70% in our conditions. Therefore, we assumed that the amplitude of the reflected laser pulse was $a_0 = 2.5$ ($a_0 = 3$ for the incident field in the experiment). The other laser parameters were identical to the experimental ones: $\tau = 25$ fs, $w_0 = 5\,\mu$m, $\lambda = 800$ nm.

The equations of motion were solved using a Boris pusher scheme, for 3×10^6 electrons. For the initial conditions, we used Gaussian distributions for all parameters (momentum components p_x, p_y, p_z and emission time t_0). These distributions were all centred on the average values extracted from 1D PIC simulations described above. The widths of these distributions were used as adjustable parameters to reproduce the experimental data and obtain the simulations results of Fig. 2. For all parameters, the widths that lead to the best agreement are found to be larger than those provided by 1D PIC simulations. This difference can be attributed to two effects: the actual variations of the interaction conditions (in particular the laser intensity) in 3D, and the effect of the incident laser field on the electrons immediately after their emission. Indeed, the interference pattern of the incident and reflected beams affects the electron dynamics on a distance of the order of the beam waist w_0 (a few micrometres, which is small compared to the overall interaction length of electrons with the reflected field), and tends to significantly broaden the initial phase space distribution (see Supplementary Movie).

The calculation is run until all electrons have escaped the laser pulse, which we consider to be true once the laser intensity at the electron position is <1% of its spatio-temporal maximum. For the sorting of electrons as a function of the number of optical cycles N_{oc}, we measure the electric field E_x on electrons and detect the number of sign changes on E_x along electron trajectories. This number, divided by two, is the number of optical cycles an electron has experienced.

References

44. Bourdier, A. Oblique incidence of a strong electromagnetic wave on a cold inhomogeneous electron plasma. Relativistic effects. *Phys. Fluids* **26,** 1804–1807 (1983).
45. Cicchitelli, L., Hora, H. & Postle, R. Longitudinal field components for laser beams in vacuum. *Phys. Rev. A* **41,** 3727–3732 (1990).

© 2015 Macmillan Publishers Limited. All rights reserved

Anticorrelated Emission of High Harmonics and Fast Electron Beams From Plasma Mirrors

Maïmouna Bocoum,* Maxence Thévenet, Frederik Böhle, Benoît Beaurepaire, Aline Vernier, Aurélie Jullien, Jérôme Faure, and Rodrigo Lopez-Martens

Laboratoire d'Optique Appliquée, ENSTA ParisTech, CNRS, Ecole polytechnique, Université Paris-Saclay, 828 bd des Maréchaux, 91762 Palaiseau cedex, France

(Received 17 December 2015; revised manuscript received 4 March 2016; published 5 May 2016)

We report for the first time on the anticorrelated emission of high-order harmonics and energetic electron beams from a solid-density plasma with a sharp vacuum interface—plasma mirror—driven by an intense ultrashort laser pulse. We highlight the key role played by the nanoscale structure of the plasma surface during the interaction by measuring the spatial and spectral properties of harmonics and electron beams emitted by a plasma mirror. We show that the nanoscale behavior of the plasma mirror can be controlled by tuning the scale length of the electron density gradient, which is measured *in situ* using spatial-domain interferometry.

DOI: 10.1103/PhysRevLett.116.185001

Over the past 30 years, solid-density plasmas driven by intense femtosecond pulses, so-called plasma mirrors, have been successfully tested as a source of high-order harmonics and attosecond extreme ultraviolet (XUV) pulses in a number of experiments [1–10], where the laser intensity typically exceeds a few 10^{14} W/cm^2. Other experiments have shown it is also possible to accelerate energetic electrons from plasma mirrors for intensities above 10^{16} W/cm^2 [11–13]. Attempting to understand each of these experimental observations invariably points to the key role played by the plasma-vacuum interface during the interaction both on the nanoscale spatially and on the sub-laser-cycle scale temporally [14,15].

It is commonly assumed that the electron density at the plasma mirror surface decreases exponentially from solid to vacuum over a distance L_g, also called the density gradient. When the laser pulse reflects on this plasma mirror, for every oscillation of the laser field, some electrons are driven towards vacuum and sent back to the plasma [16,17]. These bunches of so-called Brunel electrons [18] impulsively excite collective high-frequency plasma oscillations in the density gradient that lead to the emission of XUV radiation through linear mode conversion [19]. As illustrated in Fig. 1(a), each position x of the plasma behaves as a nanoscale oscillator of frequency $\omega_p(x) = \omega_0\sqrt{n_e(x)/n_c}$, where ω_0 is the driving laser angular frequency, n_e is the local electron density at position x, and n_c is the critical density. This periodic mechanism, called coherent wake emission (CWE), leads to efficient high-harmonics generation for very short plasma scale lengths, typically $L_g \sim \lambda/100$ [19], even for subrelativistic intensities $a_0 < 1$, where $a_0 = eA_0/mc$ is the normalized vector potential, e and m are the electron charge and mass, and c is the speed of light. However, the efficiency significantly drops for $L_g \gg \lambda/20$ [4,5,19,20]. At higher intensities $a_0 \gg 1$, the relativistic oscillating mirror (ROM) becomes the dominant mechanism for harmonic generation [16,21].

A fraction of electrons do not follow Brunel-like trajectories: they are accelerated in the density gradient towards vacuum and escape the plasma, as illustrated in Fig. 1(b). Depending on the interaction conditions, the final energy and angular spread of these electrons can be influenced by plasma waves below the critical surface [11], interference fields created by the incident and reflected laser beams [13,22,23], betatronlike motion at the plasma surface [24], or even direct laser acceleration in vacuum [25]. Here again, the plasma scale length plays a critical role: enhanced electron generation is observed typically for $0.1 < L_g/\lambda < 1$ [11,13,26] or sometimes even for $L_g/\lambda > 1$ [27–29]. To our knowledge, the anticorrelated

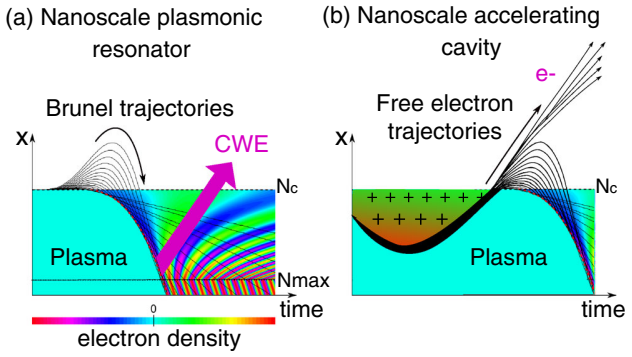


FIG. 1. Diagrams of nanoscale plasma mirror surface structures leading to (a) CWE, where electrons are pulled toward the vacuum and are sent back to the plasma where they excite high-frequency plasma waves, which radiate high-order harmonics (b) electron acceleration on the sub-laser-cycle time scale, where electrons are accelerated in the density gradient and escape from the plasma.

 © 2016 American Physical Society

emission of harmonics and fast electrons from plasma mirrors has never been investigated experimentally. In this Letter, through a controlled pump-probe experiment using subrelativistic femtosecond laser pulses, we directly observe the transition from a confined plasma that can efficiently emit laser harmonics to an extended plasma structure that accelerates fast electrons into vacuum up to a few hundred keV energies, where the laser interference field only plays a second role.

The experiment was carried out using the "Salle Noire" laser system at the Laboratoire d'Optique Appliquée (LOA) delivering up to 3 mJ energy, 30 fs pulses at 1 kHz repetition rate with high temporal contrast ($>10^{10}$) [30]. The p-polarized pulses are focused down to 1.7 μm FWHM spot size onto an optically flat fused silica target ($\sim 250 n_c$), leading to peak intensities on target $\simeq 10^{18}$ W/cm^2 ($a_0 \simeq 0.7$) for an incidence angle $\theta_L = 49.3°$, with high repeatability at 1 kHz [31]. Five percent of the main beam is picked off and focused down to 5 times the main beam spot size on target in order to induce homogeneous plasma expansion at the surface (see also Supplemental Material [32]). The plasma scale length L_g can then be varied by changing the relative delay between this prepulse and the main high-intensity pulse. We use spatial domain interferometry [33] to estimate the plasma expansion velocity c_s and find $c_s = dL_g/dt = 10.8 \pm 1.1$ nm/ps for a prepulse intensity of $\simeq 3.5 \times 10^{14}$ W/cm^2 ($a_0 \simeq 0.013$).

Harmonics emitted in the specular direction are sent into a homemade XUV spectrometer where the harmonic spectrum is resolved in the horizontal plane and the harmonic beam divergence in the vertical direction using a coupled micro-channel plate and phosphor screen detector. At the same time, a 6×17 cm Lanex screen was positioned 10 cm away, parallel to the target surface without blocking the specular direction. The angular electron emission profile in this geometry was recorded as a function of $\theta \in [-20° 30°]$, the angle with respect to target normal in the plane of incidence, and $\phi \in [-20° 20°]$, the angle with respect to target normal in the tangential plane. Note that the Lanex screen only detects electrons with energies larger than 150 keV [34]. The Lanex screen could also be replaced by an electron spectrometer for characterizing the electron energy distribution.

Figure 2(a) shows the harmonic spectrum and the electron signal as a function of pump-probe delay, hence the gradient length. The harmonic signal was integrated along the divergence angle. The plasma scale length calculated from the plasma expansion velocity is indicated on the bottom axis. The first striking result is that harmonics are generated efficiently for pump-probe delays below 4 ps, corresponding to $L_g \leq 0.05\lambda$. The spectrum extends up to the plasma frequency cutoff $\omega_c/\omega_0 = 16$ and its divergence is about $1/10$ that of the driving laser beam, which is the typical signature of CWE [20]. The plasma frequency cutoff confirms that Brunel electrons can

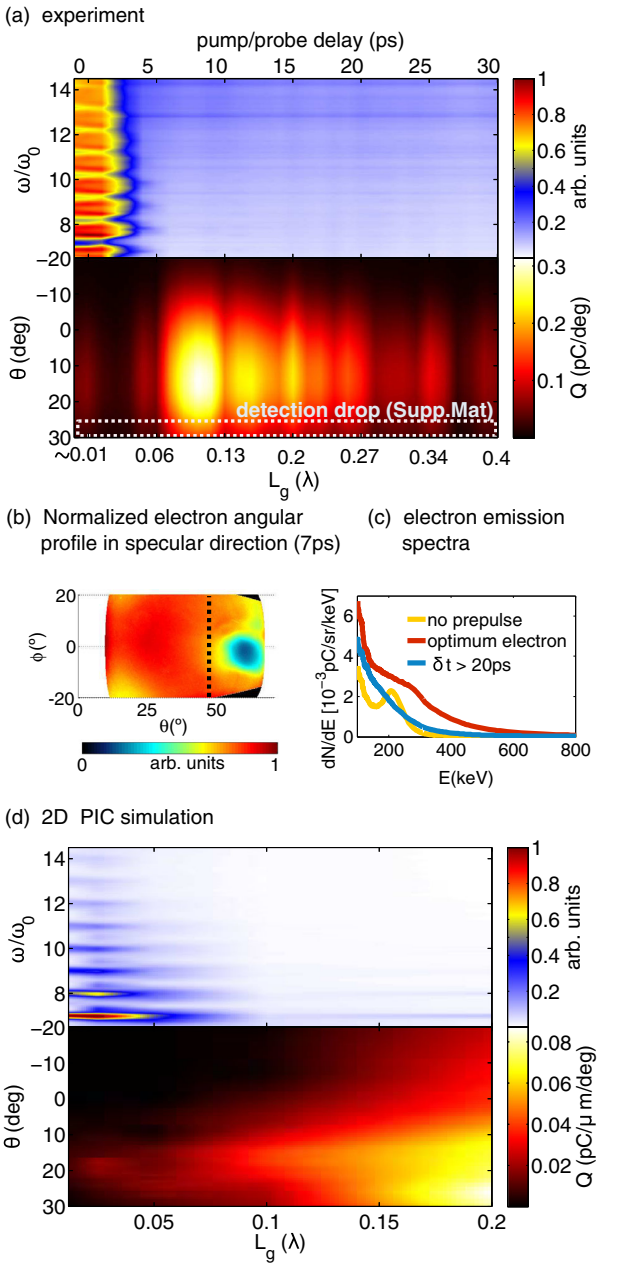


FIG. 2. (a) Experimental harmonic spectra and electron angular emission profiles as a function of pump-probe delay (top axis) between the prepulse and the main pulse. The electron signal was integrated along the tangential coordinate ϕ. The corresponding plasma scale length L_g (bottom axis) was extracted from the plasma expansion velocity $c_s = 10.8$ nm/ps measured by spatial domain interferometry [33]. (b) Electron angular distribution when the Lanex is placed perpendicular to the specular direction and after deconvolution (see Supplemental Material [32]). (c) Electron energy spectra for three typical delays. (d) Same as (a) for 2D PIC simulations with $a_0 = 0.4$ and gradient length $L_g \in [0.01\lambda\, 0.2\lambda]$.

efficiently excite collective plasma oscillations and therefore that the initial plasma scale length should be on the order of $L_g \sim 0.01\lambda$ [19] rather then rigorously 0λ. This also indicates that the temporal contrast close to the pulse peak

does not allow us to explore arbitrarily small plasma scale lengths. The drop in CWE efficiency with increasing density gradient has already been observed experimentally and is theoretically predicted to be in the range $0.02 < L_g/\lambda < 0.1$ [20,36], depending on laser intensity [19]. This can be explained with 1D considerations: the minimum time required to excite plasma waves from the critical surface $x = x_c$ to the location of maximum density $x = x_{\max}$ is $\Delta t = (L_g/c)\log(n_{\max}/n_c)$, which should be less than the laser period in order to prevent cycle-to-cycle destructive interferences. For traveling electrons, this limit reads $L_g \leq 0.17\lambda$. In our case, the drop in efficiency occurs at much lower values around $L_g \sim 0.05\lambda$ because the electron perturbation propagates at less than c and the initial perturbation strength (i.e., amplitude of plasma waves) decreases with L_g [19]. The second striking result is that a maximum electron signal is reached for a delay of 8 ps ($L_g \sim 0.1\lambda$), where harmonic emission is negligible. The ejected electrons form a large spot between 10° and 20° and drop at the edge of the Lanex at ~30°. This drop in signal is a geometrical artifact due to the anisotropic emission of the Lanex screen [34] (see Supplemental Material for details [32]). Figure 2(b) shows the full electron angular distribution for a delay of ~7 ps, obtained by moving the Lanex screen perpendicular to the specular direction. The distribution displays a hole close to the specular direction, presumably formed by the ponderomotive force of the reflected laser pulse [13,22,25,37]. Using the Lanex calibration [34], we estimate that the ejected charge reaches a maximum of ~11 pC compared to ~2 pC at zero delay. Figure 2(c) shows electron spectra respectively without prepulse, for the optimal delay for electron emission, and after 20 ps. Hence, electrons can be effectively accelerated up to ~600 keV at the optimal density gradient.

To summarize, we observe that the emission of harmonics and electrons is anticorrelated when changing the gradient scale length. These experimental results were confronted to 2D particle-in-cell (PIC) simulations, in which a $\lambda = 800$ nm, 30 fs pulse is focused onto an overdense plasma ($n_{\max} = 250n_c$) with immobile ions. The plasma density decreases exponentially with various scale lengths, from $L_g = 0.01\lambda$ to 0.2λ. The plasma density is cut at $n_b = n_c/5$, so that the plasma boundary is defined by $x_b = -\log 5 L_g$. The laser amplitude is $a_0 = 0.4$ and the incidence angle is 45°. A good spatial resolution is required for simulating CWE harmonics, so we use $\delta x = \lambda/420$. In the simulations, electrons are detected at 9λ away from the critical surface and only electrons with energies > 150 keV are detected (as in the experiment). As illustrated in Fig. 2(d), the PIC simulations qualitatively reproduce our experimental observations: the CWE emission efficiency decreases for $L_g > 0.05\lambda$ and the effective ejected electron charge increases up to ~3 pC $\cdot\, \mu\text{m}^{-1}$ for $L_g = 0.2\lambda$ compared to 0.12 pC $\cdot\, \mu\text{m}^{-1}$ when $L_g = 0.01\lambda$ (i.e., ≃10 and 0.7 pC, respectively, for a 3.4 μm spot size FWHM). The electron angular distribution was plotted over the range $\theta \in [-20°\ 30°]$ for a direct comparison with experiment. Here again, there is a very good agreement with the experiment, with a large divergence 10 pC beam ejected at ~30° when $L_g \sim 0.2\lambda$. Note that PIC simulations were first performed with the experimental vacuum laser amplitude $a_0 = 0.8$, but a strong harmonic emission attributed to the ROM emission mechanism [20] persisted for longer gradients. These simulations at high intensities suggested a correlation between ROM harmonics and electron ejection, as opposed to the anticorrelation that we observed. In our experiment, ROM emission does not occur and the harmonics are due to CWE. This indicates that the laser intensity at focus is not high enough to support ROM emission [14]. Therefore, in the simulations, the beam spot size was doubled without changing the pulse energy; i.e., a_0 was decreased to 0.4, to reproduce the anticorrelated behavior. Note that our overestimation of the experimental intensity on target may be due to a slight defocusing of the laser on target or debris reducing the overall transmission of the focusing optic, a standard problem with high repetition rate laser-plasma interaction experiments using tight focusing.

Figure 3 shows a comparison of 2D PIC simulations with a gradient length optimized for harmonic emission ($L_g = \lambda/40$) and electron emission ($L_g = \lambda/5$), respectively. In Figs. 3(a) and 3(b), one can clearly see oscillations of the electron surface at the laser period. Strong harmonic generation can be seen in Fig. 3(a). The corresponding electron trajectories are shown in Fig. 3(c), where the x coordinate (normal to the target) of electrons is plotted along time. For clarity, a single bunch of electrons is represented here, which interacts with the laser around its temporal maximum ($t = 22T$, where T is the optical period) in the center of the interference pattern. One can clearly see Brunel-like trajectories: electrons make a short excursion in vacuum before being driven back to the plasma where they trigger plasma waves. In Fig. 3(b), the amplitude of these oscillations is greater and layers of electrons are ejected from the plasma surface. The corresponding electron trajectories are plotted in Fig. 3(d). Once again, a bunch of electrons was selected for clarity. A fraction of these electrons (in red) escape from the plasma and propagate into vacuum in the interference pattern with a velocity $\simeq c/2$.

For each laser cycle, the ejection mechanism can be described as follows: (i) the laser electric field pushes electrons inside the plasma, while the heavy ions stay in place, creating a charge separation electrostatic field, i.e., a plasma capacitor which can give potential energy to electrons; (ii) half a cycle later, the laser field changes sign and both the capacitor and the laser electric force pull and accelerate electrons towards vacuum. Assuming that all the electrons originating from $x < 0$ (where $n = n_c$)

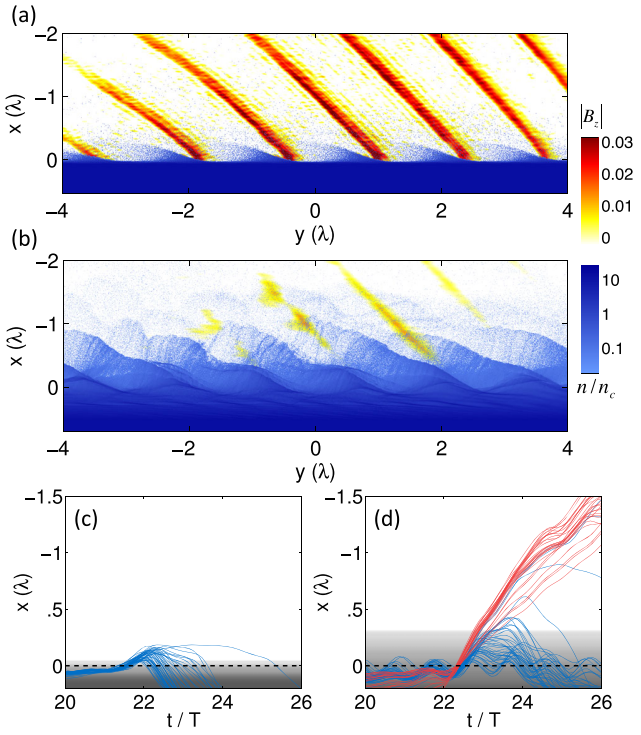


FIG. 3. (a) Snapshot from the 2D PIC simulation for $L_g = \lambda/40$. Blue, electron density (log scale). Yellow-red, reflected harmonic field (a Fourier filter was applied to keep only harmonic orders $\geq 5\omega_0$). The harmonic field comes out as a train of attosecond pulses. (b) Same as (a) for $L_g = \lambda/5$ (same instant, same color scale). (c),(d) Typical electron trajectories for $L_g = \lambda/40$ and $L_g = \lambda/5$, respectively. x is the coordinate normal to the plasma. The gray scale stands for the plasma initial density and the black dotted line ($x = 0$) shows the position of the critical density. The electrons represented here interact with the laser around its maximum ($t = 22T$). Red trajectories stand for ejected electrons.

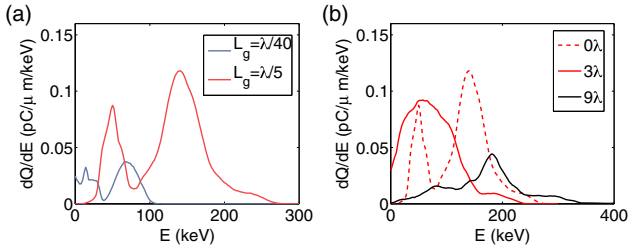


FIG. 4. Simulated ejected electron spectra at the plasma boundary x_b for $L_g = \lambda/40$ (gray line) and $L_g = \lambda/5$ (red line) as they cross the plasma critical surface. (b) Ejected electron spectra for $L_g = \lambda/5$ as they cross the plasma critical surface (dotted line), 3λ and 9λ away from the plasma surface (red and black solid line, respectively).

are pushed towards $x \geq 0$, the electrostatic potential of the remaining ions can be calculated using Poisson's equation $\Delta V_P = -n_c/\epsilon_0 e^{x/L_g}$, and reads $V_P = -n_c L_g^2/\epsilon_0$. Therefore, electrons are expected to gain more energy from the plasma for longer gradients. Figure 4(a) shows the spectrum of ejected electrons when they cross the plasma boundary at x_b. The average energy is much higher for longer gradients, thus confirming our predictions. Hence, the plasma serves as an injector of electrons into the reflecting laser [25]. In order to determine whether the electrons are mainly accelerated in the plasma or in the interference pattern, we plot the simulated electron spectra at the plasma border, at 3.3λ and 9λ away from the plasma in Fig. 4(b). Within this range, no net energy gain can be observed from the electromagnetic wave in vacuum; we conclude that the energy gain is mostly due to acceleration inside the plasma gradient. However, farther away from the plasma at 9λ, the electron spectrum broadens and the tail of the distribution reaches 400 keV, which could be the signature of ponderomotive [13,23] and/or stochastic heating in the interference pattern [38]. The formation of a hole in the experimental electron angular emission profile [see Fig. 2(b)] and the absence of a beaming as seen in Ref. [25] are more evidence that the interaction between the accelerated electrons and the laser is purely ponderomotive. Finally, from simulations and experiments, we also conclude that for $a_0 < 1$ and $L_g \sim 0.1\lambda$ electrons cannot be accelerated by plasma waves related to the CWE mechanism, as suggested in Ref. [11], otherwise, electron and harmonic emission would be optimal simultaneously.

To conclude, we observe for the first time the transition from high-harmonic emission to fast electron ejection as the electron density gradient increases at the surface of a plasma mirror driven at subrelativistic laser intensity. Our measurements reveal that both processes cannot occur simultaneously for the same density gradient. For sharp gradients ($L_g < 0.05\lambda$), electrons drive oscillations in a confined plasma, leading to efficient coherent harmonic emission in their wake. For softer gradients, electrons can be efficiently accelerated out of the plasma by the space-charge field created for $L_g \sim 0.1\lambda$. Although the interaction with the reflected laser field thermalizes the electron population and reshapes the spatial emission profile via ponderomotive interactions, most of the acceleration occurs inside the plasma density gradient. As the gradient length increases by ~40 nm, the plasma mirror behavior switches from a collection of efficient XUV resonators to a nanoscale electron accelerator.

We thank N. Naumova for useful discussions. This work was funded by the Agence Nationale pour la Recherche (under Contracts No. ANR-11-EQPX-005-ATTOLAB and No. ANR-14-CE32-0011-03 APERO), the European Research Council (under Contract No. 306708, ERC Starting Grant FEMTOELEC) and the Région Ile-de-France (under Contract No. SESAME 2012-ATTOLITE). Access was granted to the HPC resources of CINES under allocation 2015-056057 made by GENCI. Simulations were run using EPOCH, which was developed as part of the UK EPSRC funded Project No. EP/G054940/1.

*Corresponding author.
maimouna.bocoum@ensta-paristech.fr

[1] N. Burnett, H. Baldis, M. Richardson, and G. Enright, Appl. Phys. Lett. **31**, 172 (1977).
[2] R. L. Carman, C. K. Rhodes, and R. F. Benjamin, Phys. Rev. A **24**, 2649 (1981).
[3] D. von der Linde, T. Engers, G. Jenke, P. Agostini, G. Grillon, E. Nibbering, A. Mysyrowicz, and A. Antonetti, Phys. Rev. A **52**, R25 (1995).
[4] A. Tarasevitch, A. Orisch, D. Von der Linde, P. Balcou, G. Rey, J.-P. Chambaret, U. Teubner, D. Klöpfel, and W. Theobald, Phys. Rev. A **62**, 023816 (2000).
[5] F. Quéré, C. Thaury, P. Monot, S. Dobosz, P. Martin, J.-P. Geindre, and P. Audebert, Phys. Rev. Lett. **96**, 125004 (2006).
[6] Y. Nomura, R. Hörlein, P. Tzallas, B. Dromey, S. Rykovanov, Z. Major, J. Osterhoff, S. Karsch, L. Veisz, M. Zepf *et al.*, Nat. Phys. **5**, 124 (2009).
[7] J. H. Easter, A. G. Mordovanakis, B. Hou, A. G. Thomas, J. A. Nees, G. Mourou, and K. Krushelnick, Opt. Lett. **35**, 3186 (2010).
[8] A. Borot, A. Malvache, X. Chen, D. Douillet, G. Iaquianiello, T. Lefrou, P. Audebert, J.-P. Geindre, G. Mourou, F. Quéré *et al.*, Opt. Lett. **36**, 1461 (2011).
[9] P. Heißler, R. Hörlein, J. M. Mikhailova, L. Waldecker, P. Tzallas, A. Buck, K. Schmid, C. Sears, F. Krausz, L. Veisz *et al.*, Phys. Rev. Lett. **108**, 235003 (2012).
[10] J. A. Wheeler, A. Borot, S. Monchocé, H. Vincenti, A. Ricci, A. Malvache, R. Lopez-Martens, and F. Quéré, Nat. Photonics **6**, 829 (2012).
[11] S. Bastiani, A. Rousse, J. P. Geindre, P. Audebert, C. Quoix, G. Hamoniaux, A. Antonetti, and J.-C. Gauthier, Phys. Rev. E **56**, 7179 (1997).
[12] F. Brandl, B. Hidding, J. Osterholz, D. Hemmers, A. Karmakar, A. Pukhov, and G. Pretzler, Phys. Rev. Lett. **102**, 195001 (2009).
[13] A. G. Mordovanakis, J. Easter, N. Naumova, K. Popov, P.-E. Masson-Laborde, B. Hou, I. Sokolov, G. Mourou, I. V. Glazyrin, W. Rozmus *et al.*, Phys. Rev. Lett. **103**, 235001 (2009).
[14] C. Thaury, F. Quéré, J.-P. Geindre, A. Levy, T. Ceccotti, P. Monot, M. Bougeard, F. Réau, P. d'Oliveira, P. Audebert *et al.*, Nat. Phys. **3**, 424 (2007).
[15] A. Borot, A. Malvache, X. Chen, A. Jullien, J.-P. Geindre, P. Audebert, G. Mourou, F. Quéré, and R. Lopez-Martens, Nat. Phys. **8**, 416 (2012).
[16] R. Lichters, J. Meyer-ter-Vehn, and A. Pukhov, Phys. Plasmas **3**, 3425 (1996).
[17] T. Liseykina, P. Mulser, and M. Murakami, Phys. Plasmas **22**, 033302 (2015).
[18] F. Brunel, Phys. Rev. Lett. **59**, 52 (1987).
[19] C. Thaury and F. Quéré, J. Phys. B **43**, 213001 (2010).
[20] S. Kahaly, S. Monchocé, H. Vincenti, T. Dzelzainis, B. Dromey, M. Zepf, P. Martin, and F. Quéré, Phys. Rev. Lett. **110**, 175001 (2013).
[21] S. V. Bulanov, N. Naumova, and F. Pegoraro, Phys. Plasmas **1**, 745 (1994).
[22] Y. Tian, J. Liu, W. Wang, C. Wang, A. Deng, C. Xia, W. Li, L. Cao, H. Lu, H. Zhang *et al.*, Phys. Rev. Lett. **109**, 115002 (2012).
[23] N. Naumova, I. Sokolov, J. Nees, A. Maksimchuk, V. Yanovsky, and G. Mourou, Phys. Rev. Lett. **93**, 195003 (2004).
[24] M. Chen, Z.-M. Shenga, J. Zheng, Y.-Y. Ma, M. A. Bari, Y.-T. Li, and J. Zhang, Opt. Express **14**, 3093 (2006).
[25] M. Thévenet, A. Leblanc, S. Kahaly, H. Vincenti, A. Vernier, F. Quéré, and J. Faure, Nat. Phys. **12**, 355 (2015).
[26] J. P. Geindre, R. S. Marjoribanks, and P. Audebert, Phys. Rev. Lett. **104**, 135001 (2010).
[27] W. Wang, J. Liu, Y. Cai, C. Wang, L. Liu, C. Xia, A. Deng, Y. Xu, Y. Leng, R. Li *et al.*, Phys. Plasmas **17**, 023108 (2010).
[28] D. F. Cai, Y. Q. Gu, Z. J. Zheng, W. M. Zhou, X. D. Yang, C. Y. Jiao, H. Chen, T. S. Wen, and S. T. Chunyu, Phys. Rev. E **70**, 066410 (2004).
[29] W. Yu, V. Bychenkov, Y. Sentoku, M. Y. Yu, Z. M. Sheng, and K. Mima, Phys. Rev. Lett. **85**, 570 (2000).
[30] A. Jullien, A. Ricci, F. Böhle, J.-P. Rousseau, S. Grabielle, N. Forget, H. Jacqmin, B. Mercier, and R. Lopez-Martens, Opt. Lett. **39**, 3774 (2014).
[31] A. Borot, D. Douillet, G. Iaquaniello, T. Lefrou, P. Audebert, J.-P. Geindre, and R. Lopez-Martens, Rev. Sci. Instrum. **85**, 013104 (2014).
[32] See Supplemental Material at http://link.aps.org/supplemental/10.1103/PhysRevLett.116.185001 for Experimental setup and Lanex signal deconvolution, which includes Refs [25,33,34,35].
[33] M. Bocoum, F. Böhle, A. Vernier, A. Jullien, J. Faure, and R. Lopez-Martens, Opt. Lett. **40**, 3009 (2015).
[34] Y. Glinec, J. Faure, A. Guemnie-Tafo, V. Malka, H. Monard, J. Larbre, V. De Waele, J. Marignier, and M. Mostafavi, Rev. Sci. Instrum. **77**, 103301 (2006).
[35] A. Jullien, C. Durfee, A. Trisorio, L. Canova, J.-P. Rousseau, B. Mercier, L. Antonucci, G. Cheriaux, O. Albert, and R. Lopez-Martens, Appl. Phys. B **96**, 293 (2009).
[36] A. Tarasevitch, K. Lobov, C. Wünsche, and D. von der Linde, Phys. Rev. Lett. **98**, 103902 (2007).
[37] B. Quesnel and P. Mora, Phys. Rev. E **58**, 3719 (1998).
[38] Z.-M. Sheng, K. Mima, Y. Sentoku, M. S. Jovanović, T. Taguchi, J. Zhang, and J. Meyer-ter-Vehn, Phys. Rev. Lett. **88**, 055004 (2002).



On the physics of electron ejection from laser-irradiated overdense plasmas

M. Thévenet, H. Vincenti, and J. Faure

Citation: Physics of Plasmas **23**, 063119 (2016); doi: 10.1063/1.4954822
View online: http://dx.doi.org/10.1063/1.4954822
View Table of Contents: http://scitation.aip.org/content/aip/journal/pop/23/6?ver=pdfcov
Published by the AIP Publishing

Articles you may be interested in

Giga-electronvolt electrons due to a transition from laser wakefield acceleration to plasma wakefield acceleration
Phys. Plasmas **21**, 123113 (2014); 10.1063/1.4903851

Intense terahertz emission from relativistic circularly polarized laser pulses interaction with overdense plasmas
Phys. Plasmas **20**, 103115 (2013); 10.1063/1.4826508

Self-mode-transition from laser wakefield accelerator to plasma wakefield accelerator of laser-driven plasma-based electron acceleration
Phys. Plasmas **17**, 123104 (2010); 10.1063/1.3522757

Relativistic self-induced transparency effect during ultraintense laser interaction with overdense plasmas: Why it occurs and its use for ultrashort electron bunch generation
Phys. Plasmas **17**, 043102 (2010); 10.1063/1.3368791

Energetic electrons and protons generated from the interaction of ultrashort laser pulses with microdroplet plasmas
Phys. Plasmas **12**, 113105 (2005); 10.1063/1.2135767



Reuse of AIP Publishing content is subject to the terms at: https://publishing.aip.org/authors/rights-and-permissions. Downloaded to IP: 129.104.29.1 On: Tue, 09 Aug 2016 13:59:29

On the physics of electron ejection from laser-irradiated overdense plasmas

M. Thévenet, H. Vincenti, and J. Faure
Laboratoire d'Optique Appliquée, ENSTA ParisTech, CNRS, Ecole Polytechnique, Université Paris-Saclay, 828 bd des Maréchaux, 91762 Palaiseau Cedex, France

(Received 20 April 2016; accepted 12 June 2016; published online 29 June 2016)

Using 1D and 2D PIC simulations, we describe and model the backward ejection of electron bunches when a laser pulse reflects off an overdense plasma with a short density gradient on its front side. The dependence on the laser intensity and gradient scale length is studied. It is found that during each laser period, the incident laser pulse generates a large charge-separation field, or plasma capacitor, which accelerates an attosecond bunch of electrons toward vacuum. This process is maximized for short gradient scale lengths and collapses when the gradient scale length is comparable to the laser wavelength. We develop a model that reproduces the electron dynamics and the dependence on laser intensity and gradient scale length. This process is shown to be strongly linked with high harmonic generation via the Relativistic Oscillating Mirror mechanism. © *2016 Author(s). All article content, except where otherwise noted, is licensed under a Creative Commons Attribution (CC BY) license (http://creativecommons.org/licenses/by/4.0/).*
[http://dx.doi.org/10.1063/1.4954822]

I. INTRODUCTION

The interaction of ultra-high intensity lasers with overdense plasmas is of particular importance for applications such as fast ignition for inertial confinement fusion,[1,2] ion acceleration,[3,4] and high harmonic generation (HHG). In all these fields, electrons accelerated at the front surface are the main pathway for energy transfer between the laser and the plasma,[5] and they also drive most of the physical phenomena of interest. High harmonic generation in this regime is described by the Relativistic Oscillating Mirror (ROM): electrons from the front surface of the solid target form a very dense sheet of electrons which is driven by the intense laser pulse and radiates high harmonics. This interaction offers the opportunity to generate intense attosecond bursts of X-UV radiation which can then be used as a unique tool to probe matter on extreme scales.[6–9]

Harmonic emission via the ROM mechanism is efficient in the *plasma mirror* regime, i.e., when the laser impinges the target at oblique incidence in p-polarization on an overdense plasma with a very short density gradient. Experiments have shown that the electron emission is efficient when the gradient scale length is around $L \simeq \lambda_0/10$, where λ_0 is the laser wavelength.[10] Such solid density plasmas with very short gradients ($L < \lambda_0$) are referred to as *plasma mirrors* because they essentially behave like mirrors that reflect the incident laser pulse with high reflectivity[11] and little spatial deformation, provided the intensity is not too large.[12]

In parallel to HHG, many experiments have measured electrons emitted in the backward direction, i.e., ejected from the front surface of the target toward vacuum. These experiments usually produce large divergence electron beams with energies ranging from hundreds of keV (Refs. 13–17) to few MeV.[18] Some experiments reported on beams emitted in the specular direction,[18] while others reported on beams emitted along the surface[19] or in the normal direction.[20] The diversity in the results can be explained by the fact that these experiments used different gradient scale lengths and intensities. Experiments with a controlled gradient[18,21] as well as numerical simulations showed that the electron emission is more efficient when the gradient scale length is around $L \simeq \lambda_0/10$. Evidently, the gradient scale length is a crucial parameter as it determines the dominant laser absorption mechanism: $\boldsymbol{J} \times \boldsymbol{B}$ heating[22] and vacuum heating[23–25] at short L, resonant absorption[26] at intermediate L, or parametric instabilities at longer L.

Although efficient HHG via the ROM mechanism and electron ejection seem to occur in the same parameter range, almost no effort has been made to understand these emissions as part of the same mechanism. In addition, electron ejection from the front surface is not well understood: several numerical studies report on the subject[27–30] but so far, no theory has been developed in order to explain and predict electron ejection. Some models have been developed in the context of HHG in order to describe the dynamics of the plasma surface,[31,32] but these models are not useful for describing electron emission because of the strong hypothesis that they rely upon.

The goal of this article is to investigate the mechanism of electron ejection for a large range of parameters and to relate it to high harmonic generation. We focus on the case of plasma mirrors, i.e., short density gradients. In Section II, we present a comprehensive numerical study using 1D particle-in-cell (PIC) simulations. These results are used to elaborate a scenario of electron ejection and acceleration, which is described in Section III. In Section IV, we present a 1D model which highlights the main ingredients that are responsible for electron ejection. The model agrees well with the results of the 1D PIC simulations. Finally, Section V extends the study to 2D PIC simulations which confirm the 1D study. It is found that HHG and electron ejection are correlated at short gradient scale lengths.

 © Author(s) 2016.

Reuse of AIP Publishing content is subject to the terms at: https://publishing.aip.org/authors/rights-and-permissions. Downloaded to IP: 129.104.29.1 On: Tue, 09 Aug 2016 13:59:29

II. PARAMETRIC STUDY USING 1D PIC SIMULATIONS

The geometry of the interaction and the notations are depicted in Figure 1(a): x is the direction normal to the target and x–y is the plane of incidence. The electric field of the incident laser pulse $\mathbf{E_i}$ and its wave vector $\mathbf{k}$ are in the x–y plane, while the laser magnetic field is parallel to the z-axis. The laser field impinges the surface with an incident angle θ. This problem is inherently 2D, even in the case where the laser is modeled by a plane wave.

In order to transform this 2D problem into a 1D problem, we move to the boosted frame first introduced by Bourdier,[33] as illustrated in Figure 1(b). This new reference frame S' is obtained by performing a Lorentz transform to a frame moving at $\mathbf{v} = c\sin\theta\mathbf{e_y}$, with c being the velocity of light. Therefore, in the boosted frame, the plasma is no longer at rest but drifts with velocity $\boldsymbol{v_d} = -c\sin\theta\boldsymbol{e_y}$. In addition, it is straightforward to show that the wave vector is now perpendicular to the surface $\boldsymbol{k_0'} = k_0'\boldsymbol{e_x}$ and the incident electric field is along the y-axis: $\mathbf{E_i'} = E_0\cos\theta\mathbf{e_y}$, where E_0 is the laser amplitude in the laboratory reference frame. In the boosted frame, this problem is now purely 1D and can be studied extensively using 1D PIC simulations. In addition, it separates the laser electric field $\boldsymbol{E_i}$, which is along y, from the plasma electric fields, $\boldsymbol{E_p}$ which is now along x.

In the boosted frame, the physical quantities are modified according to the Lorentz transformation. For the laser frequency, lengths along y, and plasma density, this reads

$$\omega_0' = \omega_0\cos\theta, \quad dy' = dy\cos\theta, \quad n' = n/\cos\theta.$$

Accordingly, the laser electric field and laser magnetic field amplitude transform to

$$E_0' = E_0\cos\theta, \quad B_0' = E_0\cos\theta/c.$$

We now adopt the following normalization scheme:

$$t' \equiv \omega_0' t', \quad x' \equiv k_0' x',$$
$$v' \equiv v'/c, \quad p' \equiv p'/m_e c,$$

where m_e is the electron mass. All fields are normalized as follows:

$$E' \equiv \frac{eE'}{m_e\omega_0' c}, \quad B' \equiv \frac{eB'}{m_e\omega_0'},$$

where e is the electron charge. Therefore, in the boosted frame, the normalized electric field amplitude remains unchanged, $a_0' = eE_0'/m_e\omega_0' c = a_0$. Finally, we choose to normalize the density by the critical density in the laboratory frame $n_c = \epsilon_0 m_e\omega_0^2/e^2$ (as opposed to n_c' in the boosted frame): $n' \equiv n'/n_c$. In the following, all quantities are considered in the boosted frame, except if specified otherwise, and for the sake of clarity, the prime symbols will be skipped.

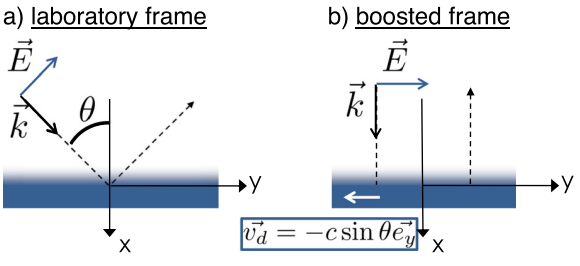


FIG. 1. Geometry of the interaction—(a) in the lab frame—(b) in the boosted frame obtained after a Lorentz transform at velocity $\mathbf{v} = c\sin\theta\mathbf{e_y}$.

The main parameters affecting the emission of backward electrons are (i) the laser amplitude a_0, (ii) the plasma density gradient scale length L, (iii) the angle of incidence θ, and (iv) the pulse duration. In this study, we will restrict ourselves to the case of femtosecond pulse durations, typically 20–30 fs, as used in most current ultra-high intensity experiments. In order to study the role of the main parameters a_0 and L, we performed a set of one hundred 1D particle-in-cell (PIC) simulations, each requiring little computer resources.

In the laboratory frame, a 800 nm, 25 fs laser pulse impinges on a solid-density plasma with an angle of incidence $\theta = 45°$. Its amplitude is varied from $a_0 = 0.2$ to $a_0 = 10$. The plasma bulk density is $250n_c$, corresponding to an ionized SiO_2 target, and the gradient length is varied from $\lambda_0/100$ to λ_0 (i.e., in normalized units $L = 0.04$ to $L = 4.4$). We assume the density gradient to have an exponential shape $n(x) = n_c e^{x/L}$, so that at $x = 0$, the electron plasma density reaches n_c. The density gradient is artificially cut at the plasma edge x_e defined as $n(x_e) = 0.2n_c$. This cutoff verifies $n(x_e) < \cos\theta n_c$, where $\cos\theta n_c$ is the density at which the obliquely incident laser is reflected in the low-intensity regime. The simulations were performed in the boosted frame; hence, numerical conditions are given in this frame: the numerical space-step was $\delta x = 1/700$, and we used 1000 particles-per-cell for good statistics. The simulation box was $\Delta x = 130$ large. Ions were mobile (we took oxygen ions to represent the lightest ions in a Silica target), but simulations with immobile ions yielded very similar results.

When simulating the ejection of electrons with 1D simulations, two effects must be considered. First, the laser does not diffract away, so that the laser intensity is greatly overestimated as soon as the propagation distance is larger than a Rayleigh length. Second, charged particles are represented by charged surfaces. Therefore, the electrostatic force between two charged particles does not depend on the distance r between them, while it decreases in $1/r^2$ in a 3D geometry. As electrons leave the target, the plasma surface becomes positively charged and exerts a recall force that does not depend on the electron position. If one runs a 1D simulation long enough, all electrons will eventually return to the plasma, and the ejected charge will always tend toward zero. In order to obtain realistic results, we chose to consider that electrons are ejected if they cross a plane located at $d = 30$ from the plasma edge (i.e., at $7\lambda_0$ from the plasma edge). This distance was chosen (i) much smaller than the Rayleigh length of most current experiments, so that the 1D approximation remains valid, and (ii) much larger than the gradient lengths we studied, so that electrons are considered to be detected far from the plasma surface. This point is quite crucial as detecting electrons too close to the plasma surface will considerably overestimate the ejected charge, while

Reuse of AIP Publishing content is subject to the terms at: https://publishing.aip.org/authors/rights-and-permissions. Downloaded to IP: 129.104.29.1 On: Tue, 09 Aug 2016 13:59:29

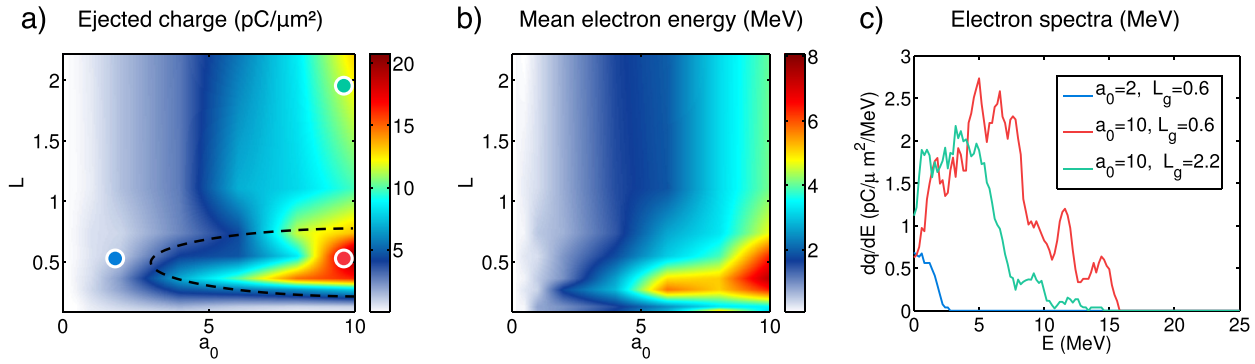


FIG. 2. Results of a 1D PIC simulation scan (a_0,L). (a) Ejected charge. Particles were detected at a distance $d = 30$ from the target, and the charge was integrated all along the simulation. (b) Mean energy of the ejected electrons. (c) Electron spectra from 3 simulations with parameters indicated by the color circles in panel (a).

detecting them too far leads to wrong results due to the invalidity of the 1D approximation.

Figure 2(a) shows the ejected charge as a function of a_0 and L. First, it is clear from Fig. 2 that there are no ejected electrons when the gradient scale length is $L = 0$. This has been explained by the gyromagnetic effect:[34] with $L = 0$, the plasma behaves as a perfect conductor. The magnetic components of the incident and reflected waves are added together, resulting in a strong magnetic field that prevents electrons from escaping the plasma. This effect is neutralized with longer gradient. For a given value of a_0, the ejected charge increases with L, reaches a maximum for $L = L_{max} \simeq 0.4$ (i.e., $\sim\lambda_0/10$), and then slowly decreases. We find that the value of the optimum gradient L_{max} depends little on a_0 in this range. Evidently, the results also show that the ejected charge increases with the laser amplitude a_0. In Fig. 2(b), the mean energy of ejected electrons is plotted in the same parameter space. It varies in a similar fashion as the ejected charge: the higher the ejected charge, the more energetic the electrons. The electron spectrum is plotted on panel (c), for three different simulations represented by the color circles in Fig. 2(a). The red and green curves stand for $a_0 = 8$ and a gradient length, respectively, $L \simeq L_{max}$ and $L \gg L_{max}$. The electron spectra are quite broad, and electron energies are in the few-MeV to 10 MeV range.

These findings agree qualitatively with recent experimental results[18,21] showing that the number of ejected electrons reaches a maximum for a density gradient on the order of $\lambda_0/10$.[21] We also note that at long gradients $L > 2$, the ejected charge increases again, see the green circle in Fig. 2(a). However, we will not focus on the case of longer gradients as we find the ejection mechanism to be quite different from the short gradient case.

In Section III, we will explain the physical mechanism for electron ejection in the regime where $L < 1$. In particular, we will show that the plasma fields due to charge separation at the target surface are keys to accelerating and ejecting electrons.

III. INSIGHTS INTO THE MECHANISM OF ELECTRON EJECTION

Let us now focus on the details of this ejection mechanism. Figure 3 shows the reflected field and the density of ejected electrons at the plasma edge ($x_e = -0.2$) versus time for an optimal case $a_0 = 5$ and $L = 0.55$. Electrons are ejected out of the plasma in the form of a train of attosecond bunches, which are then injected inside the reflected laser pulse at a precise phase, as observed in Refs. 29 and 35. One can clearly see that they leave the plasma at a phase corresponding to a zero of the electric field. Note also that the reflected electric field is extremely distorted and the sharp peaks indicate a rich harmonic content, as expected from high harmonic generation by the ROM mechanism.[11] Besides, the charge contained in each attosecond electron bunch can vary strongly between two consecutive periods, showing that the ejection during one period may affect subsequent periods.

To simplify the problem further, we now focus on the generation of a single attosecond bunch of electrons during a single optical period. We performed a simulation with a top-hat temporal amplitude profile for the incident pulse. In this case, the incident driving fields are simply written as

$$\boldsymbol{E_i} = a_0 \sin(t - x)\boldsymbol{e_y}, \qquad \boldsymbol{B_i} = a_0 \sin(t - x)\boldsymbol{e_z},$$

and the initial electron/ion speed is $\boldsymbol{v} = -\sin\theta\boldsymbol{e_y}$. For $E_i > 0$, the electric force accelerates electrons in the $-y$ direction, allowing them to reach speed $v_y \gtrsim -1$ as soon as $a_0 > 1$.[32] The $\boldsymbol{v} \times \boldsymbol{B_i}$ force is then directed towards the $+x$ direction, so that it pushes electrons which concentrate and form a sharp density peak into the plasma.

This is shown in Fig. 4(a), where a snapshot of the electron density and the fields is plotted as a function of position x. The sharp density peak reaches a maximum depth x_M at

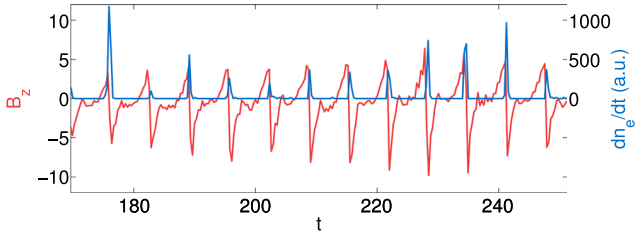


FIG. 3. 1D PIC simulation result for $a_0 = 5$ and $L = 0.55$. Red line: reflected magnetic field at the plasma edge ($x_e = -0.2$) versus time (a Fourier filter was applied to remove the incident field). Blue line: density of ejected electrons versus time at the same position.

Reuse of AIP Publishing content is subject to the terms at: https://publishing.aip.org/authors/rights-and-permissions. Downloaded to IP: 129.104.29.1 On: Tue, 09 Aug 2016 13:59:29

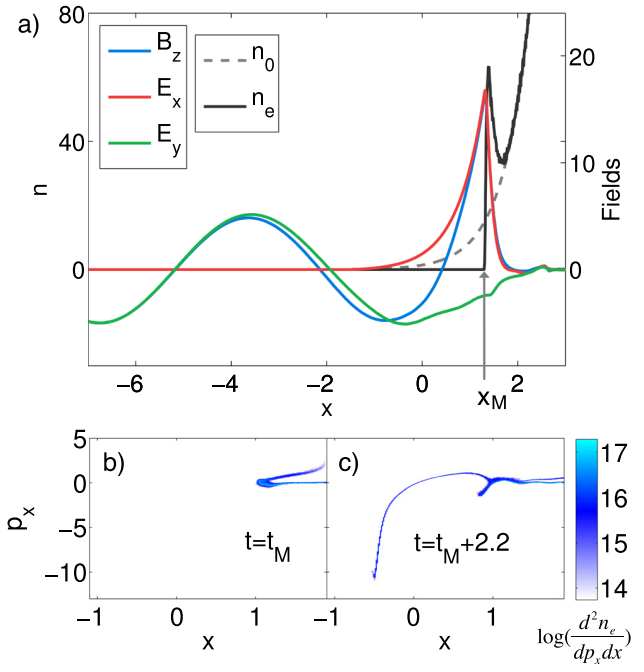


FIG. 4. (a) Density and fields at maximal depth ($t = t_M = 14.7$). The black and dashed grey lines stand for the electron and ion densities, respectively. Color lines are magnetic field B_z (blue), electrostatic field E_x (red), and electric field E_y (green). (b) and (c) Phase space (x,p_x) at $t = t_M$ and $t = t_M + 2.2$, respectively.

t_M, after which it travels back towards the $-x$ direction. Fig. 4(a) shows the density at $t = t_M$, for which all the electrons initially at $x < x_M$ are gathered in the peak. The motion of the density peak during one laser period can be described as a push(i)–pull(ii) mechanism.

(i) Push phase: During the first half-period, the incident laser field pushes electrons inside the plasma while the ions are not displaced, which builds up an electrostatic plasma field $\boldsymbol{E_p}$ along x. Because the plasma is drifting, this charge separation also induces plasma currents which are the source of magnetostatic plasma field $\boldsymbol{B_p}$ along z.

At $t = t_M$, the peak reaches an extremum position with $p_x = 0$. At this point, the forces due to the incident wave, the reflected wave, and the plasma fields cancel out along the x direction. The maximum peak position can be derived from this balance, as presented in Ref. 32 for a step-like density profile. It is hereafter extended to the case of a density gradient, as in Ref. 12.

We first assume that all electrons with initial position $\chi < x$ concentrate in the density peak at x. Therefore, the plasma electrostatic field can be obtained from Maxwell-Gauss equation

$$\frac{\partial E_p}{\partial x} = \frac{1}{\cos^2\theta}(n_i - n_e). \tag{1}$$

By integrating between $-\infty$ and x, we obtain

$$\boldsymbol{E_p} = \frac{1}{\cos^3\theta} L e^{x/L} \boldsymbol{e_x}. \tag{2}$$

Similarly, integrating Maxwell-Ampere's equation gives $\boldsymbol{B_p} = \frac{\sin\theta}{\cos^3\theta} L e^{x/L} \boldsymbol{e_z}$. At the extremum position x_M, the total force along x cancels: $v_y(B_i + B_p) + E_p = 0$. In addition, at x_M, the laser reflects off the surface and we assume that the boundary conditions of a perfect conductor can be applied for the incident and reflected laser fields, so that the y component of the total electric field and the z component of the total magnetic field verify $E_y(x_M, t_M) = 0$ and $B_z(x_M, t_M) = 2a_0$. We further assume that the electron speed in the peak at $t = t_M$ is $\boldsymbol{v} = (0, -1)$. The balance equation along x reduces to

$$2a_0 + \frac{\sin\theta}{\cos^3\theta} L e^{x_M/L} - \frac{1}{\cos^3\theta} L e^{x_M/L} = 0. \tag{3}$$

Solving for x_M, we obtain

$$x_M = L \log\left[\frac{2a_0 \cos^3\theta}{L(1 - \sin\theta)}\right]. \tag{4}$$

This equation gives an estimate of the surface position at maximum depth that fits within less than 20% error in the worst case in the whole parameter range ($0.5 < a_0 < 10$, $0.06 < L < 6$) when compared to PIC simulations. At t_M, the target surface is similar to a plasma capacitor in which electrons are able to gain energy. The maximum fields of this plasma capacitor can be expressed as

$$E_p(t_M, x_M) = \frac{2a_0}{(1 - \sin\theta)}, \tag{5}$$

$$B_p(t_M, x_M) = \frac{2a_0 \sin\theta}{(1 - \sin\theta)}. \tag{6}$$

Clearly, the plasma capacitor has larger fields for large a_0 and incidence angle approaching grazing incidence. Also note that for large angles θ, the plasma fields are larger than the laser fields. From the electric field, one can estimate the maximum energy gain in this plasma capacitor: $\Delta\gamma \simeq E_p(x_M)L \propto a_0 L$.

(ii) Pull phase: During the following half-period, the incident field changes sign so that the $v_y B_i$ force now pulls electrons toward vacuum and breaks the balance of the force along x. The electron peak is then accelerated toward vacuum ($x < 0$) and radiates an attosecond electromagnetic bunch.[36] A small fraction (<1%) of electrons in the density peak escapes the plasma and travels along the reflected pulse. This is shown in Figs. 4(b) and 4(c), where the phase space is represented at $t = t_M$ and $t > t_M$, respectively. For $t > t_M$, one can see a jet of electrons traveling towards vacuum with $x < 0$ and $p_x < 0$.

The orbits of such an electron are detailed in Fig. 5. Panel (a) shows the magnetic field B_z (color scale) and the electron density n_e (grey scale) versus time and space. The electron trajectory is plotted as a dashed yellow line in Fig. 5(a). It originates from deep inside the plasma around $x = x_M$ and is released in the plasma capacitor at $t = t_M$.

The electron velocity components v_x and v_y are plotted in panel (b). The electron drifts with initial speed $v_y = -\sin\theta$, and at t_M, as the laser electric and magnetic fields change sign, it is strongly accelerated toward vacuum in a fraction—typically a tenth—of an optical cycle. It then propagates with $v_x \gtrsim -1$ and oscillates in the interference

Reuse of AIP Publishing content is subject to the terms at: https://publishing.aip.org/authors/rights-and-permissions. Downloaded to IP: 129.104.29.1 On: Tue, 09 Aug 2016 13:59:29

pattern created by the incident and reflected fields, while closely remaining in phase with the reflected field. Panel (c) shows the electric field along the electron trajectory. The initial energy gain is given by the electrostatic field E_x at $t \geq t_M$ until it leaves the plasma. The electric field E_y seen by the electron is the superposition of fast oscillations in the incident field and a slow phase shift in the reflected field. The reflected field along the electron trajectory is represented by the dashed line.

Figure 5 gives insights on the ejection mechanism: (i) electrons are accelerated toward vacuum by the electrostatic field $\boldsymbol{E_p}$ of the plasma capacitor, and (ii) electrons are then able to stay in phase in the reflected field and gain additional energy from the transverse laser field E_y over a long distance via vacuum laser acceleration.[21] After t_M, Figs. 5(b) and 5(c) show that the incident field has relatively little effect other than provoking an oscillation of the transverse velocity.

To confirm that this scenario is valid for all ejected electrons, we compute the work of the electric fields along the trajectories of ejected electrons. The total electric field reads $\boldsymbol{E} = E_p \boldsymbol{e_x} + (E_i + E_r)\boldsymbol{e_y}$ with E_r the laser reflected field amplitude, and the works yield

$$\Gamma_x = -\int_0^t E_p v_x dt, \quad \Gamma_y = -\int_0^t (E_i + E_r) v_y dt, \qquad (7)$$

where Γ_x and Γ_y represent the energy gain due to the plasma field and the laser field respectively.

The result for a large number of electrons is shown in Fig. 6 for the case with $a_0 = 10$ and the optimal gradient $L = 0.55$. For $x = 0$, i.e., around the plasma edge, the energy gain is dominated by Γ_x, which means that it is due to the plasma field $\boldsymbol{E_p}$. On the other hand, as the electrons move away from the plasma surface ($x = -6$), the energy gain is dominated by Γ_y, which shows that additional energy gain occurs in the laser field via vacuum laser acceleration. Finally, at $x = -12$, the average Γ_x is negative, meaning that the recall force from the non-neutral plasma surface is decelerating electrons, an effect which is exaggerated in 1D as discussed previously.

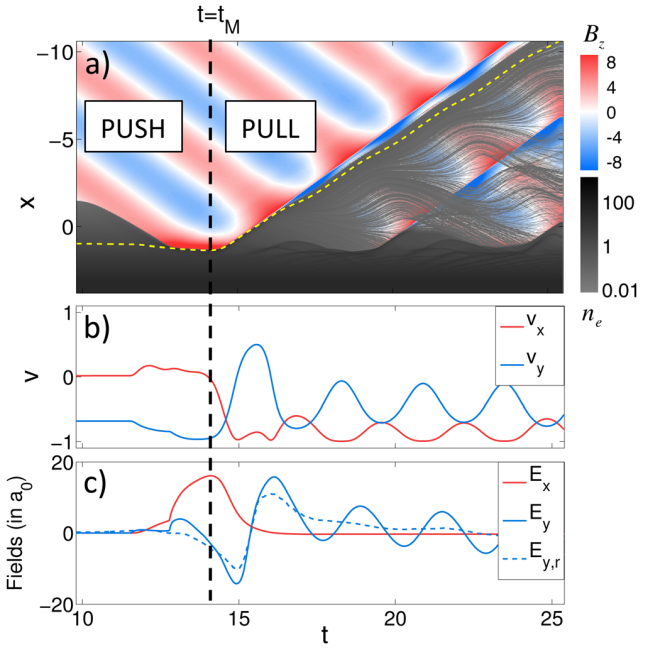


FIG. 5. Dynamics of an ejected electron for parameters $a_0 = 5$ and $L = 0.55$. (a) Greyscale: electron density $n_e(x,t)$. Color scale: magnetic field $B_z(x,t)$. The yellow dashed line represents the trajectory of an ejected electron. (b) Velocity components of the ejected electron. (c) Electric fields seen by the ejected electron along its trajectory.

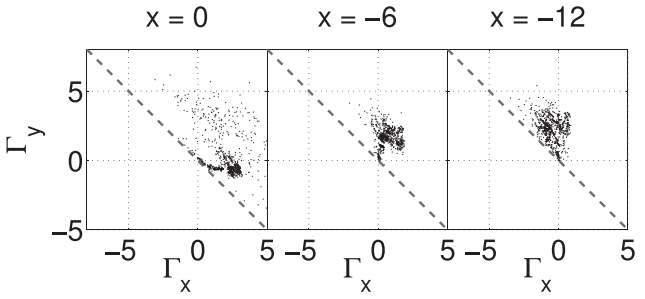


FIG. 6. Work of the electric fields calculated when electrons cross different planes $x = 0$, $x = -6$ and $x = -12$ (simulation parameters are $a_0 = 10$ and $L = 0.55$). The Γ_x represents the energy gain in the plasma field while the Γ_y represents the energy gain in the transverse laser field.

Finally, when the hypothesis $L < 1$ is broken, in particular, when $L \gg 1$, this ejection scenario is not valid anymore. Indeed, the formation of a large density peak does not occur for larger gradients, as shown in Figs. 7(a) and 7(b), where the electron density profile is plotted at $t = t_M$ for a short and a long gradient, respectively. It is readily seen that for the long gradient case, the density in the peak is ten times lower and the width of the peak is also much larger. Consequently, the plasma capacitor does not form and electrons cannot be accelerated efficiently by the plasma field.

IV. SIMPLIFIED 1D MODEL OF ELECTRON EJECTION

In the previous discussion, we found that the energy gain in the plasma capacitor scales as $\propto a_0 L$, explaining qualitatively why the ejected charge increases with L and a_0, in the limit of small gradients. However, a more quantitative model would be useful for estimating the ejected charge and typical ejected energy. Several models have been developed for high harmonic generation,[36,37] surface motion,[32,38,39] or electron jets inside the plasma.[40] However, Ref. 36 does not describe electron dynamics and Ref. 37 assumes that all electrons are gathered on an oscillating surface which cannot

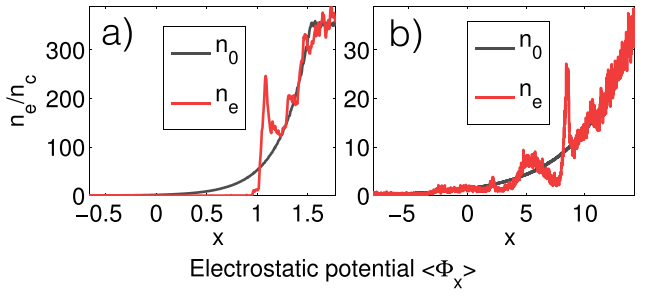


FIG. 7. (a) Electron density at $t = 0$ (black) and $t = t_M$ for $a_0 = 8$ and $L = 0.55$. (b) Same as (a) for $L = 4.4$.

Reuse of AIP Publishing content is subject to the terms at: https://publishing.aip.org/authors/rights-and-permissions. Downloaded to IP: 129.104.29.1 On: Tue, 09 Aug 2016 13:59:29

escape the plasma border. The model developed in Ref. 39 assumes a high density step $n_e \gg n_c$, which is not compatible with a density gradient. Hence, none of them is suitable for describing backward electron acceleration under oblique incidence with a density gradient.

The model developed by Gonoskov in Ref. 32 describes very well the peak dynamics at very large intensity ($a_0 \gg 1$) under oblique incidence and for a step-like density profile. However, the density peak is assumed to always travel at the speed of light $v = 1$, i.e., infinite energy, and the model cannot be used to solve the equations of motion.

We now propose a simple numerical model to illustrate the ejection process during one optical cycle. The incident laser wave is approximated by a monochromatic plane wave with $a_0 > 1$. Ions are immobile. We assume $L \ll 1$ so that electrons are gathered in a density peak of width $d \ll L$. In the boosted frame, the ion density profile reads $n_i(x) = n_0(x) = e^{x/L}/\cos\theta$. We consider an electron in the density peak and describe its motion starting from $t = t_M$. First, the equations of motion for an electron in the density peak are derived. Second, we find the appropriate initial conditions. Third, this set of equations is solved numerically and compared with results of PIC simulations.

Electrons are driven by (i) electromagnetic fields and (ii) plasma fields. We describe the motion of electrons in the density peak during the pull phase, during which the reflected field is generated. The incident laser electric field is written $\boldsymbol{E_i} = -a_0 \sin(t - x + \phi_{M,i})\boldsymbol{e_y}$, where the phase $\phi_{M,i} = x_M - t_M$ is chosen so that the laser field changes sign at (t_M, x_M). For the reflected field, we neglect the harmonic content of the field and simply write $\boldsymbol{E_r} = a_0 \sin(t + x + \phi_{M,r})\boldsymbol{e_y}$ with $\phi_{M,r} = -x_M - t_M$.

Concerning the plasma field, it is crucial to include electron screening in the density peak in order to be able to model the ejected charge. Indeed, when an electron j is located on the front edge of the peak ($x_j = x_M$), it experiences the full plasma field $\boldsymbol{E_p}$ (see Fig. 8). On the contrary, an electron located at $x_j > x_M$ experiences a screened plasma field $\boldsymbol{E_p} - \boldsymbol{E_s}$, where $\boldsymbol{E_s} = E_s\boldsymbol{e_x}$ stands for the electronic screening field, and is less likely to escape the plasma. As seen before, the plasma fields amplitude at the position of electron j, $x_j(t)$ can be obtained by integrating Maxwell-Gauss's equation, giving

$$E_p - E_s = \frac{1}{\cos^2\theta}\left(\int_{-\infty}^{x_j(t)} n_i(x)dx - \int_{-\infty}^{x_j(t)} n_e(x)dx\right).$$

The first term E_p is evidently the unscreened plasma electric field from Eq. (2), while the second term is the screening electric field coming from electrons in the density peak.

Since the shape of the density peak cannot be calculated analytically, the second integral cannot be evaluated easily. Therefore, the screening field E_s is derived by assuming that there is no trajectory crossing:[23] if electrons j and k in the density peak verify $x_j(t_M) < x_k(t_M)$, then $x_j(t) < x_k(t)$ at any time $t \geq t_M$. With this assumption, the number of electrons on the left of electron j, i.e., $x < x_j(t)$, is constant along time (see Figure 8).

Hence, the integral of the electron contribution in the Maxwell-Gauss equation is conserved

$$E_s = \int_{-\infty}^{x_j(t)} \frac{n_e(x,t)}{\cos^2\theta}dx = \int_{-\infty}^{x_j(t_M)} \frac{n_e(x,t_M)}{\cos^2\theta}dx = \sigma_j, \qquad (8)$$

where σ_j is the initial surface charge on the left of electron j. Therefore, the screening field E_s is simply determined by the surface charge σ_j, and there is no need to know the details of the shape of the density peak. This electronic surface charge screens the plasma field E_p and reduces the acceleration of electrons. Note that this screening field is constant in time and therefore it has a considerable effect on the electron trajectories. As the electron peak moves along x and y, it radiates a magnetic field B_s through Maxwell-Ampere equation which is responsible for the reflected field. Neglecting the high harmonics, this radiation comes down to a monochromatic plane wave that we include in the equation of motion. Finally, taking these effects into account, the equation of motion for electron j reads

$$\begin{aligned}\frac{d\boldsymbol{p_j}}{dt} = &+a_0 \sin\big(t - x_j(t) + \phi_{M,i}\big)\big[\boldsymbol{e_y} + \boldsymbol{v_j}(t) \times \boldsymbol{e_z}\big] \\ &-a_0 \sin\big(t + x_j(t) + \phi_{M,r}\big)\big[\boldsymbol{e_y} - \boldsymbol{v_j}(t) \times \boldsymbol{e_z}\big] \\ &-\frac{L}{\cos^3\theta}e^{x_j(t)/L}\big[\boldsymbol{e_x} + \sin\theta\boldsymbol{v_j}(t) \times \boldsymbol{e_z}\big] + \sigma_j\boldsymbol{e_x}. \qquad (9)\end{aligned}$$

The first and second lines are for the incident and reflected waves, the third line is for the plasma capacitor fields, and the last line is the screening field. The initial conditions are taken at $t_0 = t_M$, when electrons in the density peak are located at $x_M < x < x_M + d$. Since $d \ll L$, we assume that all electrons start at $x = x_M$ and use the expression of x_M given above.

The initial momentum of electrons is $p_{x0} = 0$ because at t_M the peak position is extremal. The transverse momentum

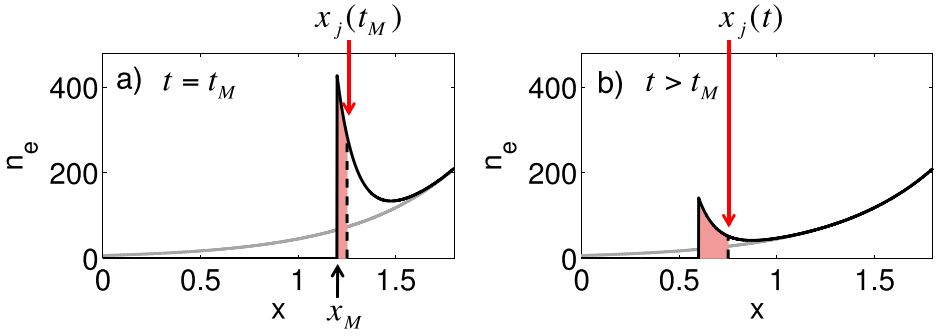


FIG. 8. (a) Sketch of the electron density at $t = t_M$. The black dotted line stands for x_{j0}, the position of electron j at $t = t_M$, the initial time for our model. The red area shows the initial charge on the left of electron j. (b) Same as (a) for $t > t_M$. In agreement with the hypothesis of no trajectory crossing, the charge on the left of electron j is conserved along time: the surface of the red area is the same for all $t \geq t_M$.

Reuse of AIP Publishing content is subject to the terms at: https://publishing.aip.org/authors/rights-and-permissions. Downloaded to IP: 129.104.29.1 On: Tue, 09 Aug 2016 13:59:29

p_y is derived from the conservation of the canonical momentum $P_y = p_y - a_y = P_{y0}$. The peak reaches its maximum depth when the incident field changes sign, i.e., $a(t_M, x_M) = a_0$. The initial conditions are the same for all electrons and read

$$\begin{cases} x_0 = x_M \\ p_{x0} = 0 \\ p_{y0} = -\tan\theta - a_0. \end{cases}$$

Finally, the only difference between electrons j and k is the initial charge on the left side of the electron, i.e., the term σ_j in Equation (9). These equations are solved numerically for different values of σ_j. The ejected charge can be determined by increasing σ_j until a threshold value σ_{max} above which the electron is not ejected; the ejected charge is then simply σ_{max}. An example is given on Fig. 9, where electron trajectories are plotted for $a_0 = 8$ and $L = 0.55$, from a PIC simulation (a) and using the model (b). There is no trajectory crossing in the PIC simulation before $t = 9$, which validates our hypothesis. The global dynamics is very well reproduced.

The following ejection criterion was adopted in the model: an electron is considered to be ejected if p_x is negative during 3 periods. This criterion is different from the one we adopted for PIC simulations because we assumed no trajectory crossing, which is not valid for a large time range.

Figs. 9(c) and 9(d) show the ejected charge plotted versus L and a_0, respectively. The model reproduces the global trends: the charge increases with a_0 and L. It overestimates the ejected charge because the ejection criterion is much more stringent for the PIC simulation than for the model. The linear scaling of ejected charge with a_0 is well reproduced. The scaling with the density gradient does not fit as well, which can be explained by the fact that as $L \to 1$, the plasma capacitor model collapses. Besides, for very large intensities, the ion motion becomes significant and may affect the interaction. Remarkably, our simple model also reproduces the trends and the order of magnitude for the ejected electron energy. This is shown in Figs. 9(e) and 9(f).

To illustrate the role of plasma effects, the model was run with no ion plasma fields (removing the third line in Equation (9), in the same conditions as Fig. 9(c)). The ejected charge never exceeded 1 pC/μm^2, which clearly validates the plasma capacitor model for electron ejection. When we run the model with no reflected field, we find that the ejected charge increases linearly with the gradient scale length L instead of saturating at longer gradients. This shows that the reflected field also plays a role in the details of the ejection.

V. 2D PIC SIMULATIONS

We now show the results of 2D PIC simulations in order to confirm the validity of the 1D study. We also use this more realistic 2D geometry to study the correlation between electron ejection and high harmonic generation. Indeed, the ejected electrons are part of the density peak that oscillates in

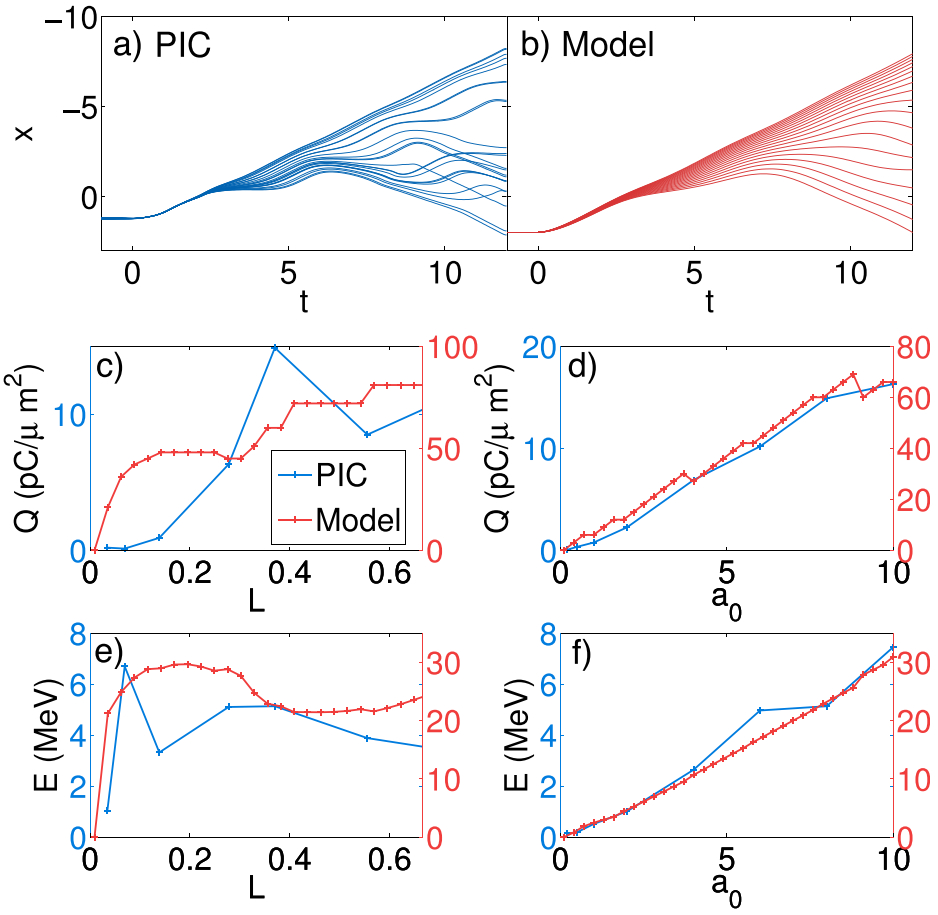


FIG. 9. (a) Electron trajectories from PIC simulation $a_0 = 8$ and $L = 0.55$. (b) Electron trajectories from the model, with the same parameters. In both cases, $t = 0$ stands for t_M. (c) Ejected charge versus L for $a_0 = 8$ from PIC simulations and our model. (d) Ejected charge versus a_0 for $L = 0.36$ from PIC simulations and our model. (e) Same comparisons between the PIC simulations and the model but for the average energy of the ejected electrons.

Reuse of AIP Publishing content is subject to the terms at: https://publishing.aip.org/authors/rights-and-permissions. Downloaded to IP: 129.104.29.1 On: Tue, 09 Aug 2016 13:59:29

the plasma. When this density peak is accelerated toward vacuum, it radiates the reflected field and its high harmonics via the ROM mechanism. Thus, the ejected electrons and the ones that radiate the high harmonics should be closely related and we expect HHG to be correlated to the ejected charge.

The 2D simulations are run in the laboratory frame and the normalization is done as follows:

$$t \equiv \omega_0 t, \quad x \equiv k_0 x,$$
$$v \equiv v/c, \quad p \equiv p/m_e c,$$

with ω_0 and k_0 the laser angular frequency and wave vector in the lab frame, respectively.

Modeling simultaneously electron ejection and HHG in a 2D PIC simulation is challenging. On the first hand, for HHG, one should use a spatial mesh of the order of the Debye length $\Delta x \simeq \lambda_{De} = 0.036\sqrt{\frac{T_{e[\mathrm{keV}]}}{n_{e,max}}}$, where T_e is the plasma electron temperature in keV and $n_{e,max}$ is the maximum electron density. This condition is used for limiting the finite grid instability.[41] In our case, it reads $\Delta x = 10^{-3}$ for an electron temperature $T_e = 0.1$ keV and bulk density $n_0 = 250$.

On the other hand, ejected electrons should be detected far from the plasma surface, at least at a distance larger than the spot size, and ideally larger than the Rayleigh length, which requires a large 2D simulation box size $D = 600$. Satisfying both condition leads to a simulation box with $10^6 \times 10^6$ cells with 10^{11} particles, which is far too large for this study. Hence, we released these conditions and ran the simulations with $n_0 = 100$ and $T_e = 0.1$ keV. The simulation results converge when using a spatial mesh as small as $\Delta x = 0.021$. The simulation box size was $D_x \times D_y = 530 \times 200$.

A 800 nm, laser pulse impinges the solid-density plasma with a $\theta = 45^\circ$ incidence angle. The pulse duration is 25 fs, its spot size is 3.4 μm FWHM, and its amplitude is $a_0 = 3$. We performed simulations for the following gradient scale lengths: $L = 0.2, 0.8, 1.6, 3.1, 6.3$. The ejected electrons are detected with two electron probes. The first one is parallel to the plasma surface and located at a distance of 160 away from the plasma surface to record electrons emitted around the specular direction. The second one is perpendicular to the plasma surface and 160 from the reflection point, to record electrons ejected along the plasma surface.

The 2D simulations reproduce the main phenomena depicted in the 1D PIC simulations: at each optical cycle, electrons are pushed and form a sharp density peak. This gives rise to a plasma capacitor in which electrons gain energy and are ejected. Jets of electrons are ejected at precise phases of the reflected laser field (at zeros of the electric field) and further propagate first in the interference pattern and then in the reflected field.

More qualitative results are shown in Fig. 10. The black line on panel (a) shows the total ejected charge (i.e., on both electron probes) as a function of the gradient length. As previously, the ejected charge increases with the gradient scale length until it reaches a maximum for $L \simeq 1.7$. This qualitatively confirms the observations from the 1D PIC simulations, although the optimal gradient length L_{max} is longer: $\simeq 1.6$ instead of $\simeq 0.5$ in 1D.

Previous experiments showed that for short gradients, electrons are emitted between the normal and specular direction, so that the electron beam is not symmetric around the specular direction. This asymmetry can be explained by the dynamics of electrons in the reflected field while they undergo vacuum laser acceleration.[21]

To take into account this asymmetric emission, the ejected electrons are sorted as a function of their final emission angle. We define Q_-, the ejected charge of electrons with angles $<45^\circ$ (i.e., between the normal and specular directions) and Q_+ as the charge for electrons emitted with angles $>45^\circ$ (i.e., between the specular and grazing directions). Fig. 10(a) shows that Q_- decreases for gradients above $L \simeq 1.7$, while on the contrary Q_+ increases for long gradients. The behavior

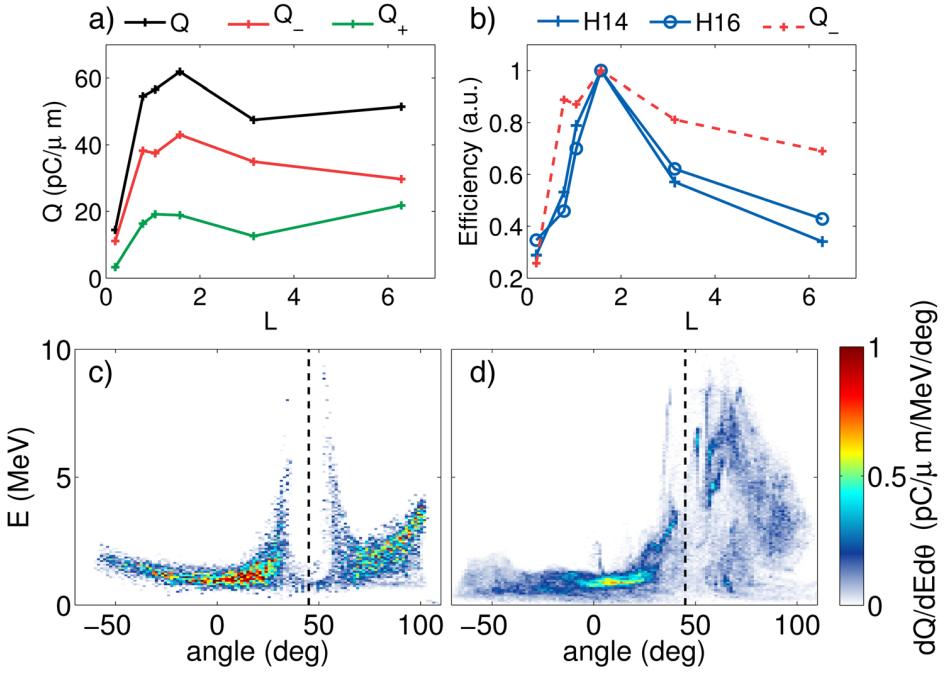


FIG. 10. Results of 2D PIC simulations for $a_0 = 3$ and various gradient lengths. (a) Ejected charge as a function of the gradient length. Electrons are sorted depending on their final emission angle: Q_+ is the charge for electrons with $\theta > 45^\circ$, and Q_- is the charge for electrons with $\theta < 45^\circ$, so that $Q = Q_- + Q_+$. (b) Correlated emission of harmonics and charge Q_-. (c) and (d) Final angle-energy distribution for $L = 0.8$ and $L = 6.3$ respectively. The vertical dashed black line shows the specular direction.

Reuse of AIP Publishing content is subject to the terms at: https://publishing.aip.org/authors/rights-and-permissions. Downloaded to IP: 129.104.29.1 On: Tue, 09 Aug 2016 13:59:29

of Q_- is consistent with the plasma capacitor scenario while the opposite behavior of Q_+ indicates a different ejection mechanism which dominates for longer gradients. These two regimes give rise to significantly different angular distributions, as seen in Figs. 10(c) and 10(d). Panel (c) shows the angle-energy distribution in the case of a short gradient ($L = 0.8$) for which the majority of electrons are ejected with angle $\theta < 45°$. In this case, the ponderomotive force digs a hole close to the specular direction as it pushes electrons away from the laser pulse.[21] Panel (d) shows the case of a longer gradient ($L = 6.3$): more electrons are ejected along the target, indicating a different emission process.

Finally, Fig. 10(b) represents the harmonics signal as a function of the gradient scale length. The harmonics efficiency peaks for $L \simeq 1.8$ and decreases for longer gradients, and follows identical variations as the charge Q_-. This confirms that electron ejection in the plasma capacitor (represented by Q_-) and the high harmonic generation via the ROM mechanism are correlated.

In a very recent work,[17] it was observed that electron ejection and harmonic generation were anti-correlated, as opposed to our present findings. This is because in Ref. 17, the laser intensity was not relativistic ($I < 10^{18}\,\mathrm{W/cm^2}$) and harmonics were generated via a completely different mechanism, the so-called coherent wake emission.[42] In coherent wake emission, the electrons return to the dense plasma and excite a plasma wake which in turn radiates. This mechanism is efficient only when the plasma gradient is sufficiently small ($L \simeq 0.15$),[11] in which case electron ejection does not occur.

VI. CONCLUSION

We have studied the process of electron ejection, or backward emission, when a solid target with a short density gradient is irradiated by an ultra-intense laser at an oblique incidence. An extensive numerical study provides insights into the ejection mechanism in the case of short gradients $L < \lambda_0$. In this case, the laser pushes electrons inside the density gradient and sets up a high density peak of electrons associated with a large charge-separation field, akin to a plasma capacitor. Electrons can gain enough energy in this plasma field to be expelled from the plasma surface into the vacuum and injected into the reflected field in which they eventually gain additional energy. A model is presented for the ejection process, solving the electron dynamics in simplified fields, which reproduces well the trends of PIC simulations. Finally, our 1D study is completed by 2D PIC simulations validating the ejection mechanism and showing that electron ejection is closely correlated to harmonic emission via the Relativistic Oscillating Mirror mechanism.

Electrons accelerated at these plasma surfaces have very specific characteristics: they are emitted with MeV energy, at a given phase of the field and with an attosecond bunch duration. Therefore, these plasma mirrors are ideal for injecting electrons into a laser field and accelerating them via vacuum laser acceleration, as demonstrated in Ref. 21. All these processes result in the generation of a source of MeV electrons with high charge, large divergence, and femtosecond duration. Using few-cycle laser pulses could permit the generation of a single sub-femtosecond electron bunch, which in conjunction with the attosecond harmonics pulse could be used to probe matter in extreme conditions.

ACKNOWLEDGMENTS

This work was funded by the Agence Nationale pour la Recherche (under Contract No. ANR-14-CE32-0011-03 APERO) and the European Research Council (under Contract No. 306708, ERC Starting Grant FEMTOELEC). Access was granted to the HPC resources of CINES and CCRT under Allocation No. 2015-056057 made by GENCI. Simulations were run using EPOCH, which was developed as part of the UK EPSRC funded Project No. EP/G054940/1.

[1]M. Tabak, J. Hammer, M. E. Glinsky, W. L. Kruer, S. C. Wilks, J. Woodworth, E. M. Campbell, M. D. Perry, and R. J. Mason, Phys. Plasmas **1**, 1626 (1994).
[2]S. D. Baton, J. J. Santos, F. Amiranoff, H. Popescu, L. Gremillet, M. Koenig, E. Martinolli, O. Guilbaud, C. Rousseaux, M. R. Le Gloahec *et al.*, Phys. Rev. Lett. **91**, 105001 (2003).
[3]A. Maksimchuk, S. Gu, K. Flippo, D. Umstadter, and V. Y. Bychenkov, Phys. Rev. Lett. **84**, 4108 (2000).
[4]X. H. Yuan, Y. T. Li, M. H. Xu, Z. Y. Zheng, M. Chen, W. X. Liang, Q. Z. Yu, Y. Zhang, F. Liu, J. Bernhardt *et al.*, Phys. Plasmas **15**, 013106 (2008).
[5]W. L. Kruer, *The Physics of Laser Plasma Interactions* (Addison-Wesley Publishing Co., 1988).
[6]M. Drescher, M. Hentschel, R. Kienberger, M. Uiberacker, V. Yakovlev, A. Scrinzi, T. Westerwalbesloh, U. Kleineberg, U. Heinzmann, and F. Krausz, Nature **419**, 803 (2002).
[7]M. Uiberacker, T. Uphues, M. Schultze, A. J. Verhoef, V. Yakovlev, M. F. Kling, J. Rauschenberger, N. M. Kabachnik, H. Schröder, M. Lezius *et al.*, Nature **446**, 627 (2007).
[8]A. L. Cavalieri, N. Müller, T. Uphues, V. S. Yakovlev, A. Baltuška, B. Horvath, B. Schmidt, L. Blümel, R. Holzwarth, S. Hendel *et al.*, Nature **449**, 1029 (2007).
[9]E. Goulielmakis, Z.-H. Loh, A. Wirth, R. Santra, N. Rohringer, V. S. Yakovlev, S. Zherebtsov, T. Pfeifer, A. M. Azzeer, M. F. Kling *et al.*, Nature **466**, 739 (2010).
[10]S. Kahaly, S. Monchocé, H. Vincenti, T. Dzelzainis, B. Dromey, M. Zepf, P. Martin, and F. Quéré, Phys. Rev. Lett. **110**, 175001 (2013).
[11]C. Thaury and F. Quéré, J. Phys. B **43**, 213001 (2010).
[12]H. Vincenti, S. Monchocé, S. Kahaly, G. Bonnaud, P. Martin, and F. Quéré, Nat. Commun. **5**, 3403 (2014).
[13]R. Kodama, K. A. Tanaka, Y. Sentoku, T. Matsushita, K. Takahashi, H. Fujita, Y. Kitagawa, Y. Kato, T. Yamanaka, and K. Mima, Phys. Rev. Lett. **84**, 674 (2000).
[14]L. M. Chen, J. Zhang, Y. T. Li, H. Teng, T. J. Liang, Z. M. Sheng, Q. L. Dong, L. Z. Zhao, Z. Y. Wei, and X. W. Tang, Phys. Rev. Lett. **87**, 225001 (2001).
[15]Y. T. Li, J. Zhang, Z. M. Sheng, H. Teng, T. J. Liang, X. Y. Peng, X. Lu, Y. J. Li, and X. W. Tang, Phys. Rev. Lett. **90**, 165002 (2003).
[16]D. F. Cai, Y. Q. Gu, Z. J. Zheng, W. M. Zhou, X. D. Yang, C. Y. Jiao, H. Chen, T. S. Wen, and S. T. Chunyu, Phys. Rev. E **70**, 066410 (2004).
[17]M. Bocoum, M. Thévenet, F. Böhle, B. Beaurepaire, A. Vernier, A. Jullien, J. Faure, and R. Lopez-Martens, Phys. Rev. Lett. **116**, 185001 (2016).
[18]A. G. Mordovanakis, J. Easter, N. M. Naumova, K. Popov, P.-E. Masson-Laborde, B. Hou, I. Sokolov, G. Mourou, I. V. Glazyrin, W. Rozmus *et al.*, Phys. Rev. Lett. **103**, 235001 (2009).
[19]M. Chen, Z. M. Sheng, J. Zheng, Y. Y. Ma, M. A. Bari, Y. T. Li, and J. Zhang, Opt. Express **14**, 3093 (2006).
[20]Y. T. Li, J. Zhang, L. M. Chen, Y. F. Mu, T. J. Liang, Z. Y. Wei, Q. L. Dong, Z. L. Chen, H. Teng, and S. T. Chun-Yu, Phys. Rev. E **64**, 046407 (2001).
[21]M. Thévenet, A. Leblanc, S. Kahaly, H. Vincenti, A. Vernier, F. Quéré, and J. Faure, Nat. Phys. **12**, 355 (2015).
[22]W. L. Kruer and K. Estabrook, Phys. Fluids **28**, 430 (1985).
[23]F. Brunel, Phys. Rev. Lett. **59**, 52 (1987).
[24]L. M. Chen, J. Zhang, Q. L. Dong, H. Teng, T. J. Liang, L. Z. Zhao, and Z. Y. Wei, Phys. Plasmas **8**, 2925 (2001).

Reuse of AIP Publishing content is subject to the terms at: https://publishing.aip.org/authors/rights-and-permissions. Downloaded to IP: 129.104.29.1 On: Tue, 09 Aug 2016 13:59:29

[25]L. M. Chen, M. Kando, M. H. Xu, Y. T. Li, J. Koga, M. Chen, H. Xu, X. H. Yuan, Q. L. Dong, and Z. M. Sheng, Phys. Rev. Lett. **100**, 045004 (2008).
[26]D. W. Forslund, J. M. Kindel, K. Lee, E. L. Lindman, and R. L. Morse, Phys. Rev. A **11**, 679 (1975).
[27]H. Ruhl, Y. Sentoku, K. Mima, K. A. Tanaka, and R. Kodama, Phys. Rev. Lett. **82**, 743 (1999).
[28]Z. M. Sheng, Y. Sentoku, K. Mima, J. Zhang, W. Yu, and J. Meyer-ter-Vehn, Phys. Rev. Lett. **85**, 5340 (2000).
[29]N. M. Naumova, I. Sokolov, J. Nees, A. Maksimchuk, V. Yanovsky, and G. Mourou, Phys. Rev. Lett. **93**, 195003 (2004).
[30]J.-P. Geindre, R. S. Marjoribanks, and P. Audebert, Phys. Rev. Lett. **104**, 135001 (2010).
[31]T. Baeva, S. Gordienko, A. P. L. Robinson, and P. A. Norreys, Phys. Plasmas **18**, 056702 (2011).
[32]A. A. Gonoskov, A. V. Korzhimanov, A. V. Kim, M. Marklund, and A. M. Sergeev, Phys. Rev. E **84**, 046403 (2011).
[33]A. Bourdier, Phys. Fluids **26**, 1804 (1983).
[34]J.-P. Geindre, P. Audebert, and R. S. Marjoribanks, Phys. Rev. Lett. **97**, 085001 (2006).
[35]Y. Tian, J. Liu, W. Wang, C. Wang, A. Deng, C. Xia, W. Li, L. Cao, H. Lu, H. Zhang *et al.*, Phys. Rev. Lett. **109**, 115002 (2012).
[36]T. Baeva, S. Gordienko, and A. Pukhov, Phys. Rev. E **74**, 046404 (2006).
[37]R. Lichters, J. Meyer-ter-Vehn, and A. Pukhov, Phys. Plasmas **3**, 3425 (1996).
[38]J. Sanz, A. Debayle, and K. Mima, Phys. Rev. E **85**, 046411 (2012).
[39]A. Debayle, J. Sanz, and L. Gremillet, Phys. Rev. E **92**, 053108 (2015).
[40]H. Ruhl, J. Opt. Soc. Am. B **13**, 388 (1996).
[41]C. K. Birdsall and A. B. Langdon, *Plasma Physics via Computer Simulation* (CRC Press, 2004).
[42]F. Quéré, C. Thaury, P. Monot, S. Dobosz, P. Martin, J.-P. Geindre, and P. Audebert, Phys. Rev. Lett. **96**, 125004 (2006).

Reuse of AIP Publishing content is subject to the terms at: https://publishing.aip.org/authors/rights-and-permissions. Downloaded to IP: 129.104.29.1 On: Tue, 09 Aug 2016 13:59:29

université PARIS-SACLAY | ÉCOLE DOCTORALE Ondes et Matière (EDOM)

Titre : Modélisation de la réflexion d'une impulsion laser sur un miroir plasma dans le régime relativiste : de l'accélération d'électrons à la génération d'harmoniques

Mots clefs : laser femtoseconde, plasma, électrons relativistes

Résumé : Lorsqu'une impulsion laser est focalisée à une intensité relativiste sur une cible solide, le matériau est instantanément ionisé et forme un miroir plasma, c'est-à-dire un plasma surdense avec un court gradient de densité sur sa face avant. La réflexion de l'impulsion laser génère alors des harmoniques élevées dans l'impulsion réfléchie, et des électrons peuvent être accélérés hors de la cible. Si la génération d'harmoniques est bien comprise, la dynamique des électrons éjectés restait, à ce jour, mal expliquée. Cette thèse théorique et numérique révèle cette dynamique en suivant trois axes de recherche. D'abord, à l'aide de simulations numériques de type particle-in-cell, nous identifions le mécanisme d'éjection des électrons de la surface à l'échelle du cycle optique. Nous montrons qu'il existe une longueur de gradient optimale pour l'éjection d'électrons, ce qui a été vérifié sur deux lasers femtosecondes (le laser de la *Salle Noire* au LOA et le laser UHI100 au CEA). Ensuite, après l'éjection du plasma, les électrons peuvent être accélérés par les champs laser de l'impulsion réfléchie par un processus appelé *accélération laser dans le vide* (VLA). Nous montrons que ce mécanisme a permis d'accélérer des faisceaux d'électrons de charge élevée (3 nC) jusqu'à des énergies relativistes (10 MeV) lors d'expériences sur UHI100. Finalement, nous expliquons comment l'éjection d'électrons est corrélée avec l'effet du Miroir Oscillant Relativiste qui produit des harmoniques dans le régime de très haute intensité.

Title: Modeling the interaction between relativistic laser pulses and plasma mirrors: from electron acceleration to harmonic generation

Keywords: femtosecond lasers, plasmas, relativistic electrons

Abstract: When a laser pulse with a relativistic intensity is focused onto a solid target, the material is instantly ionized and forms a plasma mirror, an overdense plasma with a short density gradient on its front side. During the laser pulse reflection, high harmonics are generated in the reflected pulse, and electrons can be accelerated out of the target. While the mechanisms for high harmonic generation (HHG) are well-known, the acceleration of electrons remained unclear. This theoretical and numerical thesis unravels the mechanisms for ejection and acceleration of electrons, following three research lines. First, using particle-in-cell numerical simulations, we identify the ejection mechanism. We show that there is an optimal gradient length for electron ejection, which was verified in experiments on two femtosecond ultraintense lasers: the *Salle Noire* laser at LOA and UHI100 at CEA. Second, after being ejected from the plasma surface, electrons can be accelerated by the laser fields in the reflected pulse via the *Vacuum Laser Acceleration* (VLA) mechanism. We show that this mechanism lead to high-charge (3 nC) electron beams with relativistic energy (10 MeV) during experiments on the UHI100 laser. Finally, we demonstrate that electron ejection is inherently linked with the Relativistic Oscillating Mirror effect responsible for HHG in the high-intensity regime.

Université Paris-Saclay
Espace Technologique / Immeuble Discovery
Route de l'Orme aux Merisiers RD 128 / 91190 Saint-Aubin, France